

Force Identification using Extracted Modal Parameters,
with Applications to Glide Height Testing
of Computer Hard Disks

by

John Charles Briggs

B.S. Mech. Eng. M.I.T. 1986
M.S. Mech. Eng. M.I.T. 1988

Submitted to the Department of
Mechanical Engineering
in Partial Fulfillment of the Requirements
for the Degree of

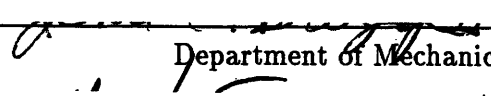
Doctor of Philosophy
in
Mechanical Engineering

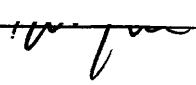

at the


Massachusetts Institute of Technology

February 1991

©Massachusetts Institute of Technology, 1991
All Rights Reserved

Signature of Author _____

Department of Mechanical Engineering
February 1991

Certified by _____


Dr. Ming-Kai Tse
Committee Chairman

Accepted by _____

Professor Ain A. Sonin
Chairman, Graduate Committee
Department of Mechanical Engineering

MASSACHUSETTS INSTITUTE
OF TECHNOLOGY

APR 26 1991

LIBRARIES

Force Identification using Extracted Modal Parameters, with Applications to Glide Height Testing of Computer Hard Disks

by

John Charles Briggs

Submitted to the Department of Mechanical Engineering
in February 1991 in partial fulfillment of the
requirements for the Degree of Doctor of Philosophy
in Mechanical Engineering

Abstract

There are a great number of engineering problems where direct measurement of forces is not possible. These situations can arise if the environment where the measurement is to be made is either hostile or inaccessible for the placement of a force transducer. Under such conditions, we may be limited to estimating the forces by means of vibration sensors mounted on the structure remote from the source.

This thesis presents a new technique for estimating forces from vibration signals. The technique can be used even when the force location is not known a priori. The basic principle of the technique is that when an impulse force (e.g. an impact) excites a structure, it excites different vibration modes at unequal levels depending on the location at which the impulse excites the structure. As a result, the frequency response of the structure creates a different *pattern* for each force input location on the structure. Thus, it is possible to determine the location of the input force, simply by looking at the vibration patterns of the structure in the frequency domain. To quantify the vibration patterns, a technique known as modal parameter extraction is used. The technique extracts a modal constant for each mode of vibration in the frequency range of interest. Modal constants extracted from experimental data can be compared using pattern matching to a database of known patterns of modal constants, to estimate the impact location. The magnitude of the experimental force impulse can then be determined by the relative scaling between the database and the experimentally extracted modal constants.

This *force identification technique* was demonstrated with an application to quality control of computer hard disk drives. During operation, the read/write head (slider) of a hard disk drive is separated from the disk surface by an air bearing. Impacts can occur between the slider and large asperities on the disk surface. There is currently no way to directly measure these impact forces, so they must be estimated from vibration signals generated by the head/disk impacts. The force identification technique was applied to this problem, and found to be able to determine both the location of impact and the magnitude of the impact force. It was found that the phase information in the vibration signal is very important in determining the correct impact location.

Thesis Committee: Dr. Ming-Kai Tse, Chairman
Professor Richard H. Lyon
Professor Ernest Rabinowicz
Professor Derek Rowell

Acknowledgments

The research presented in this thesis would not have been possible without the aid of a great number of people.

I would first and foremost like to thank Dr. Ming-Kai Tse, my thesis advisor. The limited space here really does not allow me to express the number of ways that he has helped me, but I will try to hit the highlights. Dr. Tse not only advised me for this thesis, but for my B.S. and M.S. theses as well. He has managed to secure funding for me, without which graduate school would not have been possible. Guidance and advice have always been at close reach, despite his very busy schedule. Thank you Ming.

In addition to Dr. Tse, my thanks goes out to the other three members of my committee, Prof. Derek Rowell, Prof. Richard H. Lyon, and Prof. Ernest Rabionwicz. Their advice helped shape the direction of my thesis.

I am also grateful to the IBM Corporation (San Jose, CA) for their financial support of this project. The interest of Ben Hu, Sylvia Lee, Sam So and others was of great help in directing my research. The Nashua Corp. also supported me early in my research. Their contribution of finances, instrumentation, and hard disk supplies is most appreciated.

The most direct assistance to my research came from Mun-Kee Chang, my research partner. He deserves particularly to be recognized for his suggestion of using modal analysis and also for his experiments with the ball impact technique on the small 3380 slider.

This research was performed at the M.I.T. Laboratory for Manufacturing and Productivity (LMP). I would like to thank all the people at LMP that have helped me over the last three years including, Cliff Federspiel, Peng Yun Gu, Matt Besen, Thomas Malone, Hyun-Ju Vega, Jae-Bok Song, Fred Cote, and Georgia Nagle.

The advice of family always plays a big role in shaping ones future, particularly in the choice of college. It would not have been possible for me to attend M.I.T. as an undergraduate if it were not for the assistance, both financial and moral, of my parents, June and Charles Briggs. It would have also been very difficult to withstand the intense challenges of M.I.T. without the support of my loving wife Sue Ellen. When I decided to go to graduate school, it was with Sue Ellen's support and consent. However, I do not think that she realized that it would take so long and require her to sacrifice so much.

This thesis was prepared using PCT_EX by Personal Tex Inc., on a Compaq 386 and an IBM PS/2 50Z. The figures were created using Corel Draw. Many of the graphs were made by Matlab and Lotus 123 and then imported into Corel Draw. Most of the figures in Chapter 2 were scanned into the PC, traced with Corel Trace, and then extensively touched up inside Corel Draw.

Contents

Abstract	2
Acknowledgments	3
1 Introduction	11
1.1 General Introduction	11
1.2 Scope of Thesis	12
1.3 Outline of Thesis	12
2 Literature Review	14
2.1 Scope	14
2.2 Force Identification Techniques	15
2.2.1 Accelerance Method	17
2.2.2 Modal Model Method	19
2.3 Acoustic Emission Research	22
2.3.1 Materials Testing	23
2.4 Glide Height Testing Research	25
2.4.1 Impact Modeling	29
2.4.2 Acoustic Emission	34
2.5 Summary	36
3 FEM and Modal Analysis	37
3.1 Introduction	37
3.2 Finite Element Modeling of Dynamic Systems	37
3.3 Modal Analysis	40
3.4 FEM Model of 3380 Slider	43
3.5 Modal Analysis of 3380 Slider	48
3.6 Glide Height Tests on Bump Disks	58
3.7 Ball Impact Tests on 3380 Slider	65
3.8 Ball Impact Tests on an Enlarged Slider	69
3.8.1 Hertzian Contact Analysis for Nylon Ball Drops	74

3.8.2	Nylon Ball Drops on Force Transducer	84
3.8.3	Calculation of FRF's Based on Hertz Contact Force Data.	88
3.8.4	Comparison of FEM/Modal Analysis and Ball Drop Data.	88
3.9	Summary	92
4	Force Identification Technique	94
4.1	Overview of Technique	94
4.2	Modal Parameter Extraction	96
4.2.1	Magnitude Only Technique	98
4.2.2	Magnitude and Phase Technique	105
4.3	Pattern Matching	124
4.4	Summary	127
5	Application to Glide Height Testing	129
5.1	The Use of Force Identification in Glide Height Testing	129
5.2	Results of the Magnitude Only Technique	130
5.3	Results of the Magnitude and Phase Technique	133
5.4	Comparison of the Two Techniques	145
5.5	Summary	147
6	Discussion	149
6.1	Strengths and Limitations of the New Technique	149
6.2	Summary	154
7	Conclusions	155
	Bibliography	157
A	Hertzian Contact Analysis	160
A.1	Ball Drop on a Semi-infinite Elastic Half-Space	164
A.2	Analysis for a 0.28 mm Ball Drop on 3380 Slider	165
B	FFT's on Transient Signals	169
B.1	Application to Ball Drop	174
C	Input File for FEM Model of Slider	178
D	Programs for Modal Analysis and Force Identification	183
D.1	Modal Analysis Programs	183
D.1.1	ABA_READ.C	183
D.1.2	S380TLAC.M	196
D.1.3	S380.M	201
D.1.4	MODAL.M	202

D.1.5	FRF_ACC.M	203
D.2	Force Identification using Magnitude and Phase	204
D.2.1	USCO2MAT.M	205
D.2.2	RE_TAPER.M	206
D.2.3	FIND_ALL.M	213
D.2.4	PATMATCH.M	219

List of Figures

2.1	The effects of smoothing transfer functions. (From Lyon 1987)	16
2.2	Modal model force identification procedure applied to a beam. (From Hollandsworth 1989)	21
2.3	Force identification on a truss structure using the spectral method. (From Doyle and Farris 1989)	24
2.4	Sketch of a typical head gimbal assembly (HGA) and 3380 style slider.	27
2.5	Sketch of an asperity contacting the slider.	28
2.6	Two dimensional and three dimensional defect maps of the disk surface.	30
2.7	Coefficient of restitution model of slider/asperity impact. (From Benson 1987)	32
2.8	AE transducers mounted on the HGA. (From Yeack-Scranton 1986)	35
3.1	Sketch of a 20-node brick element.	38
3.2	Diagram of 3380 Slider.	44
3.3	FEM Model of 3380 slider.	45
3.4	Mode shapes of 3380 slider.	46
3.5	Comparison of different FEM models of the slider.	47
3.6	PZT mounted on the top of the slider and AET transducer mounted at the arm.	50
3.7	Sensor and input locations on slider.	51
3.8	FRF's for input locations 3001 - 3013 with sensor at location 15251. Linear scale.	52
3.9	IBM AE glide height testing.	53
3.10	FRF's for input locations 3001 - 3013 with sensor at location 15251. Log scale.	55
3.11	Comparison of FRF's for sensors at locations 15251 and 9251. Linear scale.	56
3.12	Comparison of FRF's for sensors at locations 15251 and 9251. Log scale.	57
3.13	Change of modal constants with impact location.	59
3.14	Change of modal constants for both friction and normal forces.	60
3.15	Schematic of glide height test equipment.	62
3.16	Profile of bump disk.	63
3.17	AE glide height data.	64
3.18	Experimental setup for ball impact tests on 3380 slider.	66
3.19	FRF's from ball drop tests on 3380 measured using an AET Pico transducer.	67
3.20	Schematic of HGA with two PZT sensors mounted on it.	70

3.21	FRF's measured from a PZT on the slider and PZT at the base of the HGA.	71
3.22	Diagram of enlarged aluminum slider showing the dimensions.	72
3.23	Diagram of input and sensor locations for the enlarged aluminum slider.	73
3.24	Schematic of ball drop apparatus for enlarged slider.	75
3.25	Acceleration versus time traces for 6.35, 12.70, and 25.4 mm diameter nylon balls.	76
3.26	FFT's of the ball drop data.	77
3.27	Semilog plot of FFT's of the ball drop data.	78
3.28	Data from Hertzian contact analysis for a 6.35 mm (1/4") nylon ball.	79
3.29	Data from Hertzian contact analysis for a 12.7 mm (1/2") nylon ball.	80
3.30	Data from Hertzian contact analysis for a 25.4 mm (1") nylon ball.	81
3.31	Effect of sampling rate on Hertz contact force data.	83
3.32	FFT's of nylon ball drop forces calculated from Hertzian contact theory.	85
3.33	Schematic of experimental setup for ball drop tests on force transducer.	86
3.34	Contact forces for nylon ball drop tests on force transducer.	87
3.35	FRF's for 6.35, 12.7, and 25.4 mm nylon ball drops.	89
3.36	Logarithmic FRF for 6.35, 12.7, and 25.4 mm nylon ball drops.	90
3.37	Theoretically and experimentally determined FRF's for enlarged slider.	91
4.1	Preview of force identification technique.	95
4.2	Sample acceleration data.	102
4.3	Sample acceleration data with assumed phase information.	103
4.4	Sample acceleration data converted to real numbers and weak points removed.	104
4.5	Comparison of the sample acceleration data and the reconstructed FRF curve.	106
4.6	Demonstration of linear phase taper.	107
4.7	Frequency response and modal constants for an example system.	109
4.8	Acceleration signal showing the effects of sampling.	110
4.9	Acceleration signal A showing the effects of shifting the origin.	111
4.10	Acceleration signal B showing the effects of shifting the origin.	112
4.11	One percent noise added to the acceleration signal.	114
4.12	Demonstration of a procedure for removing linear phase taper.	115
4.13	Nyquist plot of receptance showing the circle-fit method.	118
4.14	Determining the resonance frequency.	120
4.15	Determining the loss factor η_r	123
4.16	Block diagram of force identification technique.	128
5.1	Experimental setup for ball drop tests on the enlarged slider.	131
5.2	Impact forces created by nylon ball drops.	132
5.3	Patterns of modal constants.	134
5.4	Error plots from pattern matching of ball drop tests from 76 mm height.	135
5.5	Error plots from pattern matching of ball drop tests from 152 mm height.	136
5.6	Error plots from pattern matching of ball drop tests from 305 mm height.	137

5.7	Forces estimated from pattern matching.	138
5.8	Experimental setup with photosensor added.	139
5.9	Illustration of pattern match with phase data.	141
5.10	Error plots for pattern matching with phase, locations 1-7.	142
5.11	Error plots for pattern matching with phase, locations 8-14.	143
5.12	Forces estimated for pattern matching with phase.	144
5.13	Error plots for an impact at a location between 2 and 3.	146
6.1	Phase diagrams of the slider showing the effect of including different modes in the pattern matching.	153
A.1	Impulse input approximated by a half-sine pulse.	161
A.2	Two balls coming into dynamic contact.	163
A.3	Deflection vs time for 0.28 mm carbide ball dropped on an Al ₂ O ₃ TiC slider. . . .	167
A.4	Force vs time for 0.28 mm carbide ball dropped on an Al ₂ O ₃ TiC slider.	168
B.1	A second order system and its impulse response.	170
B.2	Response of a second order system calculated for 256, 512, and 1024 points. . . .	172
B.3	Receptance of a second order system calculated 512 points.	173
B.4	Receptance of a second order system calculated 1024 points.	175
B.5	Possible error in input location.	176
B.6	Error in receptance caused by error in force input waveform.	177

List of Tables

2.1	Engine forces predicted using accelerance algorithm. (From Starkey 1989) A unit force is applied at one location, location 4, in the x direction. Forces are predicted at one, two, and three locations. The difference between the actual and predicted force is the error.	18
3.1	Natural frequencies of 3380 slider.	48
3.2	Comparison of natural frequencies of 3380 slider determined by FEM and by ball impact experiment.	68
3.3	Mechanical Properties of nylon 66 and Aluminum.	82
3.4	Peak contact forces for nylon balls dropped from a height of 305 mm onto an aluminum surface.	84
3.5	Contact time for nylon balls.	88
3.6	Comparison of natural frequencies of enlarged slider determined by FEM and by experiment.	92
4.1	Finite difference table for determining the location of the natural frequency. . . .	121
A.1	Mechanical Properties of Tungsten Carbide and Al_2O_3TiC	165

Chapter 1

Introduction

1.1 General Introduction

In vibration analysis, it is a common situation to be only able to measure the vibration of a system without being able to directly measure the source of the vibration. It is, in principle, possible to determine these inputs using a system model and the measured vibration of the system. This is known as an *inverse problem*.

This thesis is concerned with vibration problems where the input source location and magnitude are unknown, but the input source is known to be a very short force pulse. This type of input is fairly common in vibration problems and is typically the result of impact between two objects. In machine components, it may be the result of gear teeth meshing or parts being formed. Impact can also result when manufactured parts are dropped into a bin or a chute. In all these situations it would be difficult or impossible to directly measure the forces created at impact. Thus, if these forces are of interest, they must be estimated from vibration measurements taken at some distance away from the source of the vibration.

Another area where this problem is of interest, is acoustic emission (AE) monitoring. Acoustic emission is the name given to the high frequency sound that a piece of material gives off when it deforms or fractures. For example, when metal is deformed, micro-mechanical deformation of the solid occurs. As dislocation lines pass over each other or large particles are sheared, each deformation event radiates some of the deformation energy away in the form of structure-borne sound. Unfortunately, these events occur within the body of the solid metal and cannot be monitored directly. The events can only be monitored by vibration transducers (AE transducers) mounted on the outside surface of the test specimen. The characteristics and locations of these events must be estimated from the vibration measurements.

In any of these problems, the goal is to estimate the magnitude of a pulse (or impact) force source from remote vibration measurements, i.e. to solve the inverse problem. This would seem like an easy task, considering all that is available in dynamic Finite Element Modeling (FEM) software, but it is not. When a forward problem is being solved, it is worked from cause to effect. The force is applied to the body and the vibration response is calculated from

the equations of elasticity and dynamics. But, when an inverse problem is being solved, it is worked backward from effect to cause. This has two major difficulties. The first is that small errors in vibration measurements may become large errors in the calculated force. The second is that force sources at different locations can result in the same levels of measured vibration. Thus with an inverse problem, solutions may not be unique.

1.2 Scope of Thesis

In this thesis an alternative way is offered to solve this class of inverse problems (hereafter referred to as Force Identification Problems). The technique uses the combined techniques of modal parameter extraction and pattern matching to try to solve problems where the source is an impulse force with unknown location and unknown magnitude. The key to its ability to solve the force identification problem comes from the fact that it assumes that the force source is of a very simple type, i.e. a pulse. A pulse is very simple because, if thought of in the frequency domain, it is nearly a constant for low frequencies. Thus one can simplify the force identification process by limiting the form of the solution. The experimental results presented in later chapters show that the technique can accurately predict impact force magnitude and location despite substantial noise in the vibration data.

The force identification technique, presented in this thesis, was developed in response to a need in a specific application, although it may be useful in many other situations. The application of interest in this research was to identify the impact force in a read/write head of a hard disk, when the head impacts a bump on the disk surface. This application is of considerable interest in the magnetic hard disk manufacturing industry and, in-particular, in a quality control (QC) technique known as glide height testing.

In hard disks, the read/write head (or slider) does not actually touch the disk surface during operation. It is isolated from the disk surface by a dynamic air bearing. If, however, there are asperities on the disk surface, then the air bearing may not be able to isolate the slider from the disk. To assure that the disk is free from unwanted asperities, the disk manufacturers perform glide height tests on the disks. In glide height tests, a special low-flying head is flown over each track of the disk. During the test, an AE transducer is used to monitor for high levels of vibration that indicate that the head has contacted a bump on the disk. The problem is that the AE vibration is only a very indirect measure of the impact force. As a result it is important to be able to "back calculate" the impact force magnitude from the AE vibration level. This can be done using the force identification technique developed in this thesis.

1.3 Outline of Thesis

The chapters of this thesis are laid out so that the more general aspects of force identification technique are separated from the application to glide height testing. The general techniques are first presented and then the application to glide height testing is shown. Many readers

may not be interested in the specific application of glide height testing, but the application demonstrates, in a very concrete way, the strengths and weaknesses of the technique. For this reason, the reader is encouraged to at least skim the sections on the application.

Chapter 1 of this thesis is the introduction. It is intended to give the reader a brief overview of the purpose of the thesis. Chapter 2 is a review of the literature with discussions about the other techniques that have been used to solve force identification problems. Chapter 3 presents some basic information about FEM and modal analysis that is needed for the reader to understand some of the more complex procedures on modal parameter extraction in Chapter 4. An FEM model and modal analysis of the read/write head (slider) are also presented in Chapter 3, together with experimental data to verify that the theoretical analysis is correct. Chapter 4 presents the force identification technique developed in this thesis. It shows how modal parameter extraction and pattern matching can be used to solve this class of inverse problems. Chapter 5 demonstrates the application of the force identification technique to the problem in glide height testing. Chapter 6 gives a general discussion of the force identification technique, its advantages and disadvantages, and assesses its usefulness for the glide height testing problem. Chapter 7 concludes the thesis with information about what has been accomplished through this research effort and what needs to be done in the future. At the end of the thesis are a bibliography, several Appendices and computer program listings.

Chapter 2

Literature Review

2.1 Scope

This thesis is concerned with the problem of force identification in general, and the problem of determining impact forces in glide height testing of computer hard disks in particular. Thus, the literature related to these two areas will be reviewed. Although the glide height literature is relatively easy to identify, the general force identification literature is very difficult to isolate due to the diverse interests of individual researchers.

Researchers in the following fields are interested in force identification, even though they do not necessarily label their work as force identification per se:

1. Machinery diagnostics
2. Modal testing
3. Impact engineering
4. Acoustic emission

Certainly researchers in these fields are interested in more than just force identification. However, research on force identification problems shows up in the literature of all four of these fields. It should be noted that the label of “force identification” is the author’s choice in this research, and is by no means universal. Other researchers may use phrases such as “inverse problem”, “waveform recovery”, “AE source identification”, and “inverse filters”. In any case, selected research on force identification will be reviewed from all four fields, as well as from glide height testing, to highlight the state-of-the-art in these areas.

This thesis also makes use of the techniques of modal parameter extraction and pattern matching. These fields are more well developed and will not be reviewed here. However, appropriate references are given in Chapters 4 and 5 when the techniques are discussed. There are some very good books available on these subjects.[1][2]

2.2 Force Identification Techniques

When forces on a structure cannot be measured directly, it is possible, in principle, to estimate these forces from vibration signals measured from a remotely located vibration transducer. To do this, the relationship between the forces applied at one location and the vibrations produced at the sensor location, must be known. This relationship is known as the *transfer function* (or the Green's function) of the system. If the input force is called $x(t)$, the output vibration $y(t)$, and $h(t)$ is the transfer function (impulse response), then the relation between them is

$$y(t) = x(t) * h(t), \quad (2.1)$$

where the $*$ symbol indicates a mathematical convolution. The convolution symbol is a shorthand way of writing the convolution integral.

$$y(t) = \int_{-\infty}^{\infty} x(t - \tau)h(\tau)d\tau \quad (2.2)$$

In the frequency domain, the companion relation to Equation 2.1 can be obtained by taking the Fourier transforms (FT) of the variables, i.e.

$$Y(\omega) = X(\omega)H(\omega), \quad (2.3)$$

where, ω is radian frequency. Hence, convolution in the time domain is transformed into multiplication in the frequency domain.

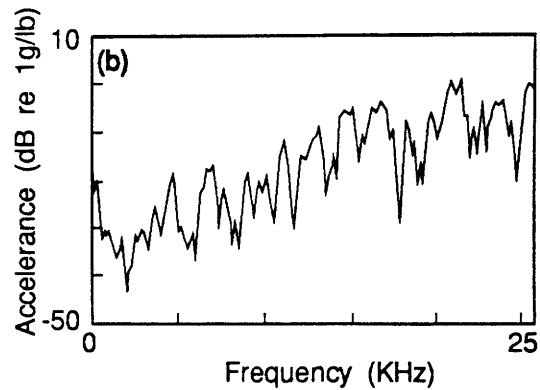
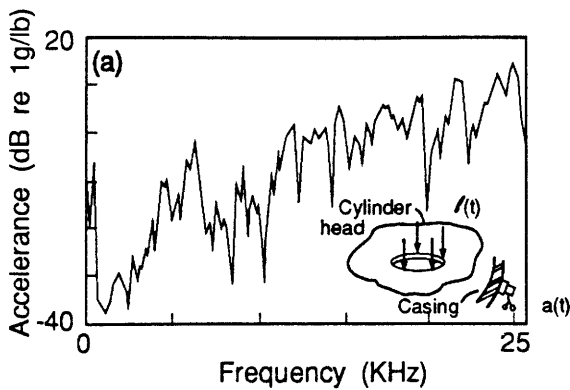
In force identification problems, the vibration signal $y(t)$ or $Y(\omega)$ is the only measurable quantity. This vibration signal is affected by both the input force and the transfer function of the system. The problem is that the input force $x(t)$ and the transfer function $h(t)$ are inextricably woven together, i.e. they cannot be separated. The obvious solution is to measure the transfer function $h(t)$ of the structure ahead of time. Then, the input force can be calculated from

$$X(\omega) = \frac{Y(\omega)}{H(\omega)}, \quad (2.4)$$

and $x(t)$ can be determined from inverse FT of $X(\omega)$. Unfortunately, the practical application of Equation 2.4 is not nearly as neat and clean as the mathematics suggest. The principle difficulty is with the way that noise or errors affect the calculation of the forces. Structures, and also their transfer functions, are usually resonant in nature. The magnitude of the frequency domain transfer function $|H(\omega)|$ consists of a number of resonant peaks separated by valleys or anti-resonance regions. The magnitude of $|H(\omega)|$ in these antiresonance frequency ranges is very small and the experimentally measured values of $|H(\omega)|$ in these frequency ranges can be heavily corrupted by noise. The same is true for the measured vibration signal $Y(\omega)$. When $X(\omega)$ is calculated from Equation 2.4, it can be so distorted by noise that the time domain force waveform $x(t)$ calculated from it will not be accurate at all.

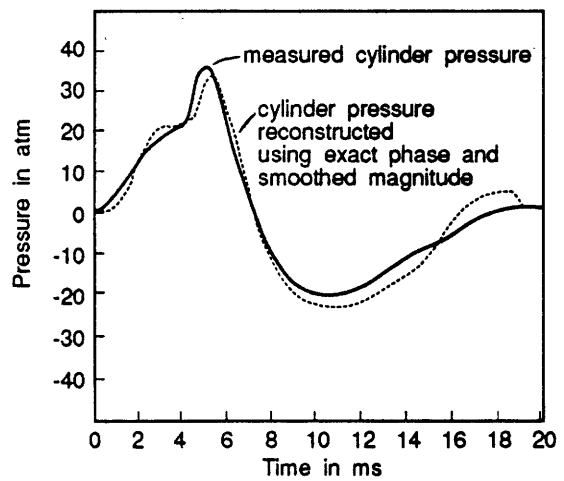
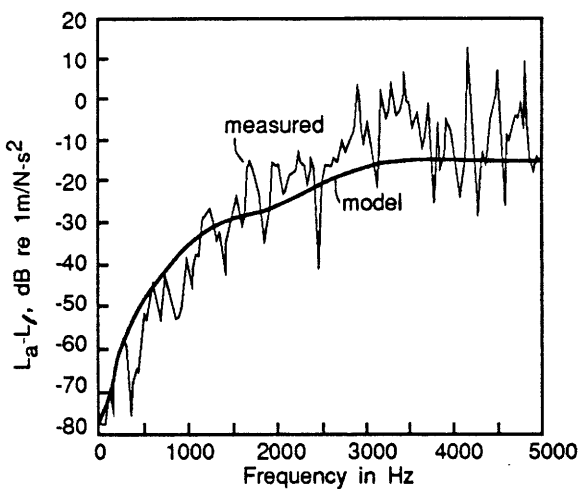
To improve this condition, the measured transfer function can be smoothed. The smoothing removes some of the sharp dips in $|H(\omega)|$ and improves the calculation of $x(t)$. Lyon 1987 [3]

I)



Measured transfer acceleration from valve seat force to engine casing. Curve (b) is smoothed by a three-point running average to eliminate sharp minima.

II)



This example shows the magnitude of the transfer function smoothed to a model transfer function. It also shows the quality of the pressure vs. time curve for recovered cylinder pressure in an internal combustion engine.

Figure 2.1: To improve the inverse process, the transfer function can be smoothed. I) One way is to use a running average filter on the transfer function. II) Another way is to use a system model. (From Lyon 1987)

has demonstrated the effects of smoothing as shown in Figure 2.1. The top pair of graphs show the effects of using a three-point running average to smooth the transfer function of an engine block from the valve seat to the engine casing. The bottom pair of graphs show an even stronger smoothing for the transfer function of the engine block used to recover the combustion pressure. The figure also shows a comparison between the measured combustion pressure and the reconstructed pressure calculated from the acceleration signals and the smoothed transfer function. The agreement is very good and perhaps better than might be expected by the general application of this technique to other structures or systems. Additionally, Lyon illustrated the importance of good phase information in the inverse process. It should be noted that the engine block transfer function has a high modal overlap, i.e. resonant modes are closely spaced in frequency. As a result, not much of the frequency range of the transfer function is occupied by the antiresonance regions that can be so detrimental to the inverse process. Thus, this high modal overlap might be partially responsible for the high accuracy of the recovered pressure signals in this particular structure. In other work [3], Lyon demonstrated a technique for separating the output spectrum into the source spectrum and the transfer function spectrum using a cepstrum windowing technique. The technique works very well for some systems. However, the general applicability of the technique is still being investigated.

2.2.1 Accelerance Method

Researchers with a background in modal analysis tend to have a different approach to the force identification problem. There are two different approaches that are demonstrated in the literature: namely 1) the *accelerance model* and 2) *the modal model* (also called the modal coordinate transformation technique). Both of these methods will be reviewed here.

Okubo 1985 [4] was one of the first researchers to perform force identification experiments using the accelerance model. As he clearly points out in his paper, the accelerance model is a simple extension of the direct inverse technique for the use of multiple vibration measurements. Using multiple measurements, the forces can be estimated using a least squared method.

$$\{\ddot{X}\}_n = [H]_{n \times m} \{F\}_m \quad (2.5)$$

$$\{F\} = [H^T H]^{-1} H^T \{\ddot{X}\} \quad (2.6)$$

- where,
- $[H]$ = the transfer function matrix, accelerance
 - $\{\ddot{X}\}$ = vector of Fourier transform of the acceleration signals
 - $\{F\}$ = vector of Fourier transform of the predicted forces
 - T = the Hermitian transpose, because $[H]$ is complex
 - m = number of forces to be predicted
 - n = number of responses measured, $m \ll n$

Equation 2.5 is actually a simple extension Equation 2.3 to multiple measurements. The same is true of Equations 2.6 and 2.4 . Regrettably, there is a notational change which is common

# of Forces Predicted	Condition (K)	F_{x4} Amp.	F_{x4} Phase	F_{x1} Amp.	F_{x1} Phase	F_{y1} Amp.	F_{y1} Phase
Actual Force		1.000	0.0	0.000	0.0	0.000	0.0
1	1.0	1.400	1.9				
2	4.4	0.955	-24.0	0.043	-13.0		
3	7.3	0.943	-30.0	0.308	-3.0	0.023	12.0

Table 2.1: Engine forces predicted using accelerance algorithm. (From Starkey 1989) A unit force is applied at one location, location 4, in the x direction. Forces are predicted at one, two, and three locations. The difference between the actual and predicted force is the error.

in the literature. The input to the system has changed from $X(\omega)$ to $\{F\}$ and the output from $Y(\omega)$ to $\{\ddot{X}\}$. The former notation is common among the signal processing literature and the latter notation is common among the modal testing literature. Since $[H]$ is a function of frequency, Equation 2.6 must be calculated at each frequency of interest. The accelerance model uses a greater number of acceleration measurements than the number of forces to be predicted. The redundant measurements helps to reduce the errors in the calculated forces.

Okubo applied the accelerance method to a computer model of a beam with two vibration modes. He studied the effects of simulated noise as well as errors in the natural frequencies, mode shapes and damping factors. The greatest contributor to error, in Okubo's simulations, was noise in the anti-resonance region of the acceleration signal. However, he only predicted the magnitude of the forces in the frequency domain and not the phase or the time domain force signals. In general, the greatest contributor to the time domain error is probably phase error (for example, see Lyon [3] page 195). Therefore, his conclusion that noise in the anti-resonance region was the greatest cause of error, may not hold true for time domain waveforms. Okubo also applied the accelerance model to predicting forces in milling machines, automotive engines, and air conditioners. Although Okubo claimed that the accelerance model worked well, the details of the experiments were vague and the success of the technique questionable.

Starkey 1989 [5] investigated the causes of error in the forces predicted using the accelerance model. He maintained that the "ill-conditioned" nature of Equation 2.6 is due to the fact that the matrix $[H^T H]$ is frequently close to being singular. The condition number¹ K of $[H^T H]$ was investigated for the example problem of estimating forces in an automotive engine. He found that the condition number of $[H^T H]$ was the worst at frequencies near resonance. He also found that the condition number became greater (worse) as the number of forces to be predicted increased. Table 2.1 shows some typical forces predicted using the accelerance model.

¹The condition number of a matrix describes how close that matrix is to being singular. A condition number of 1 is good (far from singular) and the higher condition number is, the closer the matrix is to being singular. If the matrix is nearly singular, large errors can be expected in the solution.

A 30 Hz sinusoidal force was applied at one location (location 4 in the x direction) in the engine and acceleration measurements were taken at 12 locations. Then, the acceleration model was used to calculate the force at one location (F_{x4}), then at two locations (F_{x4} and F_{x1}), and finally at three locations (F_{x4} , F_{x1} , and F_{y1}). The table indicates that the condition number of the matrix gets increasingly worse as more forces are predicted.

Starkey states that “the results predicted the . . . amplitude with reasonable accuracy.” The word *reasonable* is very subjective, but Table 2.1 shows the objective reality. When only one force was predicted, the acceleration model estimated a force magnitude of 1.4, 40% error. When the values for two forces were predicted, the error in force F_{x4} was only 4.5% but F_{x1} was predicted to be 0.043 when it is actually zero. Furthermore, the amount of error in the predicted phase in of F_{x4} increased sharply. When three forces were predicted, the error in force F_{x4} was only 5.7%, but force F_{x1} was estimated to be 0.308 when it is actually zero. It is interesting to notice that the estimate of the magnitude of force F_{x4} got better when two forces were predicted, compared to when only one force was predicted. This is exactly opposite of what would be expected from considering the condition number. Therefore the higher accuracy of the predicted force F_{x4} was probably just serendipitous. It should be pointed out that Starkey set the experiment up under the best possible conditions: 1) force applied at a location where the acceleration data had the greatest S/N ratio, 2) the frequency of 30 Hz was chosen because it was away from the resonances, and 3) the signals from 12 accelerometers were used as the input to the acceleration model. Therefore, tests run under the best conditions still have as much as 40% error in the predicted forces. Starkey concluded his paper by saying, “less than five-percent errors in the acceleration can yield meaningless force predictions with well over 100 percent error.” Clearly, a better force identification procedure is needed.

2.2.2 Modal Model Method

In the modal model force identification technique, it is assumed that the system dynamics can be adequately modeled by a modal model. This means that the response of the system in the frequency domain should be a number of resonant peaks which indicate the different vibrational modes of the system. The standard equation of dynamics for a structure is usually transformed, as follows, into modal coordinates:

$$[M]\{\ddot{q}\} + [C]\{\dot{q}\} + [K]\{q\} = [\phi]^T\{F\} \quad (2.7)$$

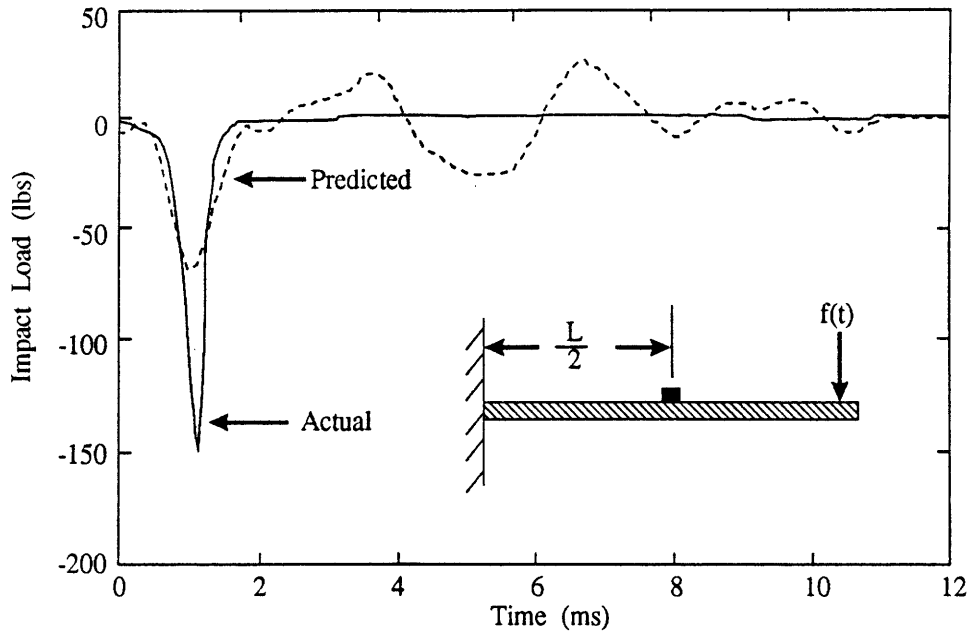
$$\{\ddot{x}\} = [\phi]\{\ddot{q}\} \quad (2.8)$$

Here, $[M]$, $[C]$, and $[K]$ are the modal mass, damping, and stiffness matrices, which are all diagonal. Also, $\{q\}$ is the acceleration vector in modal coordinates and $[\phi]$ is the matrix of eigenvectors. The idea of using modal coordinates $\{q\}$ rather than the actual system coordinates $\{x\}$ is simply a mathematical convenience. When modal coordinates are used the modal matrices, such as $[M]$, in Equation 2.7 are diagonal. This simply makes the computation easier. It is probably best to think of modal coordinates as a mathematical abstraction and not to try to attach some physical significance to them. It may be useful to note that if this were

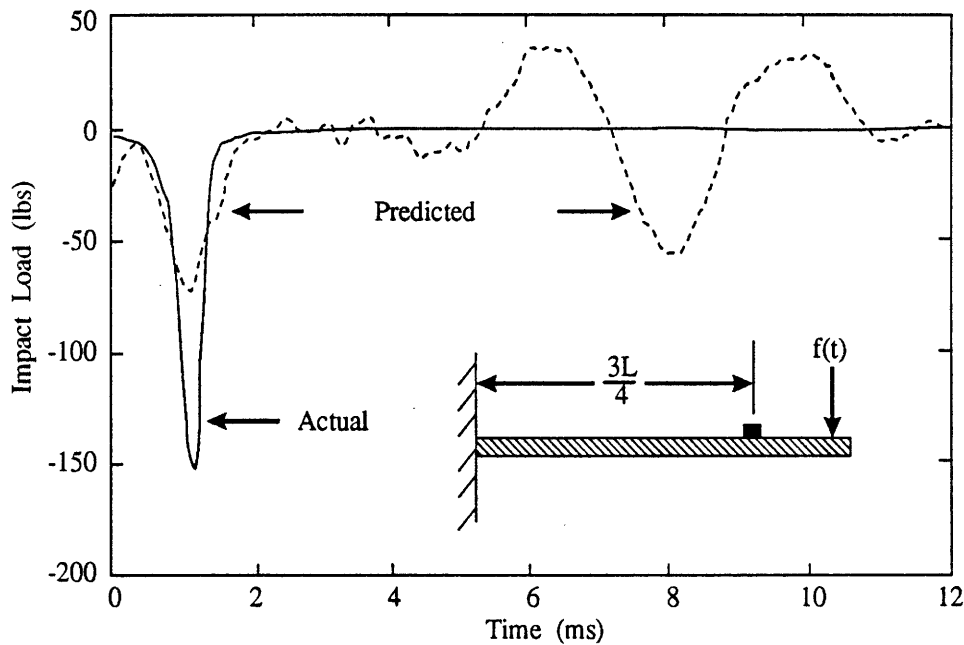
a controls problem, the modal coordinates would be called “state variables.” Equation 2.7 can be manipulated, in a similar manner to Equation 2.6, and be used to predict forces from acceleration data, see Hansen 1990 [6] for details. The advantage of the modal model force identification technique is that the transformation to modal coordinates reduces the amount of computation needed. The disadvantage is that a good modal model of the system is needed before the technique can be used. Any error in the curve fitting (that is part of building a modal model) will create a systematic error in the predicted forces. It is also important to have a number of vibration modes within the frequency range of interest.

Hollandsworth 1989 [7] used the modal model technique to predict impact forces on a $991 \times 64 \times 13$ mm ($39 \times 2.5 \times 0.5$ ”) cantilever beam. Due to the simple geometry, Hollandsworth developed his modal model from vibration theory for beams. Figure 2.2 shows the results of the application of the technique. In the experiments, an impact hammer was used to create a force pulse at the end of the beam. Three accelerometers were placed on the beam at various locations. The acceleration signals were used as the inputs to the modal model force identification procedure. Figure 2.2 shows that predicted force waveforms do show a pulse at the time that the force impact actually occurs. The magnitude of the predicted pulse was about 50% smaller than the actual magnitude. Furthermore, the predicted forces show a great deal of ringing after this pulse. A smoothing parameter was applied to the acceleration data prior to doing the force identification calculation. Hollandsworth claimed that this smoothing parameter was very important to getting good results. The justification for the use of this smoothing parameter and the logic behind the choice of its magnitude were not given in the paper. The large errors in the predicted forces of this study, make the value of the modal model technique questionable, at least in its current manner of implementation.

Another paper, written by Hansen and Starkey 1990 [6], investigated the ill-conditioned nature of the modal model force identification technique. Hansen’s experiments were performed on a $1524 \times 51 \times 6$ mm ($60 \times 2 \times 0.25$ ”) free-free steel beam. A series of modal tests were performed to develop the modal model of the beam. Then, an analysis was performed to study the condition of the matrix inverse. This is similar to what was done by Starkey 1989 [5] for the accelerance model. Hansen investigated the effect of placing three accelerometers at different locations on the beam. He found that the combination of accelerometer placements made a enormous difference on the condition number of the matrix. For the best combination of accelerometer locations, the condition number $K = 1$. For the worst combination, $K = 370$. (Recall that $K = 1$ is good and large numbers indicate that the matrix is nearly singular.) This means that the placement of the accelerometers is very important to the accuracy of the predicted forces. Hansen also studied the effects of including different groups of vibration modes in the model, e.g. modes 3-5 or modes 4-6. Depending on the combination, the condition number ranged from 1 to 629. Computer simulation of the modal model force identification technique showed that the errors in the predicted forces ranged from 40% at under the best conditions ($K = 1$) to 186% under less favorable conditions ($K = 144$). The errors were not calculated for the worst conditions. Unfortunately, there does not seem to be any easy way to tell which combinations of accelerometer locations and groups of modes will yield the best



Force prediction with accelerometer at $L/2$, $B=0.001$.



Force prediction with accelerometer at $3L/4$, $B=0.001$.

Figure 2.2: Impact forces on a beam predicted from a modal model force identification technique. (From Hollandsworth and Busby 1989)

results for a given structure.

The techniques that have been discussed so far, transfer function smoothing, cepstrum windowing, accelerance method, and modal model method have all achieved some degree of success at predicting forces in a force identification problem. Unfortunately, most researchers have indicated that quality of the force identification is poor. Some of the researchers found that under the best conditions, the predicted forces were in error by greater than 40%. The force identification technique, presented later in this thesis, takes a very different route to solving this problem. Although a modal model is used, a pattern matching technique is employed to do the force identification, rather than through the use of direct calculation. The other key difference is that the technique developed in this thesis, is only applicable to problems where the input force is a short duration pulse. But for this type of problems, the new technique produces encouraging results.

2.3 Acoustic Emission Research

Acoustic emission (AE) research was developed out of the discovery that deforming metal emitted audible sound. Materials researchers were very interested in the technique because it could be used to detect the onset of permanent deformation or damage in a sample of material being tested. Modern AE researchers have a broad range of interests. AE is no longer measured in only the audible range. In fact, AE is more commonly measured in the 100 KHz to 1 MHz range by a vibration sensor placed directly on the test system. It is no longer restricted to testing of materials in a laboratory. AE has been used for in-process monitoring of structures, proof-testing of pressure vessels, diagnostics of manufacturing processes, and various other interesting applications.

In terms of the source (force) identification problem, some of the most carefully thought out research was performed by Hsu et.al. 1981 [8] at the National Bureau of Standards. In these works, Hsu developed methods to characterize the three main elements of an AE measurement system: 1) the source, 2) the structure, and 3) the AE sensor. He developed a computer program to calculate the Green's function (transfer function or impulse response) of an infinite plate. The program can predict the displacement at any location on the plate surface due to an impulse at the center of the plate. The program uses ray tracing to follow the paths of the waves produced at the source and predicts the resulting displacement at the sensor location. This requires following the paths of the p-waves (pressure), s-waves (shear), and the Rayleigh waves (surface). It is further complicated by the phenomenon of mode conversion. Each time a wave hits a surface of the plate, it creates another p-wave and an s-wave. Thus, as time goes on, more and more waves must be traced. As a result, the program for calculating the surface deflections of the plate can only be used for calculating short time periods (say 40 μ s) following the impulse force input. After this initial period, not only does the computation become very intensive, but the resonance of the structure will start to become important due the reflections of the waves from the boundary of a real (non-infinite) plate. Thus the technique is limited to processing transient events, e.g. impacts.

Hsu used the Green's function of plates in a simple deconvolution technique to back-calculate the applied forces at the center of the plate. This technique is clearly a force identification method for infinite plates, although it might never be called by that name in the AE literature. Although Hsu's predicted forces were in good agreement with measured forces, the tests were performed under the best possible conditions² and the technique is limited to infinite plates.

More recently, other researchers have been working to replace the computationally expensive ray tracing technique with a spectral formulation. The spectral formulation processes waves in terms of wave number rather than tracing ray paths. Rizzi and Doyle 1989 [9] developed the spectral formulation and applied it to force identification problems on an half plane. Doyle and Farris 1989 [10] used a more general spectral formulation for solving force identification problems on truss structures. Figure 2.3 shows schematic of their experimental setup and the quality of the results. In the experiments, a force hammer was used to create a short duration force pulse on the aluminum truss structure. The resulting vibration was measured with both accelerometers and strain gages. The spectral formulation was used to back-calculate the forces at the impact location. The lower part of Figure 2.3 shows a comparison between the measured forces and the predicted forces. The agreement is quite good, especially when the predicted forces are based on the accelerometer measurements. Although the results are better than have been seen with either the accelerance modal or modal models, Doyle gave no indication of how easy or difficult it is to achieve results of this quality. Furthermore, the technique is limited to truss structures and cannot be used for more general structures.

It should also be realized that the techniques of Hsu, Rizzi, and Doyle, **can only be used for transient events** and rely on processing the "first arrival" waves. The resonance of the structure, that occurs a short time after the impact, is not part of the model. This is the opposite of the techniques presented earlier which generally ignore the first arrival waves and concentrate on the structural resonance.

2.3.1 Materials Testing

Researchers who use AE to monitor tensile or compression testing of materials, are also interested in a specialized form of force identification. An AE burst indicates that some form of micromechanical deformation has occurred inside the specimen. The researchers would like to be able to determine what form of micromechanical deformation caused the AE pulse. Unfortunately, the complex and uncontrollable nature of the deformation combined with the resonant nature of the AE transducers usually used, have required that this type of work be almost entirely empirical. Researchers have repeatedly tested many materials and tried to find characteristics in the AE signals that can be used to discriminate between different modes of deformation.

Egle et.al. 1981 [11] claimed to be able to differentiate between different modes of deformation in nodular cast iron using AE spectral characteristics. Nodular cast iron is often regarded

²They used a well-characterized broadband displacement transducer and made an extraordinary effort to polish the surface of the plate used in their experiments.

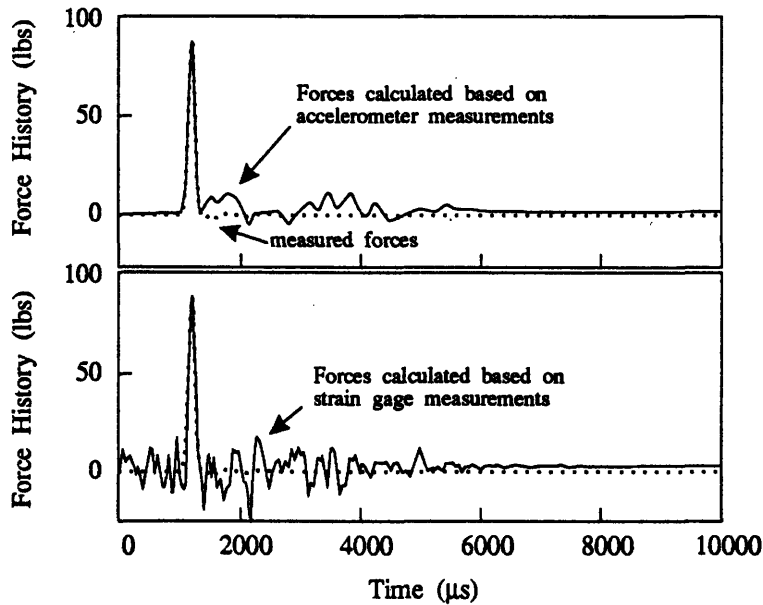
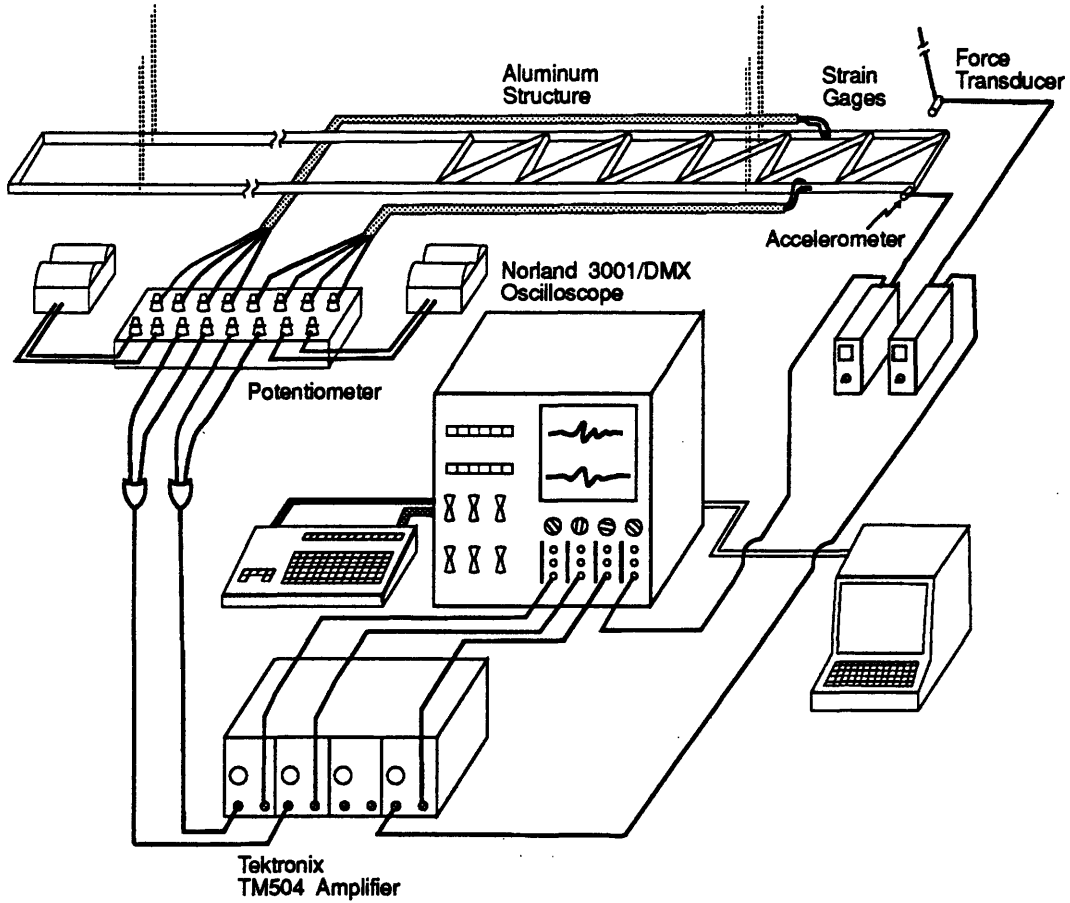


Figure 2.3: Demonstration of the use of spectral analysis method for 3-D frames for solving the force identification problem. The upper part shows the experimental setup and the frame used. The lower part shows a comparison between the measured force (dashed) and the force predicted from the strain and accelerometer measurements. (from Doyle and Farris 1989)

as an ideal material for this type of research. Its deformation characteristics are such that the initial deformation is due to *dislocation mechanisms* whereas later deformation is due to *fracturing of particles*. Thus, the AE signals from two different deformation mechanisms can be measured in one test, without changing sensors or specimens. Egle's tests showed that during the time when fracturing of particles was the dominant deformation mechanism, the AE spectrum was different than when the dominant deformation mechanism was dislocation motion. Thus Egle concluded that he could distinguish between the two deformation mechanisms based on the pattern formed by the AE spectrum. While this may be true, there is one other important factor that was not considered explicitly in Egle's work.

When deformation occurs in a tensile test specimen, the sources of AE come from different locations inside the specimen. In other words, the source location is moving. This means that the frequency response function (FRF) between the source location and the AE sensor location is changing during the test. Thus, it is expected that the AE spectrum would be a function of the AE source location. Egle's research did not take this into account. Was the change in spectrum that he saw due to a change in AE source mechanism, or simply due to a change in AE source location? One possible explanation of his data is the following. Early in the test, when deformation is coming from dislocation motion, the AE source location is randomly distributed throughout the body of the test specimen. Later in the test, when the deformation is coming from particle cracking, the specimen has started to neck down and the AE source location has become concentrated in one section of the specimen. In this way, the change in spectrum could have been due to a change in source location and not necessarily due to a change in source mechanism. Again, this is not to say that Egle's conclusions were necessarily wrong, it is simply that they are open to interpretation.

Stephens and Pollock 1971 [12] calculated the frequency response function of a particular tensile test. The frequency response was calculated from 0 to 320 KHz. The vibration modes remain well separated in this frequency range, i.e. low modal overlap. However, their tensile test specimens were bonded together at the center so that the AE source location would remain fixed. In other words, crack propagation and failure occurred at the bond and not at any other location in the specimen. Even under these conditions (i.e. known FRF and fixed source location) they were unable to extract useful information about the force source waveform.

It should be clear from the above discussion that AE researchers generally have a different approach to force identification problems than vibration researchers. AE researchers also have specialized problems, such as poor understanding of the AE sources, resonant response of most AE transducers, and the need for analyzing high frequency (say >100 KHz) signals. This is probably the reason that AE literature is usually separated from vibration literature, even though the research from the two disciplines overlaps.

2.4 Glide Height Testing Research

The force identification technique developed in this thesis is applied to the specific problem of glide height testing. Hence it is appropriate to give a review of the glide height testing

literature.

Before discussing glide height testing, some background information needs to be given about hard disk drives. Most people who have used computers know that there are two common types of magnetic storage: floppy disk drives and hard disk drives. But most people are not aware of the significant differences between these two drive types.

In a floppy disk drive, as the name suggests, the magnetic coating is applied to a flexible plastic substrate. This is the material that can be seen through the cutaway in the floppy disk. When the disk is placed in the floppy drive and the door is closed, the read/write heads (top and bottom heads) come down in direct contact with the surface of the floppy disk. When data is needed, the computer turns the disk drive on, reads the data, and turns the disk drive off again. Thus the disk is only spinning a small fraction of the time that the computer is used.

In contrast, in hard disk drives, the magnetic coating is applied to a rigid aluminum substrate. When the computer is turned on, the drive is "spun up" to 3600 rpm (typically) and left spinning as long as the computer is turned on. The read/write heads are designed to have a dynamic air bearing form under the two rails which are cut into the bottom of the slider (read/write head), see Figure 2.4. As the hard disk spins, air very close to the surface of the disk spins with it. This air is used to lift the read/write head 150 - 500 nm off the surface of the disk.

In tribological (friction and wear) terms, the floppy and hard disk drives are as different as night and day. The floppy disk undergoes continuous rubbing as long as the drive is being used. On the other hand, the head and disk of a hard drive should never come into contact as long as the computer is turned on. Some contact between the head and the disk surface does occur in the hard disk when the drive is turned on and off, therefore even the hard disk cannot be expected to last indefinitely.

For the air bearing to work properly, the surface of the hard disk must be flat and free of asperities (bumps). If an asperity on the disk surface is larger than the height of the air bearing, then the asperity will impact one of the slider rails, as shown in Figure 2.5. Repeated impacts on the asperity could cause a fragment of the asperity to break loose, become lodged between the slider and the disk, and cause the hard disk drive to fail or "crash." This would result in the loss of the data on the disk. Thus, eliminating asperities, and the failures they can cause, is of the utmost importance to hard disk manufacturers.

The hard disk manufacturers pass the disks through several steps during the manufacturing to make the disks as flat and free of asperities as possible. However, there is always the chance that some asperities might still get through. Therefore, a quality control (QC) procedure is needed to check the completed disks for asperities.

One might think that the best way to check for asperities would be an optical technique. However, there are several reasons why an optical technique is not appropriate. Firstly, the asperities are very small (sub-micron) in size. On a disk that is 90 - 355 mm (3.5" - 14") in diameter, there would be a large area to be checked at high magnification. Secondly, the height of the asperity is not the only factor that determines whether or not a head/disk impact will occur. The slope of the bump and the runout of the disk are also factors that determine the

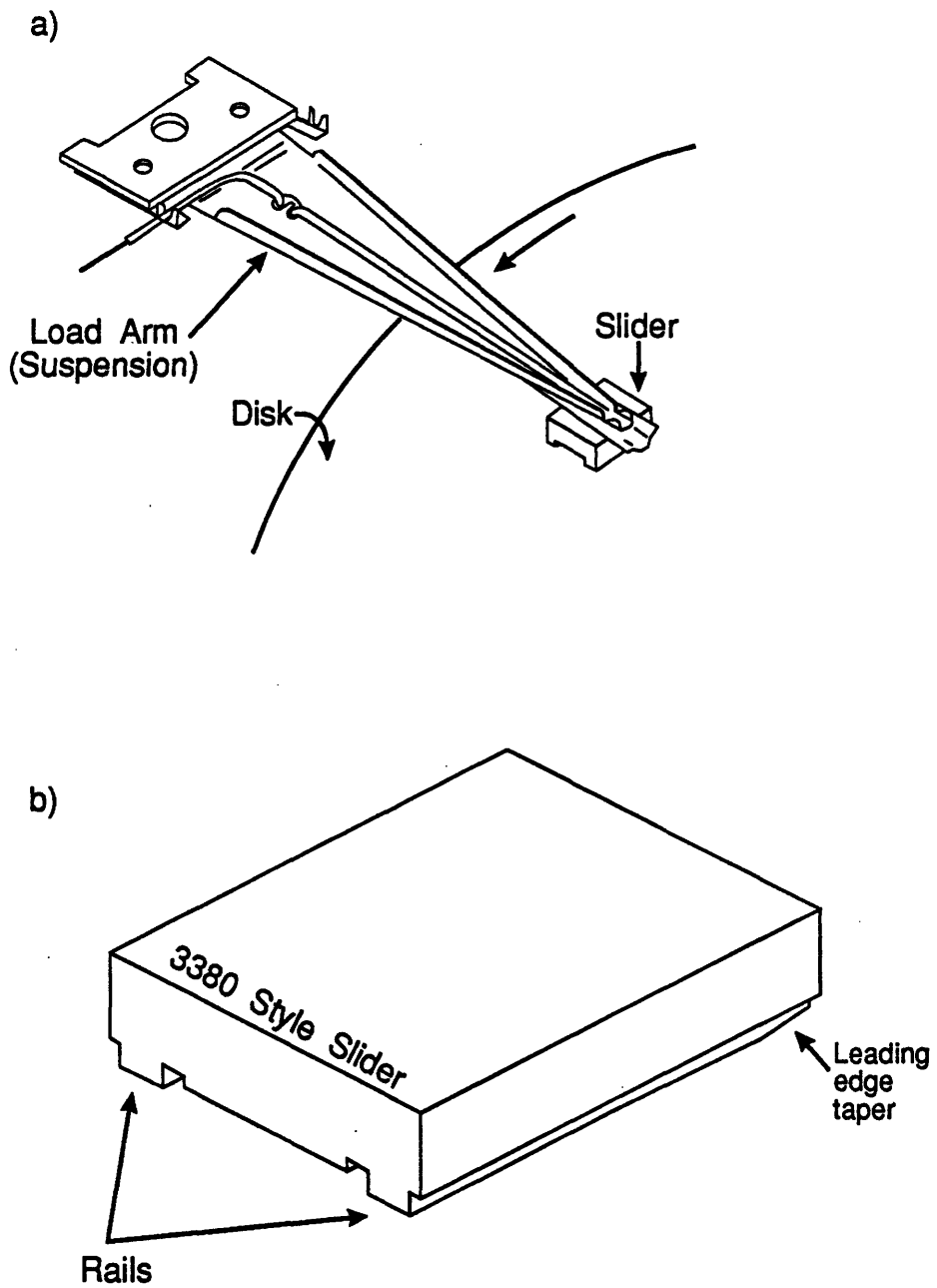


Figure 2.4: Schematic of a typical a) head gimbal assembly (HGA) and b) slider.

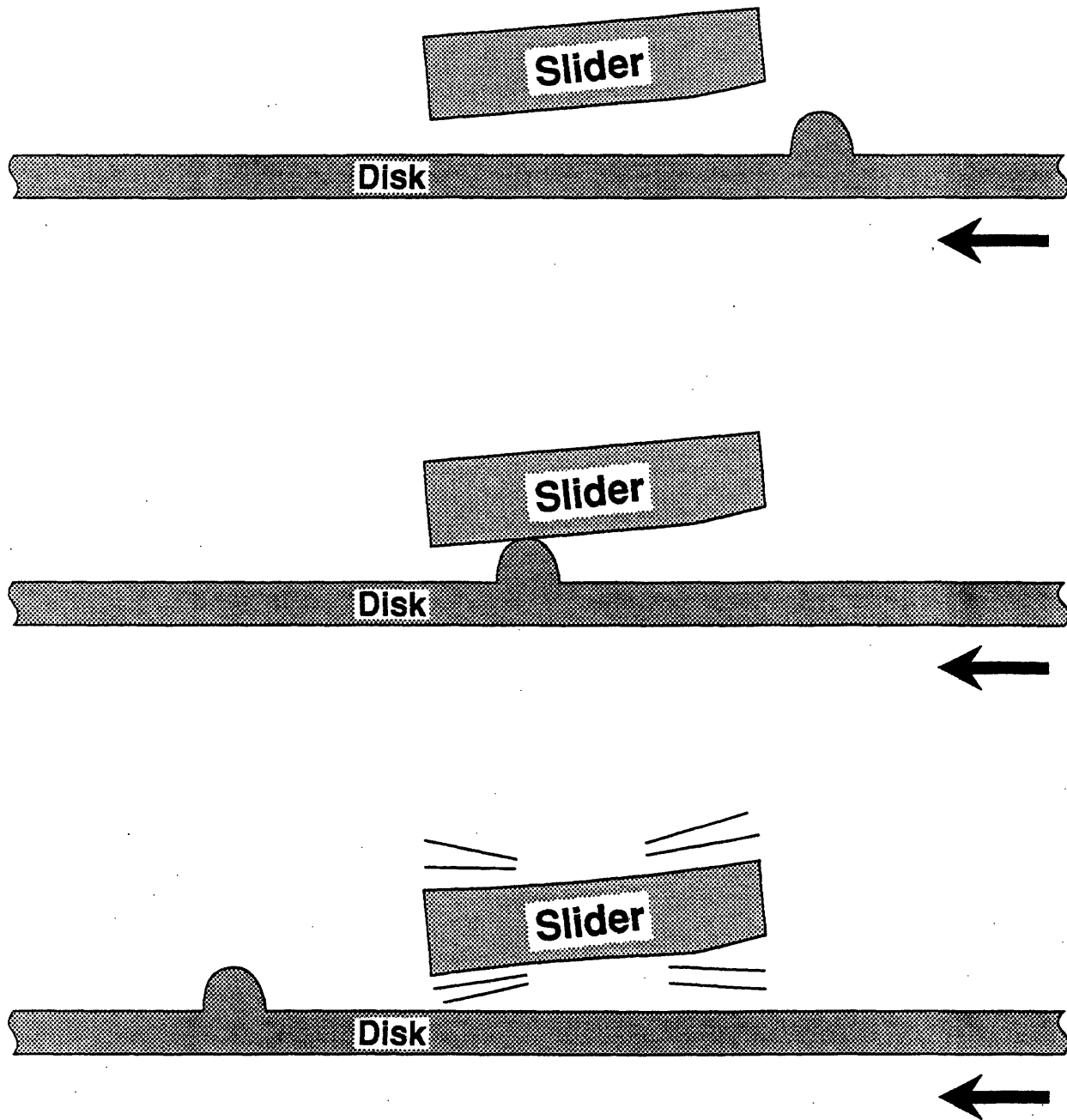


Figure 2.5: Illustration of the slider hitting an asperity on the disk surface.

possibility of impact. As a result, glide height testing is the preferred technique for checking the disk surface for asperities.

In glide height testing a special low-flying head is flown over each track of the disk surface. If an impact occurs between the head and the disk surface, the head gimbal assembly (HGA) will vibrate. This vibration signal can be detected by means of a vibration transducer (AE transducer) mounted at the base of the HGA or on top of the slider itself. In general terms, the detection of an AE burst indicates that an impact has occurred. The locations of impact on the disk surface can be plotted on a graph to show a "defect map," see Figure 2.6. This type of graph can be very useful in tracking down the cause of the asperities. For example, if a number of asperities show up in a line, the disk was probably scratched. Using the magnitude of the AE signals, a three dimensional plot can be drawn which shows how strong the AE signals were at the different locations, as shown in Figure 2.6. This type of plot should be interpreted with caution. The plot looks like the disk topography, but it is not. The strength of the AE signal is not directly proportional to the height of the asperity. Thus, the 3-D defect map only gives some general indication of the strength of the impacts.

Because of the relationship between the presence of asperities and the reliability of the hard disk drive, much research has been done to try to understand glide height testing and the general nature of head/disk impacts. The research literature can be generally divided into two areas 1) impact modeling and 2) glide height testing.

2.4.1 Impact Modeling

Most of the research in the impact modeling is really an extension of the modeling that was done to aid the designing of slider air bearings. The dynamics of the slider can be modeled by considering the slider as a rigid body, the suspension as a series of springs, and the air bearing as a non-linear spring whose spring constant must be calculated from Reynolds equation. Using this type of modeling, computer programs have been written to simulate the flying of the slider[13][14]. These programs are necessary tools in designing new sliders and adjusting the flying height of current slider designs.

To simulate a head/asperity impact is much more complicated than simply simulating the flying of the head. Impact problems in general are very difficult to model. Unless the geometry is very simple, finite element modeling (FEM) is needed. Furthermore, special "interface elements" are needed to mathematically prevent the two impacting objects from occupying the same space at the same time. Thus, a complete model of a head/asperity impact must include the following components, a FEM model of an asperity covered with interface elements, a FEM model of the slider with the rails covered with interface elements, a fluid model of the air flowing under the slider, and model of the suspension characteristics. This type of model is very complex and has never been completed.

A simpler approach to modeling a head/asperity impact is to simply consider the impact as an impulse force. This is a simple addition to the programs that exist for simulating the air bearings under normal flying conditions. An impulse can be applied (numerically) to the slider

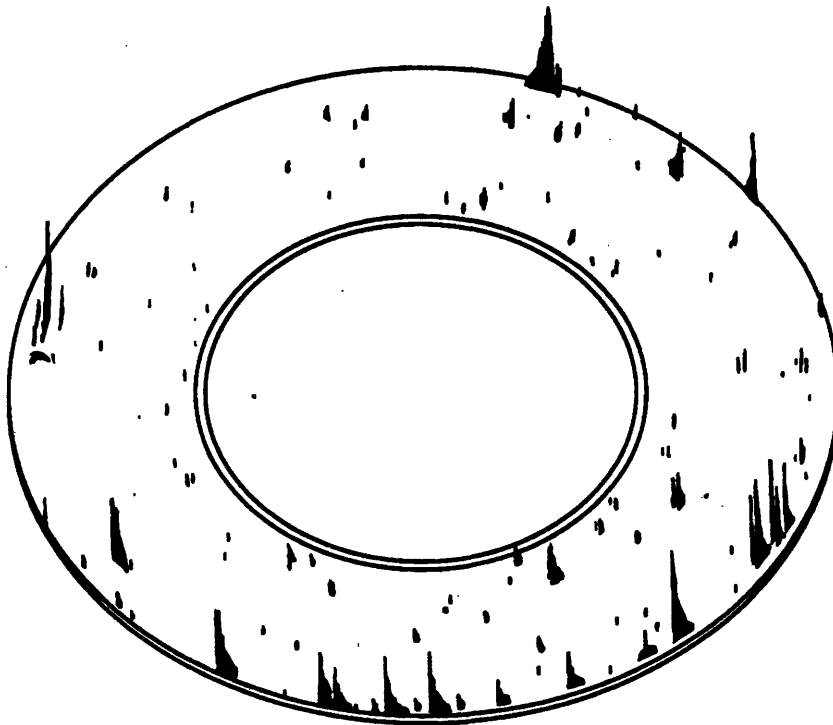
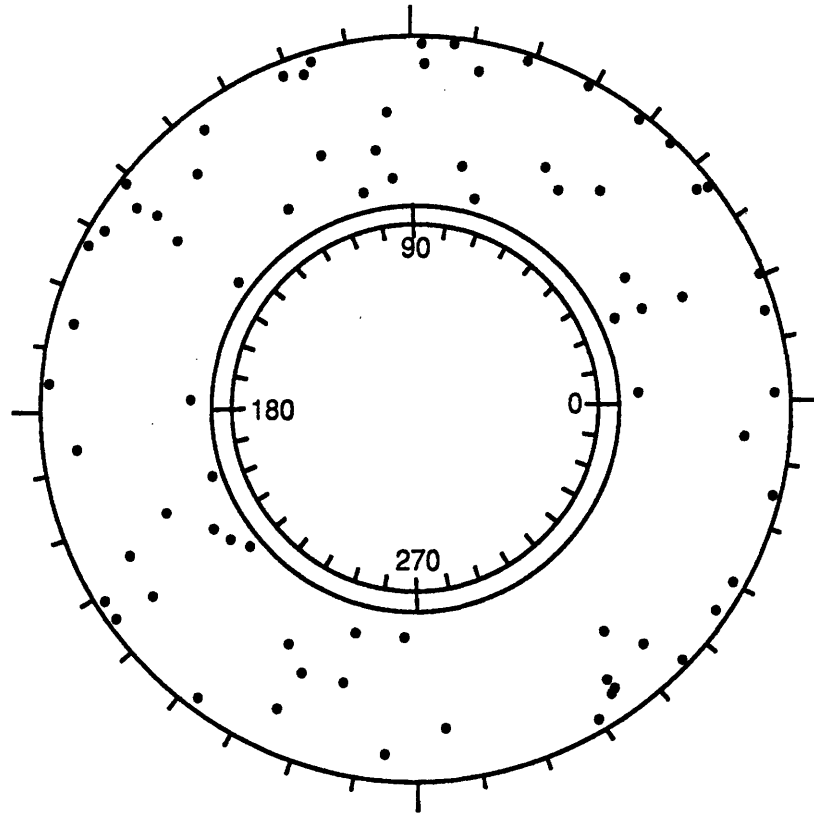
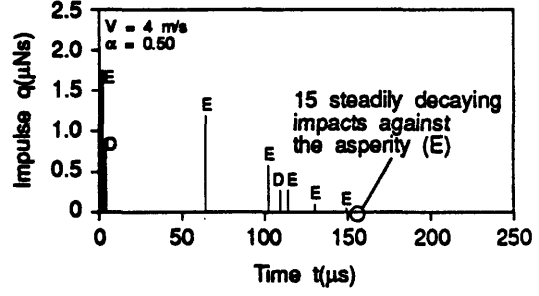
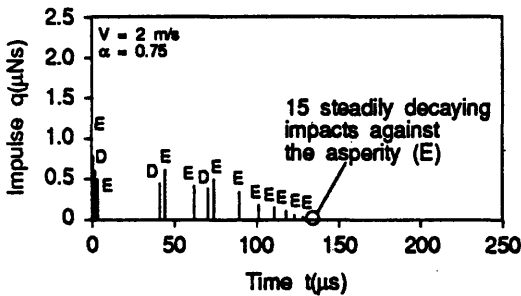
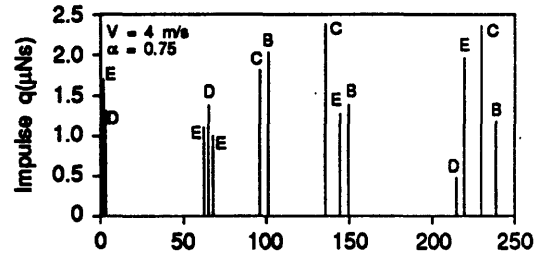
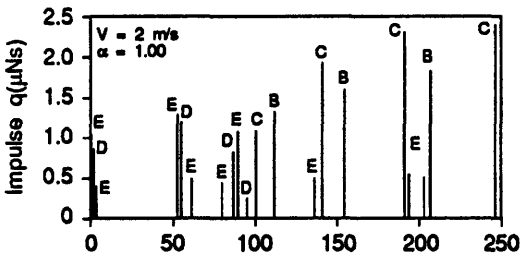
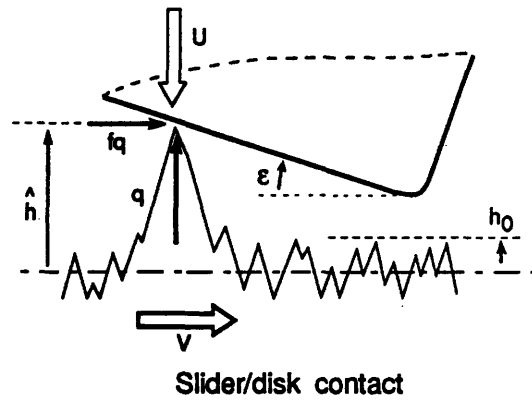
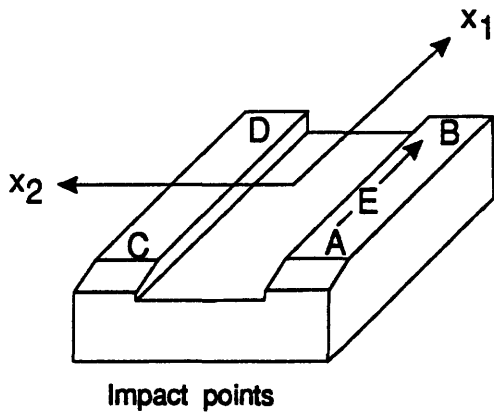


Figure 2.6: Two dimensional and three dimensional defect maps of the disk surface determined by glide height testing.

and its response observed. Unfortunately, the resulting response of the slider might not satisfy the impenetrability requirement of the slider and the disk. In other works, if a strong upward impulse is applied to one corner of the slider (to simulate an asperity impact), the slider's response might be to rotate so that the opposite corner of the slider goes downward below the height where the disk is suppose to be. This might sound a bit strange, but it really is not. In the typical air bearing computer simulation, the disk is not truly modeled. The only effect that the slider "sees" is an air bearing which supports it. If the slider "wants" to penetrate the space where the disk should be, it simply must have enough kinetic energy to overcome the air bearing stiffness. Researchers have tried to correct this situation in a very simple way. If a corner of the slider drops below the height where the disk should be, it is given an upward impulse proportional to the velocity of the corner. This is, in effect, a coefficient of restitution model of impact which requires that if a corner of the slider impacts the disk, it will rebound with a fraction of its initial velocity. The ratio of the rebound velocity to the initial velocity is the coefficient of restitution, which is always 1 or less to simulate the loss of energy from the impact. The primary contributors to this research are White 1987 [15] and the team of Benson and Talke 1987-89[16][17][18]. Figure 2.7 shows some of the results of this type of modeling, from reference [17]. The four corners of the slider have been labeled A, B, C, and D. A fifth point has been labeled E. This is a point where the slider rail might re-impact the asperity. The graphs show the series of impacts that can result from the initial impact with the asperity at location E. The immediate response of the slider is to rotate diagonally and impact at the opposite corner D. Depending on the velocity and coefficient of restitution (α) used, the slider may then either re-impact the asperity or impact one of the other corners. At each impact, a small amount of energy is lost because the coefficient of restitution is less than one. Eventually, the impacts cease and the slider continues flying normally.

It is important to realize that this type of model makes some assumptions that are not necessarily a good model of the physical reality of the impact. The most consequential assumption is that the impacts are of infinitely short duration. Clearly the slider and asperity stay in contact for some period of time. The question is, what is the length of this contact time. There are researchers who feel that the contact duration is very long [19]. In fact they believe that the slider contacts the asperity and rubs along the asperity until the asperity passes out from underneath the slider. Clearly, if that is the case, the impulse modeling is not very useful. There is another assumption made in these models. Since it is not possible to directly measure the impact force, an estimate of the magnitude of the initial impulse is used. Some researchers [20] believe that the estimated values of these impulses are too large and that no multiple contacts occur, or at least they may be rare.

Some attempts have been made to experimentally answer this question, through the use of capacitance probes or optical techniques [21] of measuring the slider's response to impact with an asperity. A recent study by Hamaguchi and Matsumoto 1990 [22] represents one of the most comprehensive attempts to answer this question. Their experimental setup consisted a capacitive-sensor slider and a tangential force sensor. Using a lumped-parameter model of the slider, suspension, and air bearing combined with the force and displacement measurements,



Impact spectra, $V = 2 \text{ m/s}$

Impact spectra, $V = 4 \text{ m/s}$

Figure 2.7: Coefficient of restitution model of slider/asperity impact. (From Benson and Talke 1987)

the impulse forces created on the slider were back-calculated. Their results showed that the Z-direction (normal) impulse was about $1.03 \times 10^{-6} \text{ N} \cdot \text{s}$ and the X-direction (tangential) impulse was $1.02 \times 10^{-6} \text{ N} \cdot \text{s}$. Further experiments were performed using the electrical resistance technique to determine the contact time between the slider and the asperity. With this technique, the electrical resistance between the slider and the disk was measured in an attempt to determine when contact is occurring. From these tests, Hamaguchi and Matsumoto concluded that the contact time was on the order of $10^2 \mu\text{s}$ and the contact force tangential to the disk was on the order of 10^{-3} N .

Unfortunately, there are several problems with Hamaguchi and Matsumoto's study. Firstly, the accuracy of the dynamic slider model is unknown. Since the model includes a linearized model of air bearing stiffness, the accuracy of the model may not be very good. As a result, the predicted magnitude of the impulses may be inaccurate. Secondly, the possible ill-conditioned nature of the inverse problem (calculation of the impulse forces) is not considered. Thus even if the model is good, the accuracy of the predicted impulses is not guaranteed. Thirdly, the disks that were used had either a radial scratch or radially deposited bump. Thus impacts occurred on both rails nearly simultaneously. Under actual operating conditions, it is probably more likely that the asperity will be relatively small and impact only one slider rail. Finally, the contact times and force magnitudes were calculated for the total duration of contact, i.e. from the initial contact until the asperity passed out from underneath the slider. This was done even though the electrical resistance data indicated that multiple contacts may have occurred. Thus the actual impact duration time is much shorter ($\approx 10 \mu\text{s}$) than they concluded.

On the positive side, Hamaguchi and Matsumoto's research did indicate a number of features of the slider/asperity contact. Their data showed that the flying height had an effect on the location where the asperity hit the rail. Large asperities (simulated by low flying heights) tended to hit toward the leading edge of the slider rail. Small asperities (simulated by higher flying heights) tended to hit toward the trailing edge. The electrical resistance data did not clearly answer the question of the occurrence of multiple slider/asperity impacts. Some of the data had the appearance that the asperity impacted the slider and then rubbed along the slider rail until it passed from underneath the slider. Other data had the appearance that multiple contacts were prevalent, similar to the simulations of Talke [18]. However, the fact that the bump was hitting both rails simultaneously may have had a significant effect on these results. Thus, applying these results to the case of a single rail impact might lead to erroneous conclusions. Furthermore, the difficulty of making these types of measurements combined with the issues raised above, means that the data should be viewed somewhat skeptically.

Unfortunately, the research on asperity impact models is generally not conclusive. It is clear that there are many unknowns. In Figure 2.7, Talke considers coefficients of restitution from 0.5 to 1, with no way of knowing what a typical value might be. There is no consideration given to the material properties of the disk or slider surfaces. Hamaguchi and Matsumoto only considered impacts with asperities that impacted both rails nearly simultaneously, and their electrical resistance measurements are inconclusive. It can be safely said that no comprehensive understanding of slider/asperity impacts exists. For simplicity, it will be assumed in this

thesis, that slider/asperity impacts are short in duration and that multiple impacts may occur under some conditions, but not often. However, the true nature of these impacts needs further research.

2.4.2 Acoustic Emission

Other researchers have been less concerned about the details of the head/asperity impacts, and more concerned about how to detect the impacts using acoustic emission (AE) transducers. One of the earliest papers was written by Kita et.al. 1980 [23]. At the time that the paper was written, only large commercial AE transducers were available. Therefore, the sensor had to be placed very far from the slider. However, Kita's paper demonstrated that AE monitoring can be used to detect asperities successfully. Very few details were given as to the characteristics of the AE signals.

One of the most significant papers on glide height testing was written by Yeack-Scranton 1986 [24]. She demonstrated two new AE sensor arrangements, as shown in Figure 2.8. The top part of Figure 2.8 shows how a small PZT ceramic sensor was mounted directly on top of the slider. The bottom half of the figure shows how a piece of PVDF plastic piezoelectric film was placed on the suspension of the slider. Scranton felt that this combination of sensors would be very useful. The PVDF sensor mounted on the suspension would measure primarily the rigid body movement of the slider. On the other hand, the PZT sensor mounted on the slider would measure the higher frequency plate bending modes of the slider. The paper discusses the effects of disk speed, burnishing, track accessing, and disk type on the measured AE. However, the paper lacked any detailed description of the high frequency AE signals.

Also published in 1986, was a paper by Boyer [25]. While it is not a research paper, it does serve as the *practical man's guide* to glide height testing. For anyone interested in the basics of setting up a glide height test facility, the paper is recommended.

Talke published a paper in 1988[26] which investigated the sources AE in a 5 1/4" disk drive. He claimed that the resonance peaks in the high frequency AE result from the time duration between the repeated impacts between the head and the disk after an initial asperity impact. This, however, is **not** true. As indicated by Yeack-Scranton in 1986 [24] and others clearly proved later, the high frequency AE results from the slider vibration (or plate modes).

Since the time that high frequency AE research began for this thesis, some other research has also been reported in the literature. Mochizuki et.al. 1988[27] indicated that the high frequency AE resulted from the slider plate modes. However, it was not until May 1989 [28], that the same researchers published a paper showing the slider modes of vibration and verified the vibration frequencies experimentally. A paper by Bogy in September 1989 [29] confirmed Mochizuki's results. The importance of knowing the source of vibration, is that some predictions can be made about how the AE signal will change if the design of the slider were to change. In earlier work, such as Kita's [23], the frequency content of the AE signal was not known. Thus the choice of frequency range monitored during glide height tests was somewhat arbitrary and experimental in nature.

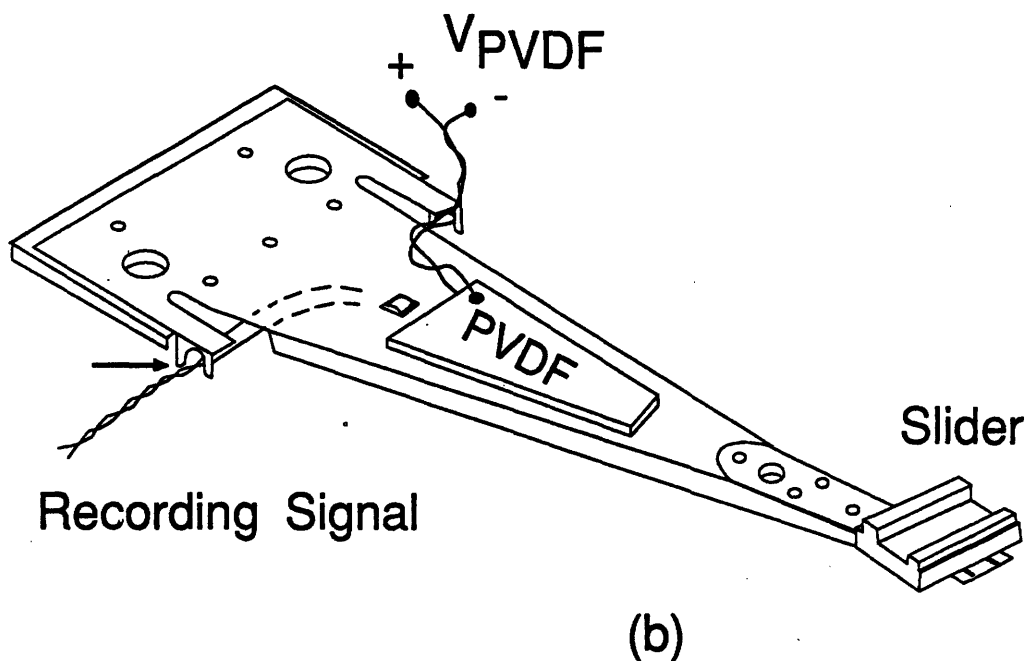
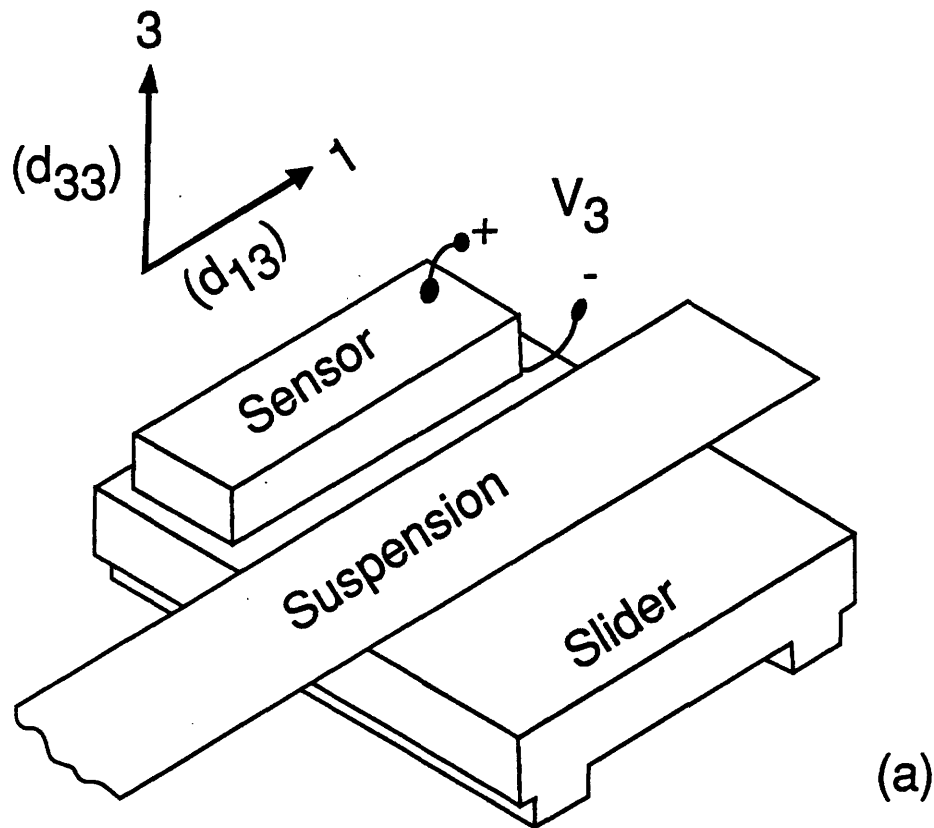


Figure 2.8: Two possible ways to mount AE transducers on the head gimbal assembly (HGA), (a) on the slider and (b) on the suspension (From Yeack-Scranton's 1986)

In this thesis, the natural frequencies of the slider were also calculated and experimentally verified, see Chapter 3 for details. More importantly, a modal analysis was performed on the slider. The modal analysis predicted the frequency response function (FRF) or spectrum of the slider. The analysis also estimated the effect of both the asperity impact and sensor locations on the FRF (or AE spectrum). It demonstrated that there are certain locations where an asperity can impact the slider rail and cause almost no vibration (in certain frequency ranges). This turns out to be a very serious problem for glide height testing, because it can lead to asperities going undetected. In Chapters 4 and 5 of this thesis, a force identification technique is proposed, and its use to solve this problem is demonstrated.

This thesis addresses three important issues related to glide height testing, which have not been approached by other researchers: 1) quantitative predictions of the frequency response function of the slider, 2) the effects of impact and sensor location, and 3) proposing a signal processing technique, based on the fundamental knowledge of the slider vibration, for extracting information about the asperity impact from the AE signal.

2.5 Summary

In this chapter some of the literature on force identification has been discussed. It has been generally found that even small amounts of noise makes direct deconvolution impractical. Other techniques such as transfer function smoothing, accelerance methods, and modal model methods, can be used to improve this situation. However, researchers frequently find that the error in the predicted forces is greater than 40%. The force identification technique presented in this thesis is a significant departure from the techniques developed by other researchers. The new technique does utilize a modal model of the system, but the force identification is done by pattern matching and not by the usual inverse techniques. One limitation of the proposed technique is that it is limited to predicting a force which is a short duration pulse.

This chapter also discussed glide height testing research. Other researchers have developed the technique, and demonstrated the use of different piezoelectric sensors for detecting head/asperity impacts. Similar to the research in this thesis, other researchers have identified the high frequency AE signal as resulting from the vibrational modes of the read/write head (slider). However, the contribution of this work is that a modal analysis has been performed and used to: 1) make quantitative predictions of the frequency response function of the slider, 2) study the effect of impact and sensor locations, and 3) develop signal processing techniques. The next chapter will show how FEM and modal analysis can be used to predict the frequency response functions (FRFs) of the slider, as well as study the effects of impact and sensor locations. Chapter 4 will discuss the new force identification technique and Chapter 5 will discuss how it can be used to interpret the AE signals from glide height testing.

Chapter 3

FEM and Modal Analysis

3.1 Introduction

The response of a dynamic mechanical system or structure to time varying forces depends, to a large extent, on the system's modes of vibrations. The force identification technique, detailed in the next chapter, makes use of this fact to solve the inverse problem of determining input forces when only the vibrations can be measured. As will be demonstrated, the extent to which different modes are excited can be used as an indicator of location of the input force. Thus, understanding the vibration modes of a system is a prerequisite to using the force identification technique.

The subjects of Finite Element Modeling (FEM) and modal analysis are quite vast, and cannot be treated here in any great detail. At the same time, the notation and details of the treatment of the subject can vary from one author to the next. For these reasons, a brief presentation will be given in this chapter to the subjects of dynamic FEM and modal analysis. This also gives an opportunity to emphasize the areas of FEM and modal analysis that are most important to the force identification technique shown in the next chapter.

The later part of this chapter is a presentation of a finite element model and modal analysis of the read/write head (slider) of a hard disk drive. Verification of the analysis is provided by experiments performed on the slider and on an enlarged model of the slider.

3.2 Finite Element Modeling of Dynamic Systems

In FEM the continuum of the structure is divided up into small "bricks" or elements (as they are usually called). These bricks represent a "finite" approximation to the actual structure, as shown in Figure 3.1. By using these approximate elements, the continuous differential equations of elasticity are replaced by linear matrix equations. The elastic stiffness of the elements is represented by a stiffness matrix \mathbf{K} , which describes the relative spring stiffness between the displacement of any two nodes. Similarly, the mass of the elements can be divided up among

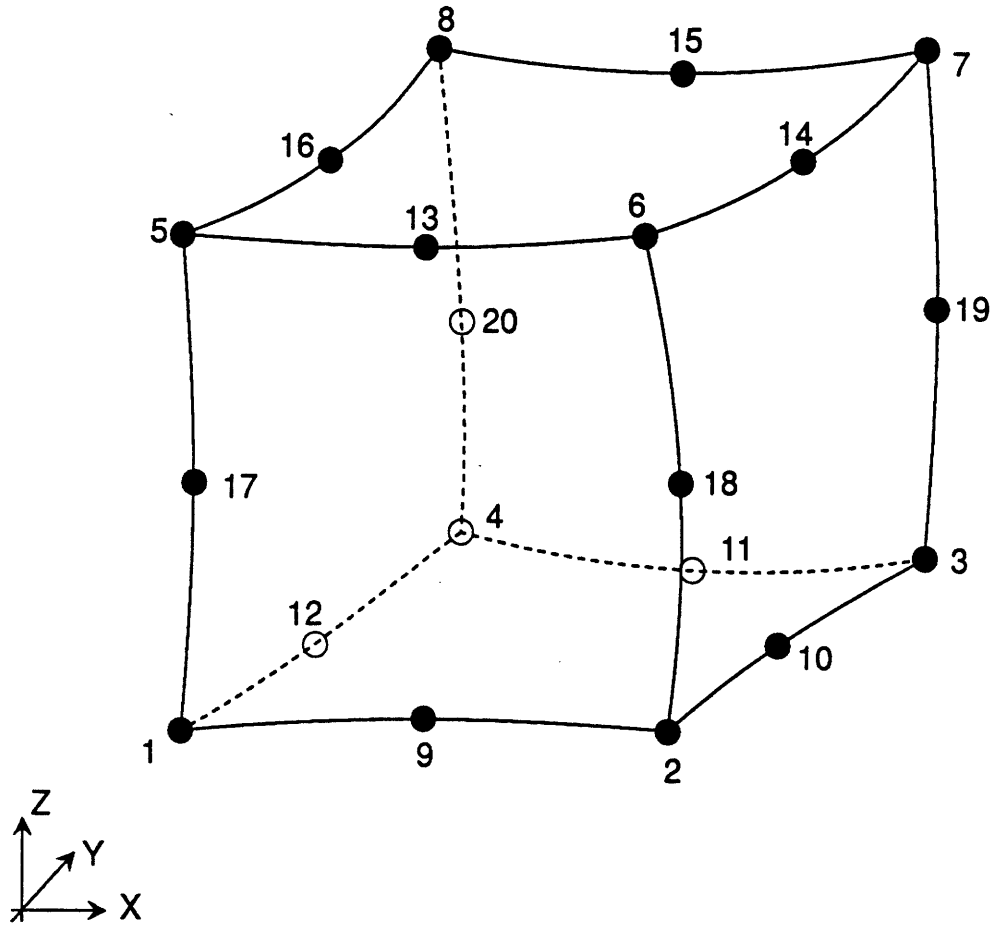


Figure 3.1: Schematic of a 3-D 20-node brick element.

the nodes and a mass matrix \mathbf{M} constructed. The two matrices can be incorporated into the equations of motion for the structure.

$$\mathbf{M}\ddot{x} + \mathbf{K}x = f \quad (3.1)$$

where x is the vector of displacements at the nodes, \ddot{x} is the acceleration of the nodes, and f is the input forcing vector.

Before one studies the forced vibration of a system, it is first necessary to study the free vibration problem where no load is applied. For free vibration, the input vector f is set to zero.

$$\mathbf{M}\ddot{x} + \mathbf{K}x = 0 \quad (3.2)$$

To solve problems of this type we should look for solutions of the form

$$x = \phi \sin(\omega(t - t_0)) \quad (3.3)$$

where ϕ is a vector of constants, t is time, and ω is the radian frequency of vibration, and t_0 is a constant. Taking the derivatives of this equation with respect to time,

$$\dot{x} = \omega\phi \cos(\omega(t - t_0)) \quad (3.4)$$

$$\ddot{x} = -\omega^2\phi \sin(\omega(t - t_0)). \quad (3.5)$$

Plugging in (3.3) and (3.5) into (3.2)

$$\mathbf{M}(-\omega^2\phi \sin(\omega(t - t_0))) + \mathbf{K}(\phi \sin(\omega(t - t_0))) = 0 \quad (3.6)$$

$$-\omega^2\mathbf{M}\phi + \mathbf{K}\phi = 0 \quad (3.7)$$

$$\mathbf{K}\phi = \omega^2\mathbf{M}\phi. \quad (3.8)$$

This is a standard eigenvalue problem with n solutions, where n is the size of the square matrix \mathbf{M} or \mathbf{K} . The n solutions come in the form of eigenvalue-eigenvector pairs.

$$(\omega_1^2, \phi_1), (\omega_2^2, \phi_2), \dots, (\omega_n^2, \phi_n) \quad (3.9)$$

Physically, the eigenvalues $(\omega_1^2, \omega_2^2, \dots, \omega_n^2)$ correspond to the square of the natural frequencies of the system. The eigenvectors $(\phi_1, \phi_2, \dots, \phi_n)$ are the displacements that describe the "mode shapes" (e.g. bending, torsion) of the system.

There are a few customs in defining the eigenvalues and eigenvectors. Eigenvalues are generally arranged so that

$$0 \leq \omega_1^2 \leq \omega_2^2 \leq \dots \leq \omega_n^2 \quad (3.10)$$

Arranged this way, ω_1 is the lowest natural frequency. A second convention is that because eigenvectors are only specified to within an arbitrary constant (i.e. ϕ_i is as good a solution as $\beta\phi_i$, where β is a constant), the eigenvectors are constructed to be M-orthonormalized. This means that the eigenvectors are orthogonal to each other and normalized to one as shown in the following equation.

$$\phi_i^t M \phi_j = \begin{cases} 1, & \text{if } i = j; \\ 0, & \text{if } i \neq j. \end{cases} \quad (3.11)$$

Here, the superscript t indicates a matrix transpose. It is also customary to define two $n \times n$ matrices

$$\Phi = [\phi_1, \phi_2, \dots, \phi_n] \quad (3.12)$$

$$\Omega^2 = \begin{pmatrix} \omega_1^2 & 0 & \dots & 0 \\ 0 & \omega_2^2 & \dots & 0 \\ \vdots & \vdots & \ddots & \vdots \\ 0 & 0 & \dots & \omega_n^2 \end{pmatrix} \quad (3.13)$$

where Φ is the eigenvector matrix, and Ω^2 is the eigenvalue matrix. It can be shown that

$$K\Phi = M\Phi\Omega^2 \quad (3.14)$$

and from Equations 3.11 - 3.14, it can be shown that,

$$\Phi^t K \Phi = \Omega^2 \quad (3.15)$$

$$\Phi^t M \Phi = I \quad (3.16)$$

where I is the identity matrix.

In this way, the model of the structure has been transformed from a spatial model (M and K) to a modal model (Ω^2 and Φ). The transformation is simply a mathematical technique that presents a new way to think about the same structure. Instead of thinking about the structure as a collection of masses and stiffnesses, it can be thought of in terms of frequencies and mode shapes. (See pages 19-21 of Ewins book[1] for a more detailed discussion.)

3.3 Modal Analysis

This type of eigenvalue - eigenvector extraction is useful for determining the resonance frequencies at which a body (or structure) vibrates. However, another technique, known as modal analysis, can use the eigenvalues and eigenvectors to determine the vibrational response of the system to various inputs.

In modal analysis, the response at one node (or given location on the structure) is measured while a sinusoidal forcing function is input at another node. Thus the forced problem of (3.1)

$$\mathbf{M}\ddot{x}(t) + \mathbf{K}x(t) = f(t) \quad (3.17)$$

must be solved. For a sinusoidal input

$$f(t) = fe^{i\omega t} \quad (3.18)$$

$$x(t) = xe^{i\omega t} \quad (3.19)$$

using (3.18) and (3.19) in (3.17) yields

$$(\mathbf{K} - \omega^2\mathbf{M})xe^{i\omega t} = fe^{i\omega t} \quad (3.20)$$

$$x = (\mathbf{K} - \omega^2\mathbf{M})^{-1}f \quad (3.21)$$

or

$$x = [\alpha(\omega)]f \quad (3.22)$$

where $[\alpha(\omega)]$ is a $n \times n$ matrix called the receptance and defined as

$$[\alpha(\omega)] \equiv (\mathbf{K} - \omega^2\mathbf{M})^{-1} \quad (3.23)$$

$$\alpha_{jk}(\omega) = \left(\frac{x_j}{f_k} \right) \quad f_m = 0; \quad m = 1, n; \neq k. \quad (3.24)$$

where the subscript j is the location (node) on the structure where the displacement is measured and the subscript k is the location (node) where the force is applied. The condition on the right is the requirement that a force only be applied at location k and at no other location. The calculation of $[\alpha(\omega)]$ can be simplified as follows.

$$(\mathbf{K} - \omega^2\mathbf{M}) = [\alpha(\omega)]^{-1} \quad (3.25)$$

$$\Phi^t(\mathbf{K} - \omega^2\mathbf{M})\Phi = \Phi^t[\alpha(\omega)]^{-1}\Phi \quad (3.26)$$

$$\text{diag}[(\omega_r^2 - \omega^2)] = \Phi^t[\alpha(\omega)]^{-1}\Phi \quad (3.27)$$

where diag means a diagonal matrix and the values of ω_r are the natural frequencies. Therefore

$$[\alpha(\omega)] = \Phi \text{diag}[(\omega_r^2 - \omega^2)]^{-1}\Phi^t. \quad (3.28)$$

Noting that

$$\begin{pmatrix} a_1 & 0 & \dots & 0 \\ 0 & a_2 & \dots & 0 \\ \vdots & \vdots & \ddots & \vdots \\ 0 & 0 & \dots & a_n \end{pmatrix}^{-1} = \begin{pmatrix} 1/a_1 & 0 & \dots & 0 \\ 0 & 1/a_2 & \dots & 0 \\ \vdots & \vdots & \ddots & \vdots \\ 0 & 0 & \dots & 1/a_n \end{pmatrix} \quad (3.29)$$

$$[\alpha(\omega)] = \Phi \operatorname{diag} \left[\frac{1}{\omega_r^2 - \omega^2} \right] \Phi^t \quad (3.30)$$

or

$$\alpha_{jk} = \sum_{r=1}^n \frac{{}_r\phi_j \cdot {}_r\phi_k}{\omega_r^2 - \omega^2} \quad (3.31)$$

In this way the values of the receptance, α , can be calculated from only the eigenvalues and eigenvectors. Physically α_{jk} gives the relationship between a sinusoidal force input (f_k) at node k , and the sinusoidal displacement (x_j) at node j . It is important to realize that ${}_r\phi_j$ and ${}_r\phi_k$ are scalars and not vectors.

It is common practice to replace the product of the two modal constants ${}_r\phi_j \cdot {}_r\phi_k$ with ${}_rA_{jk}$ and it is called the *modal constant*. This substitution is important because experimentally the individual values of ${}_r\phi_j$ and ${}_r\phi_k$ cannot be easily determined, only the product of the two can be found, ${}_rA_{jk}$.

In addition to using nodal displacement to characterize a structure's response, as in receptance, both nodal velocity and nodal acceleration are also commonly used. The ratio of velocity to force is called mobility $Y(\omega)$ and the ratio of acceleration to force is called accelerance (or inertance) $I(\omega)$. Equation 3.31 can be easily modified to express the quantities of mobility and accelerance.

$$Y_{jk}(\omega) = \frac{v(\omega)}{f(\omega)} = i\omega \sum_{r=1}^n \frac{{}_rA_{jk}}{\omega_r^2 - \omega^2} \quad (3.32)$$

$$\begin{aligned} I_{jk}(\omega) &= \frac{\ddot{a}(\omega)}{f(\omega)} = -\omega^2 \sum_{r=1}^n \frac{{}_rA_{jk}}{\omega_r^2 - \omega^2} \\ &= \sum_{r=1}^n \frac{-{}_rA_{jk}}{1 - (\omega_r/\omega)^2} \end{aligned} \quad (3.33)$$

The forms of the frequency response functions (FRF), i.e. receptance, mobility, and accelerance, presented so far have been for an undamped system. Damping can be modeled in a few different ways [1], but only proportional structural damping will be considered in this thesis. Damping can be added to Equation 3.31 by the simple addition of $i\eta_r\omega_r^2$ in the denominator.

$$\alpha_{jk} = \sum_{r=1}^n \frac{{}_rA_{jk}}{\omega_r^2 - \omega^2 + i\eta_r\omega_r^2} \quad (3.34)$$

The parameter η_r is called the loss factor and is the key parameter in structural damping.

The following two sections will show how FEM and modal analysis are applied to modeling the vibrations of the read/write head (slider) of a hard disk.

3.4 FEM Model of 3380 Slider

Most modern hard disk drives use a particular type of slider known as the 3380 style. Modeling will be restricted to this type of slider. A diagram of a 3380 slider is shown in Figure 3.2. The 3380 slider is generally made from a ceramic called alumina titanium carbide, $\text{Al}_2\text{O}_3\text{-TiC}$. This ceramic has a density of $4.28 \times 10^3 \text{ kg/m}^3$, an elastic modulus of $3.92 \times 10^{11} \text{ N/m}^2$, and a poisson's ratio of 0.35. Using this information it is possible to develop a FEM model.

The particular FEM program used is called ABAQUS and is sold by Hibbett, Karlsson, and Sorenson, Inc. Figure 3.3 shows a diagram of the slider model and Appendix C is a copy of the input file. The model consists of 258 20-node brick elements. This results in 1534 nodes and 4602 degrees of freedom. During operation the slider is suspended by a weak spring and an air bearing. Because the spring and air bearing are so weak, they have little effect on the vibration modes of the slider. For this reason, the slider was modeled as unsupported, i.e. as if it were sitting in outer space. This also has the advantage of simplifying the FEM model (because a mesh does not have to be constructed for the spring), however, it does cause the rigid body modes to show-up as eigenvalues at zero frequency. This problem can be overcome by instructing ABAQUS not to look for the lowest eigenvalues. This is done by giving ABAQUS a "shifting frequency" that is a frequency which tells the software where to look for the first eigenvalue. This eliminates the rigid body modes of the slider. Since ABAQUS uses an iterative procedure to find the eigenvalues and eigenvectors, it must be instructed as to how many eigenvalues and eigenvectors to calculate. For the slider model, the first 6 eigenvalues were calculated.

After about 9 CPU hours on a microVAX (or 2 minutes on a Cray-2 supercomputer), ABAQUS determined that 6 of the eigenvalues had converged. Table 3.1 shows the natural frequencies and Figure 3.4 shows the mode shapes.

To try to verify that the vibration frequencies in Table 3.1 are reasonable, four additional FEM models were used, see Figure 3.5. Three of the models have a courser mesh than the 258 element model, and one model has a finer mesh. These five models can be used to determine how much the natural frequencies, ω_r , of the slider change as the mesh is refined. The vibration frequencies determined by the different models are shown in Figure 3.5. The results show that the inclusion of the cut-away for the slider rails is an important feature in getting a good estimate of the natural frequencies. It can be seen that once the cut-away for the rails is included, as in the 50 element model, very little change occurs in the natural frequencies as the model is refined to 258 or 512 elements. In the modal analysis in the next section, the 258 element model is used because it gives basically the same results as the 512 element model. The 258 element model also has smaller eigenvectors that are easier to work with on the computer.

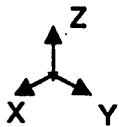
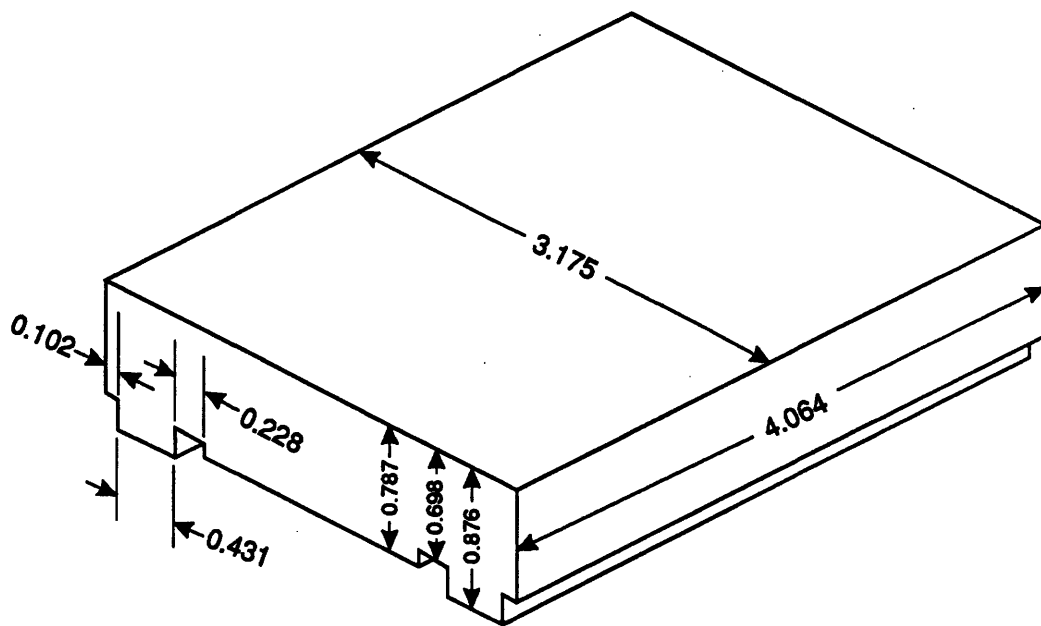


Figure 3.2: Drawing of 3380 slider with dimensions in millimeters.

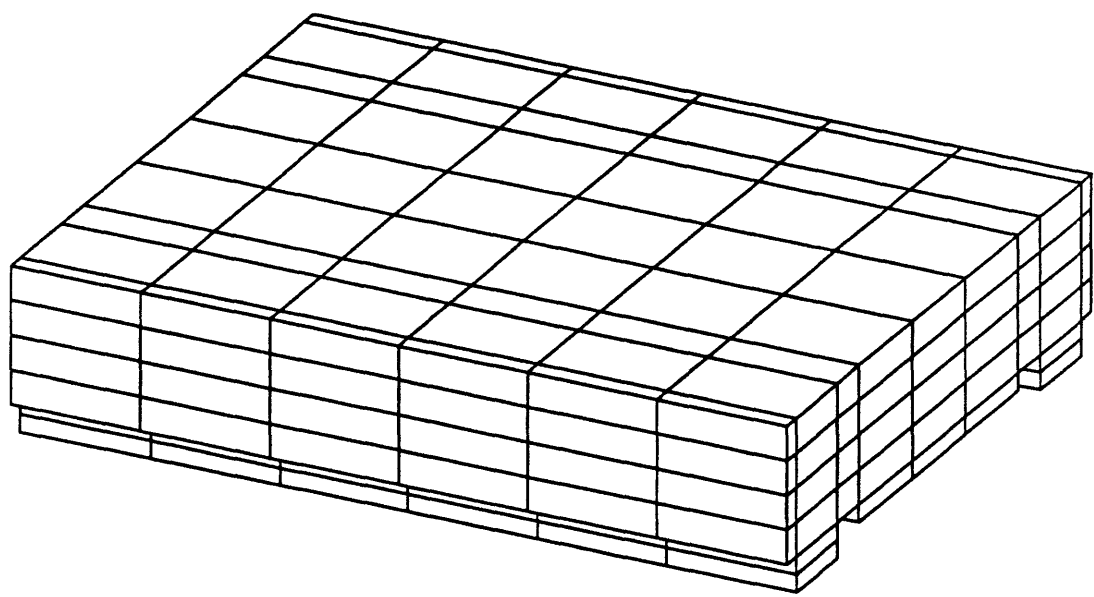


Figure 3.3: FEM model of 3380 slider with 258 elements and 4602 degrees of freedom. (Model name is 33806)

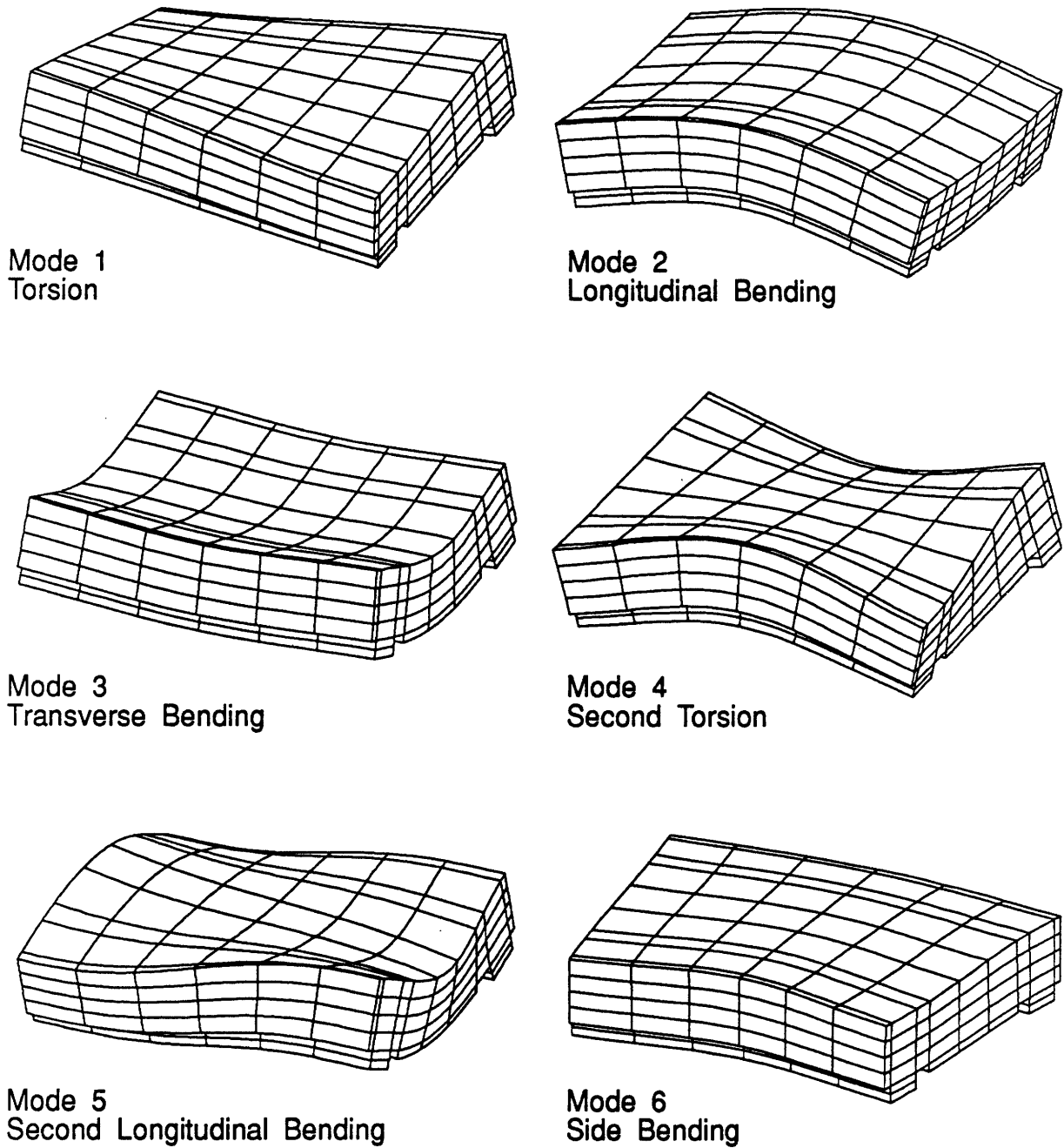
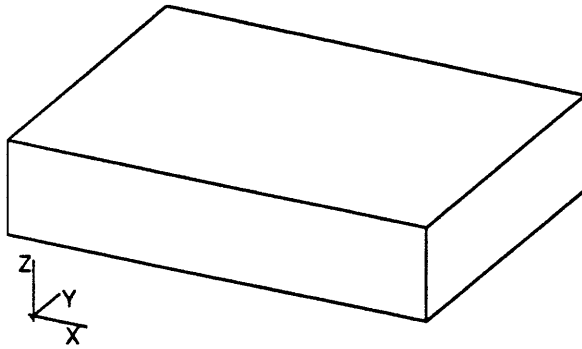
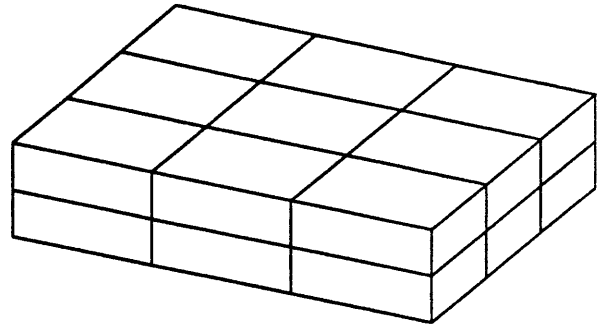


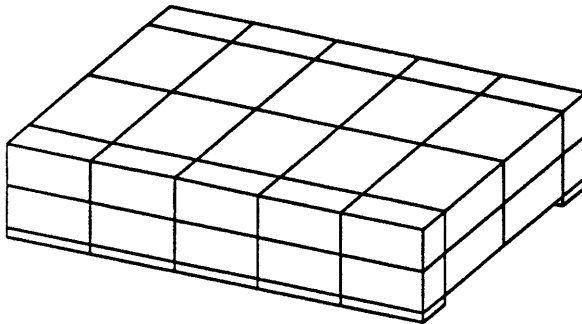
Figure 3.4: First six mode shapes of 3380 slider estimated using a 258 element FEM model with 4602 degrees of freedom.



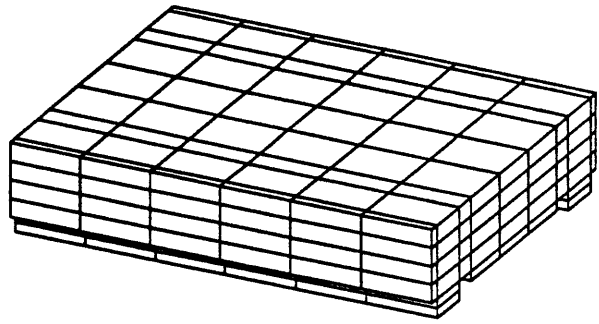
1 Element Model, Name 33801



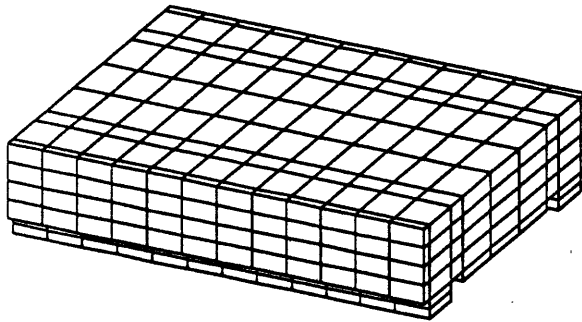
18 Element Model, Name 33803



50 Element Model, Name 33804



258 Element Model, Name 33806



516 Element Model, Name 338012

Model Name	Number of Elements	Vibration Frequency in KHz					
		Mode 1	Mode 2	Mode 3	Mode 4	Mode 5	Mode 6
33801	1	392	524	901	925	1086	1050
33803	18	348	458	747	764	887	913
33804	50	311	426	666	698	806	909
33806*	258	305	422	656	689	787	903
338012	516	305	422	656	687	786	902

Figure 3.5: Comparison of different FEM models of a 3380 slider.

* This was the model that was chosen for use in the modal analysis.

Mode	Frequency	Mode Shapes (See Figure 3.4)
1	305 KHz	Torsion
2	422 KHz	Longitudinal Bending
3	656 KHz	Transverse Bending
4	689 KHz	Second Torsion
5	787 KHz	Second Longitudinal Bending
6	903 KHz	Side Bending

Table 3.1: Natural frequencies of 3380 slider.

3.5 Modal Analysis of 3380 Slider

In Section 3.3 the analysis was given for determining the vibrational response of a system to force inputs at different locations. The system response can be determined using only the eigenvalues and eigenvectors,

$$I_{jk}(\omega) = -\omega^2 \sum_{r=1}^n \frac{r\phi_j \cdot r\phi_k}{\omega_r^2 - \omega^2 + i\eta_r\omega_r^2}. \quad (3.35)$$

The summation in (3.35) is over the whole range of eigenvectors from 1 to n , that is from the lowest modes to the highest modes. In most FEM, the higher order modes are of little practical interest and even if they were of interest they are poorly modeled (A more refined mesh would be needed to adequately model these higher modes). Therefore it is very common to use a truncated summation in (3.35), i.e.

$$I_{jk}(\omega) = -\omega^2 \sum_{r=1}^{m \leq n} \frac{r\phi_j \cdot r\phi_k}{\omega_r^2 - \omega^2 + i\eta_r\omega_r^2} \quad (3.36)$$

In this case the matrix of eigenvalues Ω would be $m \times m$ and the matrix of eigenvectors Φ would be $n \times m$.

For the 3380 slider model this truncated summation is the only practical choice. If all eigenvalues could be calculated, there would be 4602. This is clearly too many to be of practical value. Furthermore, the vibration frequencies of the modes greater than mode 6, would be above 1 MHz and be very difficult to measure experimentally. Therefore, only the first 6 vibration modes were used in the modal analysis.

The frequency response function (or accelerance) of a structure is a function of force input location and sensor location. This is indicated by the two subscripts jk on the accelerance I_{jk} . The input locations along the slider are limited to the bottom of the slider rails. It is only possible for the asperities to contact the slider along the bottom of the rails. The sensor would

typically be a small piece of PZT mounted on the top side of the slider, as shown in Figure 3.6. For modal analysis purposes, it would be convenient if the PZT sensor was small compared to the size of the slider. For this reason, the PZT sensor will be modeled as if it were a point sensor.¹ The choice of locations for the sensor and force input are shown in Figure 3.7. The input locations are listed by the node numbers of 3001 through 3013. The sensor locations used in the modal analysis are labeled 9251 and 15251. These sensor locations are intended to give a typical response of a PZT sensor mounted on the top of the slider.

The particular version of ABAQUS used for the FEM model did not have any modal analysis capabilities. In order to calculate Equation 3.36, the ABAQUS output file was downloaded to a IBM PC. The goal was to use MATLAB (a general purpose matrix manipulation program) to calculate Equation 3.36. But first the ABAQUS output file had to be converted to a form that could be read by MATLAB. A conversion program was written in C to do just that, see Appendix D for program ABA_READ.C. Inside MATLAB a program, called S380.M, was written to load the eigenvalues and eigenvectors from the files created by ABA_READ.C. Then a second program, MODAL.M was written to calculate the accelerance $I_{j,k}$ for a given pair of input and sensor locations j, k . Finally a third program, FRF_ACC.M, would use the modal constants from MODAL.M to create a graph of the frequency response function (FRF) for the pair of nodes j, k , see Appendix D for MATLAB Programs.

Figure 3.8 shows the FRF's for seven different impact locations along one of the slider rails, see Figure 3.7 for the locations. The seven graphs are arranged in such a way that the symmetry of the slider response can be demonstrated. The graphs should be viewed top left to bottom left, then bottom right to top right. Viewed this way the graphs are shown in the order of impact at the leading edge (3001) to middle (3007) to trailing edge (3013) of the slider. It is clear from these graphs that the location of the input force causes a very significant difference in the vibrational response of the slider.

Consider, for a moment, just the torsional mode of vibration, whose resonance frequency is 305 KHz. When impact occurs at the leading edge (3001) of the rail, there is a strong excitation of the torsional mode. As the impact location moves toward the center (3007), the magnitude of the torsional vibration decreases to zero. Then as the impact location moves from the center (3007) to the trailing edge (3013), the strength of the torsional mode increases again.

This change in vibration magnitude with impact location was found to be useful in explaining unexpected results observed in glide height test data. Figure 3.9 shows some typical glide height test data. It was found that the low frequency AE had a very linear relationship with flying height, whereas the high frequency AE had a dip in the AE vs flying height curve. At the time that the data was taken, there was no clear understanding of what was being measured. The bandwidth of the AE signal monitored in these tests, was chosen more or less at random. As it turns out, the high frequency band (200-400 KHz) was monitoring primarily the torsional

¹The issue of miniature sensor design for glide height testing is beyond the scope of this thesis. However, it should be pointed out that there are three main problem with the PZT sensor, 1) it is not small compared to the slider and should not be considered a point sensor, 2) It is a resonance transducer and does not have a flat response, and 3) the way it is mounted it may substantially changes the resonance frequencies of the slider.

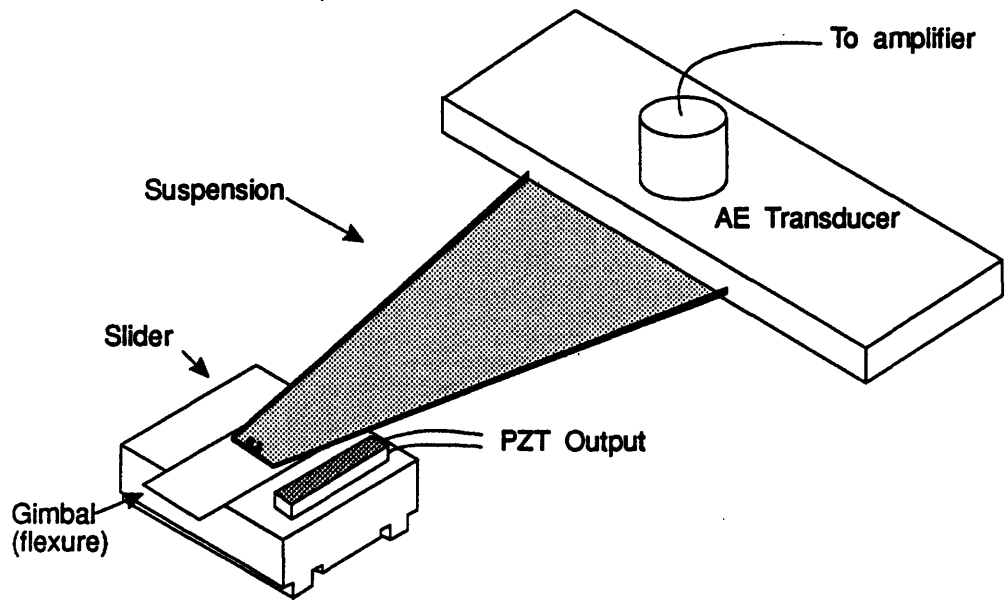


Figure 3.6: Schematic of HGA (head gimbal assembly) with PZT mounted on the slider and AE transducer mounted at the base of the HGA.

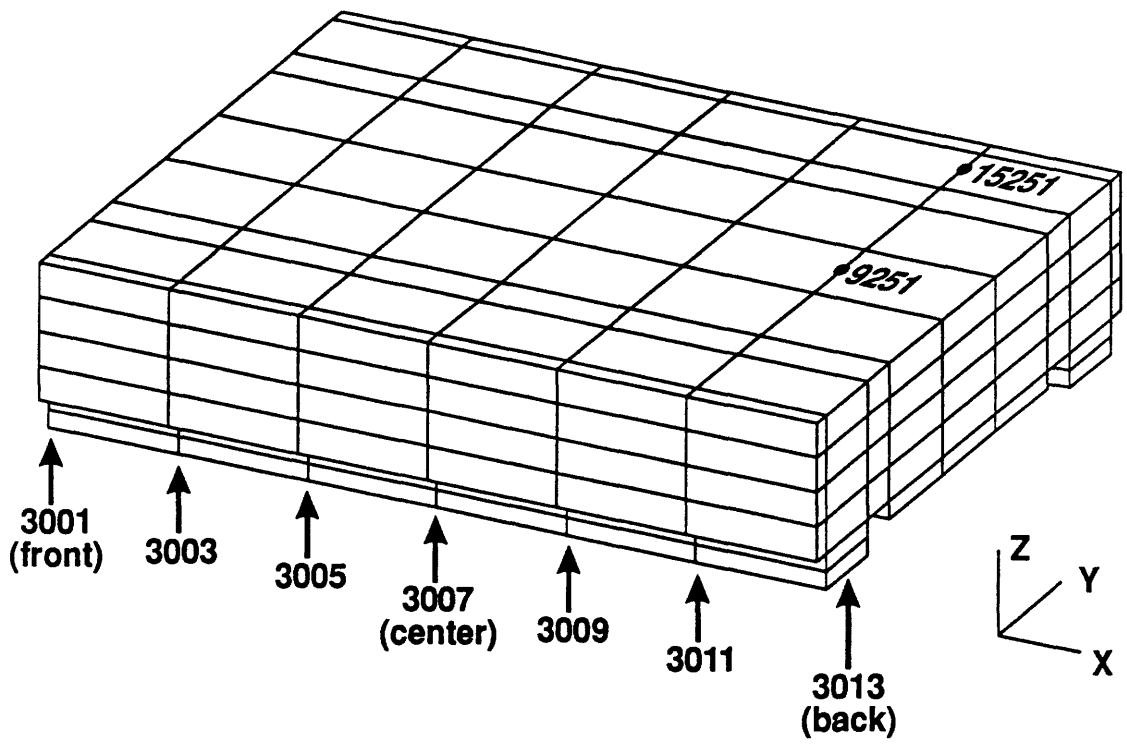


Figure 3.7: FEM model of 3380 slider showing input locations along the rail and sensor locations along the top of the slider.

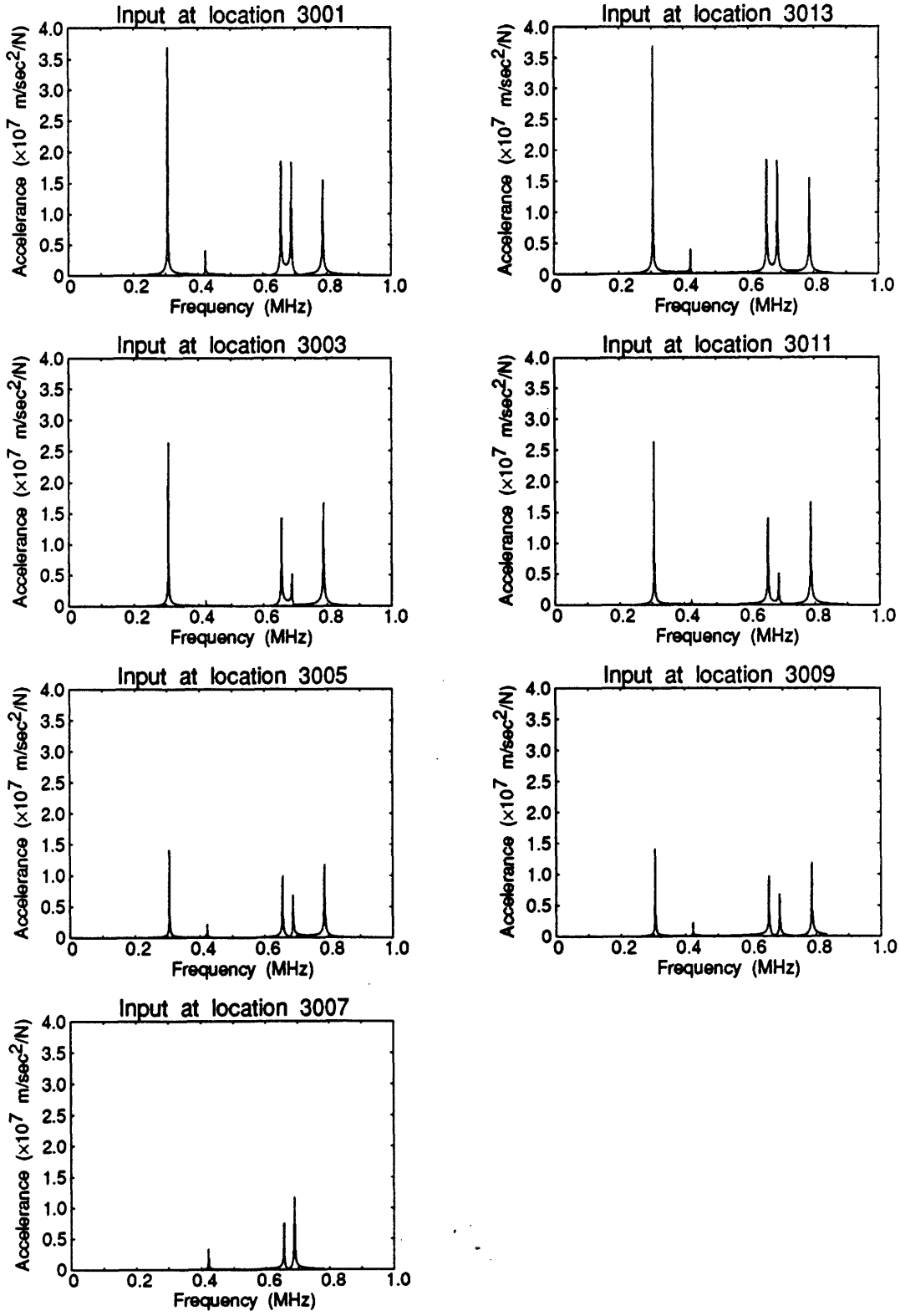


Figure 3.8: Accelerance functions for input forces at locations 3001 through 3013 along the rail. The sensor is located at location 15251. Both the forces and accelerations are measured in the Z direction.

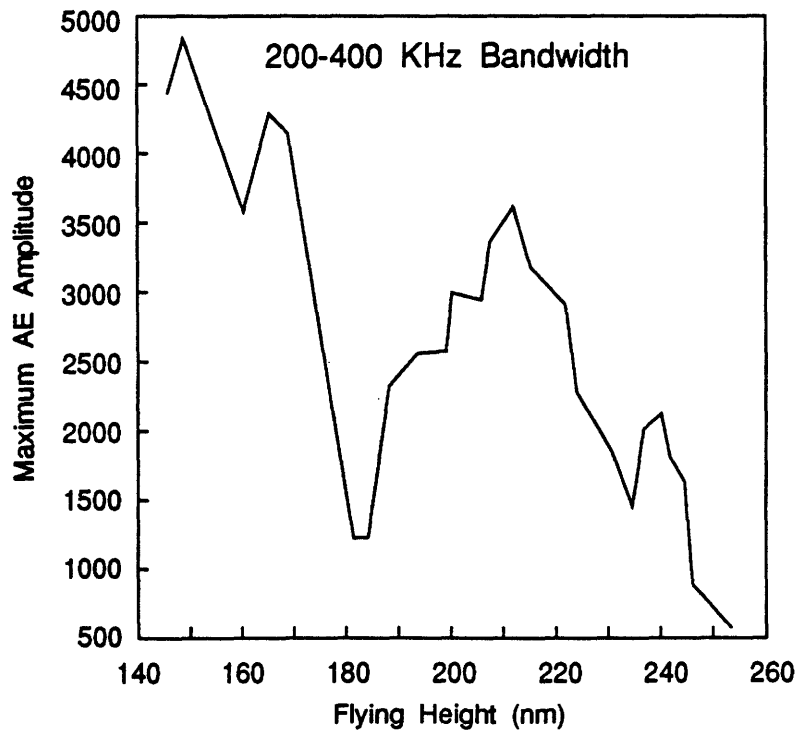
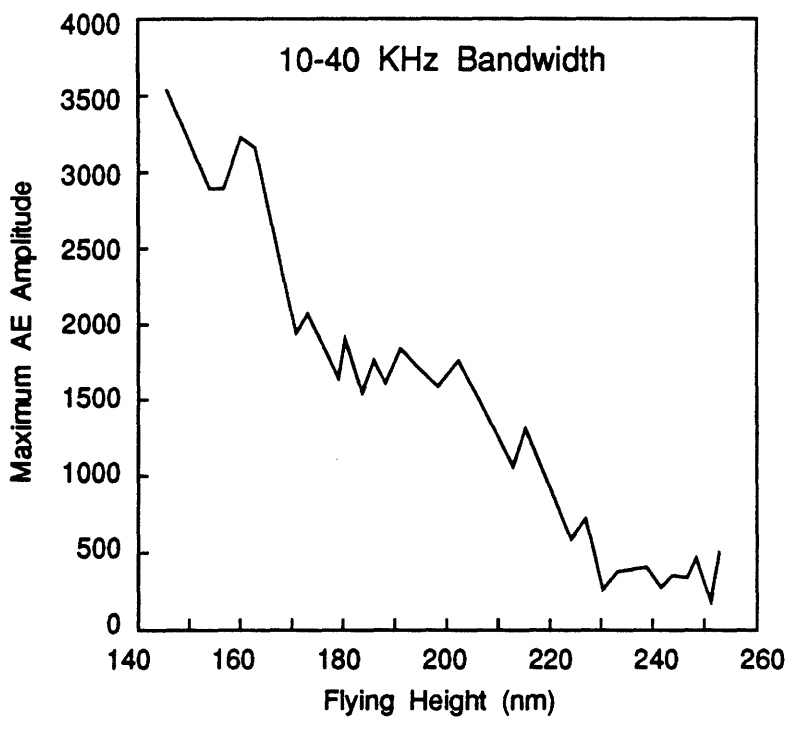


Figure 3.9: Typical low frequency (10-40KHz) and high frequency AE (200-400KHz) as a function of flying height during a glide height test.

mode (305 KHz) of vibration of the slider.

With the benefit of the modal analysis, it is fairly clear why there is a dip in the AE vs flying height curve. The read/write head (slider) flies at a slight angle with the leading edge higher than the trailing edge, as was shown in Figure 2.5. As a result, the change in flying height tends to change the impact location along the slider rail. For a fairly high flying height (say 220 nm), the impacts tend to occur at the trailing edge of the slider rail. For a lower flying height (say 180 nm), impacts occur more toward the center of the slider rail. At still lower flying heights (say 150 nm) impacts tend to occur at the leading edge of the slider rail. As previously explained, impacts at the leading and trailing edge of the slider both strongly excite the torsional vibration mode of the slider, whereas impacts at the center do not excite that mode. As a result, low levels of AE can be expected in the 200-400 KHz band when impacts occur at the center of the rail. Since impacts tend to occur at the center of the rail at the 180 nm flying height, it is not surprising to see the dip there.

There is a very practical significance to knowing the impact location along the rail. During glide height testing, the slider is only flown at a single height. As a result, larger asperities tend to hit towards the leading edge of the rail and smaller asperities at the trailing edge. Thus, if the impact location along the rail can be determined, then the size of the asperity can be estimated.

The frequency response functions (FRF's) show another interesting feature. Because of the symmetry in the structure of the slider body, an impact at the leading edge (3001) has the same response as an impacts at the trailing edge (3013). The FRF's at locations 3003 and 3011 are also the same. It will be shown, in Chapter 5, that this symmetry leads to difficulties in using the FRF's for diagnostic purposes. Figure 3.10 shows the same FRF's as in Figure 3.8 except that the data is plotted in a log scale and the phase of the FRF's is included. Plotted in this way, a difference can be seen between impacts at the leading edge (3001) and at the trailing edge (3013) of the slider rail. The difference can be seen in locations of the antiresonances. Furthermore, a difference can be seen in the phase. The most obvious difference is that for impact locations 3001 - 3005, the phase starts at 180° and for locations 3009 - 3013, the phase starts at 0° . This fact will be used in the force identification technique presented in Chapter 5.

In glide height testing, the PZT sensor can be placed at different locations on the top of the slider. To study the effect of sensor location, the FRF's were recalculated for the sensor at location 9251 (See Figure 3.7 for node locations). The FRF's for sensor locations 9251 and 15251 are compared in Figures 3.11 and 3.12. The figures clearly indicate the strong effect that sensor location can have on the measured FRF's. Although it might seem very natural to place the PZT sensor in the center of the slider, e.g. location 9251, this will make it difficult to measure certain modes of vibration of the slider. It is probably better to place the PZT sensor off to the side, as in location 15251, so that more modes can be easily measured.

Earlier, the change in vibration magnitude of the torsional mode with impact location was discussed. Graphically, there is an easy way to show this behavior. Equation 3.34 shows that the value of the modal constant, rA_{jk} , determines the magnitude of vibration of the r th mode. By plotting the modal constant vs impact location, the effect of changing impact location can

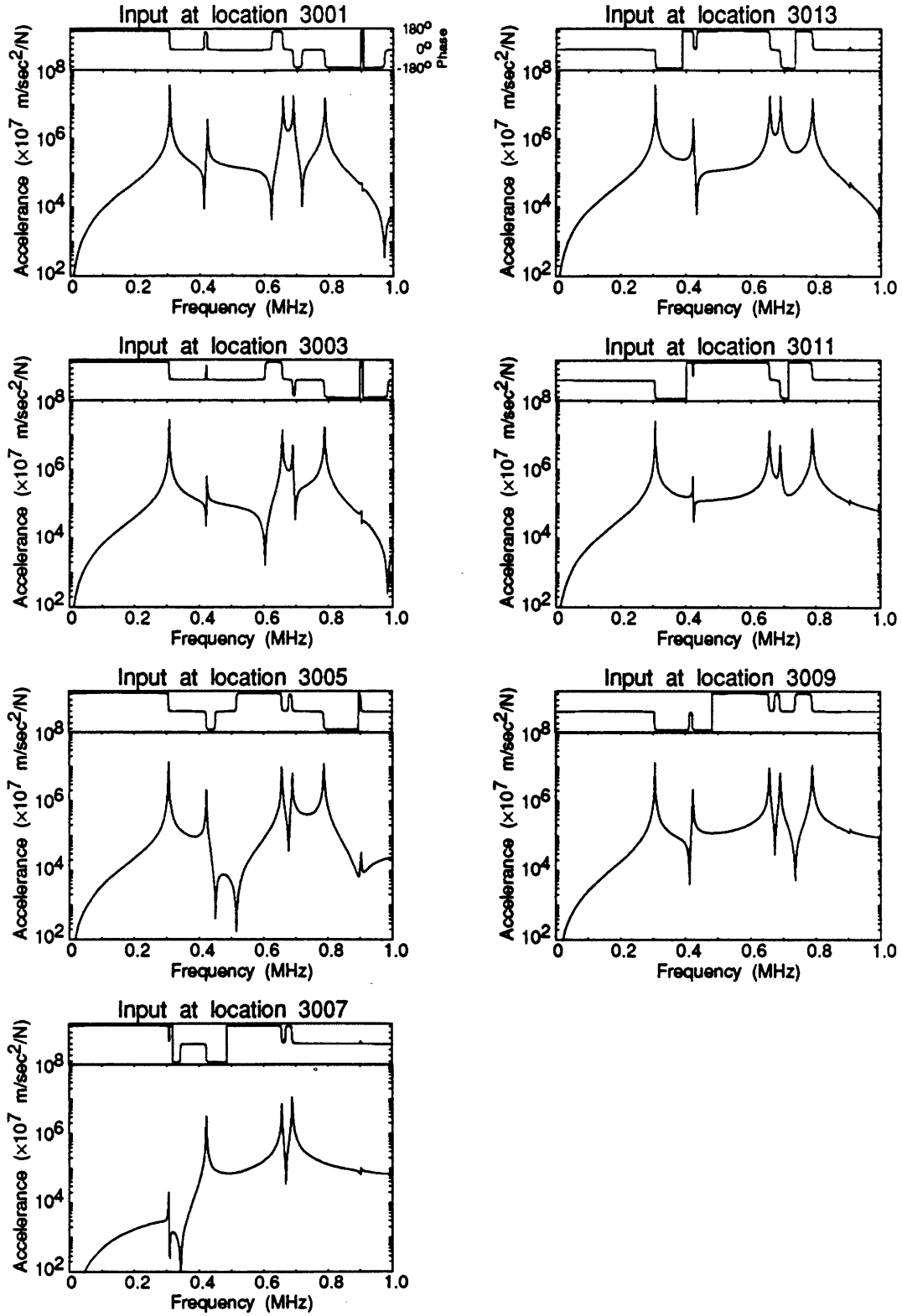


Figure 3.10: Accelerance functions for input forces at locations 3001 through 3013 along the rail. The sensor is located at location 15251. Both the forces and accelerations are measured in the Z direction.

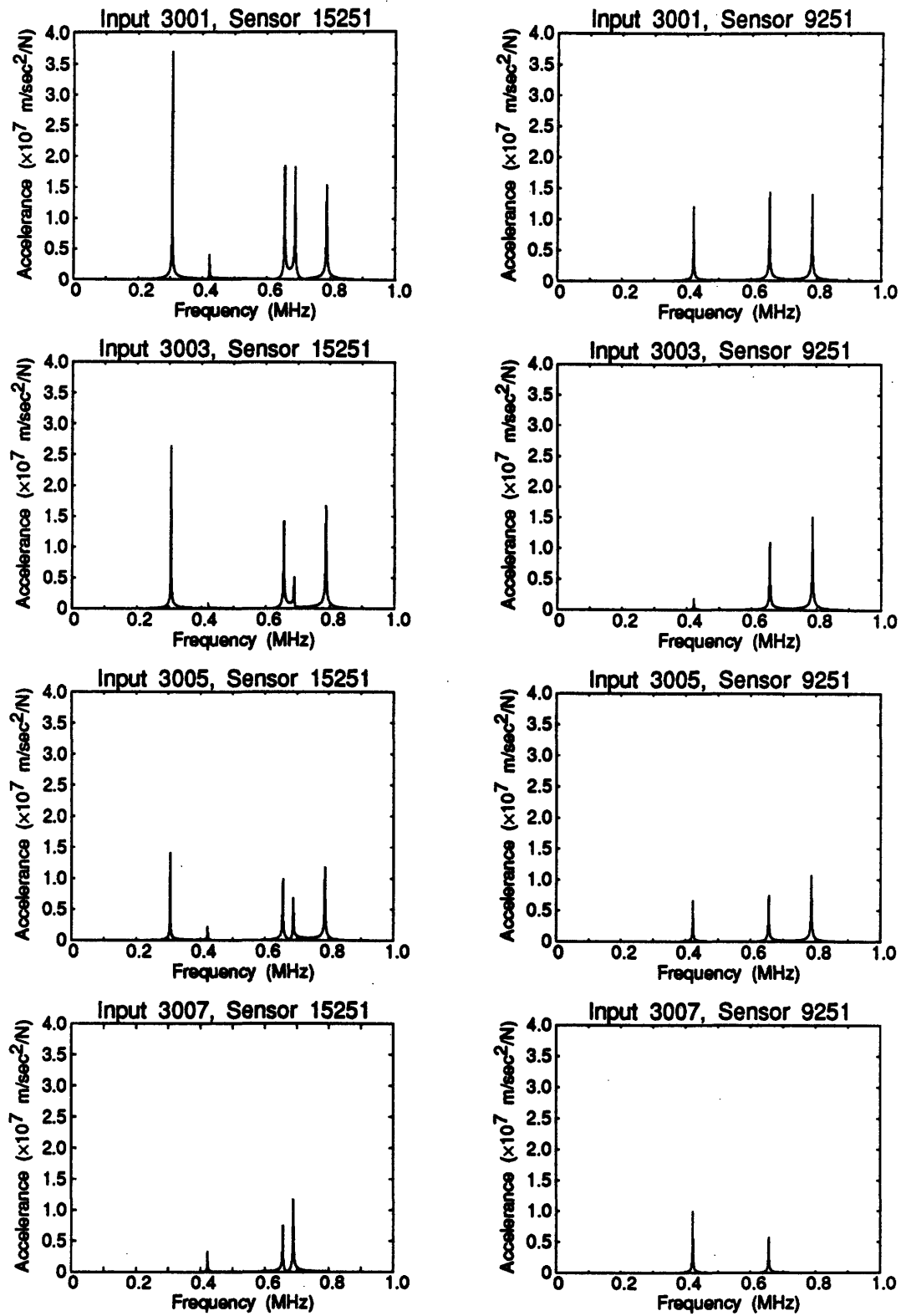


Figure 3.11: Comparison of FRF's for sensors located at locations 15251 (side) and 9251 (center).

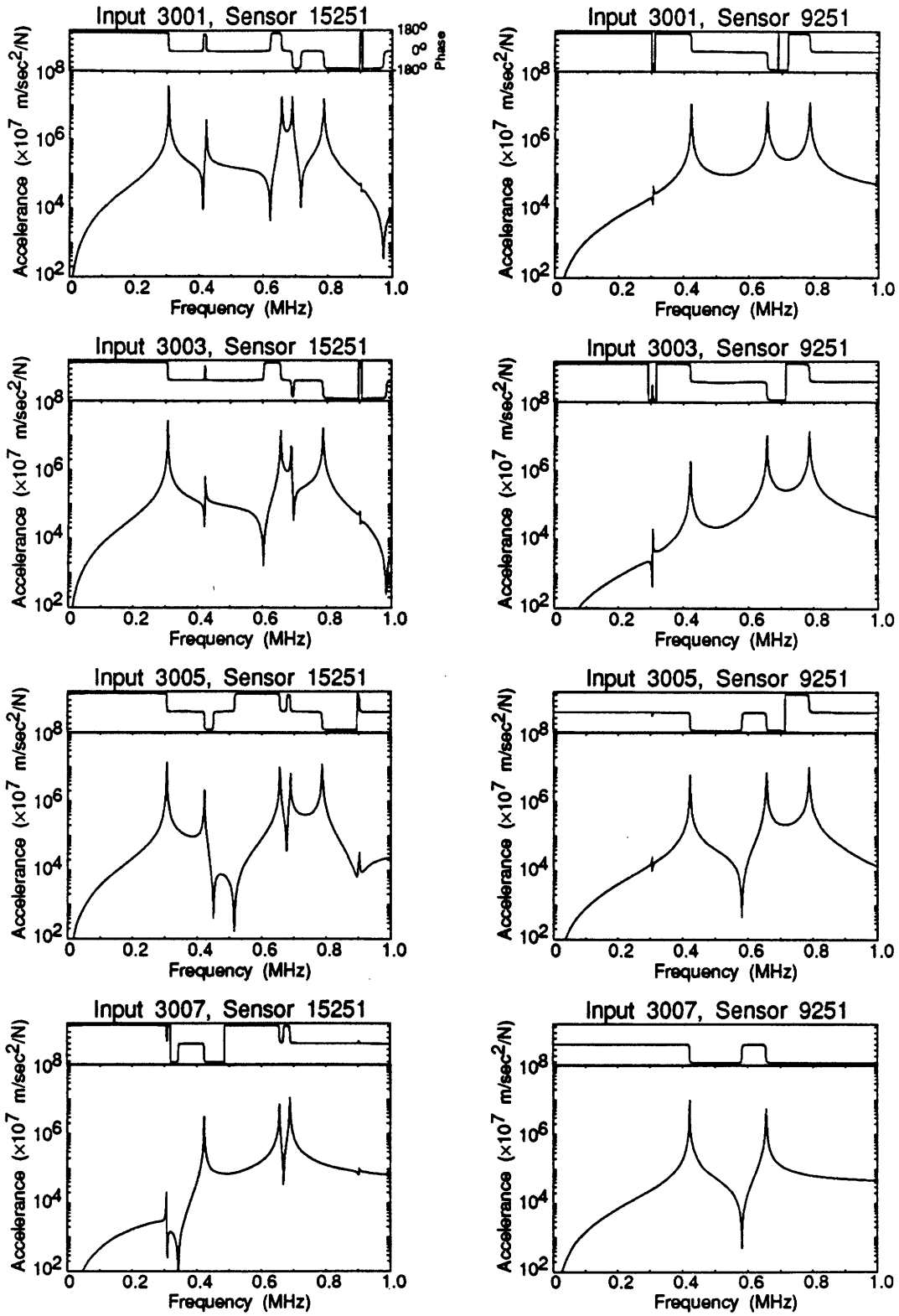


Figure 3.12: Comparison of FRF's for sensors located at locations 15251 (side) and 9251 (center).

be shown as in Figure 3.13. The modal constants can be both positive and negative. Thus if the magnitude of vibration is of interest, the absolute value of the modal constants should be considered. For the torsional mode, as already mentioned, vibration is strong for impact at the leading edge (3001) and trailing edge (3013) but not for the center (3007). The longitudinal bending mode has two locations of zero response at approximately 3003 and 3011. The graphs of the modal constants in Figure 3.13 are simply a more compact way to show the same information in the FRF's in Figures 3.8 and 3.10.

When the slider hits an asperity on the disk surface, both tangential and normal forces are created. The normal force is created by the impact and the tangential force is created by the friction between the slider and disk surface. Up to now, only the normal forces have been considered. Figure 3.14 shows the modal constants for inputs in the normal (Z direction) and tangential (X direction). It can be seen that, under most conditions, the magnitude of the modal constants for the tangential (X direction) forces is less than magnitude of the modal constants for the normal (Z direction) forces. This is even more true if the acceleration is considered rather than acceleration, i.e. if the relative magnitude of the X and Z direction forces are considered. The measured acceleration from an impact is the superposition of the results for the tangential and normal forces. Friction tests on the head/disk interface indicate that the coefficient of friction is about 0.3. Thus, the tangential force is 0.3 times the normal force. Conceptually this can be thought of by multiplying the X direction modal constants in Figure 3.14 by 0.3. Thus the contribution of the tangential forces is 0.3 times what it appears to be from the graphs of the modal constants alone. In other words, the X-direction forces are not very important. The exceptions to this statement occur when, 1) impacts are locations where the response from the normal forces is nearly zero, or 2) when mode 6 is considered. At all other times, the response of the slider is reasonably modeled by considering only the normal forces.

3.6 Glide Height Tests on Bump Disks

Whenever mathematical models of a system are developed, it is important to have some form of experimental confirmation of the model. To try to verify the FEM model and modal analysis of the slider, two types of experiments were performed. The first type of experiment was glide height tests on "bump" disks. The second type of test was ball impact tests on the slider. The bump disk tests will be discussed in this section and the ball drop tests will be discussed in the next section.

Hard disk manufacturers have developed a technique for calibrating the AE monitoring systems for their glide height test facilities. The technique uses special disk called a bump disk. The disk has an asperity of known height which is vapor deposited on the disk surface. This bump disk serves as a reference standard. When new glide heads are manufactured, they are flown over the bump disk. When the glide head hits the bump, the level of AE can be compared to previous results to determine if the glide head is working properly. The speed of the disk is varied during the test to create a range of flying heights and a curve like the one at the top of

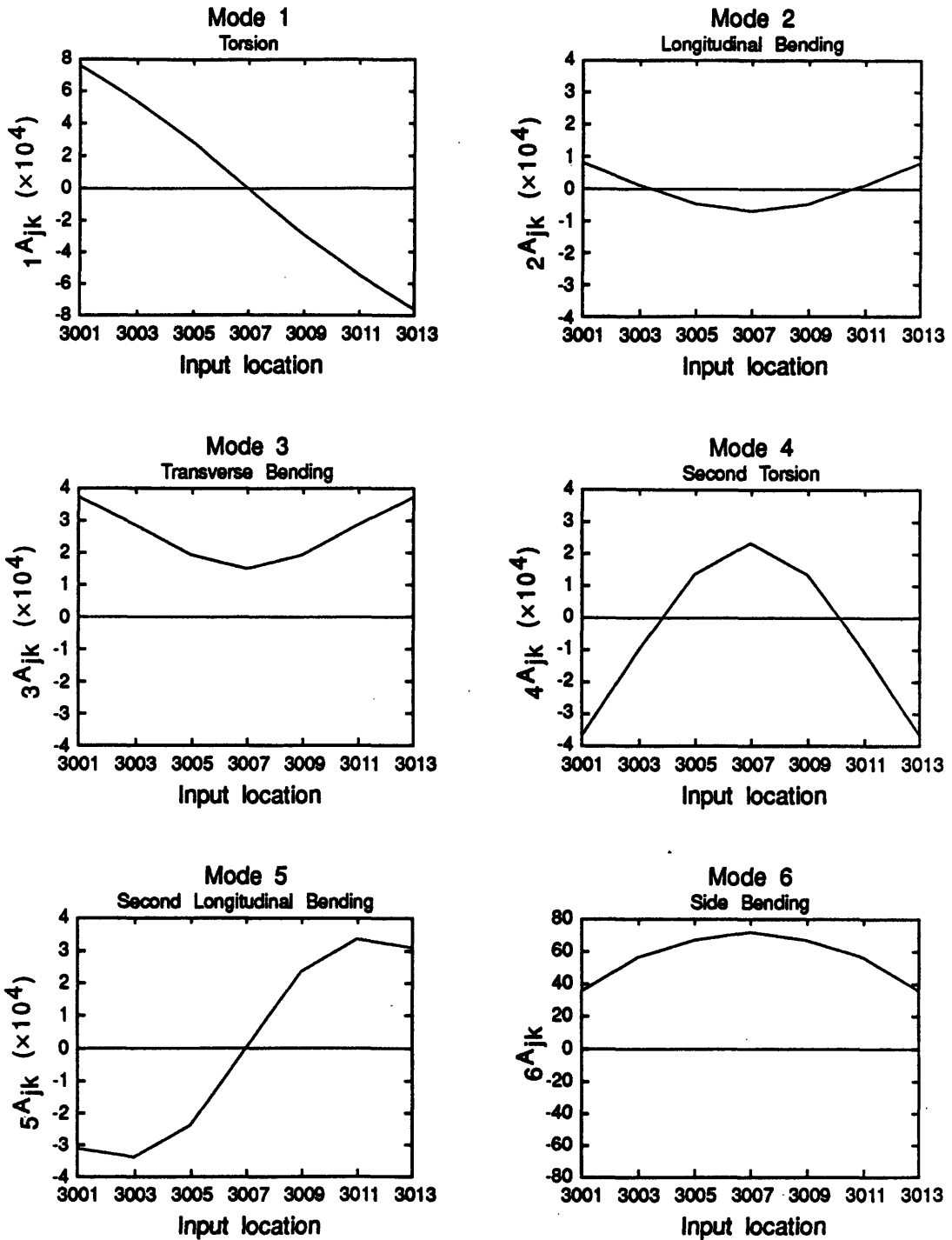


Figure 3.13: Change of modal constants with input location. The sensor location is at node 15251.

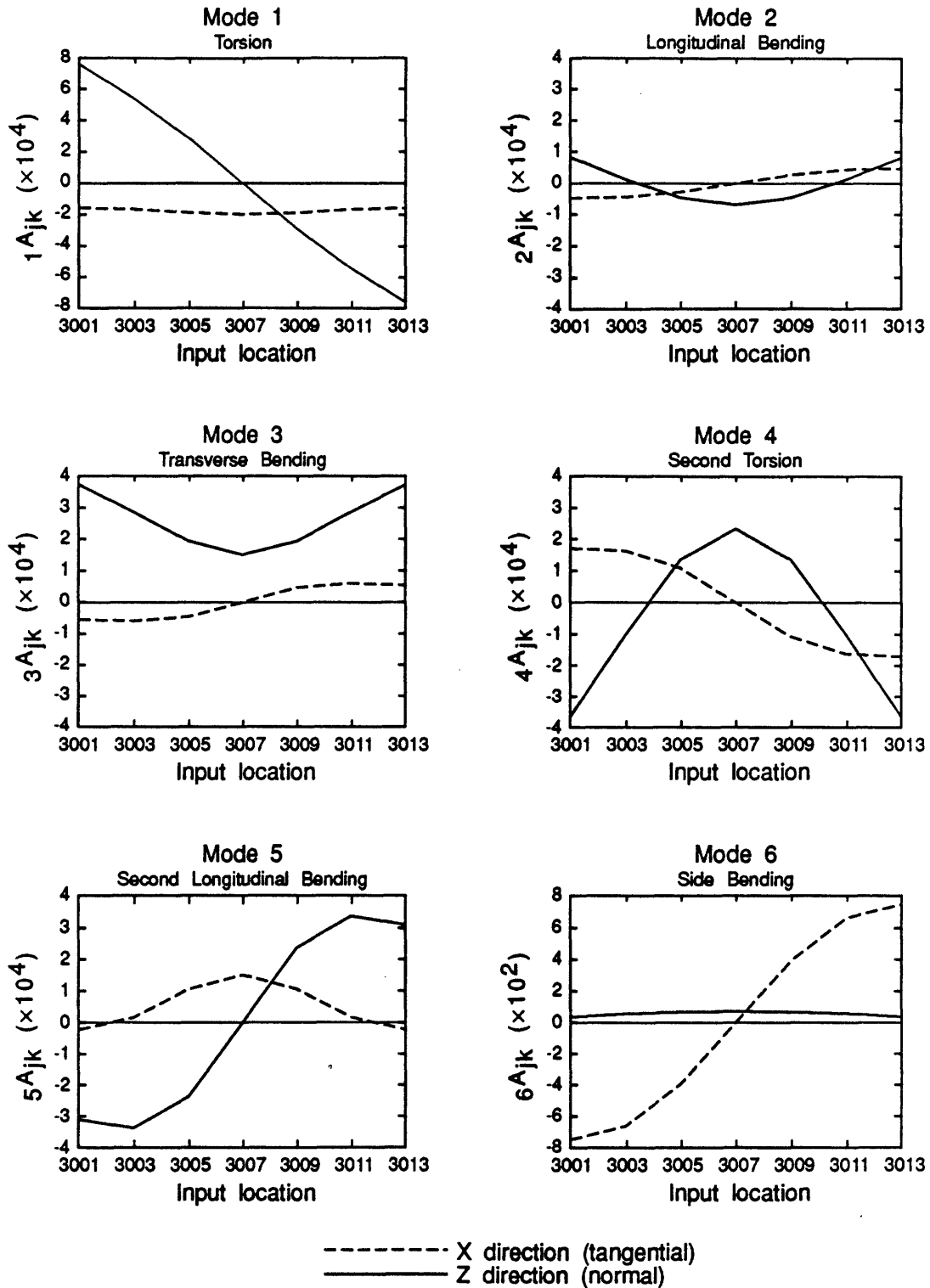


Figure 3.14: Change of modal constants with input location. The solid line is for force input in the Z direction (normal) and the dashed line is for force input in the X direction (tangential or friction). The sensor location is at node 15251.

Figure 3.9 is generated.

This calibration technique may work well enough for the manufacturer's purpose, but it presents some difficulties for a controlled study of slider/disk impacts. Before any glide height tests are run, an interferometry technique is used to determine the speed vs. flying height curve of the glide head. Then, the speed is used to control flying height, which in-turn controls the impact location along the slider rails. Unfortunately, this technique not only changes the flying height, it also changes the approach velocity of the impact. As a result, the higher flying heights in Figure 3.9 occur at a higher velocity than the lower flying heights. Since impact force is related to velocity, the impact force changes with flying height.

One way to avoid this problem is to vary flying height by varying the air pressure rather than the rotational speed of the disk. Experimentally, this is more difficult to do, but it is really the only way to get good data. Figure 3.15 shows the experimental setup for running controlled glide height tests. In the setup, a modified Seagate ST212 disk drive was placed inside a vacuum chamber. Since the slider flies on an air bearing, the flying height is controlled by controlling the amount (pressure) of air in the chamber. The chamber consists of an aluminum base plate, a plastic bell jar, and a "blow shield" (not shown). The AE is monitored using an Acoustic Emission Technologies (AET) "picotransducer" which is mounted at the base of the head gimbal assembly (HGA) as shown in Figure 3.6. The AE signal is amplified by an AET amplifier and conditioned by a Krohn-Hite filter. The signal is acquired using custom software and a Signatec 25 MHz sampling rate data acquisition board. The pressure inside the chamber is also monitored by the computer but the pressure has to be manually adjusted using a vacuum regulator valve. To control the timing of the AE sampling, an "index" signal is monitored by the computer. The index signal pulses once per revolution of the hard disk and is used to insure that data is always taken from the same location on the disk. The computer also controls the a Wilson hard disk controller via an RS232 interface. This allows the computer to turn the disk drive on and off as well as position the read/write head at different tracks on the disk. A function generator can be used to adjust the speed of the hard disk, but it was always maintained at the nominal speed of 3600 rpm.

Two types of disks were used in the tests, bump disks and scratched disks, see Figure 3.16. The bump disks were commercially made by the Plaser Co. in San Jose. The scratch disks could be made by lightly scratching the surface of a new thin film disk with an X-acto knife. Due to the accuracy of the their bumps, the bump disks were the disks of choice. But, at \$100 per disk for the bump disks, the scratch disks had to be used more often.

The tests were found to be very difficult to control. Figure 3.17 shows some typical glide height data. It is obvious, that as the pressure in the chamber increases, the level of AE decreases. Since a wide bandwidth is monitored, the AE vs flying height characteristic is not expected to be the same as the previous data, i.e. when only the 200-400 KHz range was measured. Unfortunately, before the full range of pressures (up to 14 psia) could be monitored, the bump on the disk wore out. Figure 3.17 also shows an FFT of a typical AE signal from the test. From this figure, three of the vibration modes of the slider could be identified. Most obvious is the torsional mode (mode 1).

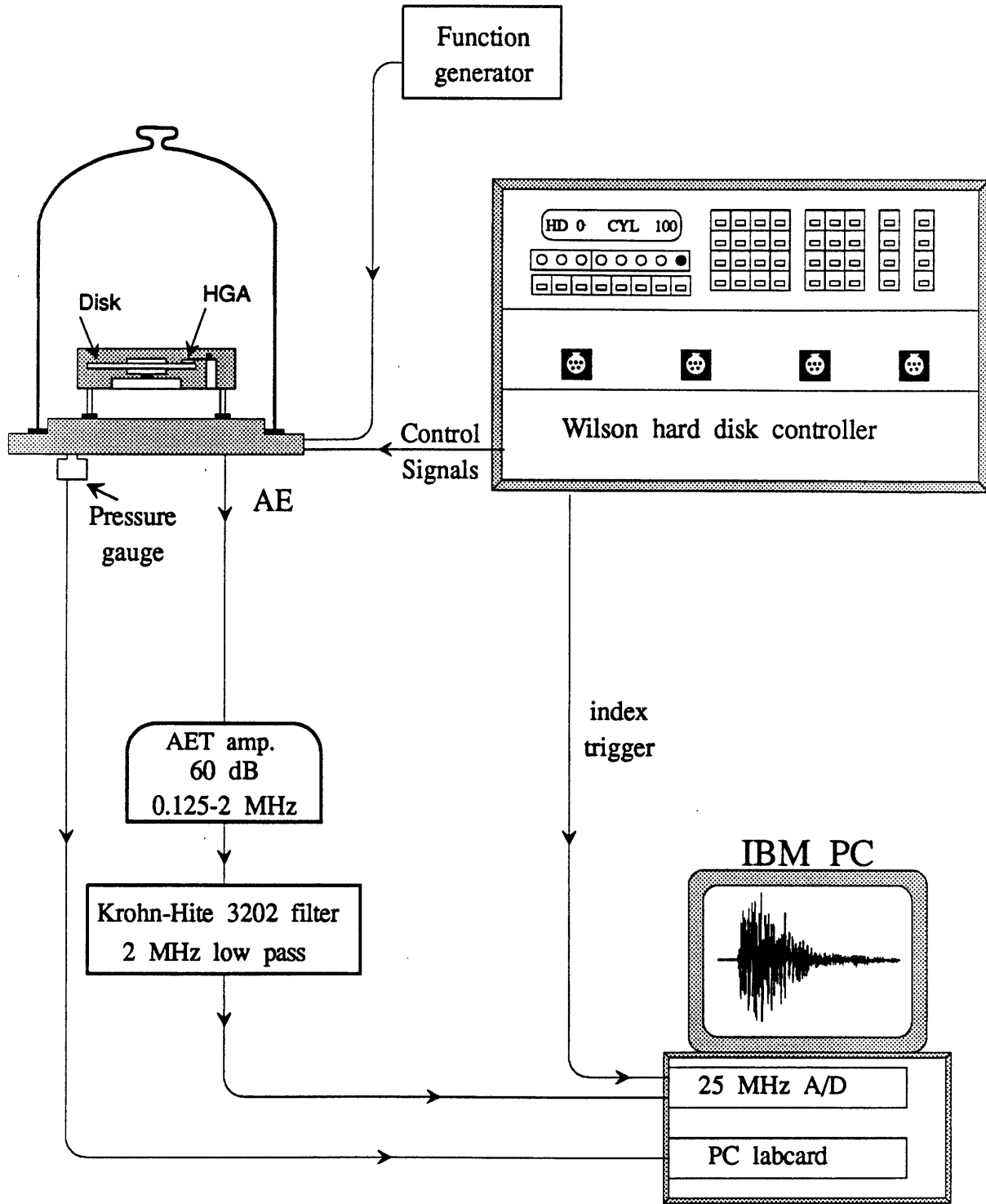


Figure 3.15: Schematic of glide height test equipment including vacuum chamber, hard disk controller, and AE data acquisition system.

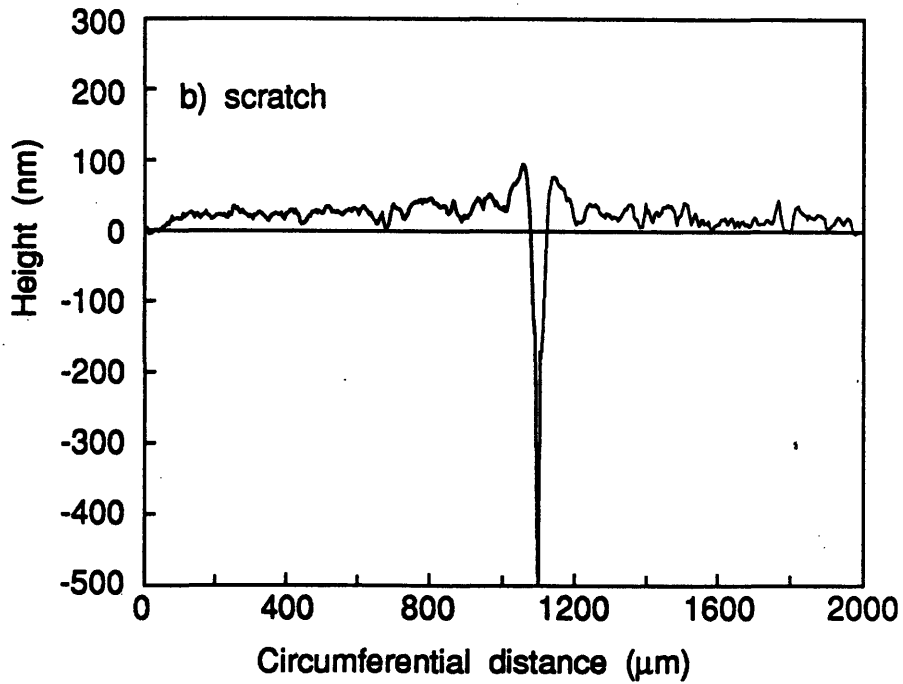
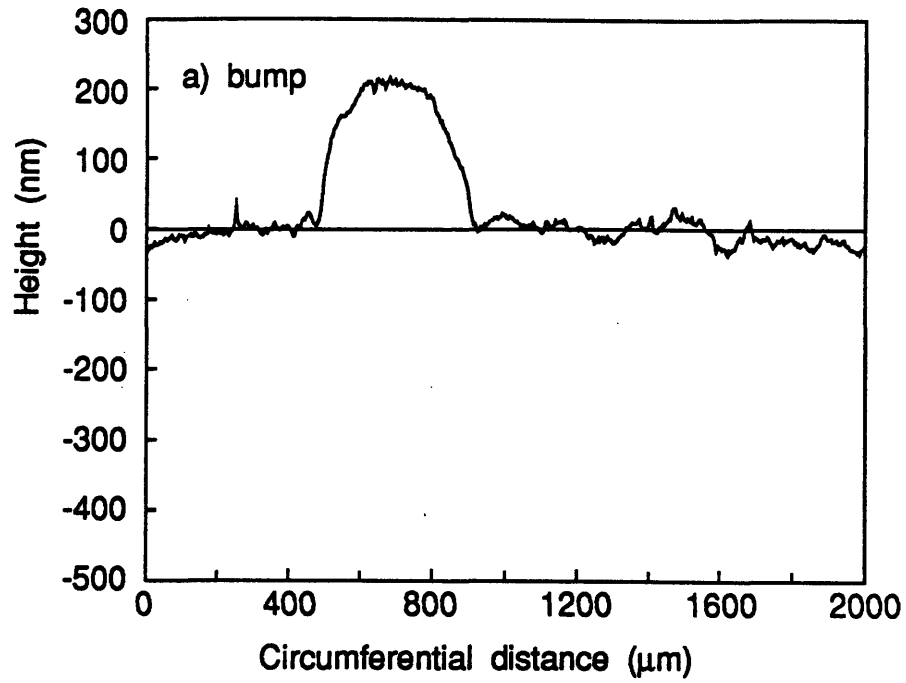


Figure 3.16: Comparison of an a) artificial bump and a b) scratch on a thin film disk. The bump disk is used commercially for calibrating glide height test equipment.

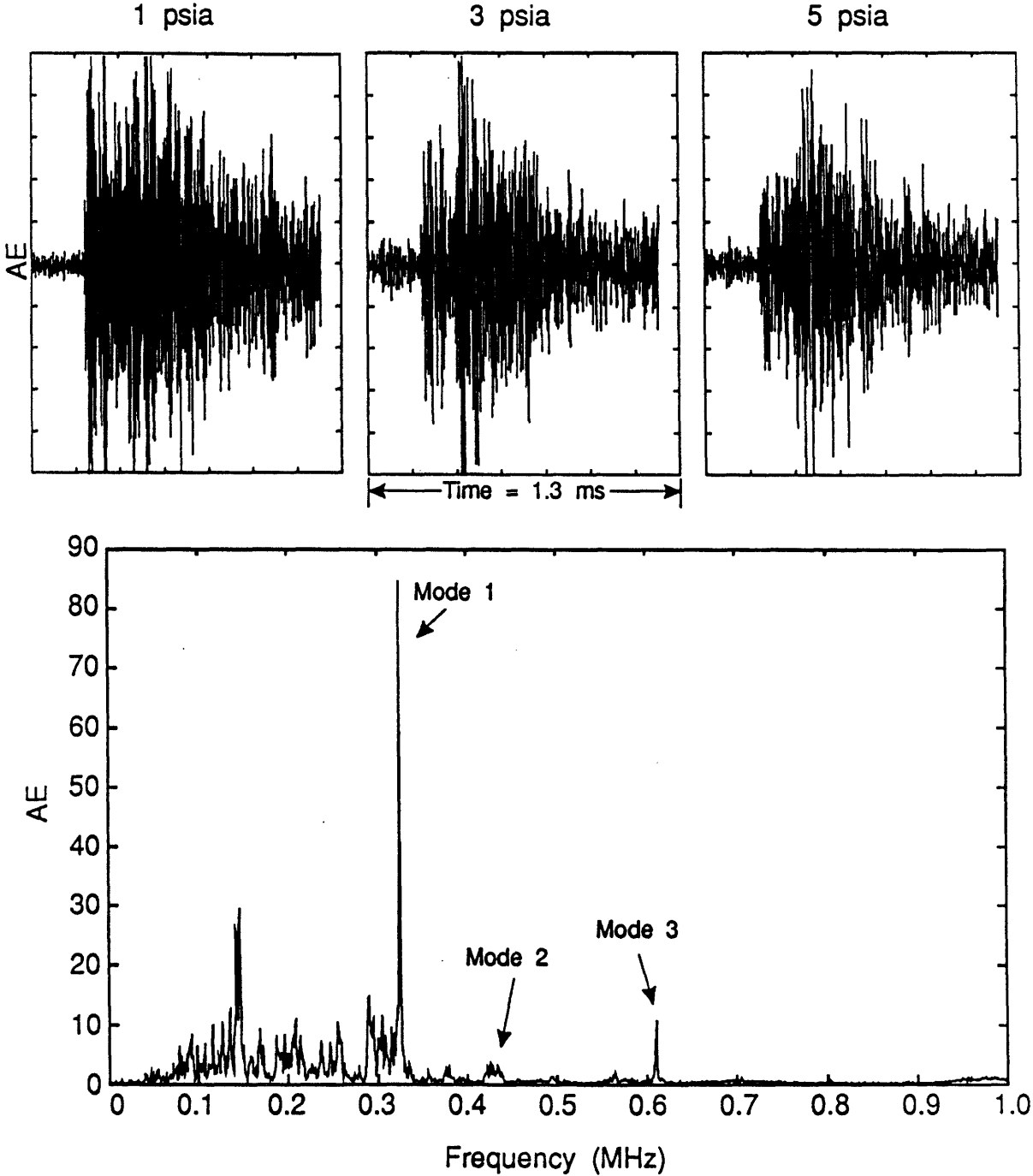


Figure 3.17: AE pulses from contact between the slider and a scratch on the disk surface. The lower plot is an FFT of a typical AE pulse.

This type of glide height test has many serious shortcomings. The first is that the test could not be run for more than a couple of minutes without the bump on the disk wearing out. Secondly, when the bump wore out, it left contamination on the bottom of the slider. This required the slider and HGA to be discarded after each use. As a result, the PZT was not mounted on the slider because a great number of expensive PZT/sliders would have been needed. Instead a commercial transducer was mounted at the base of the HGA. Monitoring the signal in this way is undesirable because the strength of the signal is lower at the base of the HGA than it is right on top of the slider. This type of glide height test, although useful, requires very quick response from the computer controlling the experiment so that wear of the bump is minimized. The experiments also require considerable financial resources for the purchase of heads and disks.

About the only useful result from the glide height tests was a partial confirmation of the resonance frequencies of the slider. The disappointing results with the glide height tests led to the development of the ball impact technique in the next section.

3.7 Ball Impact Tests on 3380 Slider

To better understand the vibrational characteristics of the 3380 slider, a ball impact technique was developed[30]. The ball impact technique is more than just a substitute for actual glide height testing. The technique allows precise location of the source of the input force into the slider. It also allows a quantitative estimate of the impact force to be calculated, a priori, using Hertzian contact theory. These two features make the ball impact a valuable tool for understanding the vibration of the slider and the whole HGA as well.

The experimental setup for performing the ball impact tests is shown in Figure 3.18. To guide the balls into impact with the slider, a glass pipet tube was used. The inner diameter of the pipet tube was just slightly bigger than the size of the ball. The positioning stage allowed the HGA to be moved in five directions. The three rotational adjustments of pitch, yaw, and roll, allowed the HGA to be positioned parallel with the X and Y directions of the linear positioning stages. Once positioned, the X-Y stage allowed the slider to be moved so that the ball could impact at any location along the bottom of the slider.

The balls used in the experiments were 0.28 mm (0.011 inch) in diameter and made of tungsten carbide. The size of the ball and its material were chosen to make the contact time (duration) as short as possible. A short contact time is necessary to excite the high frequency modes of the slider. This contact time and the contact force can be estimated using Hertzian contact theory, see Appendix A for a detailed discussion. For this size ball the contact time is estimated to be 0.74 μ s. With this contact time, the input excitation force excites all frequencies up to about 1 MHz fairly evenly, i.e. the magnitude of the force is nearly constant over this range. This makes the ball impact useful for studying at least the first six modes of vibration of the slider.

Ball impacts tests were performed at several locations along the slider rails. Figure 3.19 shows typical results for impacts at the leading edge (front) and center of the slider rail. For

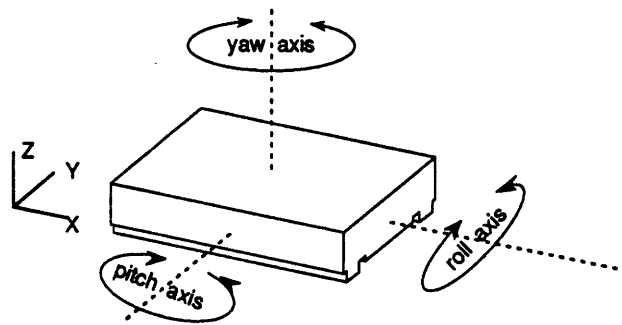
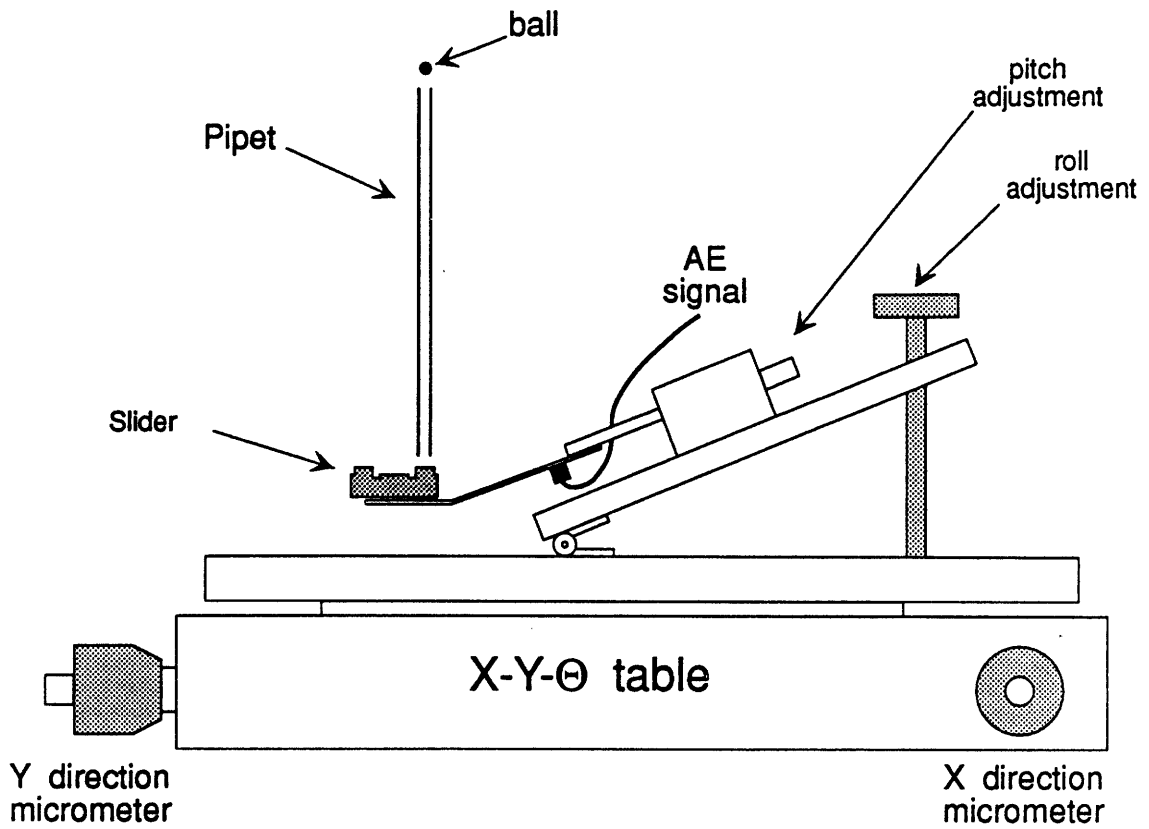


Figure 3.18: Experimental setup for performing ball impact tests on 3380 slider. Note that the Θ adjustment on the table is not shown but controls the adjustment of the yaw axis of the HGA. (after Chang 1990)

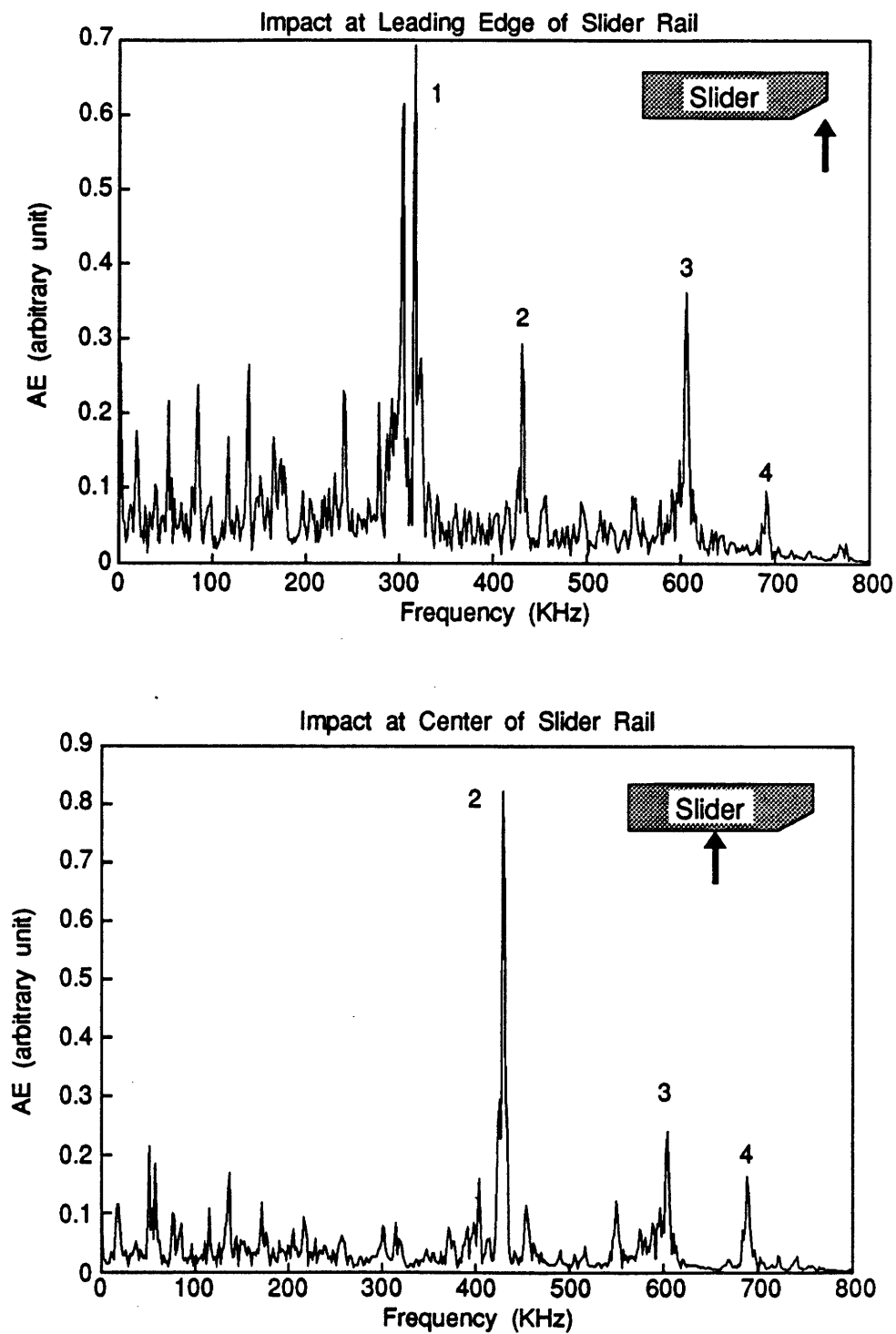


Figure 3.19: Frequency spectrum from ball drops on 3380 style slider, measured using an AET Pico transducer mounted at the arm. (after Chang 1990)

Mode	FEM	Ball impact	Vibration Mode Shape
1	305 KHz	308 KHz	Torsion
2	422 KHz	425 KHz	Longitudinal Bending
3	656 KHz	605 KHz	Transverse Bending
4	689 KHz	690 KHz	Second Torsion

Table 3.2: Comparison of natural frequencies of 3380 slider determined by FEM and by ball impact experiment.

these tests the transducer was the commercial AE transducer mounted at the base of the HGA, as was shown in Figure 3.6. The graphs clearly identify the first four vibrational modes of the slider. Table 3.2 shows a comparison between the vibrational frequencies determined by the experiments and as determined by the FEM. The frequencies of modes 1, 2, and 4 all agree within 1%. The predicted vibration frequency of the third mode (transverse bending) is in error by about 7%. There are two possible reasons for this: 1) the value of Poisson's ratio used in the FEM was in error, or 2) the depth of the cuts adjacent to the rails was incorrectly measured. It should be noted that it would be reasonable for an error in the Poisson's ratio to effect mostly mode 3. This is because the transverse bending mode (mode 3) depends more than the other modes on "plate type" $(1 - \nu^2)$ stiffening. The same is true of the depth of cut by the slider rail. It would most strongly effect the transverse bending.

More can be learned in Figure 3.19 than just the vibration frequencies. The effect of impact location is also obvious. It is clear that the torsional mode (mode 1) is strongly excited by impact at the leading edge of the slider rail. It is also clear that impact in the center of the rail does not excite this mode at all. The relative magnitude of the other vibrational modes also change with impact location. The top graph in Figure 3.19 also shows a strong unexpected peak at about 300 KHz. Further testing confirmed that this was one of the vibration modes of the gimbal supporting the slider. It should also be noted that the two graphs in Figure 3.19 are not plotted on the same vertical scale. In fact, it was found that the magnitude of the vibration (AE) varied considerably from one ball impact to the next. This was apparently the result of the ball sticking to the inside of the pipet tube as it fell. As a result, the magnitude of vibration resulting from an impact at one location cannot be directly compared with the magnitude of vibration from an impact at another location. This lack of repeatability led to the use of the enlarged slider model presented in Section 3.8.

One important decision that has to be made in glide height testing is where to place the transducer. There is a difficult tradeoff that has to be made. If the transducer is placed at the base of the HGA, rather than on the slider, then it will not have to be replaced each time the HGA has to be replaced. On the other hand, by placing the transducer directly on the slider, a higher sensitivity might be achieved.

To test out the effect of sensor location, a series of tests were performed. First, two PZT sensors were mounted as shown in Figure 3.20. The sensors were both $2.5 \times 0.30 \times 0.25$ mm in size and made from PZT-5A. Balls were dropped at different locations along the slider rail and the signals from both sensors were simultaneously acquired. Figure 3.21 shows the resulting vibration (AE) signals obtained from impact tests on the leading edge and center of the slider rail. These tests show a marked difference in the signals measured from the two different sensor locations.

Firstly, the magnitude of the vibration signal measured from the base of the HGA is about one tenth of that measured at the slider. So, measurement at the slider is more sensitive. Secondly, the torsional vibrational mode (305 KHz) is noticeably missing from the signal measured by the PZT mounted on the slider. This is believed to be the result of the way the PZT is mounted. The PZT is placed all the way across the back of the slider. Mounted in this way the PZT is divided in half by the nodal line of the torsional mode of vibration. As a result, when one half of the PZT is moving upward, the other half is moving downward. The net result is cancellation of the torsional vibration signal. Also notice that the peak at 600 KHz is detected by the PZT on the slider but not by the PZT sensor mounted at the base of the HGA. This is most likely due to the suspension of the HGA not being able to transmit this frequency up to the base of the HGA. Another result of the PZT being mounted on the slider is that the vibration frequencies change slightly due to the extra mass of the PZT sensor. Notice the peak at 390 KHz which had previously been at 426 KHz. Overall, the signal from the PZT mounted on the slider is cleaner and much stronger than the signal from the PZT mounted at the base of the HGA.

Due to difficulties in creating a reliable ball impact with the small ball and in mounting the PZT sensor, the decision was made to use an enlarged model of the slider.

3.8 Ball Impact Tests on an Enlarged Slider

An enlarged slider was machined out of aluminum and scaled 44:1 relative to the actual 3380 slider. The dimensions for this slider are given in Figure 3.22. With the enlarged slider it was again necessary to determine the range of frequencies to be excited and the size ball necessary to excite those frequencies. FEM analysis of the enlarged slider indicated that the first six vibrational modes are in the range of 3-12 KHz. Thus, compared to the 300 KHz - 1 MHz range needed for the actual 3380 slider, exciting the enlarged slider was relatively easy and almost any size ball would do. Initial tests with 4.76 mm (3/16") and 6.35 mm (1/4") diameter steel balls dropped from 305 mm (12") high, showed that plastic deformation of the aluminum occurred, leaving craters on the aluminum surface after the test. As a result, it was decided to use a less dense ball material. nylon balls were found to leave the aluminum surface undamaged and cause a strong enough vibration so that the accelerometer could easily measure the signals. Fourteen input (impact) locations were chosen along the rail of the enlarged slider. These locations and the accelerometer location are shown in Figure 3.23. The accelerometer used is a PCB 303A with 10 mV/g sensitivity and ± 500 g range.

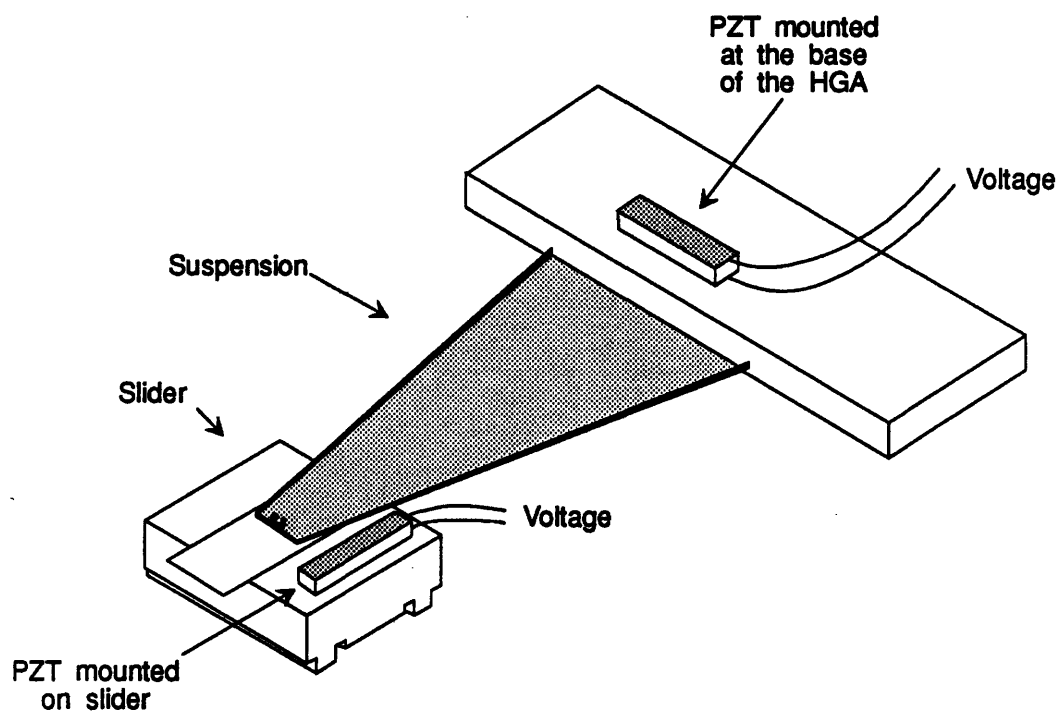
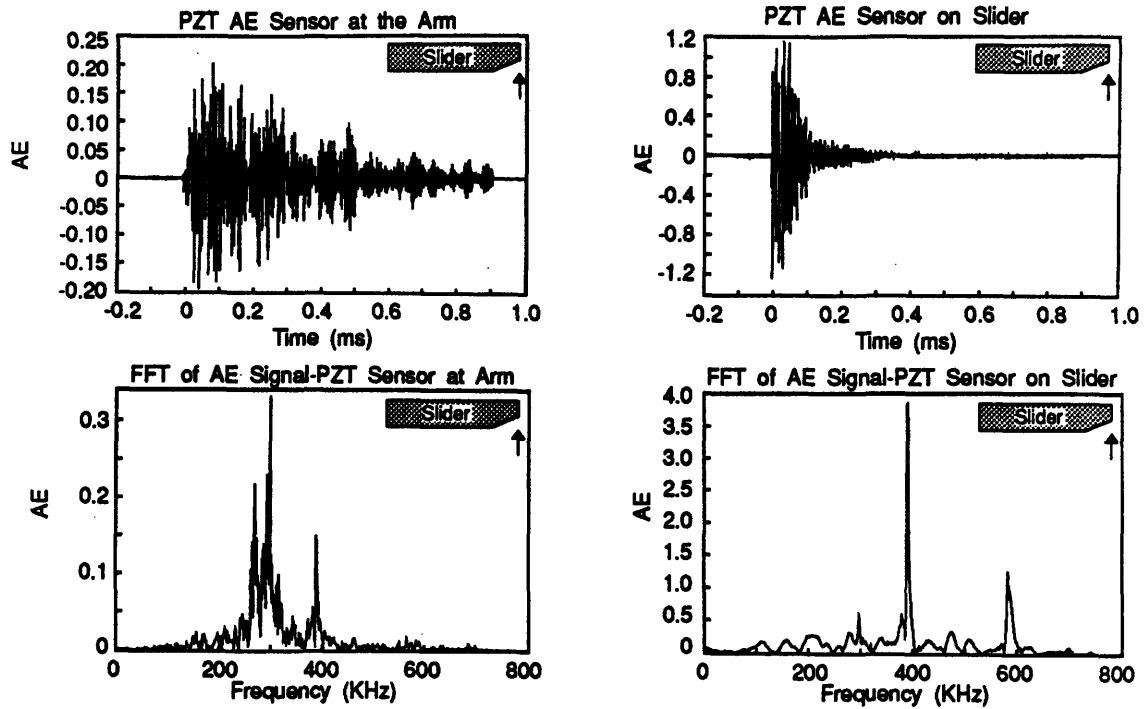


Figure 3.20: Schematic of HGA (head gimbal assembly) with PZT mounted on the slider and also mounted at the base of the HGA. (after Chang 1990)

Ball Impact at Leading Edge of Slider Rail



Ball Impact at Center of Slider Rail

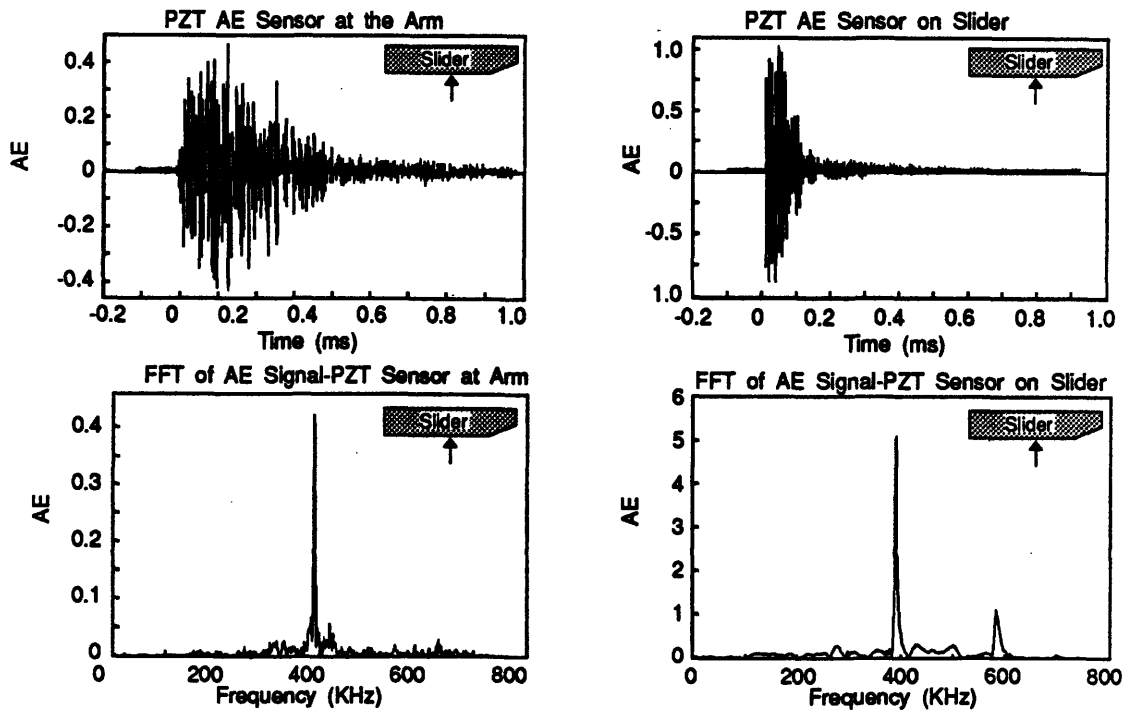


Figure 3.21: Comparison of AE signals measured by PZT sensors at the base of the HGA and on the slider. Four top graphs are for impact at the leading edge of the slider rail. Bottom four graphs are for impact at the center. (after Chang 1990).

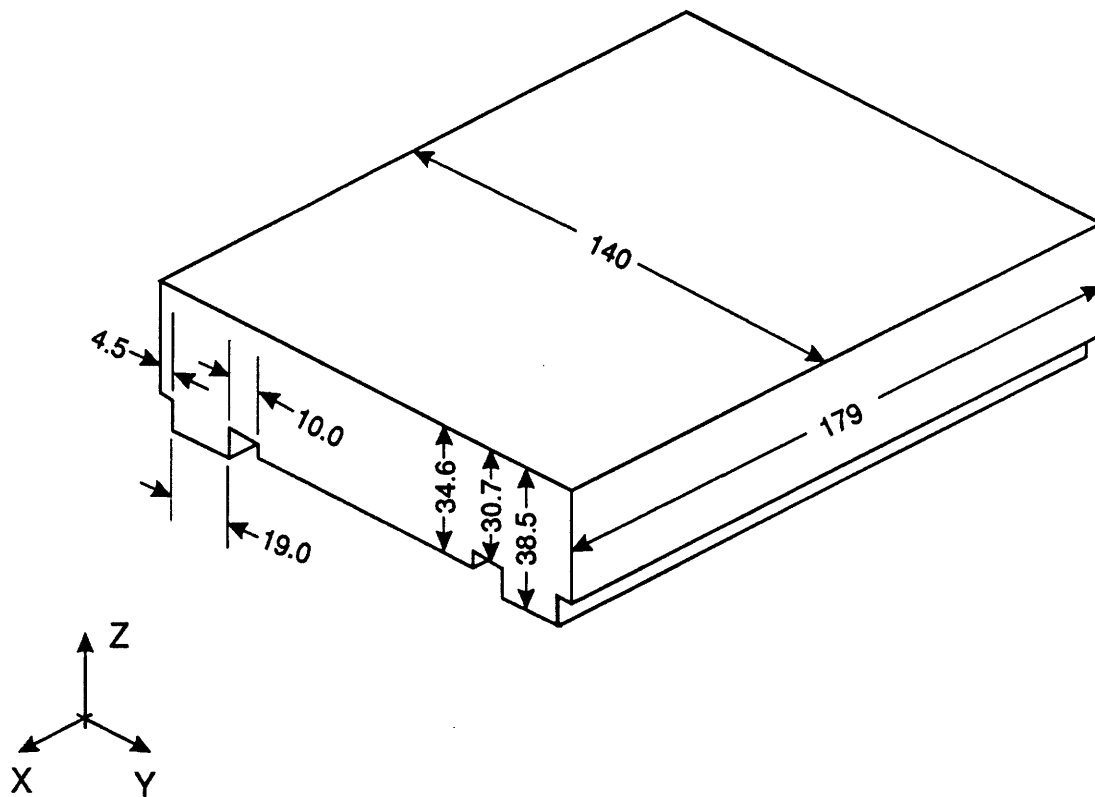


Figure 3.22: Drawing of enlarged model of 3380 slider with dimensions in millimeters.

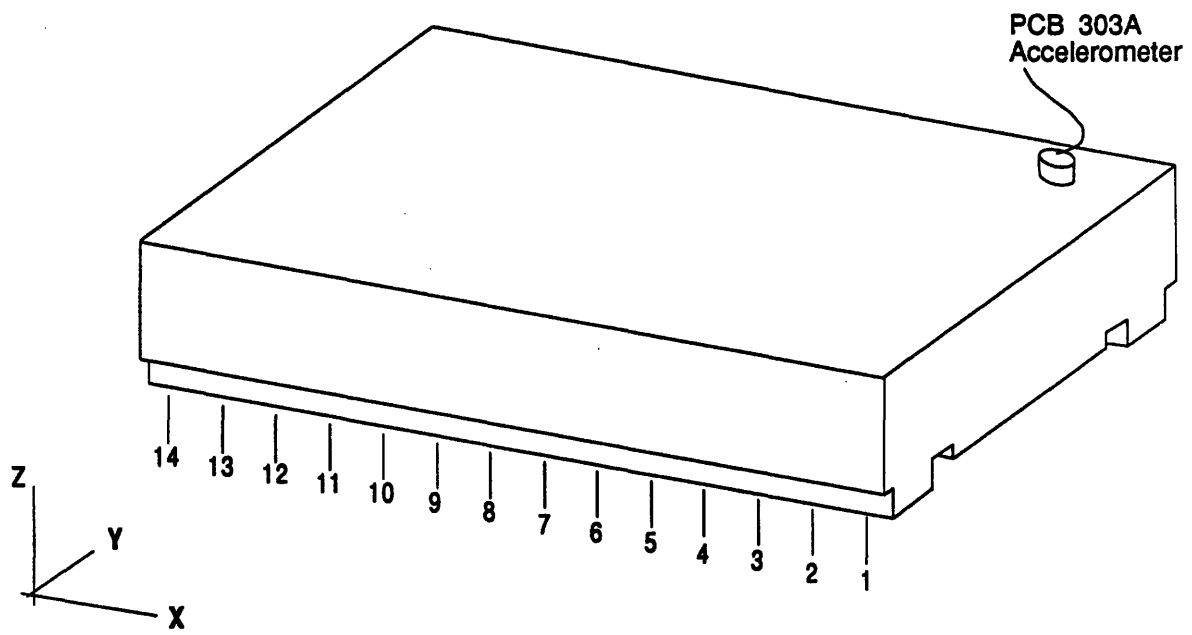


Figure 3.23: Ball drop and sensor locations on enlarged slider. Note that the enlarged slider is turned upside down during ball drop tests.

The first effect to be studied was the effect of contact time on the frequencies excited. Contact times could be varied by varying either the stiffness of the ball material or the radius of curvature of the ball. In an actual glide height test, the materials are usually fixed, but the radius of the bump on the disk may change. So for the tests with the enlarged slider, it was decided to keep the materials fixed and vary the diameter of the nylon ball. Ball diameters of 6.35, 12.70, and 25.4 mm (1/4", 1/2", and 1") were chosen and the drop height was decided to be 305 mm (12"). To guide the ball to the appropriate contact point on the slider, 305 mm (12") long copper tubes of appropriate diameters were used, as shown in Figure 3.24. The enlarged slider was placed upside down (rails upward) on a piece of low density foam. For the current set of experiments only the first input location was used, see Figure 3.23. For each ball size, the ball was dropped six times at the same location so that the repeatability of the ball drop technique could be determined.

Typical acceleration versus time traces for the ball drop tests are shown in Figure 3.25. Except for the differences in the magnitude of the acceleration, the time domain response is very similar for all three ball sizes. However, once the FFT's of these signals are taken, an additional difference can be seen between the three signals, as shown in Figure 3.26. Because of its small radius, and resulting short contact time, the 6.35 mm (1/4") nylon ball excites virtually all frequencies equally in the 0 to 25 KHz frequency range. The 12.70 mm (1/2") nylon ball, however, seems to start rolling off at around 12 KHz, as can be seen by comparison with the frequency data for the 6.35 mm (1/4") ball. The magnitude of the frequency data for the 25.4 mm (1") ball starts its roll off at about 6 KHz and is virtually zero for frequencies above 12 KHz. The same results can be seen in a semilog plot, as shown in Figure 3.27, although the results are clearer in the linear plot. In order to better understand the relationship between ball size and frequency response, a Hertzian contact analysis was performed for the nylon balls.

3.8.1 Hertzian Contact Analysis for Nylon Ball Drops

The elastic contact between a ball and a flat surface has a known theoretical solution which was found by Hertz in the 1881[31]. More recently[32] the dynamic solution for a ball dropped onto a large flat surface has also been solved. A detailed solution to this problem is presented in Appendix A and only the results of such an analysis will be given here.

As previously mentioned, we are concerned with the problem of dropping 6.35, 12.70, and 25.4 mm (1/4", 1/2", and 1") diameter nylon balls from a height of 305 mm (12") onto an aluminum surface. The properties of these two materials are given in Table 3.3. Hertzian contact analysis for the balls can predict both the displacement of the balls during contact and the resulting forces, as shown in Figures 3.28, 3.29, and 3.30 for 6.35, 12.7, and 25.4 mm diameter balls, respectively. The predicted peak forces are 38, 149, and 600 N for the for 6.35, 12.7, and 25.4 mm diameter balls respectively. Also, the contact times are 35, 71, and 141 μ s for the balls in the same order. Also shown in Figures 3.28 - 3.30 are FFT's of the force vs. time signals. (Note that the signals were padded with zeroes to account for the fact that the ball experiences no contact forces after contact.) These FFT's show that the 6.35, 12.7, and

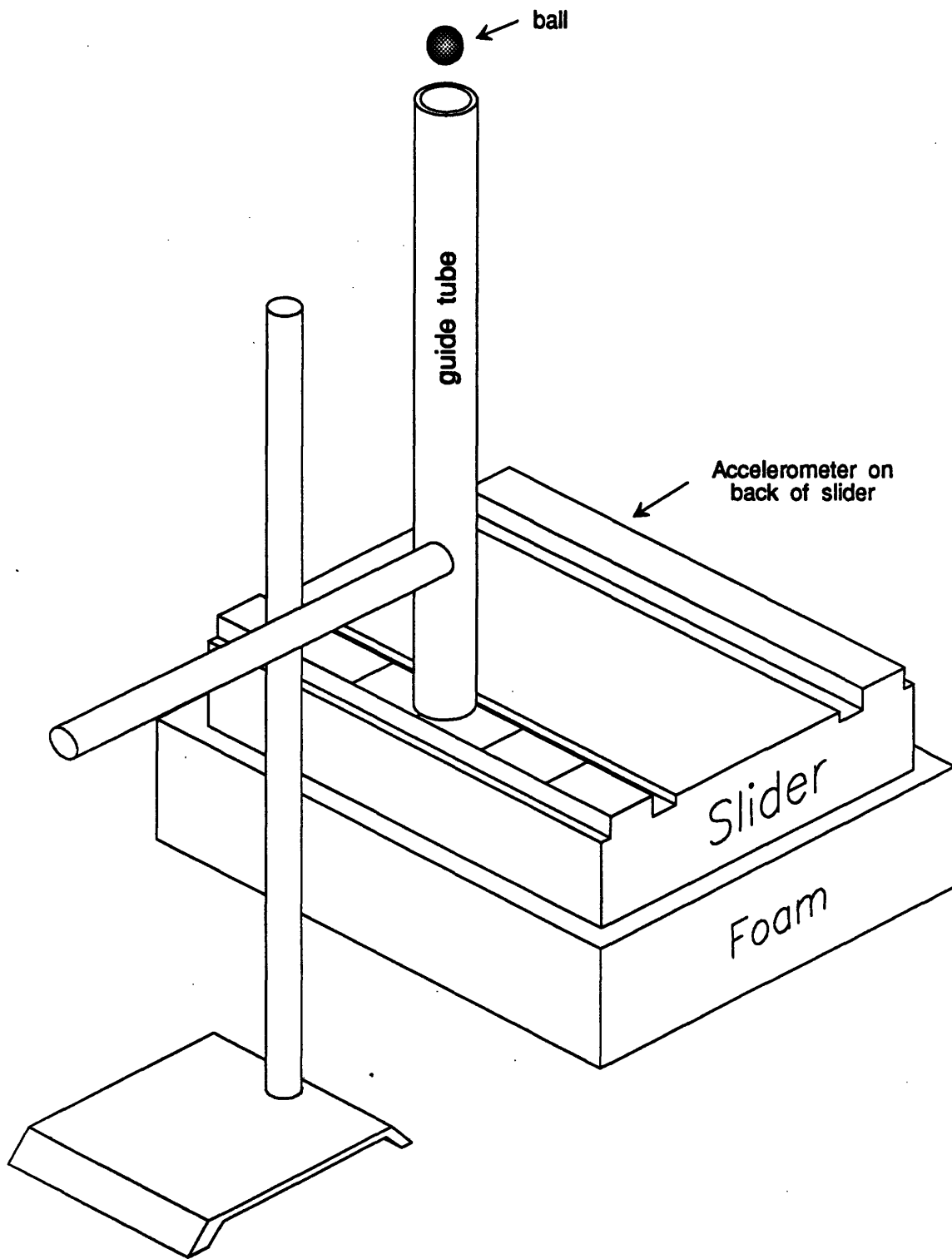


Figure 3.24: Schematic of ball drop test apparatus for ball drop test on enlarged slider.

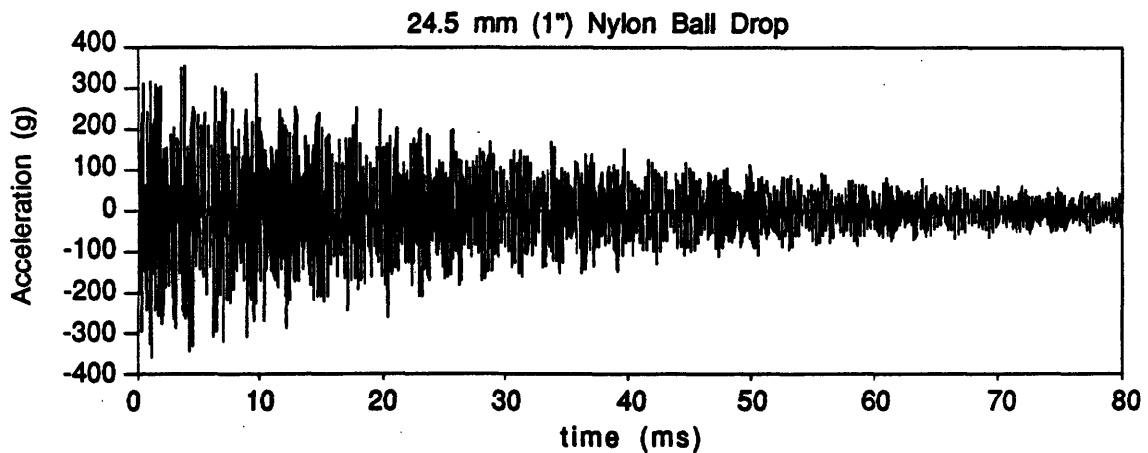
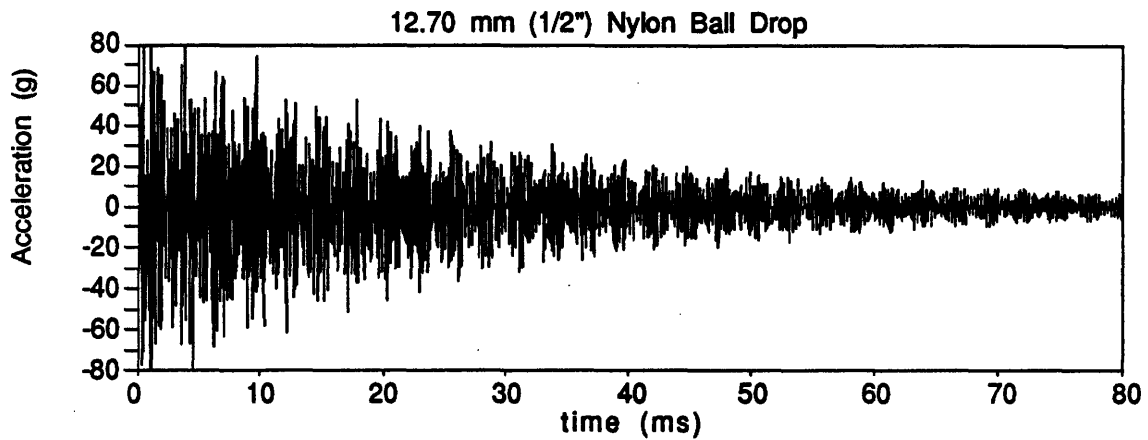
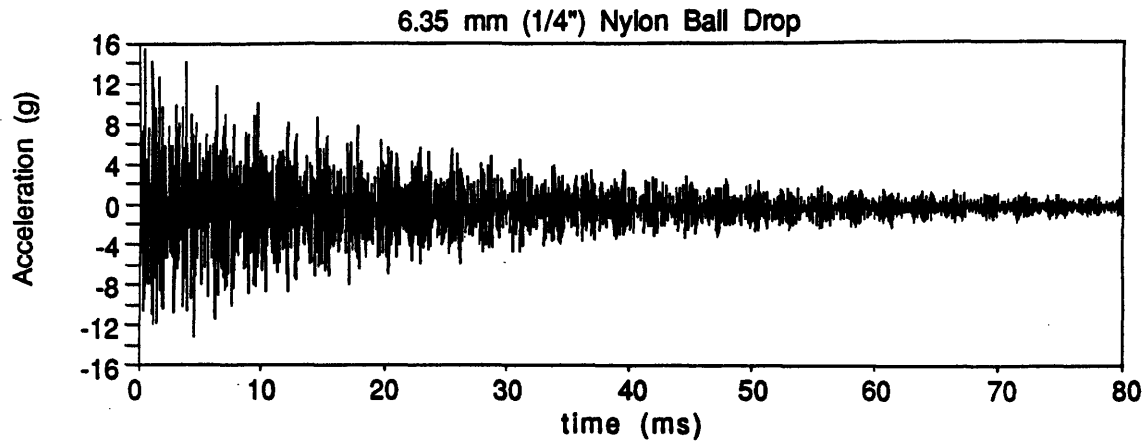


Figure 3.25: Acceleration signals from enlarged slider. Test conditions were 6.35, 12.70, and 25.4 mm (1/4", 1/2", and 1") diameter balls dropped from 305 mm (12") high onto location 1 on the enlarged slider. Sampling rate 50 KHz and 8192 samples. Only half of the recorded time trace is shown.

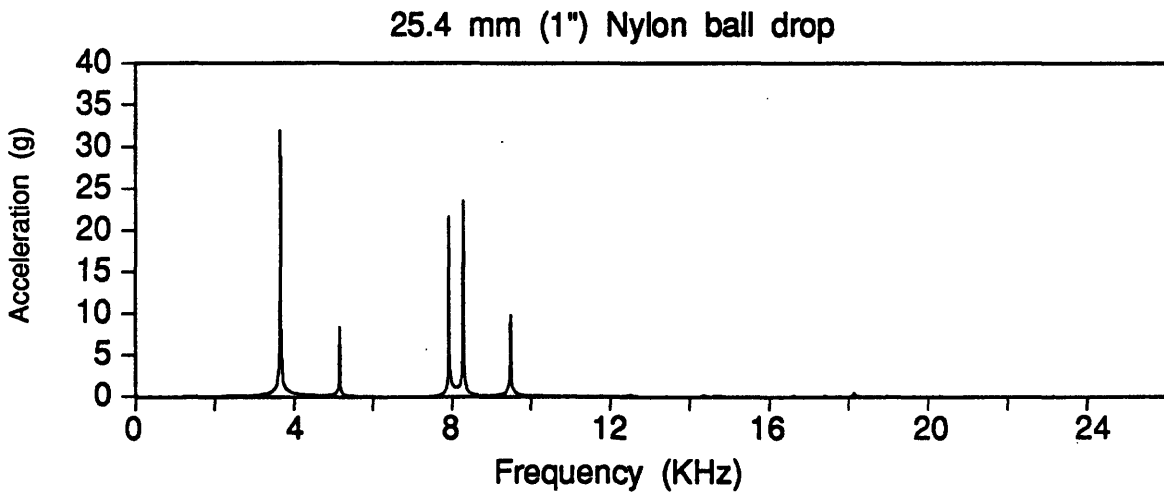
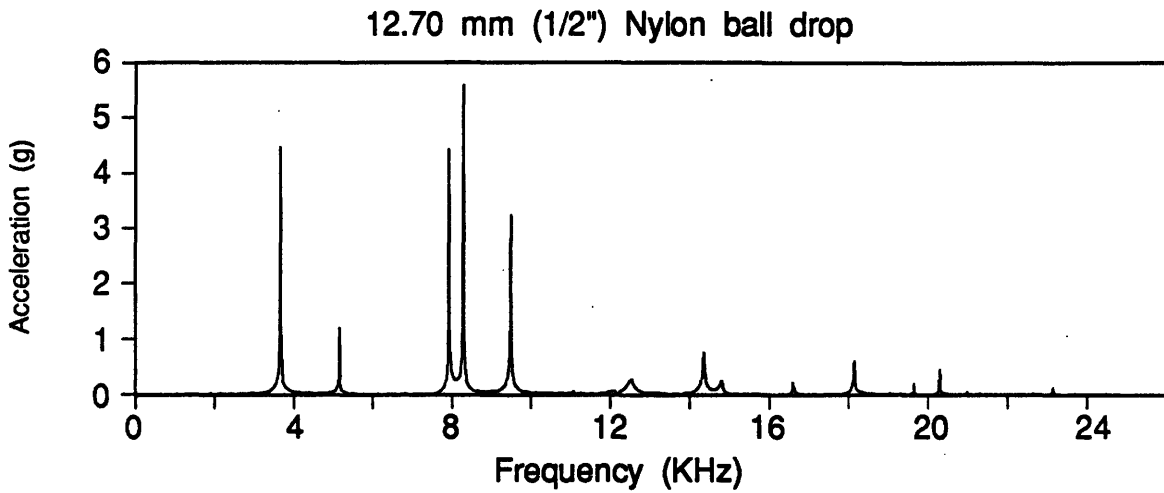
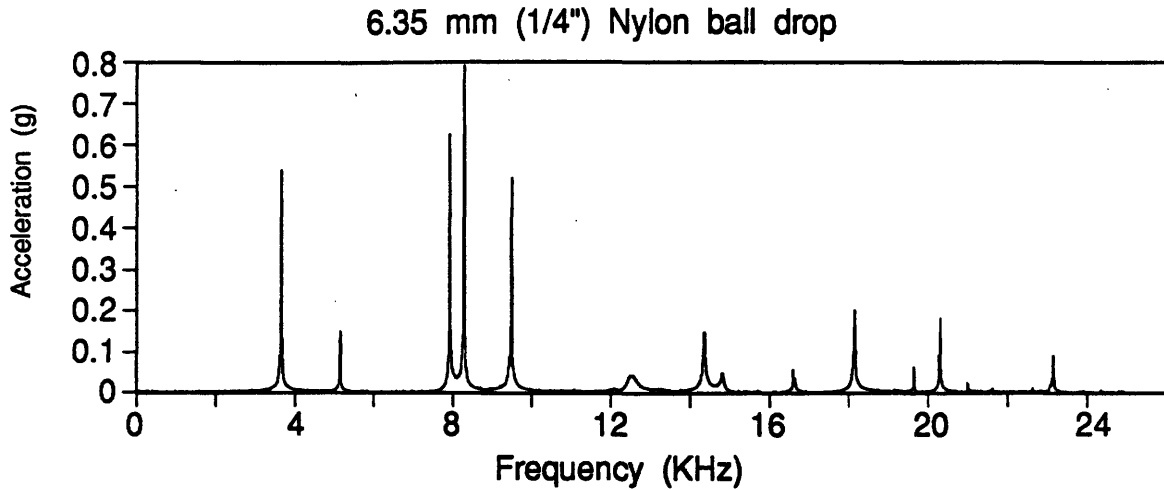


Figure 3.26: FFT's of acceleration signals from enlarged slider. Test conditions were 6.35, 12.70, and 25.4 mm (1/4", 1/2", and 1") diameter balls dropped from 305 mm (12") high onto location 1 on the enlarged slider. Sampling rate 50 KHz and 8192 samples.

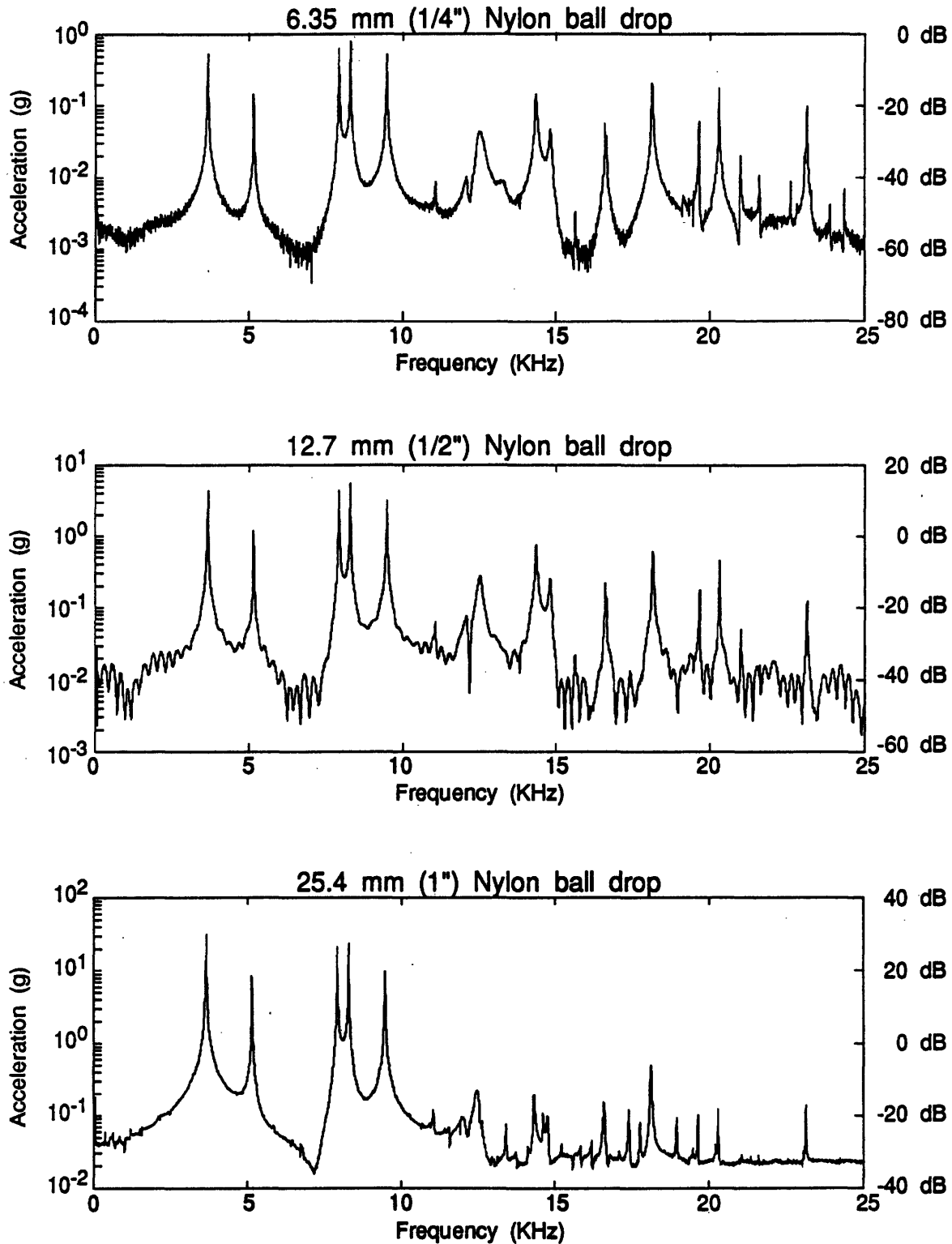


Figure 3.27: FFT's of acceleration signals from enlarged slider. Test conditions were 6.35, 12.70, and 25.4 mm (1/4", 1/2", and 1") diameter balls dropped from 305 mm (12") high onto location 1 on the enlarged slider. Sampling rate 50 KHz and 8192 samples.

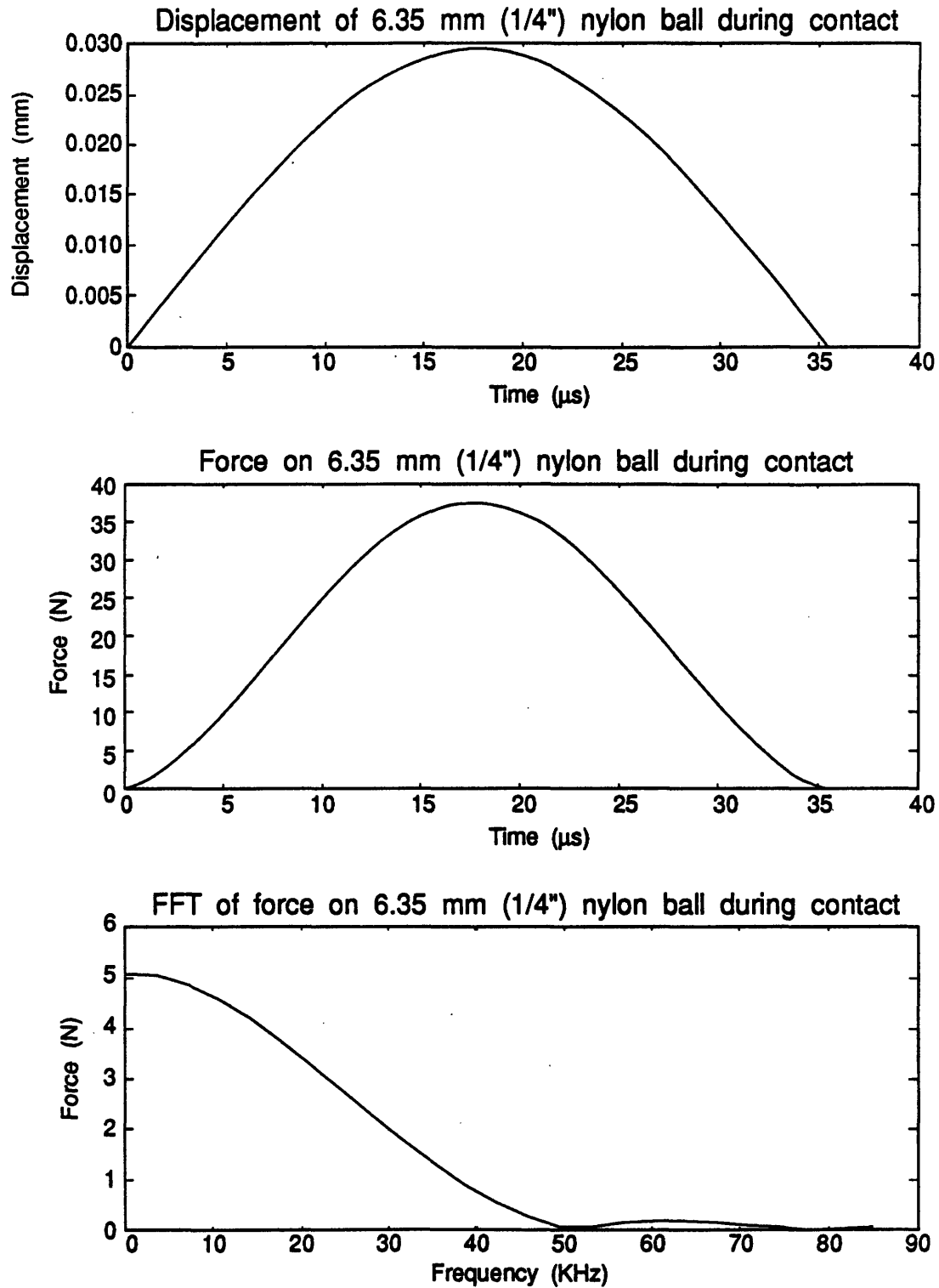


Figure 3.28: Data from Hertzian contact analysis for a 6.35 mm (1/4") nylon ball dropped from 305 mm (12") onto an aluminum surface.

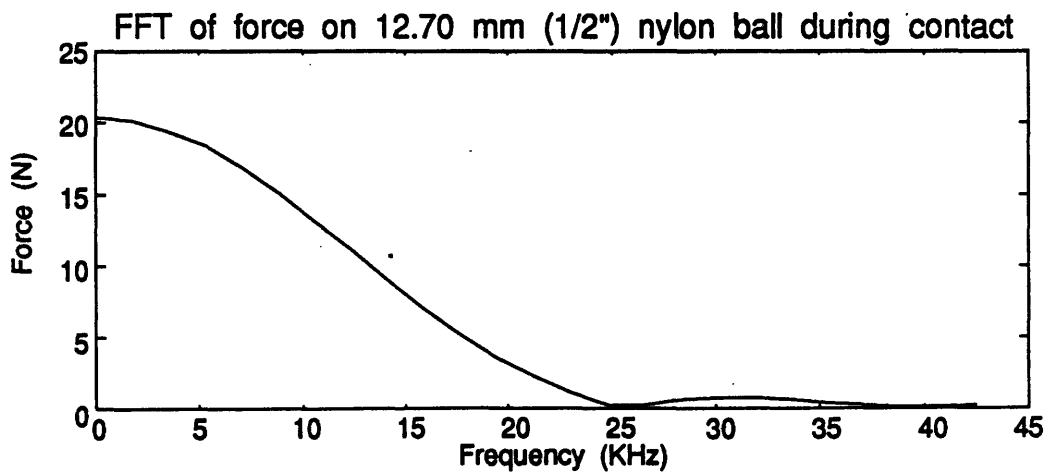
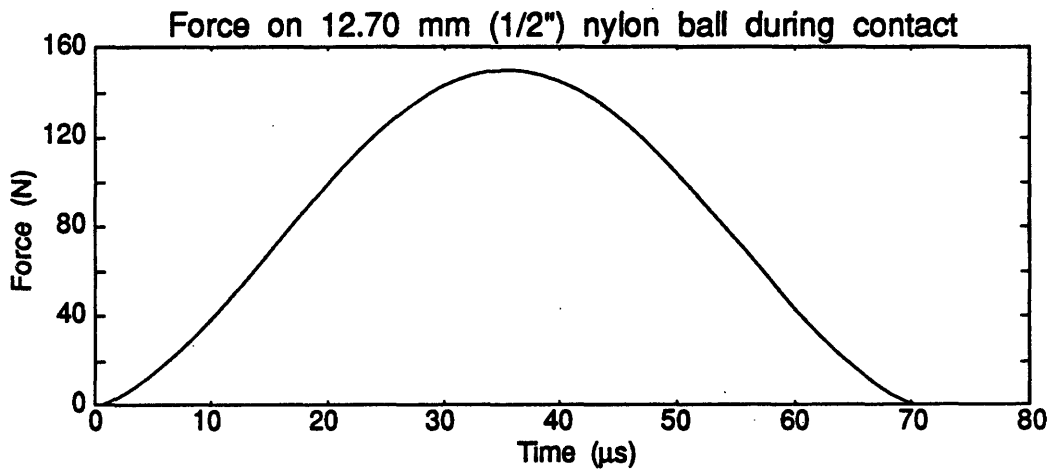
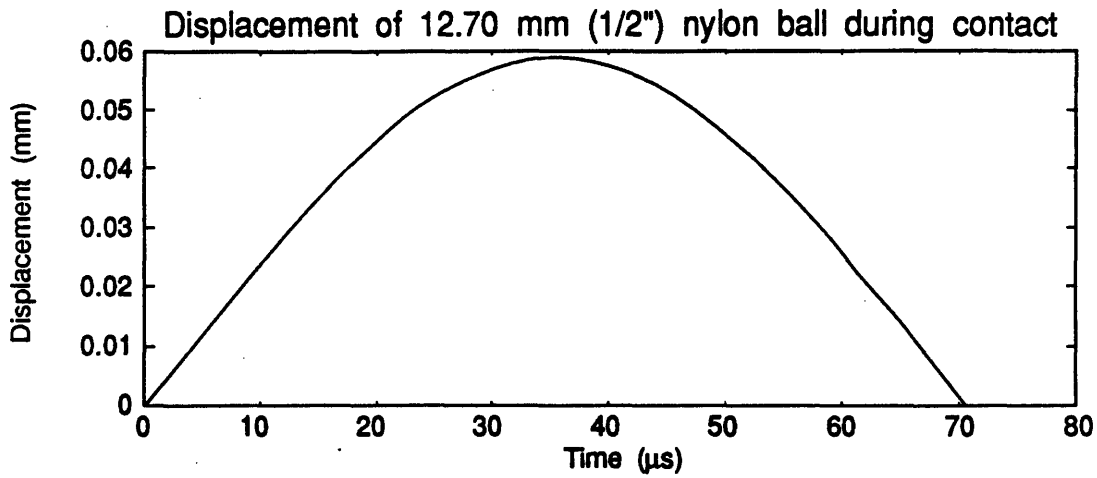


Figure 3.29: Data from Hertzian contact analysis for a 12.7 mm (1/2") nylon ball dropped from 305 mm (12") onto an aluminum surface.

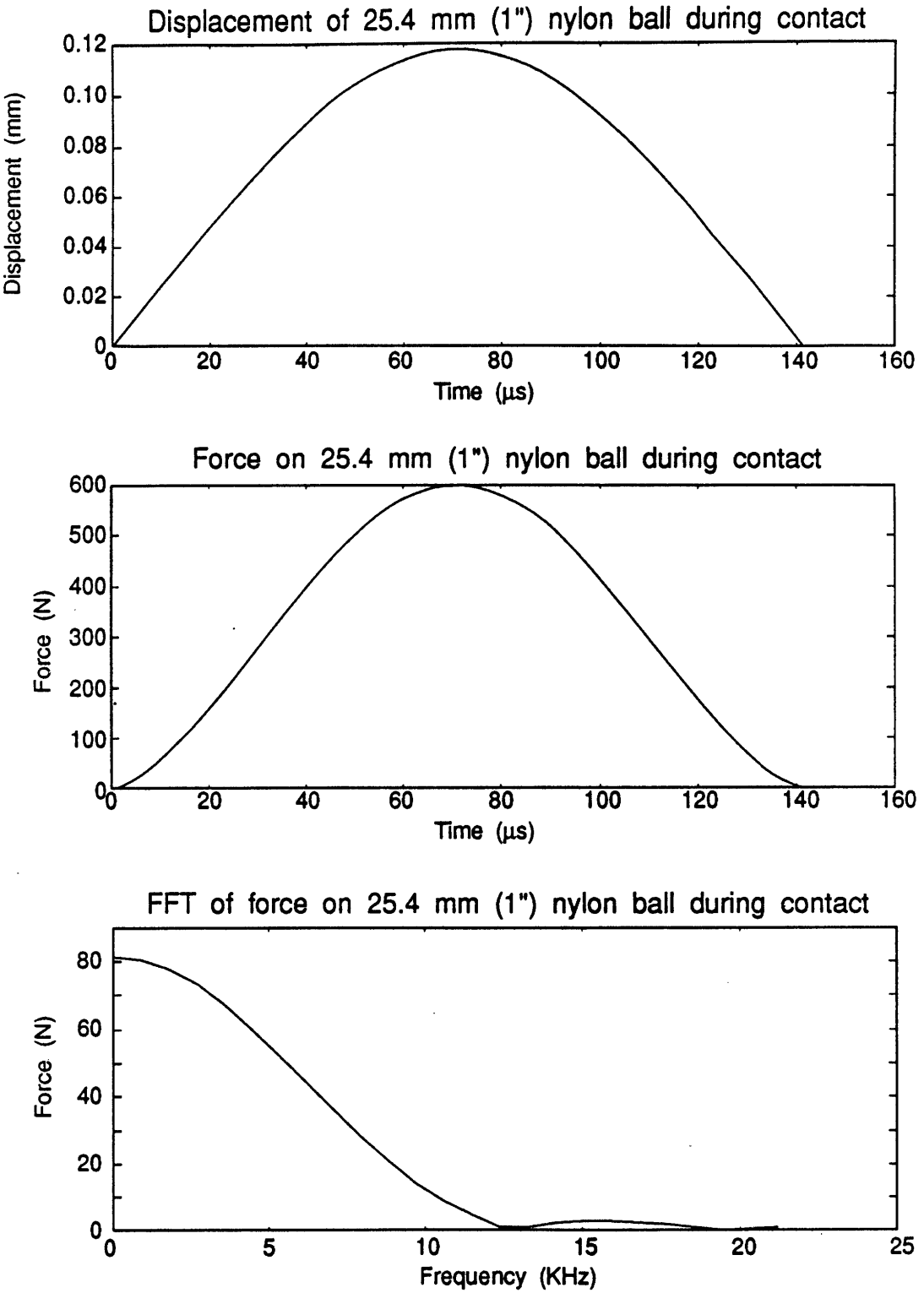


Figure 3.30: Data from Hertzian contact analysis for a 25.4 mm (1") nylon ball dropped from 305 mm (12") onto an aluminum surface.

Property	Nylon 66	Aluminum
ρ	1135 Kg/m ³	2768 Kg/m ³
E	2.75·10 ⁹ N/m ²	6.89·10 ¹⁰ N/m ²
ν	0.4	0.26
k	9.72·10 ⁻¹¹ m s ² /Kg	4.31·10 ⁻¹² m s ² /Kg

Table 3.3: Mechanical Properties of nylon 66 and Aluminum.

25.4 mm balls reach their first frequency domain zero at 50, 25, and 12 KHz respectively. This seems to agree with the results from the ball drop tests on the enlarged slider, recall Figure 3.26.

In a typical modal testing application, the impact force signal and acceleration signal would be measured simultaneously. Unfortunately, it is not possible to directly measure the contact forces created during a ball drop tests. A small impact hammer might be used, but the ball drop technique is preferred. In actual glide height testing, the impact force cannot be directly measured. So to simulate that condition, the ball drop technique is a good choice for creating the impact. Even though we are limited to not being able to directly measuring the contact forces, they can be estimated from the Hertz contact theory, so that acceleration can be calculated, for comparison with the FEM model. The most obvious way to make use of the Hertzian solution is to take the force vs time curve, e.g. the second graph in Figure 3.28, pad the signal with zeroes, and digitize it at the same rate as the acceleration signal was digitized. However, there is one more small consideration.

In order to obtain the desired frequency spectrum for the acceleration data, the acceleration signal was digitized at 50 KHz. The contact time for the balls ranges from 35 to 141 μ s. If the force vs time curves are digitized at 50 KHz, or 1 sample every 20 μ s, a very poor representation of the both the time and frequency domain signals will be obtain. In fact, for the 6.35 mm ball, the contact force data will be a impulse input, i.e. a positive non-zero value followed by a series of zeros. This would cause the frequency spectrum to be white, or flat.

The solution to this problem is simply to digitize the force signal at a faster rate than the acceleration signal. Figure 3.31 shows how the faster sampling rate improves the quality of both the time and frequency domain signals. One must be certain to keep the length of the time record the same regardless of the sampling frequency. For the case of the ball drop on the enlarged slider, 8192 points were taken of the acceleration signal at 50 KHz. This gives a record length of 163 ms. If the force signal were to be digitized at 400 KHz to give a good representation of the signal, then 65536 points should be taken to keep the record length at 163 ms. Failure to keep the record length constant can result in the following problems.

1. If the time record length is not fixed then the magnitude of the force FFT will be incorrect, and

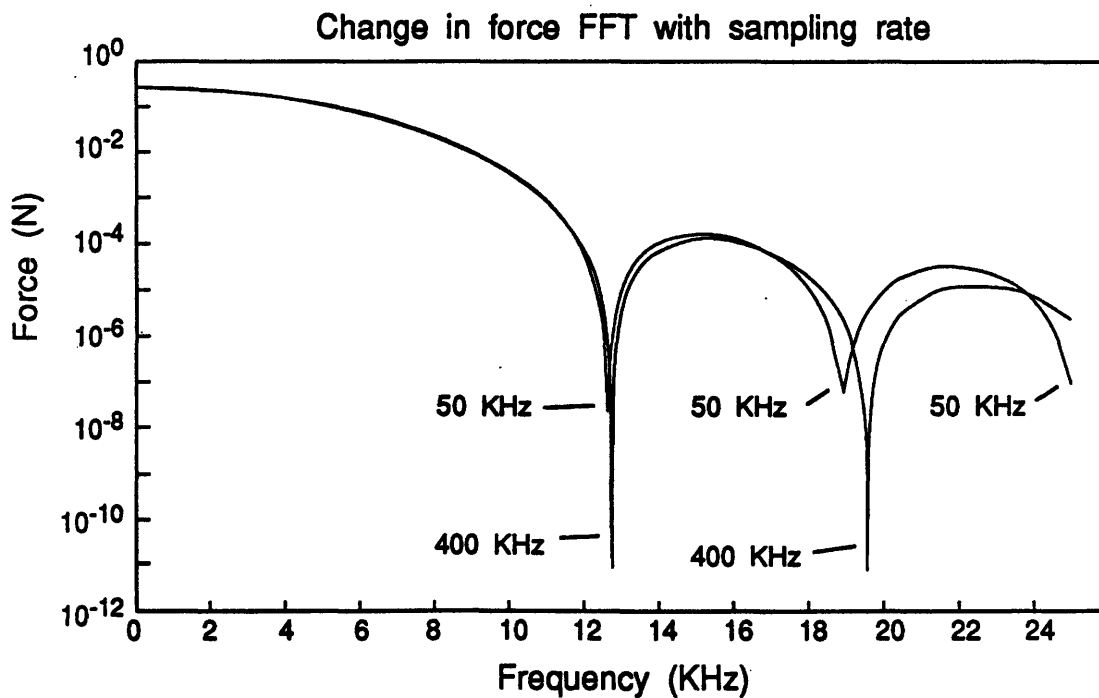
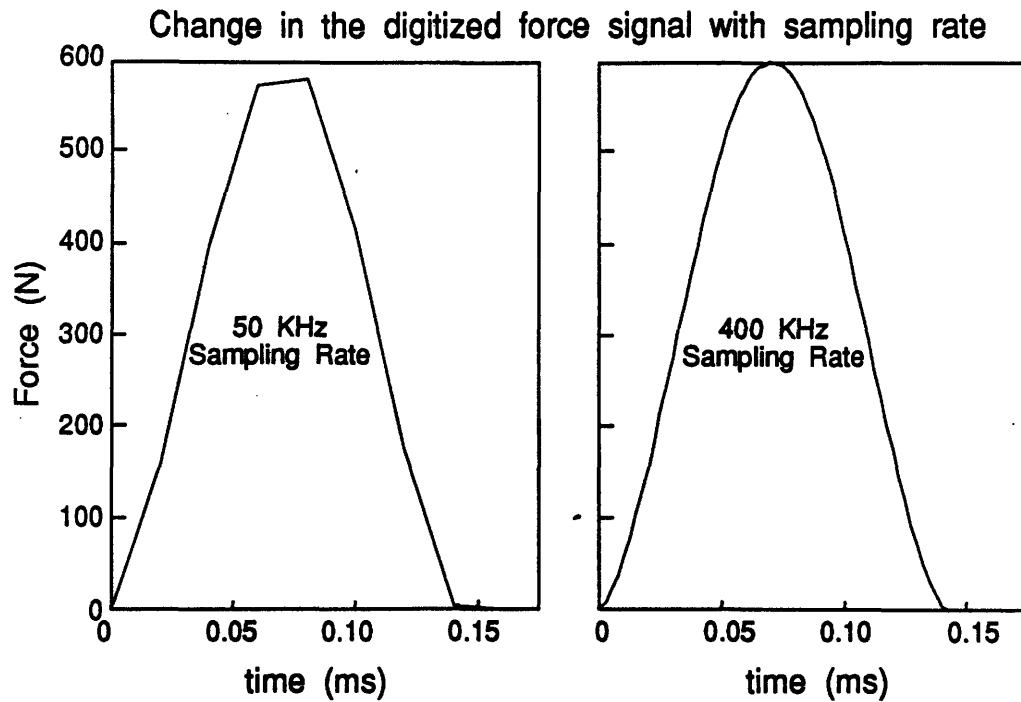


Figure 3.31: Effect of sampling rate on Hertz contact force data. Note that higher sampling rates are needed for accurate representation of time domain and frequency domain signals. Data shown is for a 25.4 mm (1") nylon ball dropped from 305 mm onto an aluminum surface.

Ball size	6.35 mm (1/4")	12.70 mm (1/2")	25.40 mm (1")
Experiment	34.8 N	155 N	644 N
Theory	38.2 N	153 N	611 N
error	-9 %	1 %	5 %

Table 3.4: Peak contact forces for nylon balls dropped from a height of 305 mm onto an aluminum surface.

2. If the time record length is not fixed then the frequency resolution of the force FFT will not match the frequency resolution of the acceleration FFT.

Keeping the time record fixed at 163 ms, the magnitude of the force FFTs for the 6.35, 12.7, and 25.4 mm nylon balls are shown in Figure 3.32.

3.8.2 Nylon Ball Drops on Force Transducer

To attempt to verify the contact times and forces predicted from the Hertz contact theory, an experiment was constructed where the nylon balls were dropped directly onto a force transducer. The experimental setup for these tests is shown in Figure 3.33. The force sensor used was PCB model 208A03 which has 2.25 mV/N (10 mV/lbf) sensitivity and ± 2227 N (500 lbf) range. A small circular aluminum disk, 12.7 diameter \times 2.5 mm (0.500" \times 0.100"), was threaded to the top part of the force transducer and a long aluminum rod 16 mm diameter \times 610 mm long (5/8" diameter \times 24") was threaded to the bottom of the force transducer. The same 305 mm (12") long copper guide tubes that were used for the ball drop tests on the enlarged slider, were used for these tests on the force transducer.

The results for the ball drop tests for 6.35, 12.7, and 25.4 mm nylon balls are shown in Figure 3.34. Tables 3.4 and 3.5 show that the contact forces and times measured agree with the values calculated using the Hertz contact theory within 10% error. There is one exception, the contact duration for the 6.35 mm (1/4") diameter ball. It is obvious from the top graph in Figure 3.34 that there is some resonance of the transducer effecting the measurement. There is almost a second bump in the force vs time signal. This is not too surprising since the transducer is only rated to work up to 10 KHz.

Overall, the agreement between Hertzian theory and experiment is really better than could be hoped for. There is probably a fairly large error in the value of the elastic modulus used in the Hertz contact theory, because its was obtained from DuPont literature and not measured experimentally. DuPont lists the elastic modulus of nylon 66 as 400,000 psi. This is apparently an indication of only one digit of precision in the measurement of the elastic modulus. Considering this fact, the agreement in the results may be better than can be reasonably believed.

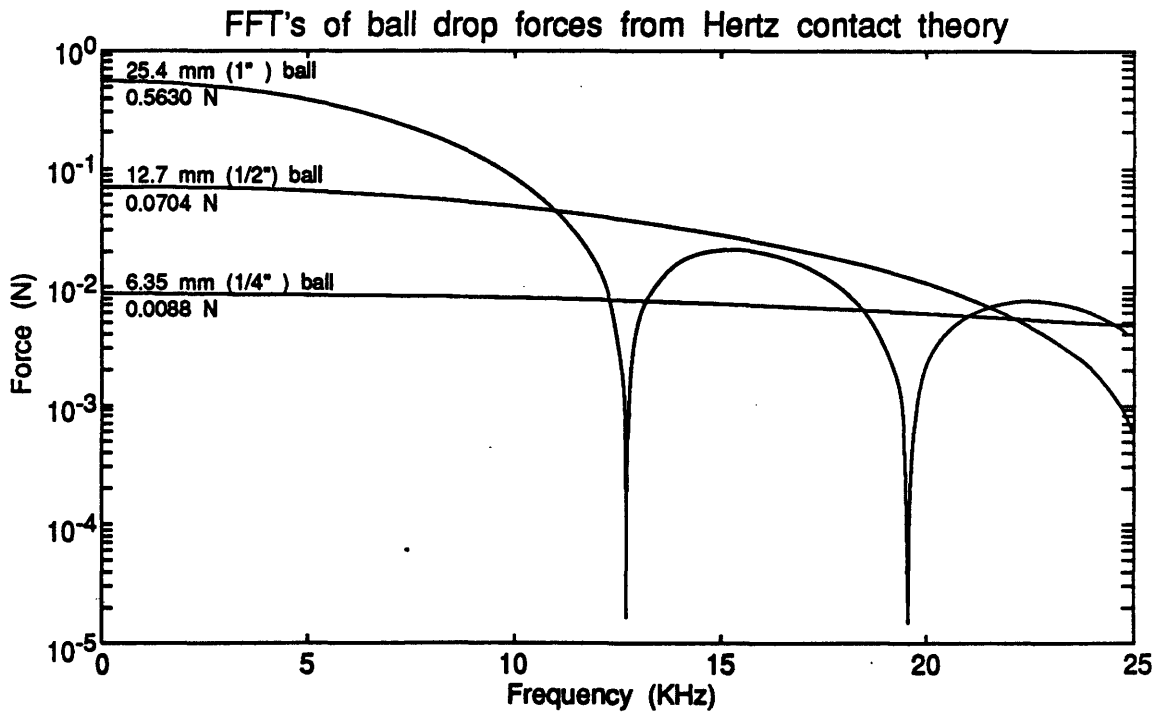
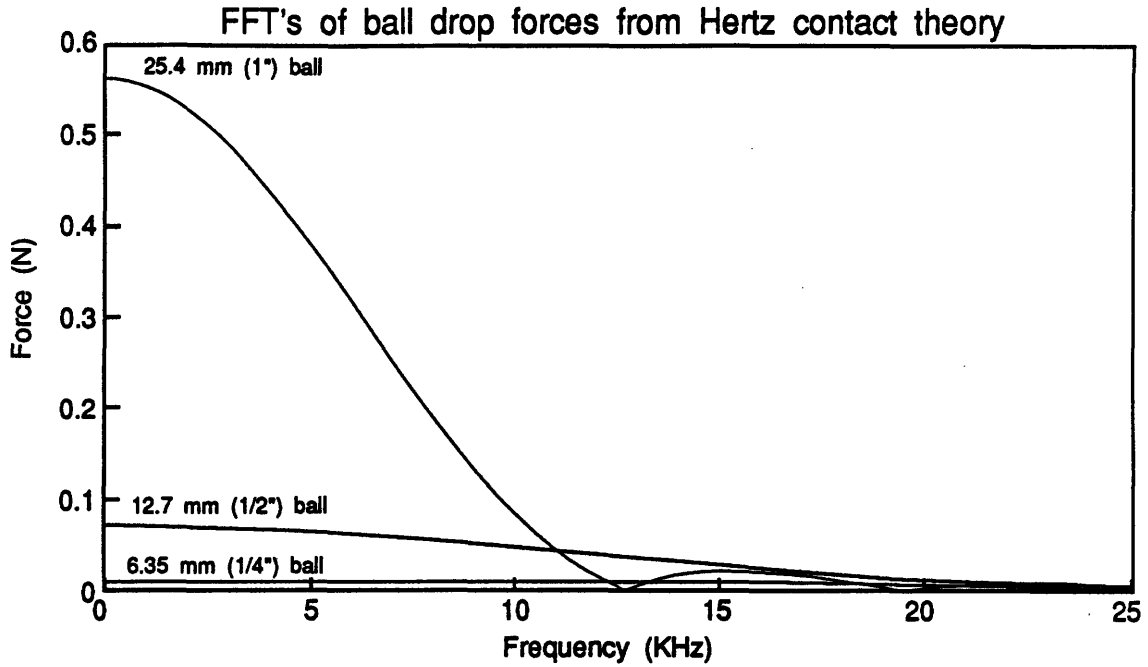
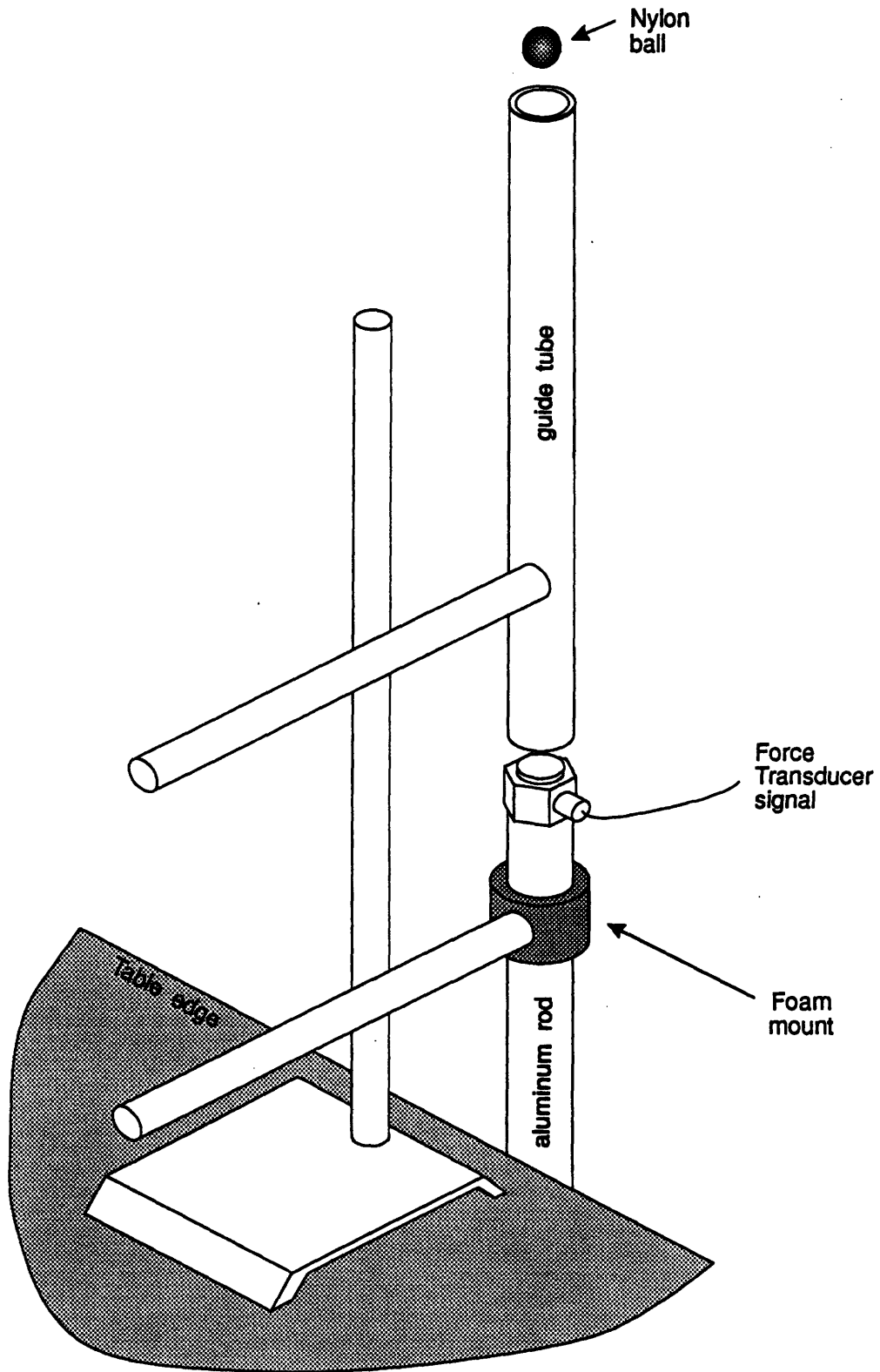


Figure 3.32: FFT's of nylon ball drop forces calculated from Hertzian contact theory, plotted in linear (top graph) and semilog (bottom graph) scales. Forces calculated based on 305 mm (12") drop of nylon balls onto an aluminum surface.

The 6.35 mm (1/4") data is calculated based on 262144 points sampled at 1600 KHz. The 12.7 mm (1/2") data based on 131072 at 800 KHz. The 25.4 mm (1") data based on 65536 at 400 KHz.



Force 3.33: Schematic of ball drop test apparatus for ball drop test on force transducer. Transducer is PCB model 308A03.

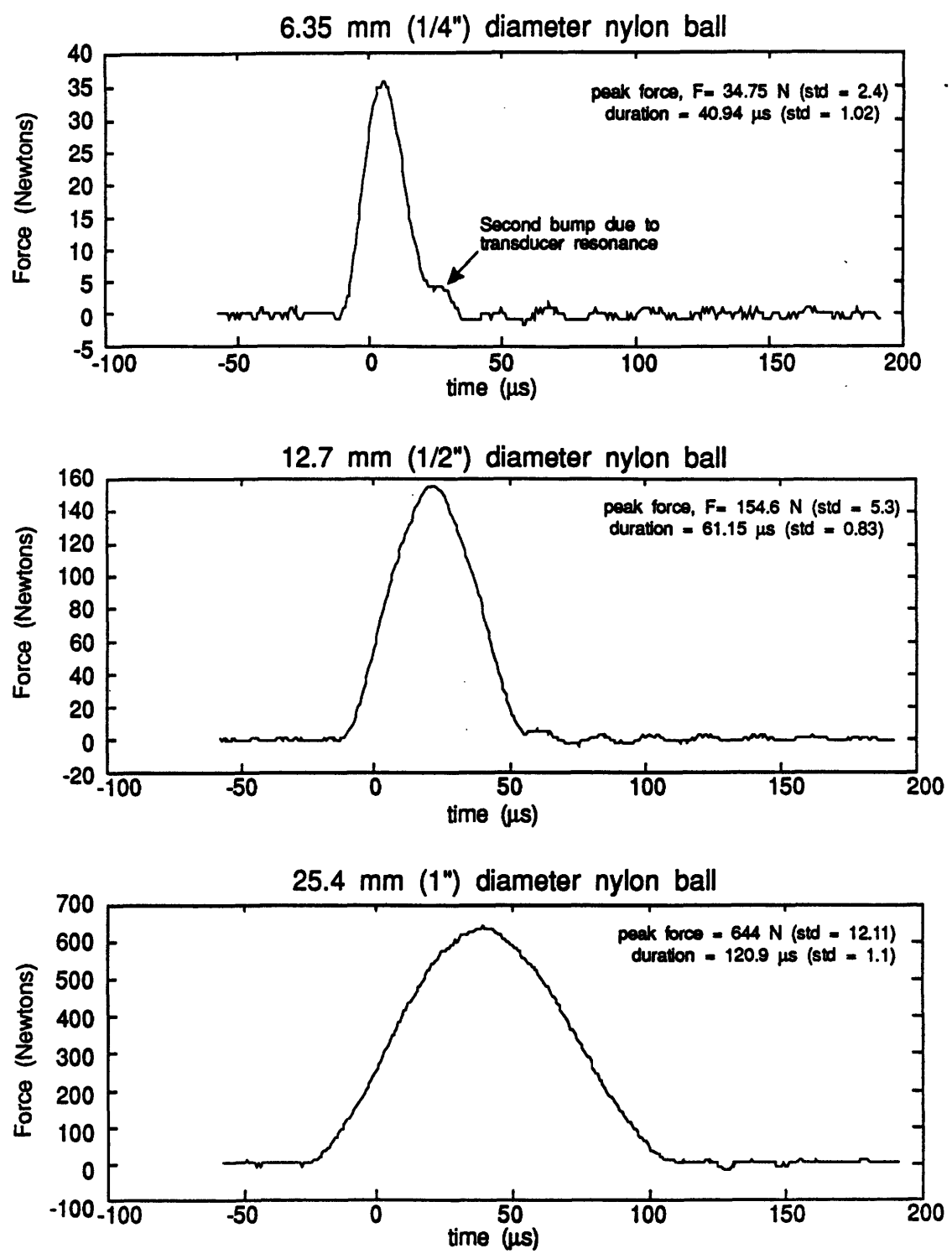


Figure 3.34: Ball drop forces for nylon balls dropped on force transducer mounted on 605 mm long x 16 mm diameter (2' x 5/8") aluminum rod. Ball drop height is 305 mm (12"). Sampling rate is 1.6 MHz and signal is 12 pole low pass filtered at 700 KHz.

Ball size	6.35 mm (1/4")	12.70 mm (1/2")	25.40 mm (1")
Experiment	40.9 μ s	61.2 μ s	121 μ s
Theory	32.2 μ s	64.4 μ s	128 μ s
error	27 %	-5 %	-5 %

Table 3.5: Contact time for nylon balls.

3.8.3 Calculation of FRF's Based on Hertz Contact Force Data.

Since the contact forces have been determined from Hertzian theory and confirmed by experiment, it is now possible to calculate the frequency response functions, specifically the accelerance, of the enlarged slider. Using the force FFTs shown in Figure 3.32 and the acceleration FFTs shown in Figure 3.26, the accelerance can be calculated by dividing the acceleration FFT by the force FFT.

The accelerance calculated for 6.35, 12.7, and 25.4 mm diameter nylon balls are shown in Figures 3.35 and 3.36 in linear and logarithmic scales, respectively. It can be seen from the figures that at low frequencies (<7 KHz) there is very good agreement between the FRFs calculated for the different size balls. At higher frequencies, however, the agreement becomes very poor, particularly for the 25.4 mm ball. This is most likely due to the error in the contact time predicted by the Hertz contact theory. Errors in the contact time effect the frequency rolloff of the force FFT and result in significant errors near the frequencies where the magnitude of the force FFT reaches zero. As a result, the FRF based on the 6.35 mm diameter ball is probably the most accurate, especially at higher frequencies.

3.8.4 Comparison of FEM/Modal Analysis and Ball Drop Data.

Having previously discussed both the theoretical FEM/modal analysis technique and the experimental ball drop/Hertzian contact technique for calculating FRFs, it is time to compare them to see how well they agree. One such comparison is shown in Figure 3.37.

The theory and experiments seem to agree reasonably well over three orders of magnitude. The agreement can be seen not only near the peaks, but in the regions between the peaks as well. However, there are some significant differences to be considered. First, as discussed earlier, the FEM/modal analysis uses an undamped model. Thus, the FRF magnitude is actually infinite at the resonant frequencies. (The graph shows a truncated peak because the curve was drawn from discrete points, not a continuous curve.) Thus the magnitudes of the FRF exactly at the peaks should not be compared, but near the peaks, the curves follow each other very closely. A second difference is that the experimental and theoretical frequencies are not exactly the same. The first peak has the best agreement at 0.25% error and the second peak has the worst

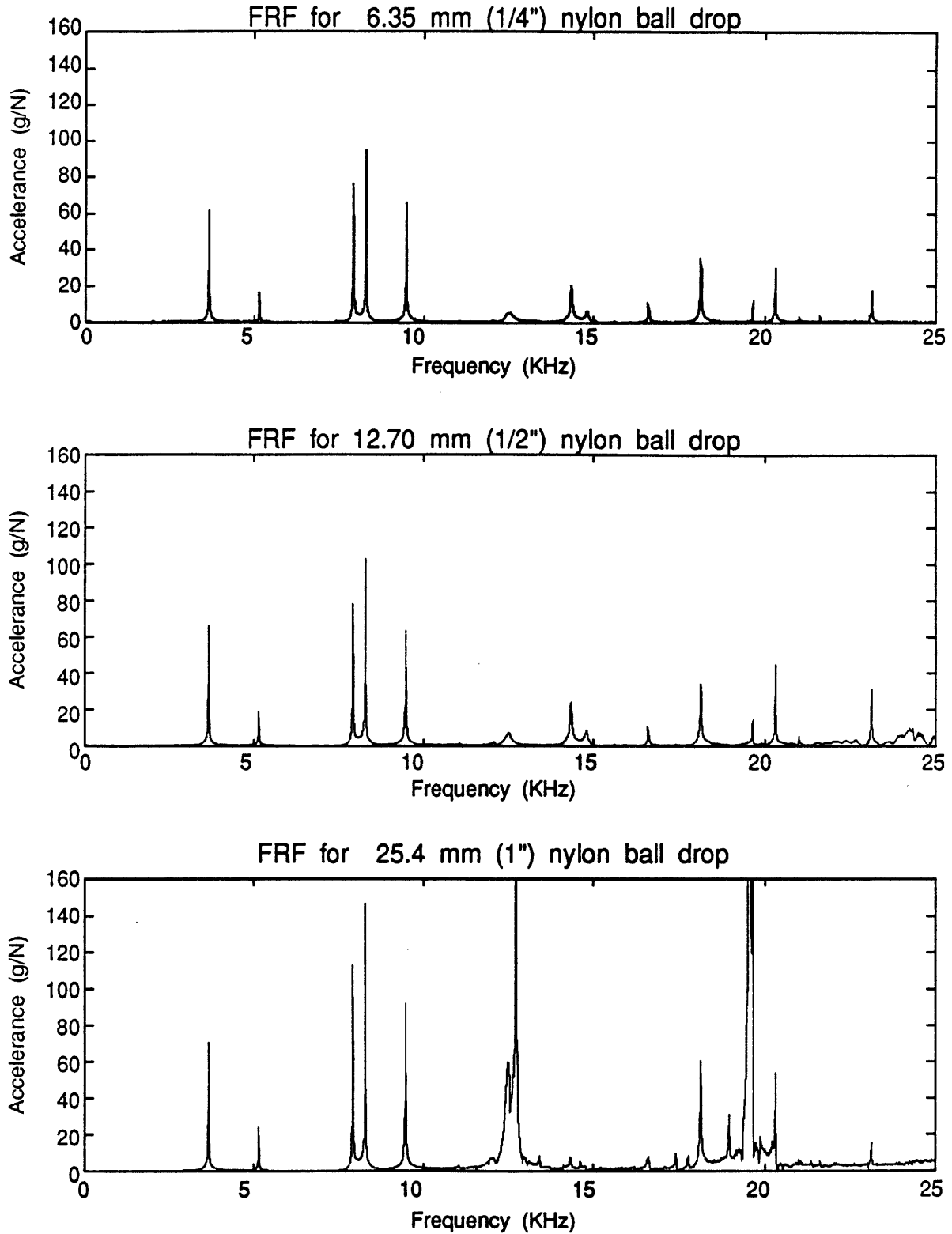


Figure 3.35: Frequency Response Functions (FRF) for 6.35, 12.7, and 25.4 mm (1/4", 1/2", and 1") nylon ball dropped on the enlarged slider. The FRF was calculated using force FFT's calculated from Hertzian contact theory. The ball was dropped at location 1 on the enlarged slider and the acceleration was measured with an accelerometer.

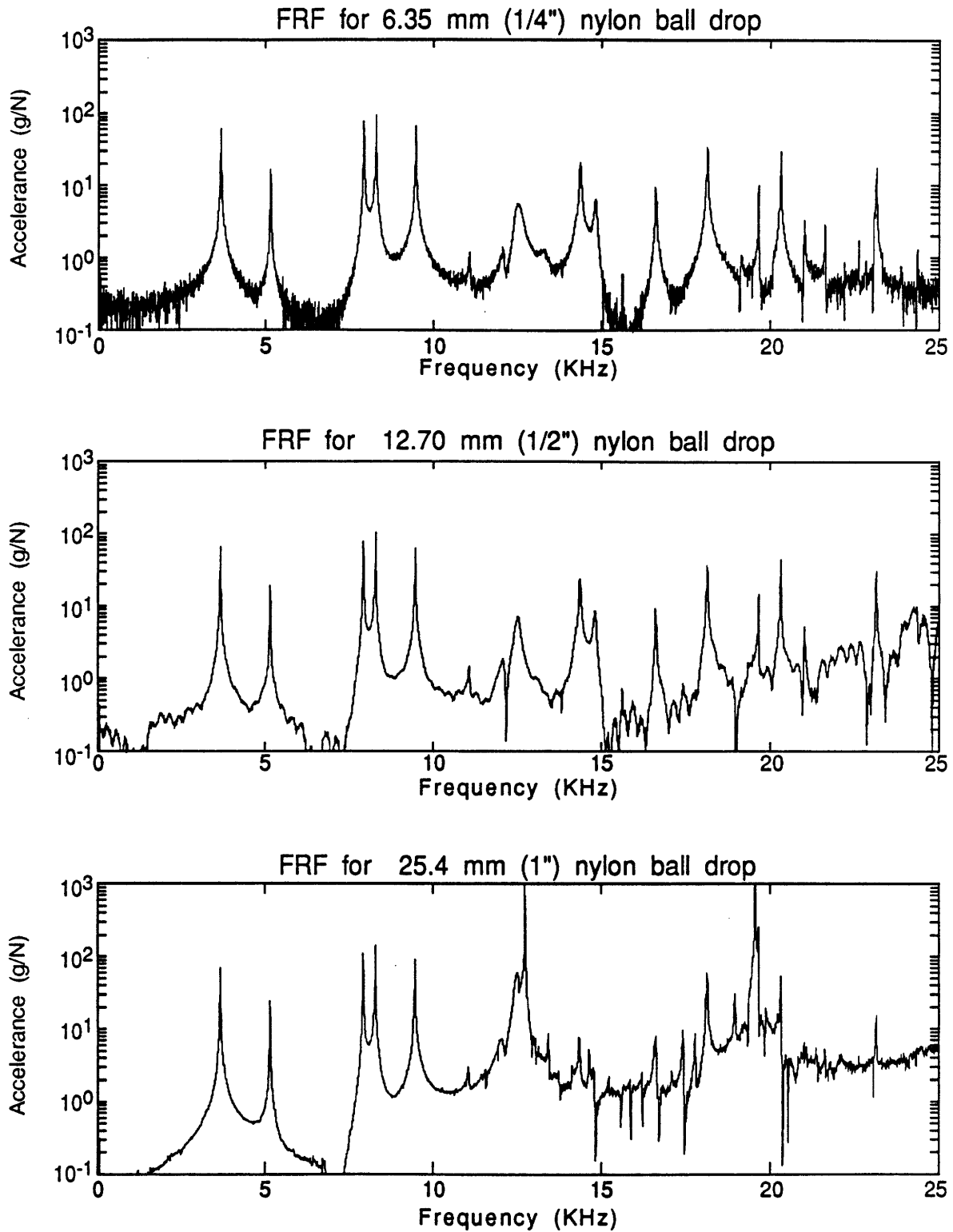


Figure 3.36: Frequency Response Functions (FRF) for 6.35, 12.7, and 25.4 mm (1/4", 1/2", and 1") nylon ball dropped on the enlarged slider. The FRF was calculated using force FFT's calculated from Hertzian contact theory. The ball was dropped at location 1 on the enlarged slider and the acceleration was measured with an accelerometer.

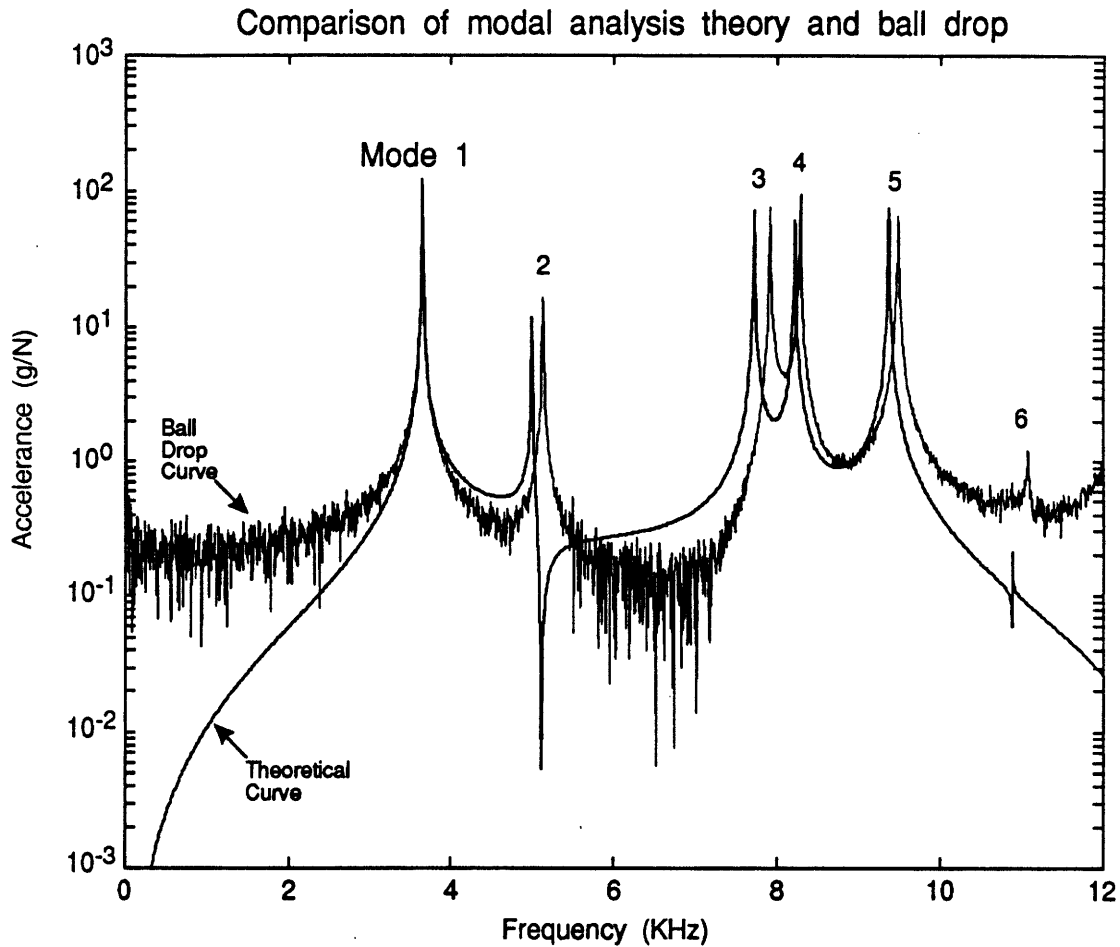


Figure 3.37: Comparison of theoretical modal analysis and ball drop on enlarged slider. The theoretical analysis is based on the 258 element FEM model of the enlarged aluminum slider.

The input is at location 3013z along the rail and sensor is at location 15251z on the back of the slider. The experimental data is based on 1/4" diameter nylon ball dropped from 12" above one of the rails of the enlarged aluminum slider. The force spectrum is based on Hertzian contact analysis sampled at 1.6 MHz for 164 ms. The acceleration is measured using PCB 303A accelerometer on the back of the slider sampled at 50 KHz for 164 ms.

Mode	FEM	Ball impact	Vibration Mode Shape
1	3562 Hz	3649 Hz	Torsion
2	5003 Hz	5139 Hz	Longitudinal Bending
3	7726 Hz	7922 Hz	Transverse Bending
4	8225 Hz	8288 Hz	Second Torsion
5	9374 Hz	9485 Hz	Second Bending

Table 3.6: Comparison of natural frequencies of enlarged slider determined by FEM and by experiment.

agreement at 2.7% error, see Table 3.6. The most likely cause of this error is inadequate mesh refinement in the FEM model. A third obvious difference is the poor agreement between the two FRF's before the first peak and after the sixth peak. This is the result of using only the first 6 vibrational modes in the theoretical modal analysis. The higher modes would increase the magnitude of the high frequency part of the theoretical FRF and the rigid body modes would increase the magnitude of the low frequency part of the theoretical FRF. A fourth significant difference between the two curves is the antiresonance predicted by the theory between the second and third peaks. The experimental data shows no such antiresonance. The cause of this difference is most likely due to the poor quality of experimental data in the antiresonance region.

Although the agreement between the theoretical and experimental FRF's is reasonable, it certainly could be improved by doing the following.

1. Refine the FEM mesh.
2. Include higher frequency vibrational modes in the FEM/modal analysis.
3. Use a 16 bit A/D converter for measuring the acceleration data.

3.9 Summary

This chapter has presented the basic techniques of FEM and modal analysis and demonstrated their use in one particular application. The results of an FEM model are a set of natural frequencies (eigenvalues) and mode shapes (eigenvectors). These results are used in the modal analysis equation,

$$I_{jk}(\omega) = -\omega^2 \sum_{r=1}^n \frac{r\phi_j \cdot r\phi_k}{\omega_r^2 - \omega^2 + i\eta_r\omega_r^2} \quad (3.37)$$

to predict the frequency response function (FRF) of the structure.

Preview of Technique

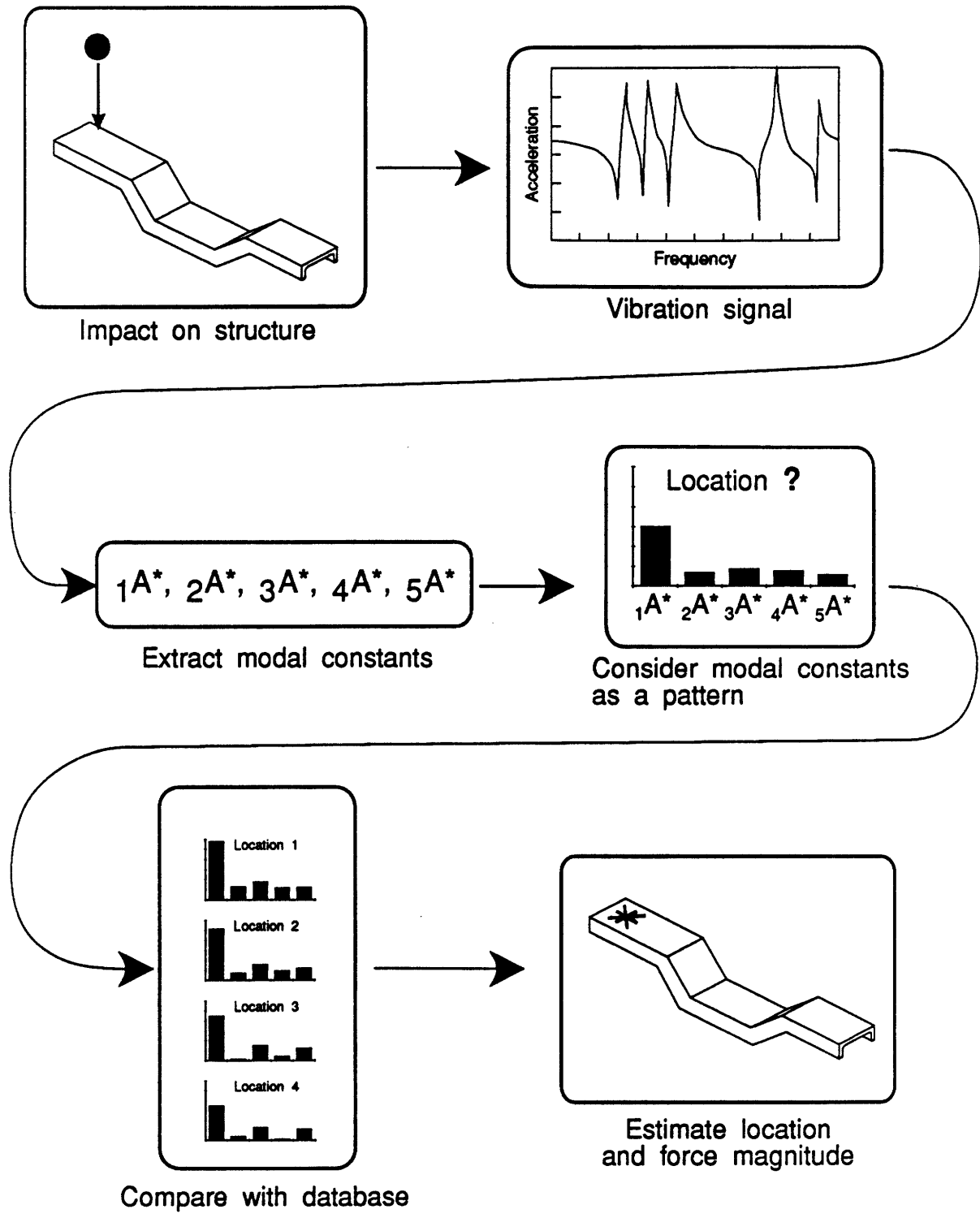


Figure 4.1: Preview of force identification using modal parameter extraction and pattern matching.

This location is unknown and the objective of the force identification technique is to predict the location of the source (impact) and the force magnitude. An acceleration signal is acquired, from an accelerometer mounted on the structure, and transformed into the frequency domain using the fast Fourier transform (FFT). Using the frequency domain acceleration signals, the modal constants for each vibrational mode of the acceleration signal can be extracted. For the purposes of the current discussion, the modal constants can just be considered as the magnitude of each resonance peak in the acceleration signal. These extracted modal constants can be considered as a pattern, i.e. they are the main features of the acceleration signal and represent a “fingerprint.” Prior to running this test, a number of tests had been run to determine the patterns of modal constants for each likely input location and a database was built. A comparison is made between the pattern of modal constants from this test and the patterns of modal constants in the database. The pattern in the database that best matches the experimental pattern, indicates the expected location of impact and also the magnitude of the impact force.

There is one significant assumption in this force identification technique. Since the modal constants are being used to identify the impact location and force magnitude, there must be a unique relationship between impact locations and a given set of modal constants, for the technique to work properly. If two locations have the same set of modal constants, then confusion can arise about the likely location of impact. This is apt to be a problem with structures that are symmetric. This situation is known as a *uniqueness* problem, and is a common difficulty faced in many inverse problem solving techniques. Uniqueness will be discussed further, later on in this chapter and in the next.

Overall, the force identification technique is constructed in the same way as any other pattern matching problem, e.g. fingerprint matching. The success of the technique depends largely on how well the *extracted features* discriminate between different classes of inputs. For example, if the values of the resonance frequencies were used in the pattern matching, the pattern matching would be useless. This is because the values of the resonance frequencies do not change with input location or input force magnitude. On the other hand, the modal constants (or magnitude of vibration) are likely to change a great deal with input location, as will be demonstrated later.

Having presented this brief description of the force identification technique, it is now time to present the details of the technique. First, the techniques of modal parameter extraction will be presented. Two types of modal parameter extraction will be illustrated. One technique uses only the magnitude of the acceleration signal while the other technique uses both the magnitude and phase. After discussing the modal parameter extraction techniques, the pattern matching technique will be explained. Finally, a summary is given of the whole force identification procedure.

4.2 Modal Parameter Extraction

In modal testing, the frequency response functions (FRF's) must be fit to some form of modal equation to extract out the necessary modal parameters. These modal parameters usually

include natural frequencies ω_r , loss factors η_r , and modal constants ${}_r A_{jk}$. The usual reason for extracting these modal constants is to experimentally deduce the mode shapes. This is done by extracting the modal constants from a set of FRF's with different input locations. The modal constants associated with a single mode can be graphed to view the mode shape. The modal constants can also be assembled to create a *modal model* of the structure which can be used to predict the response of the structure to different inputs. The modal model can even be used to predict the response of the structure to simple modifications.

For the force identification technique, there needs to be a modal model of the structure for use in the database for the pattern matching. The modal model needs to have data about all the likely input locations.

When the force identification technique is being used, there is, by assumption, no a priori knowledge about the force magnitude or location. Only the acceleration signal is available from a single test. This represents a problem for the modal parameter extraction techniques because the accelerance ($a(\omega)/f(\omega)$), which is usually used in modal parameter extraction, cannot be calculated. The force $f(\omega)$ is usually needed before any modal parameter extraction can be performed. For an input source which is a short duration force pulse, however, this problem can be overcome by a slight change in the modal parameter extraction technique.

Consider, for a moment, the typical equation, from Chapter 3, for the calculation of the accelerance.

$$I_{jk}(\omega) = \frac{a(\omega)}{f(\omega)} = -\omega^2 \sum_{r=1}^n \frac{{}_r A_{jk}}{\omega_r^2 - \omega^2 + i\eta_r \omega_r^2} \quad (4.1)$$

This would be the form of the equation to which the experimentally measured data would have to be fit. If the force $f(t)$ is a short duration pulse, then the force is nearly a constant in the frequency domain, i.e.

$$f(\omega) \approx \text{constant} \quad \text{for } \omega \text{ small.} \quad (4.2)$$

Taken to the mathematical limit, if the force is an infinitely short duration impulse, the magnitude of the force would be exactly equal to a constant. For physically realizable force pulses to be considered short duration, they must be of short duration compared to the resonance frequencies of the modes used in the analysis. Specifically,

$$t_d \ll \frac{2\pi}{\omega_m}, \quad (4.3)$$

where ω_m is the natural frequency of the highest frequency mode used in the modal analysis and t_d is the time duration of the force pulse. Once this restriction is made, Equation 4.1 can be rewritten as follows.

$$a(\omega) = -\omega^2 \sum_{r=1}^n \frac{{}_r A_{jk}^*}{\omega_r^2 - \omega^2 + i\eta_r \omega_r^2} \quad (4.4)$$

where

$${}_r A_{jk}^* = f(\omega) {}_r A_{jk} \quad (4.5)$$

The values of ${}_r A_{jk}^*$ will be called the *uncorrected modal constants*. They are called uncorrected because they must be divided by the (nearly constant, but unknown) force, $f(\omega)$ to get the correct modal constant.

The idea of using the uncorrected modal constants ${}_r A_{jk}^*$ is a simple, but important, addition to the modal parameter extraction techniques presented in the literature. This technique allows the modal constants to be extracted even though the force is not known. As will be shown later, this force can be determined using a pattern matching technique with a database of modal constants. It is important to realize that the input forces must be known when developing the database or modal model. However, the forces do not need to be known for later tests. Therefore, Equation 4.1 is used when the modal model is being created and Equation 4.4 is used for the force identification technique.

There are many modal parameter extraction techniques available [1]. Some of them curve fit in the time domain and some fit in the frequency domain. Some techniques, known as SDOF (single degree of freedom) techniques, fit only one resonance peak at a time and other techniques, known as MDOF (multiple degree of freedom) techniques, fit all resonance peaks at once. The two modal parameter extraction techniques used in this thesis will be demonstrated in the next two subsections. The first technique is a MDOF technique and it has been modified to use only the magnitude of the FRF. The second modal parameter extraction technique is a SDOF technique that uses both the magnitude and phase of the FRF to determine the modal constants. It should be noted that, while neither of these modal parameter extraction techniques are totally new, both of them have been modified to account for the fact that the force cannot be directly measured. Particularly important is the additional steps necessary for extracting the phase information under this condition. The explanations given in the next two subsections are developed using accelerance or receptance as the FRF. However, the same modal parameter extraction technique can be used on the acceleration signals to extract the uncorrected modal constants ${}_r A_{jk}^*$. When additional steps are needed to process acceleration signals, it will be clearly noted.

4.2.1 Magnitude Only Technique

The rationale for selecting the following modal parameter extraction was, in a word, simplicity. For the force identification technique to be useful as an on-line (or in-process) tool, the computer processing should be kept to a minimum. The technique is not as elegant as some other modal parameter extraction techniques, but it does provide an accurate set of modal constants.

The modal parameter extraction technique is adapted from a technique developed by Ewins (1982) [33]. The approach is to assume that for lightly damped structures, only a small error is made if the damping is neglected completely. This means that Equation 4.1 can be rewritten as

$$I_{jk}(\omega) = -\omega^2 \sum_{r=1}^n \frac{{}_r A_{jk}}{\omega_r^2 - \omega^2} \quad (4.6)$$

or

$$I_{jk}(\omega) = \sum_{r=1}^n \frac{rA_{jk}}{1 - (\omega_r/\omega)^2}. \quad (4.7)$$

In this way the complex Equation 4.1 is replaced by a real equation. The modal parameter extraction technique must fit the experimentally determined accelerance data pairs, (ω_i, I_i) into the form of Equation 4.7.

For each of the n vibrational modes in the modal analysis, there are two unknowns, the natural frequencies ω_r and modal constant rA_{jk} . The natural frequencies can be easily determined by looking for peaks in the magnitude of the accelerance $|I(\omega)|$. The peak detection scheme could be very simple, such as looking for a value of $|I(\omega)|$ that is larger than its three neighboring points on each side, i.e.

$$\begin{aligned} |I(\omega)| &> |I(\omega - 3\delta\omega)| \\ &> |I(\omega - 2\delta\omega)| \\ &> |I(\omega - \delta\omega)| \\ &> |I(\omega + \delta\omega)| \\ &> |I(\omega + 2\delta\omega)| \\ &> |I(\omega + 3\delta\omega)| \end{aligned}$$

where $\delta\omega$ is the frequency spacing between samples. Once the resonance frequencies have been determined, the only unknowns are the values of the modal constants in Equation 4.7.

Consider a specific pair of data points, $\Omega_i, I(\Omega_i)$, where Ω_i is the frequency of an individual sample. For this pair of data points Equation 4.7 can be rewritten in a vector form.

$$I(\Omega_i) = \left\{ \left(1 - \frac{\omega_1^2}{\Omega_i^2}\right)^{-1}, \left(1 - \frac{\omega_2^2}{\Omega_i^2}\right)^{-1}, \dots, \left(1 - \frac{\omega_n^2}{\Omega_i^2}\right)^{-1} \right\} \begin{Bmatrix} 1A_{jk} \\ 2A_{jk} \\ \vdots \\ nA_{jk} \end{Bmatrix} \quad (4.8)$$

However, this is only one equation with n unknowns. If a total of n individual accelerance measurements are used, then a matrix equation can be assembled as follows.

$$\begin{Bmatrix} I(\Omega_1) \\ I(\Omega_2) \\ \vdots \\ I(\Omega_n) \end{Bmatrix} = \begin{bmatrix} \left(1 - \frac{\omega_1^2}{\Omega_1^2}\right)^{-1} & \left(1 - \frac{\omega_2^2}{\Omega_1^2}\right)^{-1} & \dots & \left(1 - \frac{\omega_n^2}{\Omega_1^2}\right)^{-1} \\ \left(1 - \frac{\omega_1^2}{\Omega_2^2}\right)^{-1} & \left(1 - \frac{\omega_2^2}{\Omega_2^2}\right)^{-1} & \dots & \left(1 - \frac{\omega_n^2}{\Omega_2^2}\right)^{-1} \\ \vdots & \vdots & \ddots & \vdots \\ \left(1 - \frac{\omega_1^2}{\Omega_n^2}\right)^{-1} & \left(1 - \frac{\omega_2^2}{\Omega_n^2}\right)^{-1} & \dots & \left(1 - \frac{\omega_n^2}{\Omega_n^2}\right)^{-1} \end{bmatrix} \begin{Bmatrix} 1A_{jk} \\ 2A_{jk} \\ \vdots \\ nA_{jk} \end{Bmatrix} \quad (4.9)$$

or

$$\{I(\Omega)\}_{n \times 1} = [R]_{n \times n} \{rA_{jk}\}_{n \times 1} \quad (4.10)$$

Note that the subscripts such as $n \times 1$ indicate the size of the vector or matrix. The solution to this matrix equation can be obtained from a simple matrix inversion, $[R]^{-1}$, and the modal constants, $\{A_{jk}\}_{n \times 1}$, can be determined.

One of the difficulties with this modal parameter extraction technique is selecting a reasonable set of n points, $\{\Omega_n, I(\Omega_n)\}$, for doing the curve-fitting. Since there are n modes, or peaks, and n sets of points, there is one data point per peak. Ewins 1982 [33] suggests selecting one point from the anti-resonance region between each pair of peaks. But, this is far from the optimal use of the data because there is frequently hundreds of data points to choose from.

Fortunately, there is a relatively straight forward way to make the best use of all available acceleration data. First, the above matrix equation can be expanded to include all available data points.

$$\{I(\Omega)\}_{m \times 1} = [R]_{m \times n} \{A_{jk}\}_{n \times 1} \quad (4.11)$$

Here we have assumed that there are m data points and n vibrational modes. Now, we have m equations and n unknowns, where $m \gg n$. In other words, the system of equations is over-constrained. There is no exact solution to such equations, although an estimate of the modal constants, $\{\hat{A}_{jk}\}$, can be obtained using a least-squares or pseudoinverse solution [34]. The pseudoinverse solution to Equation 4.11 is the following,

$$\{\hat{A}_{jk}\} = ([R]^T [R])^{-1} [R]^T \{I(\Omega)\} \quad (4.12)$$

where the superscript T indicates a transpose and superscript -1 is a matrix inverse. The resulting estimates of the modal parameters, $\{\hat{A}_{jk}\}$, can be used in the original acceleration formula, Equation 4.7, to generate a reconstructed FRF for comparison with the raw acceleration data. In this way, the quality of the curve fitting process can be visually checked.

One of the biggest advantages of this modal parameter extraction technique is that by neglecting the effects of damping, the acceleration data can be considered as real rather than complex. This greatly reduces the amount of curve fitting that needs to be done, since only the real part of the acceleration needs to be curve fit. Other techniques require simultaneous curve fitting of the real and imaginary parts of the acceleration data.

The difficulty with this technique is that the frequency domain acceleration data is not truly real. The frequency domain acceleration is calculated from the FFT's of the time domain acceleration and force signals and the result is a complex FRF. If the damping is low, then the imaginary part of the acceleration will be small, except near the resonance and anti-resonance regions. In order to make the acceleration real, the imaginary part can simply be discarded. However, the data points with a large imaginary component (near resonance or anti-resonance) should not be used in the curve fitting process.

Additional difficulties are encountered if acceleration data is being curve fit, rather than acceleration data, recall the discussion surrounding Equation 4.4. The phase information in the acceleration signal is corrupted by a linear phase taper and thus cannot be used directly. Appendix B and subsection 4.2.2 discuss the detailed nature of this problem, for now it is enough to know that the phase is corrupted. Faced with this fact, the frequency domain acceleration

data must still be converted from complex to real in order to extract the modal constants. One way to do this, is to use what will be called *assumed phase*. Each time a resonance peak occurs in the frequency domain, there is a 180° drop in the phase. Also, each time an anti-resonance peak occurs in the frequency domain, there is a 180° increase in the phase. Thus it might be possible to reconstruct the phase of a lightly damped structure using only the magnitude of the frequency domain acceleration data, $|a(\omega)|$.

Unfortunately, the determination of the location of anti-resonances is much more difficult than the determination of resonances. Because anti-resonances, by their very nature, have low signal strength, their presence or absence is frequently masked by noise in the signal. An assumed phase can be still be constructed, however, by creating a 180° drop in the phase at the location of each resonance in the frequency domain. Assumed phase constructed in this way assumes that there are no anti-resonances in the acceleration data. The result of this assumption is that although the magnitude of the extracted modal constants $|_r A_{jk}|$ will be correct, the sign (+/-) will not necessarily be correct. Although this would be unsatisfactory for most purposes of modal analysis, it is perfectly acceptable for use in the pattern matching technique of the force identification procedure.

To graphically illustrate this modal parameter extraction procedure, a sample data set will be used. The data happens to be from a ball drop test on the enlarged slider model (see Chapter 5), but all the steps are general. It will be assumed that the phase information is corrupted by a linear phase taper and an assumed phase must be constructed. The sample acceleration data is shown in Figure 4.2.

The first step in the modal parameter extraction is to locate the resonance peaks. This is done by looking for points that are greater in magnitude than their three nearest neighboring points. The locations of the resonances have been marked with a \times in the figure. False peaks are some times detected as a result of poor quality data. This is particularly true when the magnitude of the acceleration $|I(\omega)|$ is low, this is a result of the limited dynamic range of the instrumentation. To overcome this problem, the regions of the acceleration data $I(\omega)$ where the magnitude is small are not searched for resonance peaks. The peak detection searching can be greatly simplified if a priori knowledge is available for the peak locations. As a result, the searching for peaks can be limited to a narrow frequency range where a peak is expected. This is done in the force identification procedure, because a modal model of the structure is already available.

The second step in the modal parameter extraction is to convert the complex acceleration into real acceleration. As indicated earlier this can be done by constructing an assumed phase, where the phase drops 180° at each resonance peak. The assumed phase for the sample data is shown in Figure 4.3. The assumed phase has not been *unwrapped*, so in some places it looks like it increases by 180° even though it actually drops by 180° .

The third step is to select the points to be used in the curve fitting of Equation 4.12. It is prudent to eliminate the data points that are of poor quality, which can occur in the frequency ranges where there is low vibration levels. Figure 4.4 shows the sample data to be used in the curve fitting. Note that the data is now real and hence no phase plot is given.

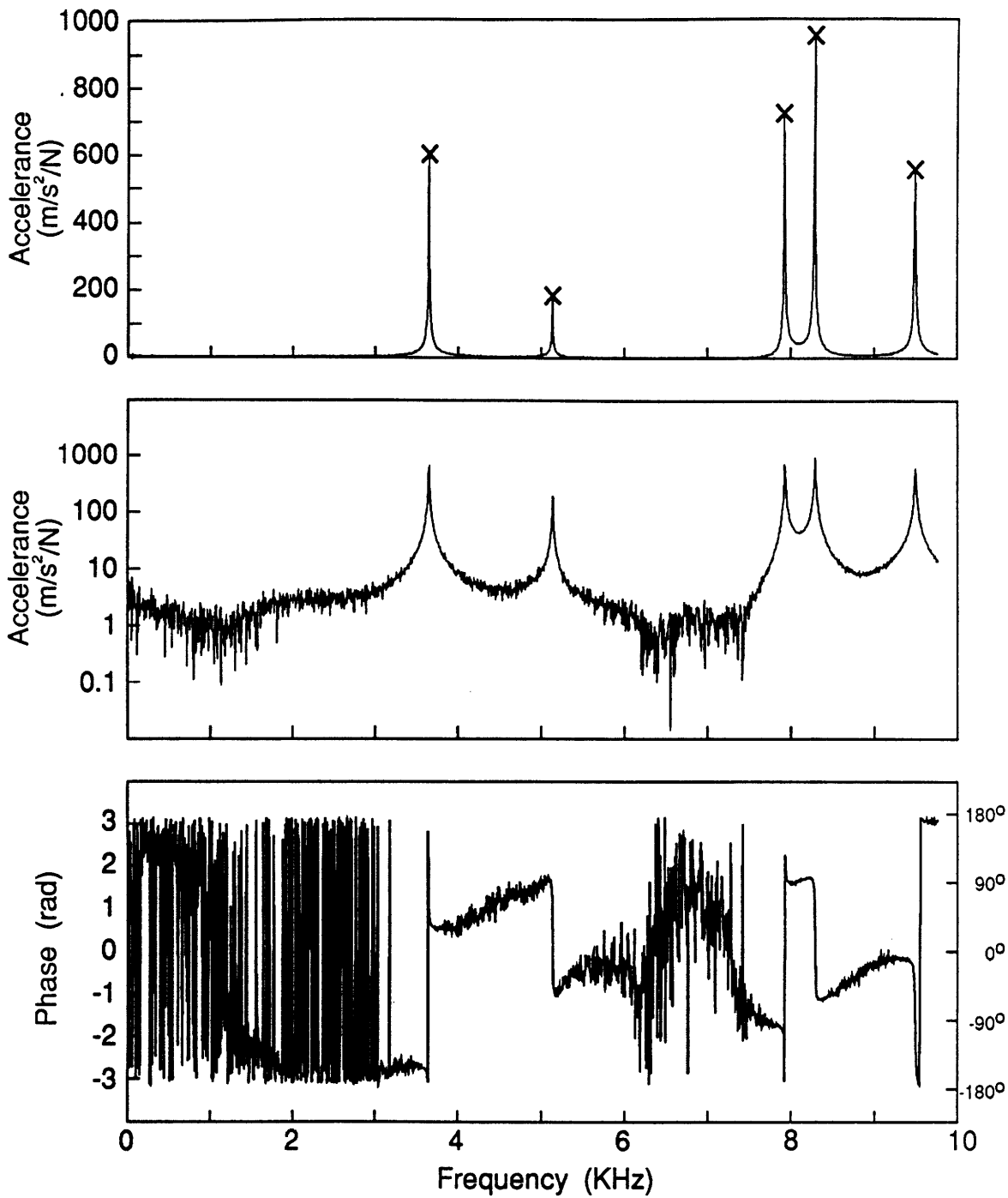


Figure 4.2: Sample acceleration data acquired from a ball drop test on an enlarged slider. Note that the resonance peaks are marked by x's.

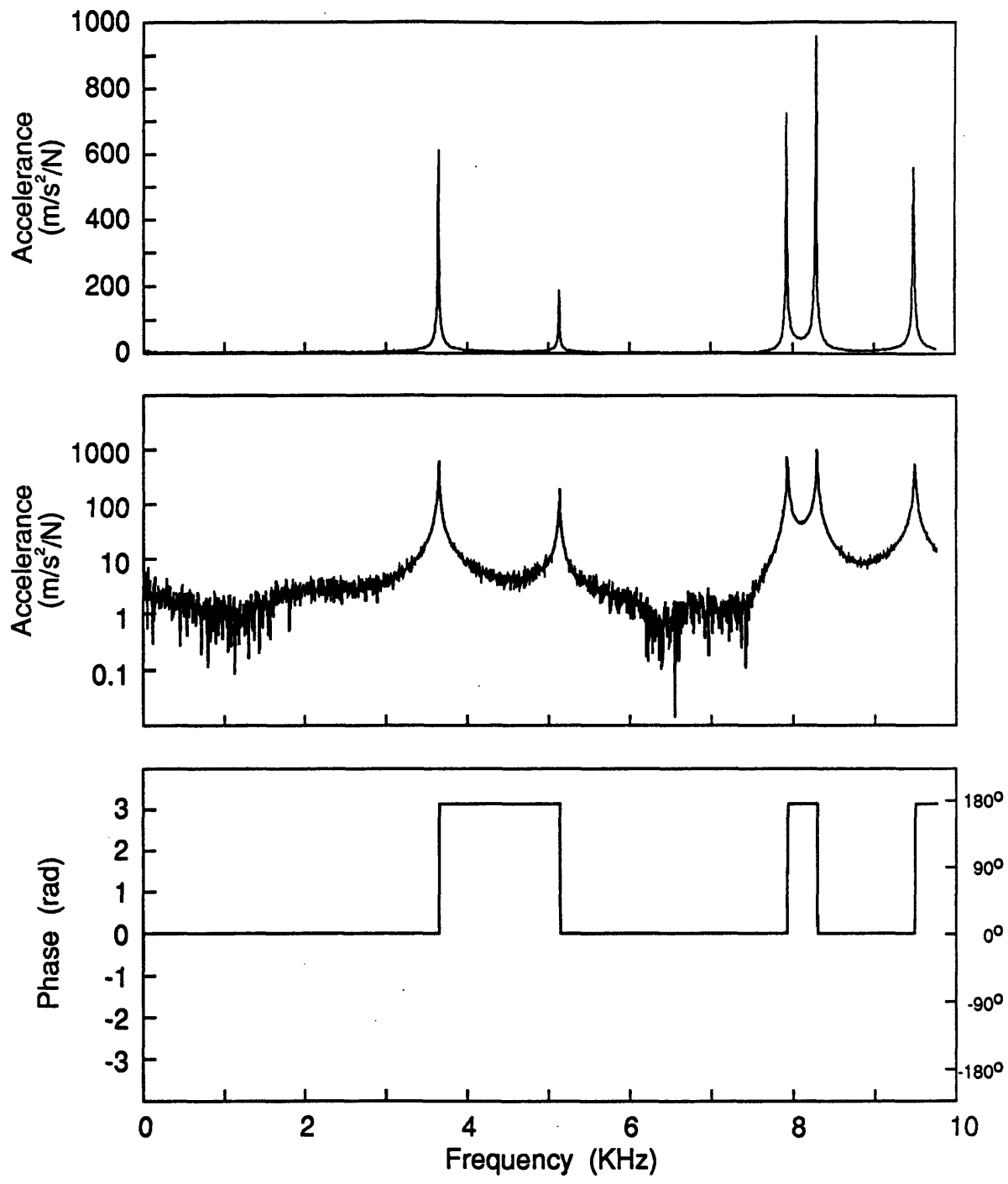


Figure 4.3: Sample acceleration data with assumed phase information.

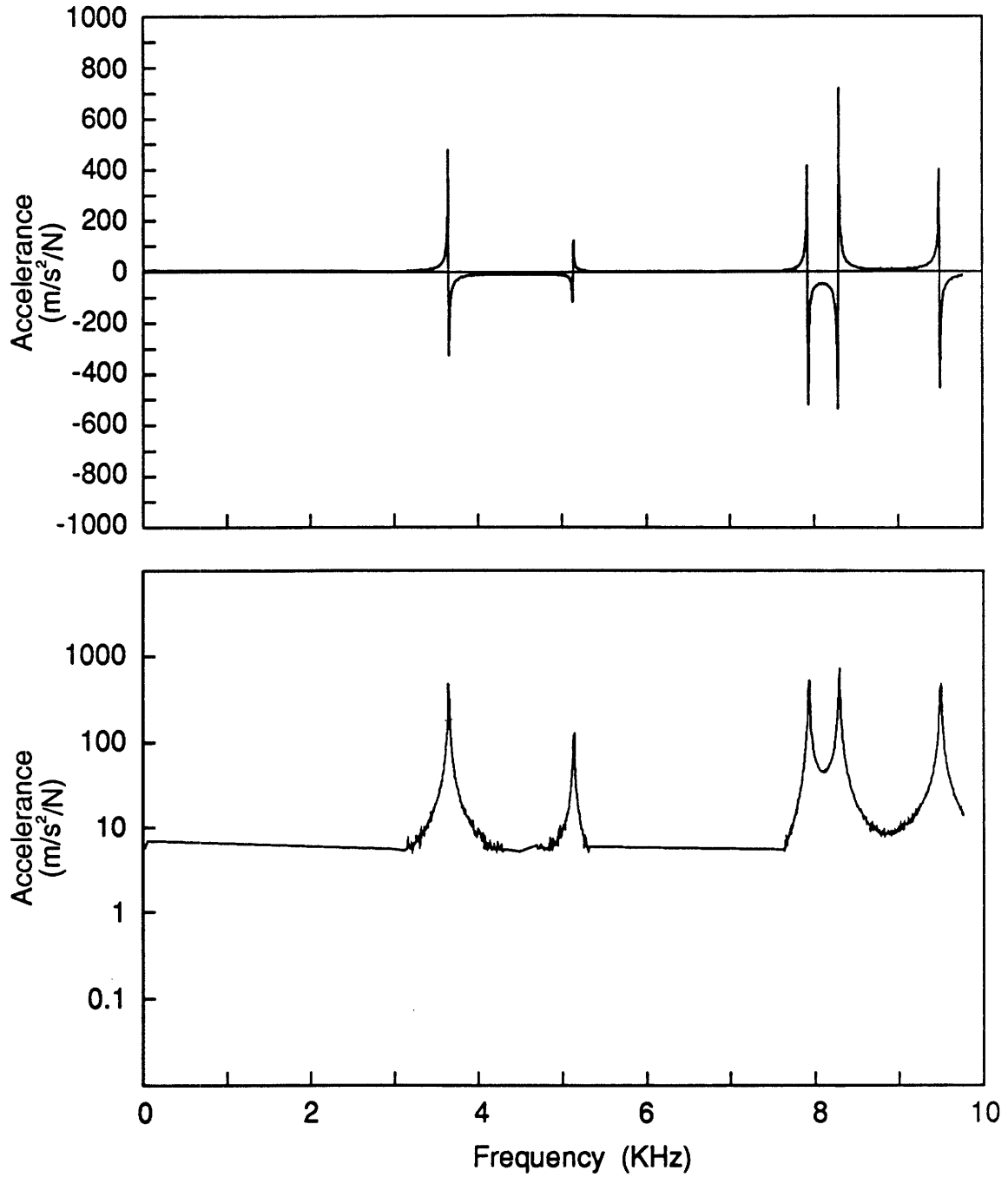


Figure 4.4: Sample accelerance data converted to real numbers and weak points removed.

The fourth and final step is to assemble the $[R]$ and $\{I(\omega)\}$ matrices in Equation 4.12, calculate the pseudo-inverse, and determine the estimates of the modal constants $\{\hat{A}_{jk}\}$. Figure 4.5 shows how the reconstructed data compares with the experimental data. The curves lay so close to each other that no difference can be seen between the two on the linear plot. On the log plot, the limited dynamic range of the instrumentation is evident. Also note that if there was an anti-resonance between two of the peaks of the measured FRF, it would not be properly identified in the reconstructed FRF because the assumed phase was used.

This modal parameter extraction technique has the distinct advantage of being more computationally efficient than other available techniques. The location of the peaks and construction of the assumed phase is only a few quick steps. The only significant computations are the initial FFT calculation and the pseudo-inverse. In terms of the force identification procedure, the biggest short coming of the technique is the lack of proper phase information, or more specifically, the fact that the proper sign (+/-) of the modal constants rA_{jk} is not known. The next subsection will present an alternative technique for extracting the modal constants, which also uses the phase information.

4.2.2 Magnitude and Phase Technique

By using the magnitude and phase of the accelerance (or acceleration) data, more information can be obtained than simply using the magnitude alone. However, the trade-off is that more computation is needed and the quality of the data becomes more important. Although the magnitude and phase information could be used in the previously presented modal parameter extraction technique, a new modal parameter extraction technique will be used in this section. Part of the reason for the use of a different modal parameter extraction technique is that some of the results, from the processing needed to correct the phase information, can be used in the new modal parameter extraction technique. This will be clarified later.

Phase Taper Removal

Before the new modal parameter extraction technique can be used, the phase of the acceleration (or accelerance) must be corrected. When acceleration signal is acquired from an accelerometer, it is acquired in what is called pretrigger mode, see Figure 4.6. In the pretrigger mode, some data is acquired before the force pulse occurs. In the time domain graph, this shows up as a time offset from time $t = 0$. In the frequency domain, there is no effect on the magnitude but it creates a linear increase in the phase with frequency as shown in Figure 4.6. The effect can also be seen in a Nyquist plot (a plot of real vs imaginary parts of the Fourier transform). The resonance peaks in the Fourier transform usually show up as circles with their centers lined up with $\pm 90^\circ$. However, with the pretrigger information included, the centers of the circles do not line up, as can be seen in the figure. In order to correct the phase data, this linear phase taper must be removed.¹

¹The problem of the linear phase taper is not an issue in normal modal analysis. Accelerance is normally used in modal analysis. Since accelerance is the ratio of acceleration to force, even though both signals have a

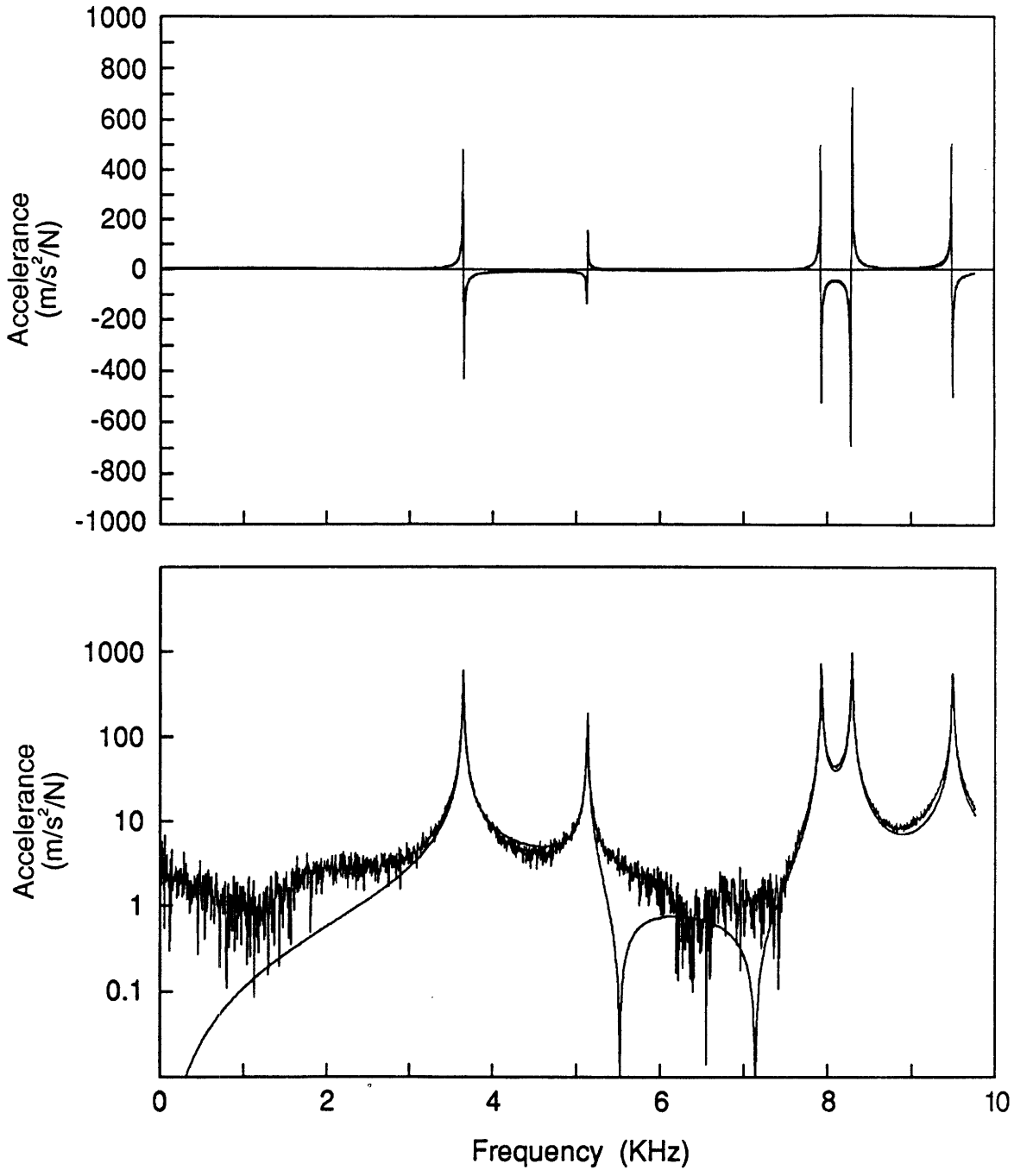
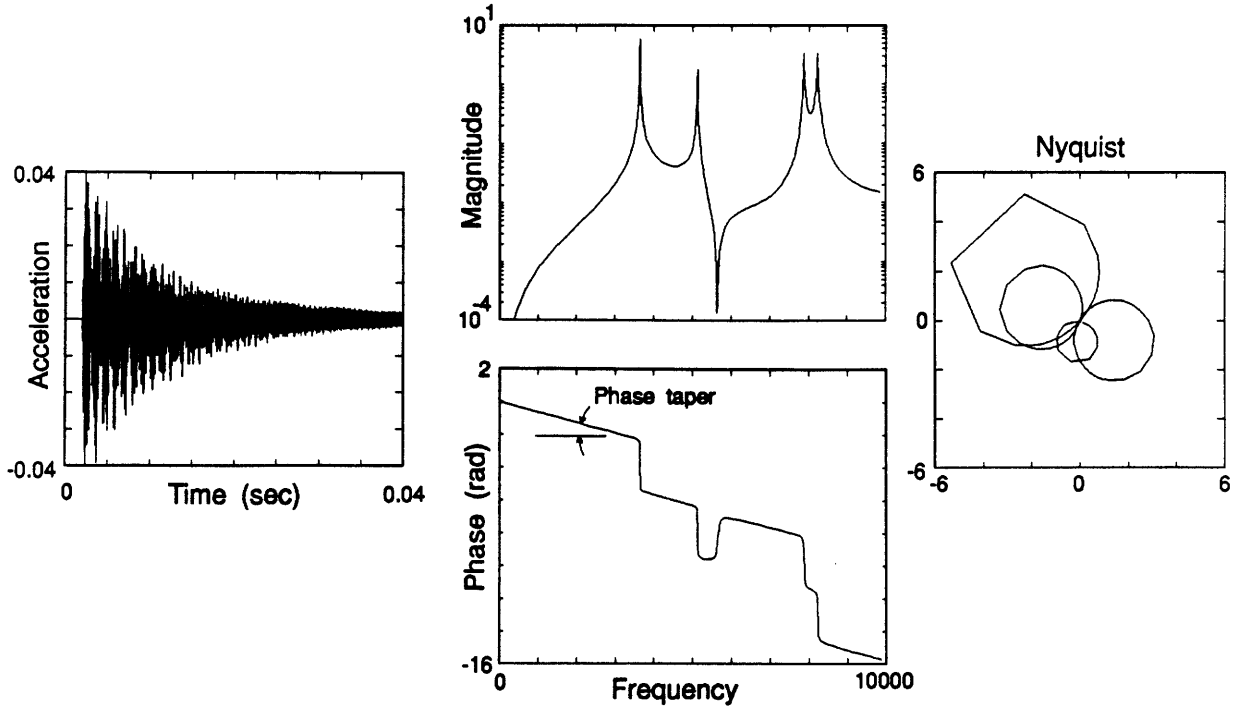


Figure 4.5: Comparison of the sample acceleration data and the reconstructed FRF curve.

Acceleration data with pretrigger information



Linear phase taper removed from the acceleration data

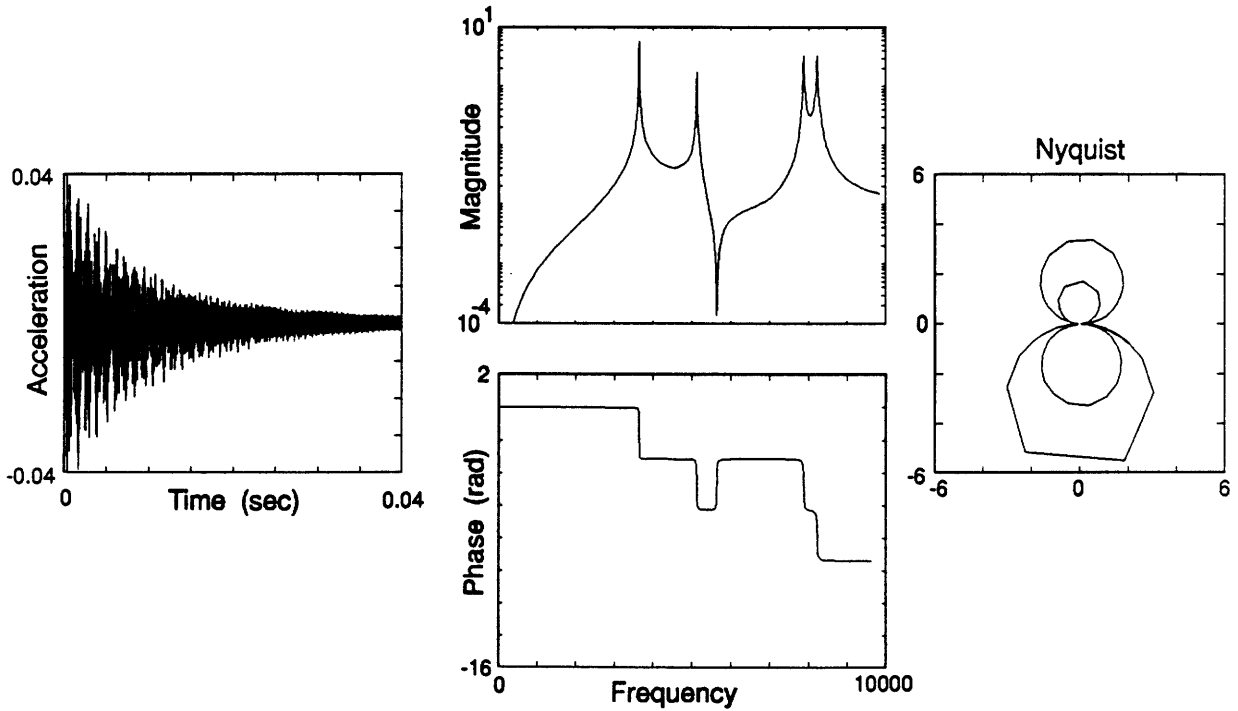


Figure 4.6: Demonstration of the effect of pretrigger information on the phase of the acceleration signal.

Fundamentally, the cause of the linear phase taper can be understood as a basic property of Fourier transforms (FT). Let a typical acceleration signal be called $a(t)$ and its Fourier transform A . This can be written in the following short hand way.

$$a(t) \leftrightarrow A \quad (4.13)$$

The \leftrightarrow symbol is simply a short hand way of showing that A is the FT of $a(t)$ and $a(t)$ is the inverse FT of A . If the acceleration signal is delayed by a small amount of time, t_0 , like it is when the pretrigger information is included, then it can be shown that the FT is the following.

$$a(t - t_0) \leftrightarrow Ae^{-j\omega t_0} \quad (4.14)$$

It is the $e^{-j\omega t_0}$ term that is responsible for the linear phase taper. The time delay has no effect on the magnitude of the FT, it just affects the phase.

There are three different ways to think about removing the linear phase taper from acceleration signal: 1) the time domain, 2) the frequency domain Bode plot, and 3) the frequency domain Nyquist plot. Each one of these domains can be obtained from the other domains, but removing the phase taper involves different processing in each domain. To illustrate the processing involving in removing phase taper, an example vibration signal was created as shown in Figure 4.7. The system has four vibrational modes and has the properties shown in the figure.

In the time domain, the digital sampling has a significant effect on the signal, as shown in Figure 4.8. The top part of the figure shows the time domain acceleration signal that might result from an impact on the example structure. The lower part of the figure shows a “blow-up” of the initial part of the signal, including the pretrigger data. The lower part also shows the effect of sampling of the signal. Two different sampling are shown and labeled signals A and B. In signal A, the sampling is taken in such a way that a sample is taken at the exact time of impact, $t = 0$. In signal B, a sample is not taken exactly at $t = 0$, but shortly before and after. Certainly, in real life, signal B is more typical. The implication of such sampling effect on our modal analysis technique is described below.

One way to attempt to remove the phase taper is to remove some of the pretrigger information. This can be done by simply removing the first few samples of the acceleration signal. (The right hand side of the signal will have to be padded with zeros to keep the record length constant.) The sets of three graphs in Figure 4.9 show the amount of phase taper that is created when various numbers of pretrigger samples are included in the time domain signal A. The top set of graphs shows that a *negative* phase taper is created by including pretrigger samples. The bottom set of graphs shows that a *positive* phase taper is created by removing too many pretrigger samples. The middle set of three graphs shows the expected result when no pretrigger samples are included, there is no phase taper and the circles in the Nyquist plot all line up with $\pm 90^\circ$. But this was for signal A. Figure 4.10 show the results for signal B. The results are similar to the previous case, except now there is no sample at $t = 0$. In this case, no matter how many pretrigger samples are included, the linear phase taper can never be fully

linear phase taper, the taper cancels out when the acceleration FFT is divided by the force FFT.

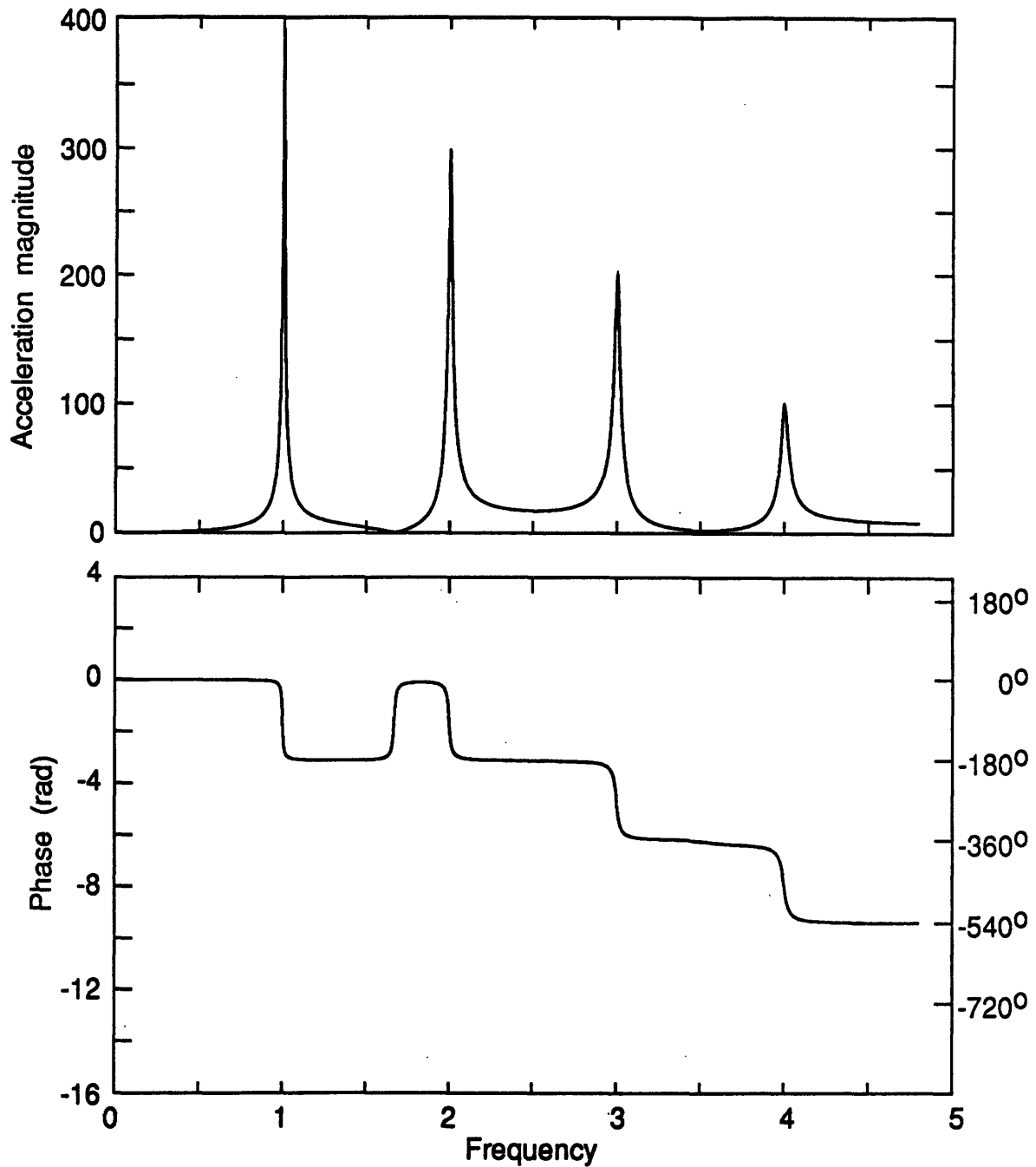


Table of modal parameters

Frequency (Hz), f_r	1	2	3	4
loss factor, η_r	0.01	0.01	0.01	0.01
Modal constant, r_{jk}	-4	-3	2	-1

Figure 4.7: Frequency response and modal constants for an example system used to illustrate the effect of pretrigger information on phase signals.

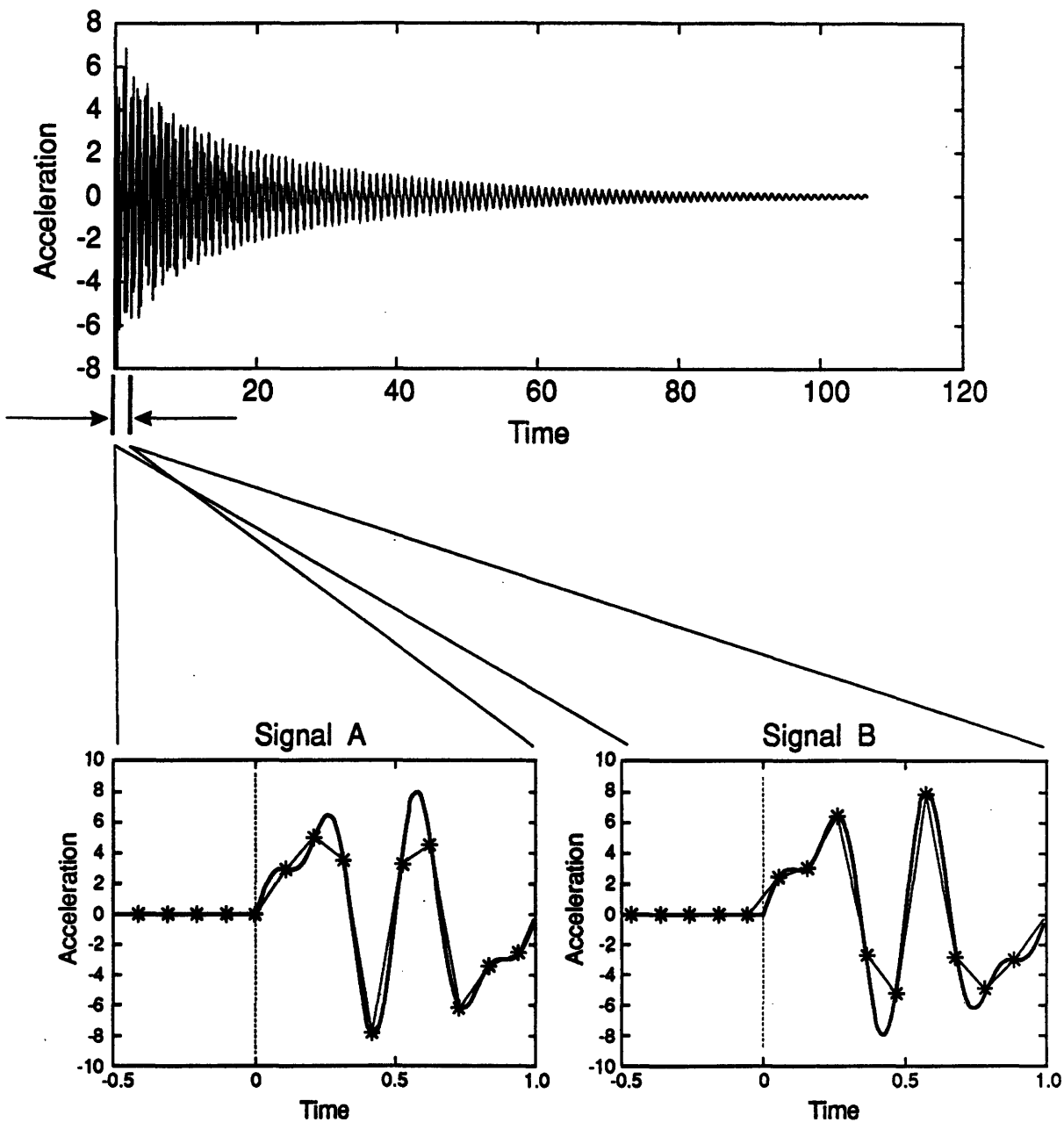


Figure 4.8: Acceleration signal showing the effects of the sampling of the signal. Note that in signal A, a sample is taken at time $t = 0$. For signal B, however, a sample is only taken slightly before and after $t = 0$.

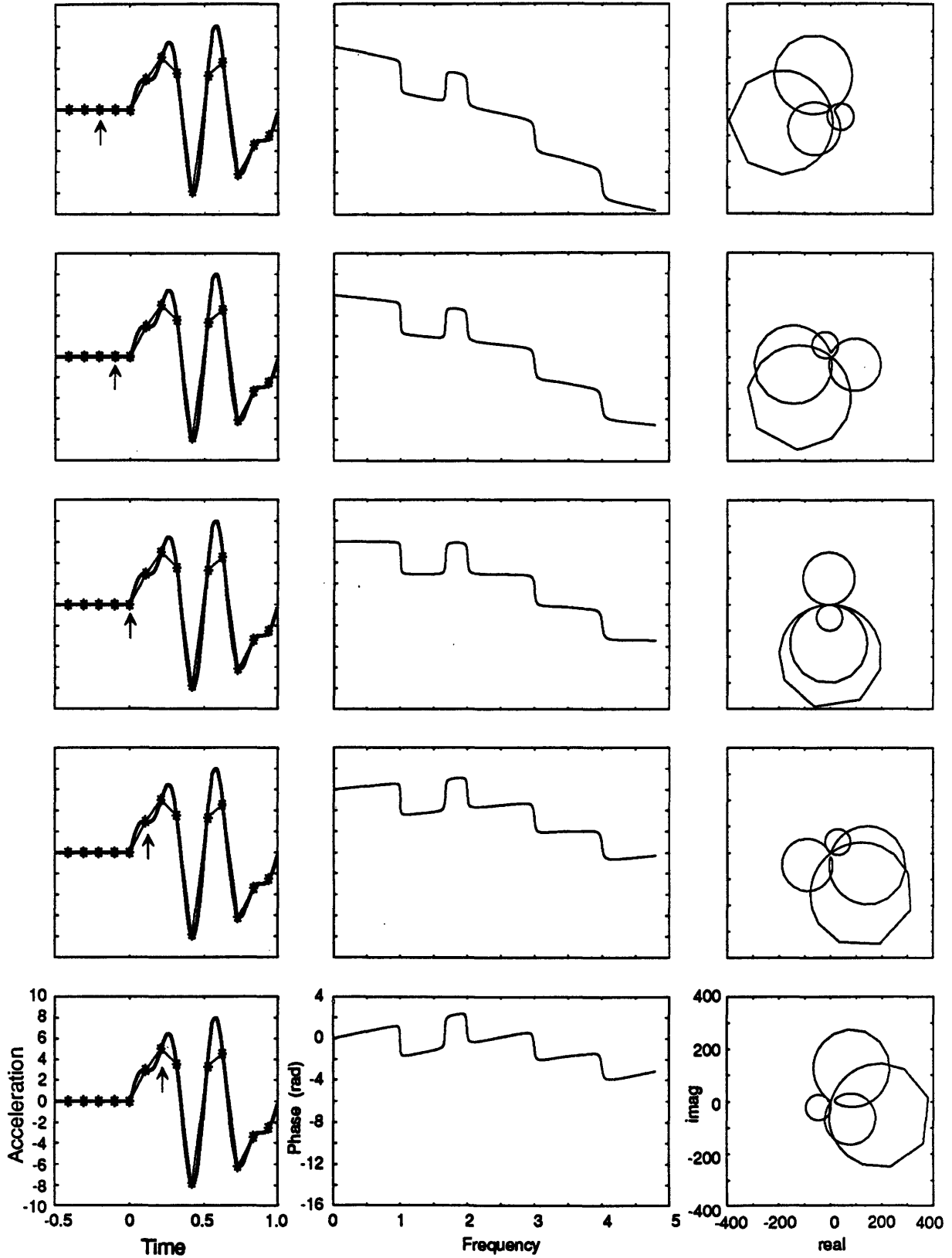


Figure 4.9: Acceleration Signal A showing the effect of shifting the origin of time, on the phase and Nyquist plots.

Note that each set of three graphs has the same scales as every other set of three graphs. The units are on the bottom set of three graphs.

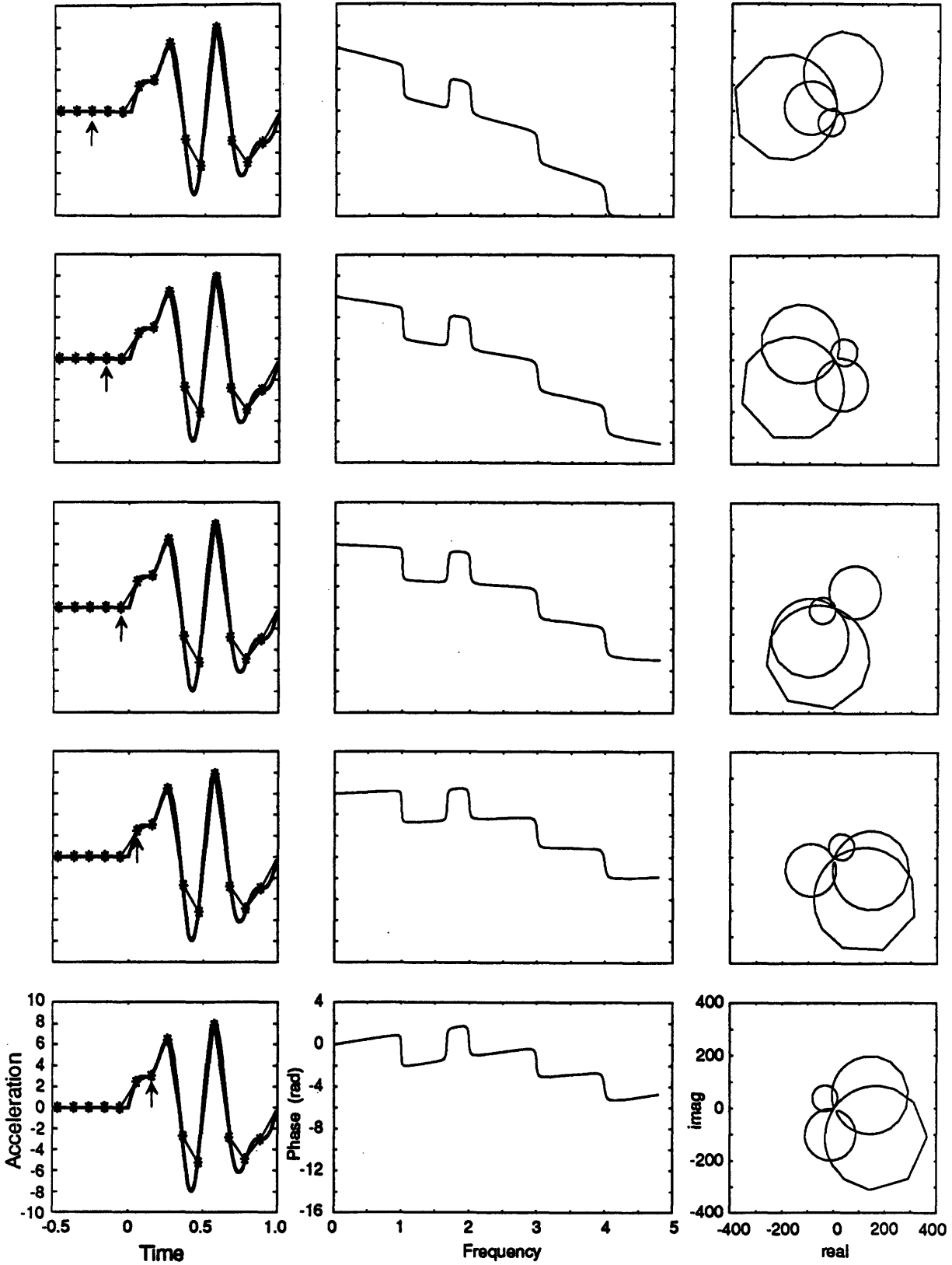


Figure 4.10: Acceleration Signal B showing the effect of shifting the origin of time, on the phase and Nyquist plots. Notice that the circles in the Nyquist plots never line up exactly at ± 90 degrees, no matter what offset time is used.

removed and the circles in the Nyquist plot never line up with $\pm 90^\circ$. It might be possible to interpolate the data in the time domain in order to exactly find $t = 0$ but it would be very difficult. In realistic acceleration signal, which have noise, it is very difficult to find the exact time when the signal begins. Overall, working in the time domain is not a good approach to removing the linear phase taper.

Another way to think about removing the phase taper, is using Bode plots in the frequency domain. This is perhaps the most obvious because the time delay of t_0 adds a phase taper of slope t_0 to the phase signal, recall the $e^{-j\omega t_0}$ term in Equation 4.14. Therefore, a simple approach might be to try to perform a linear curve fit on the phase vs frequency plot to try to determine the value of t_0 . Although this technique might work well with theoretically determined signals, such as in Figure 4.9, experimentally determined phase signals may not be appropriate for this type of curve fitting. Figure 4.11 shows the effect of adding a small amount (1% of the peak acceleration magnitude) of white noise. Although the magnitude plot is not strongly effected, the phase signal becomes very noisy, especially in the frequency ranges between the resonance peaks. Thus a small amount of noise can make removing the phase taper very difficult.

The third way to think about removing phase taper is in the frequency domain using Nyquist plots. Although most engineers have a better intuitive feel for Bode plots than Nyquist plot, Nyquist plots have some particularly nice properties for working on vibration problem. The most significant property is that for lightly damped system, the resonance peaks form circles in the Nyquist plot. As a result, the Nyquist plot emphasizes the frequency ranges near the resonance peaks, which usually have a higher signal to noise ratio than other frequencies. The fact that noise introduces very little error in the resonance peaks can be seen in the magnitude and phase plots of Figure 4.11. It is clear from this figure that the phase has the least error near the resonance peaks, thus, the frequency range near the resonance peaks is the best place to curve fit to remove the linear phase taper. Conveniently, the resonance peaks can be curve fit to a circle in the Nyquist plot.

Making use of the properties of the Nyquist plot, a procedure can be developed to remove the phase taper from the acceleration signals. This procedure is outlined in Figure 4.12. Once again, the acceleration signal from the example system is used. This time the effect of sampling is unimportant and either signal A or signal B can be used. To start the procedure off, the FFT of the acceleration signal is calculated with the pretrigger samples included, see the top of Figure 4.12. The resulting Nyquist plot consists of a set of four circles. Notice that the circles in the Nyquist plot do not line up with $\pm 90^\circ$. A circle is curve fit to the first resonance peak (it is the largest circle in this example). Since the circle should line up with $\pm 90^\circ$, enough phase taper is subtracted from the data to have the first circle line up with $\pm 90^\circ$. Lets say that the first circle has to be rotated counterclockwise through an angle of $\Delta\phi$ for it to line up with either $+90^\circ$ or -90° . Then the amount of phase taper that should be removed is,

$$\phi(\omega) = \frac{\Delta\phi}{\omega_1}\omega, \quad (4.15)$$

where ω is frequency in radians/sec and ω_1 is the natural frequency of the first resonance peak.

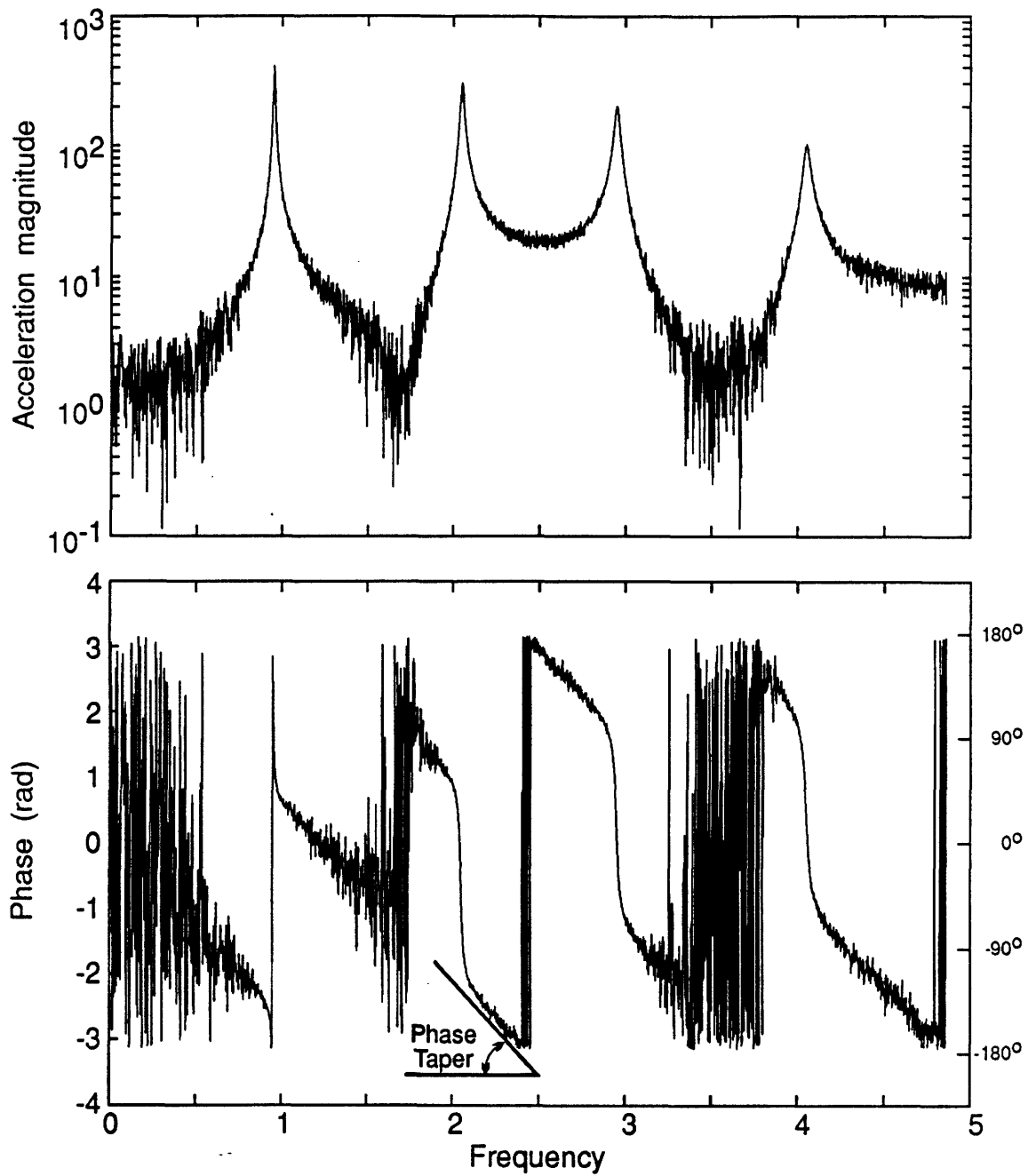
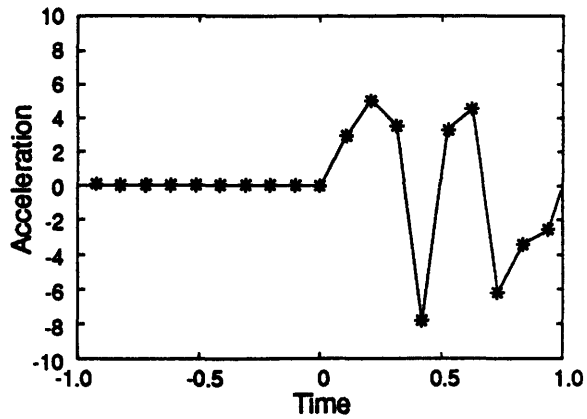
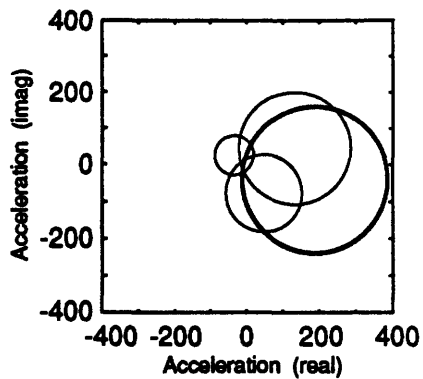


Figure 4.11: About 1% white noise has been added to the sample acceleration signal. The phase signal become particularly noisy in the regions between the resonant peaks.

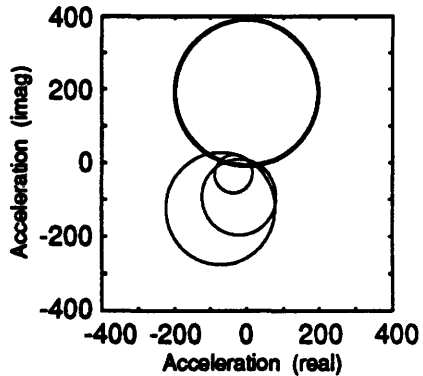
Include some of the pretrigger information in the acceleration signal. Then calculate the FFT and display it in a Nyquist plot.



Fit a circle to the first resonant peak (the largest circle in this example) and then subtract enough linear phase taper to have the circle line up with either $+90^\circ$ or -90° .



Fit circles to all the resonant peaks and calculate how close each circle is to $+90^\circ$ or -90° . If the circles do not all line up with $\pm 90^\circ$, then subtract enough linear phase to have the first resonant circle rotate 180° .



Repeat this process until all the circles line up with $\pm 90^\circ$.

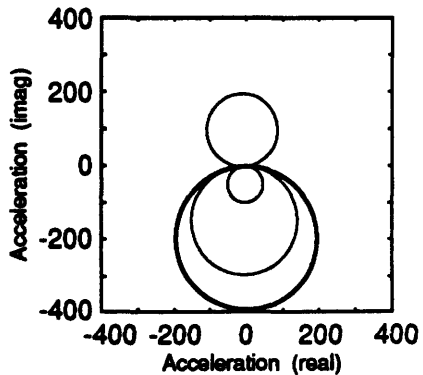


Figure 4.12: Demonstration of a procedure to remove linear phase taper from acceleration signals.

Once the phase taper $\phi(\omega)$ has been subtracted from the phase of the acceleration signal, the Nyquist diagram is replotted and circles are fit to all the resonance peaks, as shown in the third graph of Figure 4.12. If the centers of the circles of all the resonance peaks lie close to $\pm 90^\circ$, then the phase taper has been fully removed. If the peaks do not line close to $\pm 90^\circ$, then the procedure is repeated until they do. This is simply checking for consistency in the data in the Nyquist plot. For a lightly damped system, the vibration signals must be circles which line up with $\pm 90^\circ$. All the procedure does is keep subtracting a linear phase taper until this condition is reached. This procedure was found to work well with experiment data. It is very important that the phase taper be properly removed before it is used in a modal parameter extraction routine. The presence of phase taper might cause the sign (+/-) of the modal constants ${}_r A_{jk}$ to be misinterpreted. This would cause the pattern matching routine and the force identification technique to fail.

Modal Parameter Extraction

With the phase taper removed from the acceleration signals, modal parameter extraction, using the magnitude *and the phase*, can begin. As previously mentioned, a different modal parameter extraction technique will be used in this subsection than was used in the previous subsection 4.2.1. The new technique is called the circle fit method. The circle fit method has been around for a while [1]. Montalvão e Silva and Maia 1988 [35] have written an excellent review paper on the method including suggestions for speeding its implementation. Obviously, speed is important if the force identification technique is to be used as part of an in-process system. So in adapting the circle fit method for use as part of the force identification technique, every opportunity was taken to keep computation to a minimum.

It can be demonstrated that FRF's create circle-like curves in the frequency domain when plotted in a Nyquist plot. In fact, if the system exhibits structural damping, then exact circles are created in the Nyquist plot when receptance (displacement/force) is plotted. When a system is lightly damped, virtually all forms of FRF's (receptance, mobility, accelerance, and acceleration) form circles in the Nyquist plot. It is this fundamental fact that makes the circle fit technique useful for modal parameter extraction. The following discussion will use receptance $\alpha(\omega)$ as the FRF, but the technique can easily be modified for other FRF's.

When a force is applied at location k on a structure and the displacement is measured at location j , the equation for receptance is the following.

$$\alpha_{jk}(\omega) = \frac{x(\omega)}{f(\omega)} = \sum_{r=1}^n \frac{{}_r A_{jk}}{\omega_r^2 - \omega^2 + i\eta_r \omega_r^2} \quad (4.16)$$

or

$$\alpha_{jk}(\omega) = \sum_{r=1}^n \frac{{}_r C_{jk} e^{i r \phi_{jk}}}{\omega_r^2 - \omega^2 + i\eta_r \omega_r^2} \quad (4.17)$$

Here, the change from ${}_r A_{jk}$ to ${}_r C_{jk} e^{i r \phi_{jk}}$ has been made to facilitate the circle fit procedure. In this way, instead of working with the complex constant ${}_r A_{jk}$ it has been separated out into a

real modulus ${}_r C_{jk}$ and a phase angle $e^{i{}_r \phi_{jk}}$. It will be shown that the quantity ${}_r C_{jk}$ is directly proportional to the diameter of the circle in the Nyquist plot.

The frequency response function (FRF) of a structure is usually only measured over a limited range of frequencies. Under these circumstances, the modes of vibration outside the range can be modeled by including *residuals* in the receptance equation.

$$\alpha_{jk}(\omega) = \sum_{r=r_1}^{r_2} \frac{{}_r C_{jk} e^{i{}_r \phi_{jk}}}{\omega_r^2 - \omega^2 + i\eta_r \omega_r^2} + \frac{1}{K_{jk}} - \frac{1}{\omega^2 M_{jk}} \quad (4.18)$$

Here K_{jk} and M_{jk} represent the *residual* stiffness and mass of the receptance which are created by the modes outside the range of frequencies measured.

In a narrow range for frequencies around a resonance peak, the frequency response function can be approximated by the response of one mode plus a constant to account for the other modes.

$$\alpha_{jk} \simeq \frac{{}_r C_{jk} e^{i{}_r \phi_{jk}}}{\omega_r^2 - \omega^2 + i\eta_r \omega_r^2} + {}_r D_{jk} \quad (4.19)$$

The value ${}_r D_{jk}$ is a complex constant that can approximately account for the contributions of other modes in the frequency range surrounding a single resonance peak, as shown in Figure 4.13. The circle-fit procedure relies on this approximation to extract the modal parameters (${}_r C_{jk}$, ${}_r \phi_{jk}$, ω_r , and η_r) of each individual mode r .

Circle Fit Procedure

In order to fit a circle to the receptance data, it is convenient to consider the real and imaginary parts of the receptance as a set of (x_s, y_s) data pairs, as shown in Figure 4.13. The goal of the circle fit procedure is to find the circle that which best fits that data by minimizing the square of the error.

$$e_1 = \sum_{s=1}^n \left[R_0 - \sqrt{(x_s - x_0)^2 + (y_s - y_0)^2} \right]^2 \quad (4.20)$$

In other words, the circle fit procedure must find the values of x_0 , y_0 , and R_0 that make the error e_1 a minimum. The difficulty with this procedure is that Equation 4.20 cannot be manipulated to create an explicit calculation for the values of x_0 , y_0 , and R_0 . As a consequence, an iterative procedure must be used for solving this equation. This is very time consuming and not appropriate for the real time needs of the force identification technique.

This difficulty can be overcome if a non-least squares error function is used[35]. A small change in the error function in Equation 4.20 leads to a new error function.

$$e_2 = \sum_{s=1}^n \left\{ R_0^2 - [(x_s - x_0)^2 + (y_s - y_0)^2] \right\}^2 \quad (4.21)$$

This equation can be rewritten to form,

$$e_2 = \sum_{s=1}^n \left\{ c - [x_s^2 + ax_s + by_s + y_s^2] \right\}^2 \quad (4.22)$$

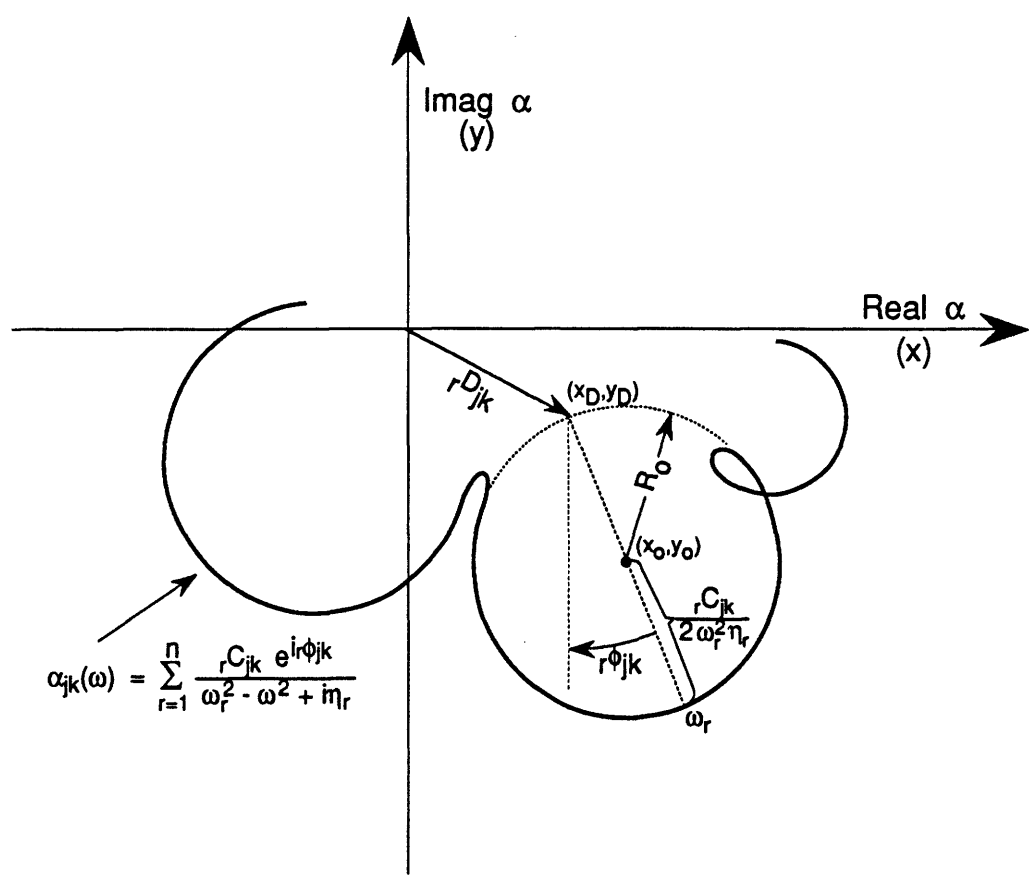


Figure 4.13: Nyquist plot of receptance showing the circle-fit method. (After Montalvão e Silva and Maia 1988.)

where

$$a = -2x_0, \quad b = -2y_0, \quad c = R_0^2 - x_0^2 - y_0^2. \quad (4.23)$$

The new error function can be minimized relative to the parameters, a , b , and c , leading to a matrix equation for the circle fit process.

$$\begin{bmatrix} \sum x_s^2 & \sum x_s y_s & -\sum x_s \\ \sum x_s y_s & \sum y_s^2 & -\sum y_s \\ -\sum x_s & -\sum y_s & n \end{bmatrix} \begin{Bmatrix} a \\ b \\ c \end{Bmatrix} = \begin{Bmatrix} -(\sum x_s^3 + \sum x_s y_s^2) \\ -(\sum y_s^3 + \sum x_s^2 y_s) \\ \sum x_s^2 + \sum y_s^2 \end{Bmatrix} \quad (4.24)$$

or

$$[Af]\{Xf\} = \{Bf\} \quad (4.25)$$

Hence, the values of a , b , and c in the vector $\{Xf\}$ can be determined from a matrix inversion.

$$\{Xf\} = [Af]^{-1}\{Bf\} \quad (4.26)$$

Then the values of x_0 , y_0 , and R_0 can be determined from

$$x_0 = \frac{a}{-2}, \quad y_0 = \frac{b}{-2}, \quad R_0 = \sqrt{c + x_0^2 + y_0^2}. \quad (4.27)$$

The resulting values for x_0 , y_0 , and R_0 represent the best circle that fits the data (x_s, y_s) according to the new error function e_2 . The important advantage of the new error function e_2 over the least squares error function e_1 is that it can be calculated directly without the expense of iterative procedures. It can be shown that new error function e_2 does not fit the data as well as the least squares error function e_1 [35]. However, the difference in the results from the two error functions is very small and in practice the new error function works about as well as the least square error function.

Determining Resonance Frequency

Determination of the precise location of the resonance frequency is important to the circle fit procedure of modal parameter extraction. It is not enough to simply find the frequency at which the magnitude of the receptance is a maximum. In fact, this is a very poor estimate of the resonance frequency. A preferred technique is to use the frequency spacing technique. The phase angle of the receptance for a single mode, excluding the effect of the residual rD_{jk} , is the following.

$$\theta_r = \tan^{-1}\{\eta_r/[1 - (\omega/\omega_r)^2]\} \quad (4.28)$$

It can also be shown that $d(\omega^2)/d\theta_r$ is a minimum when $\omega = \omega_r$; i.e.,

$$\frac{d}{d\omega} \left[\frac{d(\omega^2)}{d\theta_r} \right] = 0 \Rightarrow \omega = \omega_r. \quad (4.29)$$

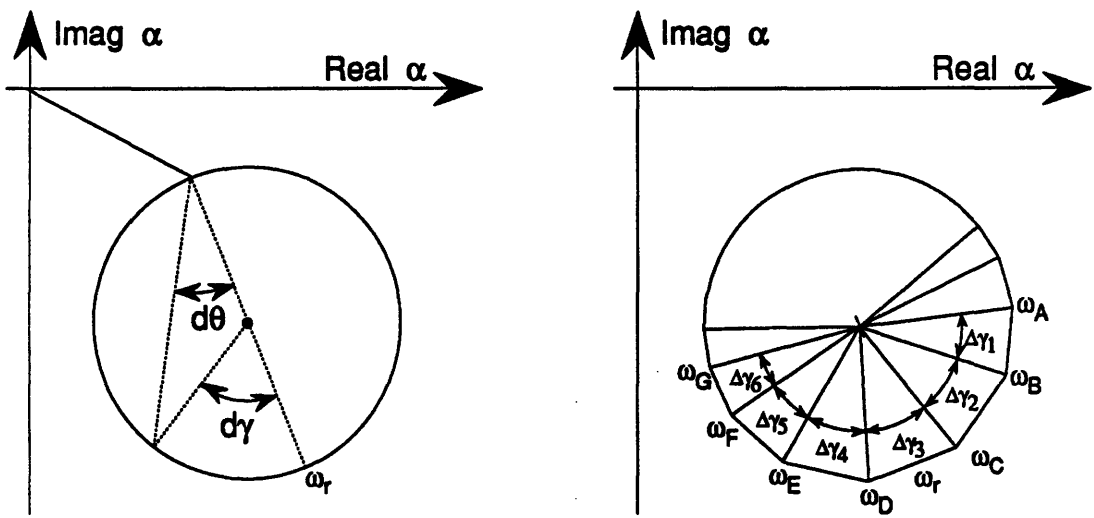


Figure 4.14: The resonance frequency, ω_r , occurs at the minimum of $d\omega^2/d\gamma$. (After Montalvão e Silva and Maia 1988.)

Frequency	γ	$\Delta\gamma$	$\Delta^2\gamma$
ω_A	γ_1		
ω_B	γ_2	$\Delta\gamma_1$	$\Delta^2\gamma_1$
ω_C	γ_3	$\Delta\gamma_2$	$\Delta^2\gamma_2$
ω_D	γ_4	$\Delta\gamma_3$	$\Delta^2\gamma_3$
ω_E	γ_5	$\Delta\gamma_4$	$\Delta^2\gamma_4$
ω_F	γ_6	$\Delta\gamma_5$	$\Delta^2\gamma_5$
ω_G	γ_7	$\Delta\gamma_6$	

Table 4.1: Finite difference table for determining the location of the natural frequency.

In words, this means that the phase angle of the receptance is changing most rapidly when the frequency is equal to the resonance frequency. This is probably fairly obvious when looking at the phase plot of a Bode plot. The phase angle quickly drops 180° at resonance.

It is evident from Figure 4.14, that minimizing $d(\omega^2)/d\theta_r$ is equivalent to minimizing $d(\omega^2)/d\gamma$. One way to locate the resonance frequency, when the frequency spacing is fixed (always the case when the receptance is determined by an FFT), is to construct a table of finite differences as shown in Table 4.1. There will be a change in sign of $\Delta^2\gamma$ when the frequency is equal to the resonance frequency. In this way it can be determined between which two data points the resonance frequency occurs. Unfortunately, with lightly damped systems, the points along the circle are widely spaced and there is still significant uncertainty of the location of the resonance frequency.

One way to reduce this uncertainty is to create a second order interpolation function using Newton's divided differences formula.

$$f(v) = f(v_0) + (v - v_0)f(v_0, v_1) + (v - v_0)(v - v_1)f(v_0, v_1, v_2) + \dots + (v - v_0)(v - v_1) \dots (v - v_{n-1})f(v_0, v_1, v_2, \dots, v_n), \quad (4.30)$$

where

$$f(v_0, v_1, v_2, \dots, v_n) = \frac{f(v_0, v_1, v_2, \dots, v_{n-1}) - f(v_1, v_2, \dots, v_n)}{v_0 - v_n} \quad (4.31)$$

For the current purposes $v = \omega^2$ and $f(v) = \theta(\omega^2)$, where θ is the phase angle. If one is looking to minimize $d(\omega^2)/d\theta$, this is equivalent to trying to maximize $d\theta/d(\omega^2)$ or $df(v)/dv$. If two data points are selected from before the resonance and two are selected from after the resonance, then it can be shown [35] that Equation 4.30 can be maximized by,

$$v = \frac{1}{3}[(v_0 + v_1 + v_2) - f(v_0, v_1, v_2)/f(v_0, v_1, v_2, v_3)]. \quad (4.32)$$

Thus by using Equation 4.32 and four data points from the receptance, the value of ω^2 can be determined by a second order interpolation.

Accurate location of the natural frequencies ω_r is very important since correct determination of the loss factors η_r (and subsequently the modal constants ${}_r C_{jk}$) is strongly dependent on the value of natural frequencies used.

Determination of Loss Factors η_r

Determination of the loss factor can be made by considering Equation 4.28 and Figure 4.15. If one considers two data points, one below the resonance frequency at ω_a and one above at ω_b , then the following equations can be written.

$$\tan(\gamma_a/2) = [1 - (\omega_a/\omega_r)^2]/\eta_r \quad (4.33)$$

$$\tan(\gamma_b/2) = [1 - (\omega_b/\omega_r)^2]/\eta_r \quad (4.34)$$

These equations can be combined into a single equation for determining the loss factor.

$$\eta_r = \frac{\omega_b^2 - \omega_a^2}{\omega_r^2} \frac{1}{\tan(\gamma_a/2) + (\gamma_b/2)} \quad (4.35)$$

It can be seen that this equation become the familiar formula for the halfpower relationship when $\gamma_a = \gamma_b = 90^\circ$

Obviously, one can choose from many different points a and b . This fact can be used to check for consistency in the value of loss factor η_r calculated. If one takes the five points below the resonance frequency and the five points above the resonance frequency, then twenty five values of η_r can be calculated. These values can be conveniently displayed in a three dimensional plot as shown in Figure 4.15. A little bit of variation in the calculated values of η_r is probably only an indication of some variation in the measured data. However, a systematic trend in the 3-D plot (such as a slope) is probably an indication that value of ω_r was not determined accurately. In the absence of any systematic errors in the 3-D plot, the average value of all the loss factors calculated can be taken to be the "true" value of η_r .

Determination of the Modal Constant

With the values of natural frequencies ω_r and loss factors η_r determined, calculation of the modulus ${}_r C_{jk}$ and phase angle ${}_r \phi_{jk}$ is easy. As shown in Figure 4.13, the value of ${}_r C_{jk}$ can be determined by,

$${}_r C_{jk} = 2R_0 \omega_r^2 \eta_r, \quad (4.36)$$

where $2R_0$ is the diameter of the circle. Also, ${}_r \phi_{jk}$ can be determined from

$${}_r \phi_{jk} = \tan^{-1}\{(x_0 - x_D)/(y_0 - y_D)\}, \quad (4.37)$$

where x_D and y_D are the values of the displaced origin as shown in Figure 4.13. In lightly damped systems, the value of ${}_r \phi_{jk}$ is always close to $\pm 90^\circ$.

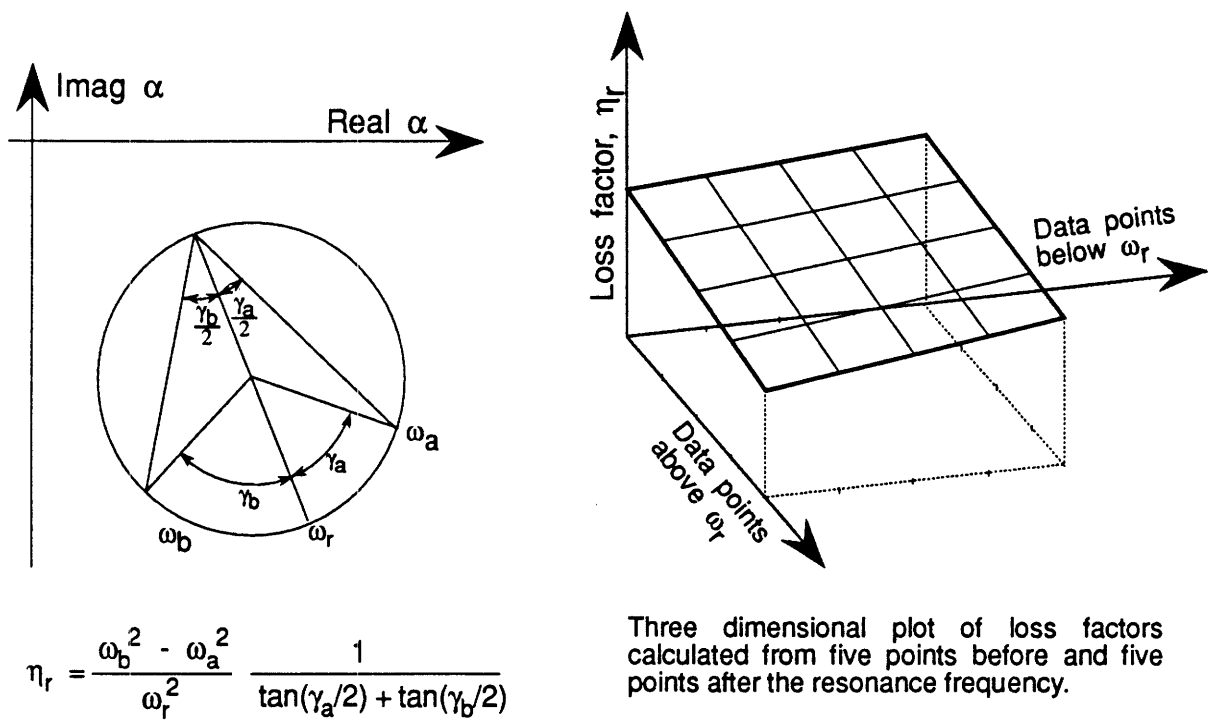


Figure 4.15: Determination of loss factor, η_r (After Montalvão e Silva and Maia 1988.)

Summary

The procedure of the circle-fit method can be summarized by the following steps,

1. Fit a circle to the data points near a resonance peak to determine x_0 , y_0 , and R_0 .
2. Find the approximate location of the resonance frequency by using a table of finite differences.
3. Accurately determine the location of the resonance frequency by using an interpolation function of $\theta(\omega^2)$.
4. Determine the value of the loss factor η_r using a few points before and after the resonance.
5. Calculate the modulus ${}_r C_{jk}$ and phase angle ${}_r \phi_{jk}$ using the location and size of the circle.

Although the circle-fit procedure seems very complicated, there is very little computation involved. The only computationally intensive operation of the five steps listed above, is fitting a circle to each resonance peak. Even this step is not as bad as it seems because only a few data points (perhaps 10 - 50) are used in each circle fit. As a result, the extraction of the modal parameters can probably be done in less time than the computation of the FFT.

It can be seen that the circle-fit modal parameter extraction method is quite different than the procedure used in Subsection 4.2.1 where only the magnitude was used. The circle-fit method requires that damping be included in the model, whereas the previous technique assumed no damping. The biggest advantage of the circle-fit method is that it only uses data from near the resonance peaks. This data is usually of the highest quality, especially for impact testing. The biggest problem with the circle-fit procedure is that the determination of the value of the modulus ${}_r C_{jk}$, or modal constant ${}_r A_{jk}$, is strongly dependent on the accuracy with which the natural frequency, ω_r and loss factor η_r are determined. As a result, small errors in ω_r and η_r tend to propagate into larger errors in ${}_r A_{jk}$. Overall the circle-fit procedure is computationally efficient, but may not be as accurate as other methods.

4.3 Pattern Matching

Once the modal constants have been extracted from the acceleration signals, the next step in the force identification technique is to use pattern matching to determine the location of the source and its magnitude. The task of the pattern matching is to compare a set of extracted modal constants (from an impact at an unknown location) with a database of modal constants from impacts at many locations on the structure. The best match will indicate the most likely impact location.

The subject of pattern matching has been around for many years and is quite well developed. Books such as Tou's *Pattern Recognition Principles*[2] provide a good introduction to the basic principles of pattern matching and its applications. Common applications include finger print

matching, reading the numbers off checks, and receiving data over a computer modem. It is important to realize that there is one very significant difference between the last two examples and the first. In the cases of reading checks and receiving data, the source is created and controlled by humans, even if the noise introduced is outside of human control. As a result, an important part of pattern matching, in these cases, is to devise a set of patterns (e.g. the way that the check numbers are written) which are easily distinguishable from each other even in the presence of noise. Thus the nature of pattern matching for these types of problems is very different from problems such as finger print matching. In finger print matching, much of the effort goes into determining the appropriate features of the finger print to use in the pattern matching. Obviously, many features of finger prints are very similar from one person to the next, such as size and spacing of the ridges. The biggest advancement in finger print matching was the discovery that the locations of the beginnings and ends of the ridges on the finger, are unique to every individual. Thus, in pattern matching problems where the features cannot be controlled, finding an appropriate set of features to use in the pattern matching is vital to the success of the technique.

In the case of the force identification problem, the features of the vibration signal cannot usually be manipulated for the purposes of improving the ability to distinguish between different impact locations. The features of the vibration signal are governed by the dynamics of the structure and it is unlikely that the designers of the structure will be willing to change the structure simply to improve pattern matching. In fact, it seems unreasonable to think that the structure should be modified just for this purpose. Therefore, the best that can be done is to extract the features of the vibration signal that best distinguish between sources at different locations. As was seen in Chapter 3, the modal constants rA_{jk} are the only modal parameters that have strong variation with impact location, and as a result, they are the only reasonable choice as features for the pattern matching.²

Once the choice of features has been decided, one must still choose from the many different pattern matching techniques available. Methods available range from the classical Bayesian estimation techniques to modern methods such as neural networks and adaptive (self-adjusting) techniques. It is not the objective of this thesis to determine the best pattern matching technique, or get involved with the subtleties of these techniques. The main objective is to determine whether or not pattern matching can be combined with modal parameter extraction to properly identify input force magnitude and location. For this reason, a very simple approach is taken to pattern matching.

The first step in the pattern matching is to assemble a database of modal constants for all impact (source) locations of interest. It will probably be the case that there is a continuous

²The way the impact problem is studied here is as a vibration problem and the only vibration parameter that changes significantly with impact location is the modal constant rA_{jk} . If the impact problem was treated as a wave propagation problem, then different features could be used in the pattern matching. In wave propagation problem, the relative arrival times of different waves could be used as a feature to distinguish different impact locations. This approach was not taken in this thesis because of the difficulties involved in getting good data of initial wave arrival, particularly in the presence of noise.

range of locations that are of interest. The database need not contain a very large number of source locations. There only needs to be enough source locations so that the spatially varying nature of the modal constants is clear. Once this condition has been satisfied, then the modal constants for the other source locations can be determined by interpolation.

The database of modal constants can be determined either from an FEM model (if it has been verified to be of good quality) or from experimental modal tests. The experimentally determined modal constants are probably preferable because they are less likely to be in error. The database of modal constants can be represented by the following matrix.

$$\begin{bmatrix} 1A_{j1} & 1A_{j2} & 1A_{j3} & \dots & 1A_{jm} \\ 2A_{j1} & 2A_{j2} & 2A_{j3} & \dots & 2A_{jm} \\ 3A_{j1} & 3A_{j2} & 3A_{j3} & \dots & 3A_{jm} \\ \vdots & \vdots & \vdots & \ddots & \vdots \\ nA_{j1} & nA_{j2} & nA_{j3} & \dots & nA_{jm} \end{bmatrix} \quad (4.38)$$

Recall that the r subscript on ${}_r A_{jk}$ indicates the vibration mode, j indicates the node of the sensor location, and k is the force input location. So in the database of Equation 4.38, there are n modes being measured, m different impact locations of interest, and the sensor is fixed at node j . Each column in this matrix represents the modal constants extracted from a test at one force input location. These columns can be thought of as patterns or sets of features of the vibration signals. Each row in the matrix represents the mode shape (or eigenvector) for the r th mode.

When a vibration signal is acquired, the modal constants must be extracted (using the one of the techniques from subsections 4.2.1 or 4.2.2) before the pattern matching can be used. Also recall that because the force signal is not measured, only the uncorrected modal constants, ${}_r A_{jk}^*$ can be extracted. Also recall that the uncorrected modal constants are related to the modal constants by the following relationship.

$$\begin{Bmatrix} 1A_{jk} \\ 2A_{jk} \\ 3A_{jk} \\ 4A_{jk} \\ 5A_{jk} \end{Bmatrix} F_k = \begin{Bmatrix} 1A_{jk}^* \\ 2A_{jk}^* \\ 3A_{jk}^* \\ 4A_{jk}^* \\ 5A_{jk}^* \end{Bmatrix} \quad (4.39)$$

or

$$\{{}_r A_{jk}\} F_k = \{{}_r A_{jk}^*\} \quad (4.40)$$

Here, F_k is the magnitude of the source (impact) force which is unknown but approximately a constant for the frequency range of interest.

For the pattern matching, the column vector on the right hand side of Equation 4.39 $\{{}_r A_{jk}^*\}$ must be compared with each column vector in the database of Equation 4.38. The simplest way to make this comparison (or match patterns) is to use a linear regression formulation.

$$F_i = (\{{}_r A_{ji}\}^T \{{}_r A_{ji}\})^{-1} \{{}_r A_{ji}\}^T \{{}_r A_{jk}^*\} \quad (4.41)$$

The vector $\{rA_{ji}\}$ is the i th column of the database in Equation 4.38 and $\{rA_{ji}\}^T$ is the transpose of this vector. The error in the fit can be determined from the following.

$$\{e\} = \{rA_{ji}\}F_i - \{rA_{jk}^*\} \quad (4.42)$$

or

$$e_i = \|\{e\}\|^2 = \{e\}^t\{e\} \quad (4.43)$$

The column of the database that produces the least error e_i indicates that i is the most probable location of the force source and F_i is the estimate of the magnitude of the input force F_k .

$$\text{minimum}(e_1, e_2, e_3, \dots, e_m) \Rightarrow F_k \quad (4.44)$$

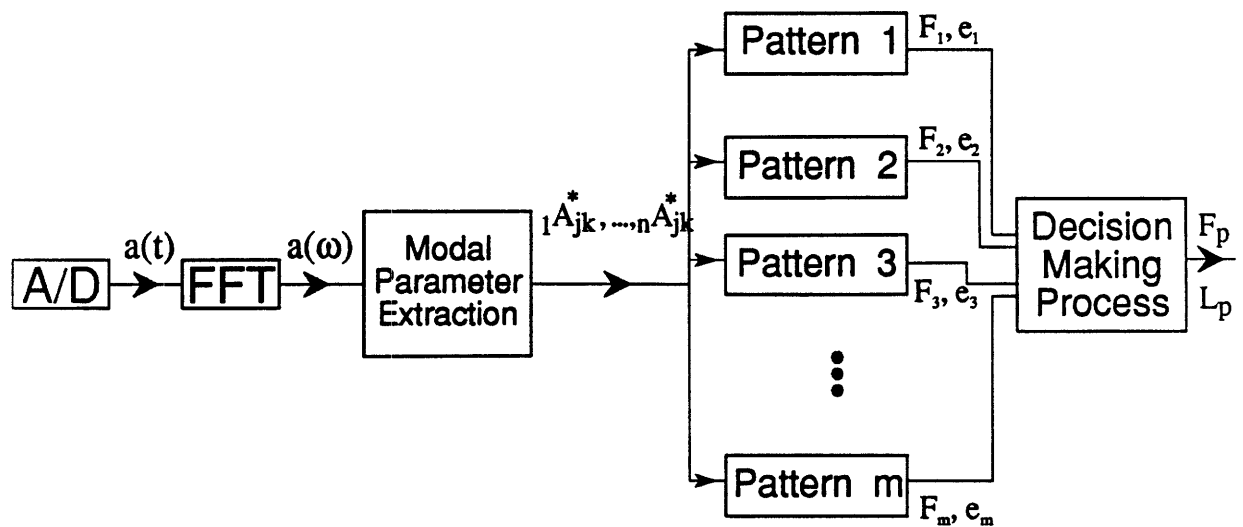
If the pattern matching is to be reliable, it is important that there be a significant difference between the minimum error e_i and the next to least error. If these two values of error are close in magnitude then confusion could arise over the predicted source location.

4.4 Summary

The overall force identification process can be described as follows. A sensor location j must be chosen and remain fixed throughout the whole process. Then, modal tests must be performed at all the likely input locations k to build a database of modal constants. Once the database is assembled then the force identification technique is ready to be used.

When a source event occurs (e.g. an impact), the resulting vibration signal $a(t)$ is acquired, as shown in Figure 4.16. The time domain signal $a(t)$ is then converted to a frequency domain signal $a(\omega)$ using a fast Fourier transform (FFT). Next, the uncorrected modal constants rA_{jk}^* are extracted from $a(\omega)$ using either the magnitude only modal parameter extraction technique or the magnitude and phase technique. The extracted uncorrected modal constants are then compared with the patterns of modal constants in the database. The pattern that is most similar (in a least squares sense) to the extracted uncorrected modal constants, indicates the most likely input location and the force magnitude F_k .

The next chapter will demonstrate the use of the force identification technique in one particular application, glide height testing. A discussion of the robustness and limitations of the force identification technique will be presented after its use is demonstrated.



Symbol	Description
$a(t)$	Time domain acceleration signal
$a(\omega)$	Frequency domain acceleration signal
${}_1A_{jk}^*, \dots, {}_nA_{jk}^*$	Extracted uncorrected modal constants
F_1, \dots, F_m	Impact force from pattern match
e_1, \dots, e_m	Error in pattern match
F_p	Predicted impact force
L_p	Predicted impact location

Figure 4.16: Block diagram of force identification process. The different patterns in the database are the modal constants ${}_rA_{jk}$ for m different source locations.

Chapter 5

Application to Glide Height Testing

5.1 The Use of Force Identification in Glide Height Testing

One application where direct measurement of impact force is not possible is in glide height testing. As the glide head (slider) flies over the surface of the disk, it may encounter an asperity which is too large to fly over. This situation will result in an impact between the bottom of the slider rails and the asperity. Asperity impacts are likely to occur at many different locations along the bottom of the slider rails. Thus, the impact location (position on the rail) is not known a priori. Since no one has figured out how to put an array of force sensors along the slider rails, we are faced with complication of trying to “back calculate” the impact force and location from vibration signals.

The glide height testing problem fits the basic requirements of the force identification technique. The input force is a short duration pulse, i.e. it is an impact between the slider and an asperity. Although the time duration of the impact cannot be directly measured, experimental data indicates that it is of short enough duration to excite the five lowest vibrational modes of the slider, i.e. up to 1 MHz in frequency. Even though it was the goal of this thesis to use the force identification technique on actual glide height tests with the slider, it was simply too difficult to conduct the experiments, as was discussed in Chapter 3. Even the use of the ball drop technique with the small slider proved difficult, when it was found that the repeatability of the small ball impact was very poor. As a result, all the experimental results in this chapter were performed with ball drop tests on the enlarged slider. The enlarged slider is a scaled model of the actual slider and the results should be representative of the results that would have been obtained with the actual slider, if the tests could have been performed.

The next two sections of this chapter, will present experimental data from force identification studies on the enlarged slider. The first section uses the magnitude only modal parameter extraction technique and the next section uses the magnitude and phase modal parameter extraction technique. After the two techniques are presented a discussion is given of the relative merits of the two techniques and what might be done to improve the techniques.

5.2 Results of the Magnitude Only Technique

The experimental setup for conducting the ball drop tests on the enlarged slider is shown in Figure 5.1. Fourteen equally spaced locations were marked along the middle of one of the slider rails. The marks are 12.7 mm (1/2") apart and are used at the locations for the input force, i.e. ball impact. The impact force is created by dropping a 6.35 mm (1/4") nylon ball through a copper guide tube onto the locations marked on the slider rail. In order to vary the magnitude of the impact force, three different length copper tubes were used. The tubes were 76, 152, and 305 mm (3, 6, and 12") long. The impact force created from the impact of the nylon balls can be predicted from Hertzian contact theory, as shown in Figure 5.2. The forces were experimentally verified by procedure outlined in Chapter 3. The magnitude of the impact forces created by the ball drop are related to the square root of the height of the ball drop. This is because the impact velocity $v = \sqrt{mgh}$. As a result, the relative magnitude of the impact forces are 1, 0.707, and 0.5 for the 305, 152, and 76 mm drop heights respectively, as can be seen from Figure 5.2.

The vibration signal is measured from an accelerometer mounted on the back of the slider, see Figure 5.1. The accelerometer is model 303A made by PCB Corp. The output signal from the accelerometer is sent to the PCB power unit model 480A10. Then the signal is passed through a Tektronix AM502 differential amplifier then filtered by Krohn-Hite 3202 filter which was set as a 12 pole low pass filter at 22 KHz. Finally, the signal is acquired by a Compaq 386 computer using Metrabyte 12-bit DASH-16 board and Unkelscope software. The Metrabyte board was set to acquire 8192 samples at 50 KHz. After each test the acceleration data was stored on the hard disk for future (off-line) processing.

Before the force identification technique could be used, a database of modal constants had to be assembled. To do this, a series of 14 tests were run by dropping the ball from 305 mm (12") onto each of the 14 locations marked on the enlarged slider. The frequency response functions (accelerance) for each of the 14 tests were calculated using the acceleration signal and the theoretically predicted force signal. The modal constants ${}_r A_{jk}$ were extracted from the frequency response functions to create a database. Only the first five vibration modes were included in the database. The resulting database is a 5×14 matrix.

$$\begin{bmatrix} 1A_{j1} & 1A_{j2} & 1A_{j3} & 1A_{j4} & \dots & 1A_{j14} \\ 2A_{j1} & 2A_{j2} & 2A_{j3} & 2A_{j4} & \dots & 2A_{j14} \\ 3A_{j1} & 3A_{j2} & 3A_{j3} & 3A_{j4} & \dots & 3A_{j14} \\ 4A_{j1} & 4A_{j2} & 4A_{j3} & 4A_{j4} & \dots & 4A_{j14} \\ 5A_{j1} & 5A_{j2} & 5A_{j3} & 5A_{j4} & \dots & 5A_{j14} \end{bmatrix} \quad (5.1)$$

The subscript j in this matrix is the location of the accelerometer and the numbers 1 - 14 are the input locations along the slider rail. Because the magnitude only modal parameter extraction technique was used on the data, the sign (+/-) of the extracted modal constants might not be correct. For this reason, the modal constants in the database are all made to be positive.

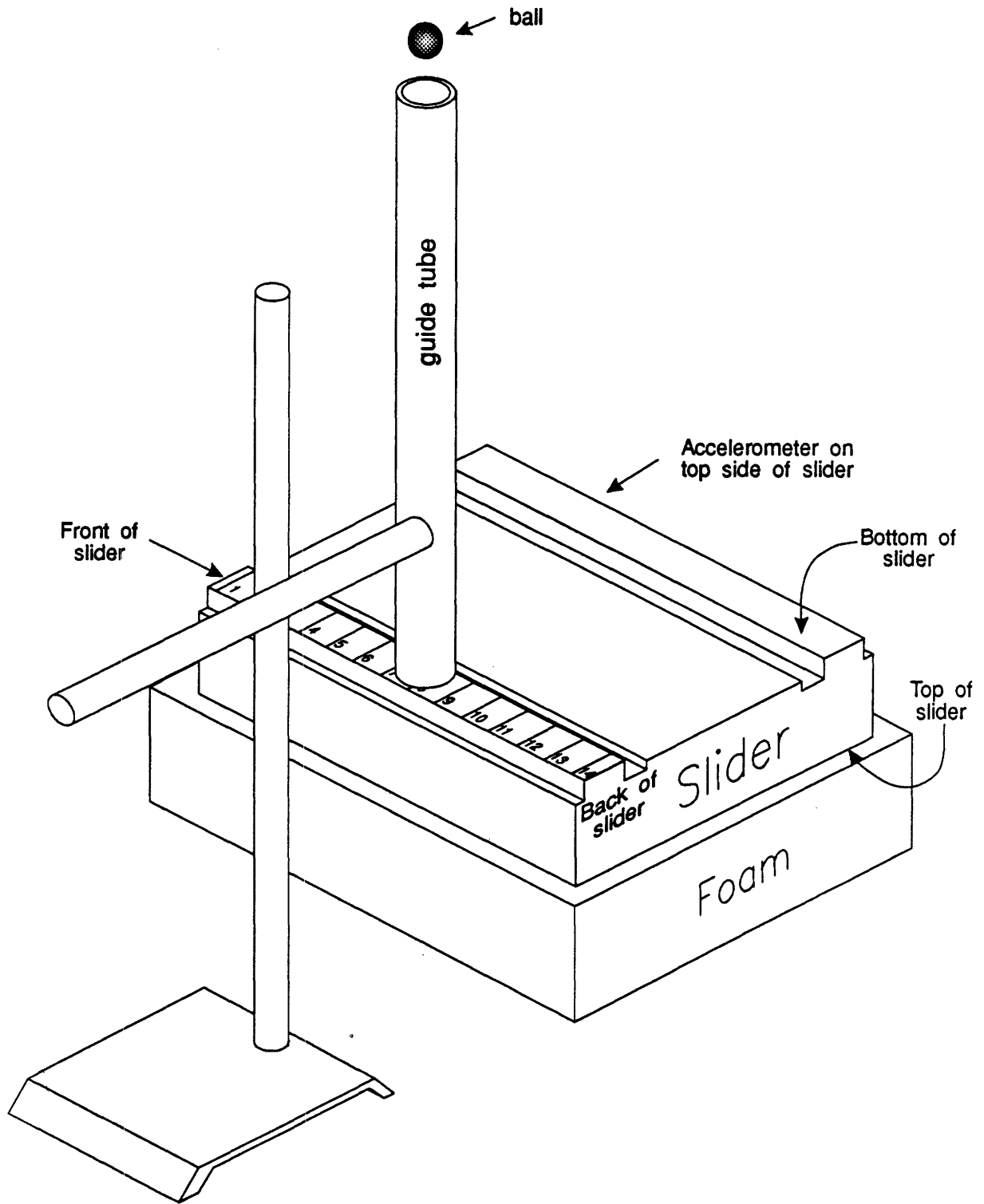


Figure 5.1: Schematic of ball drop test apparatus used for testing the force identification technique. Guide tubes of 76, 152, and 305 mm can be used.

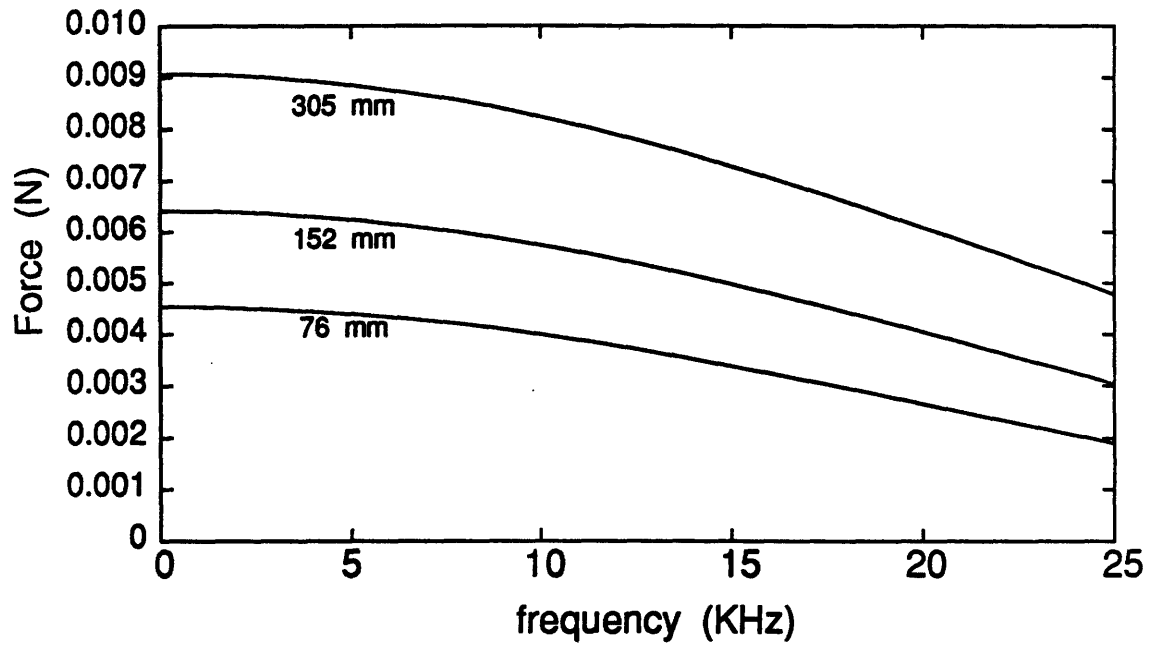
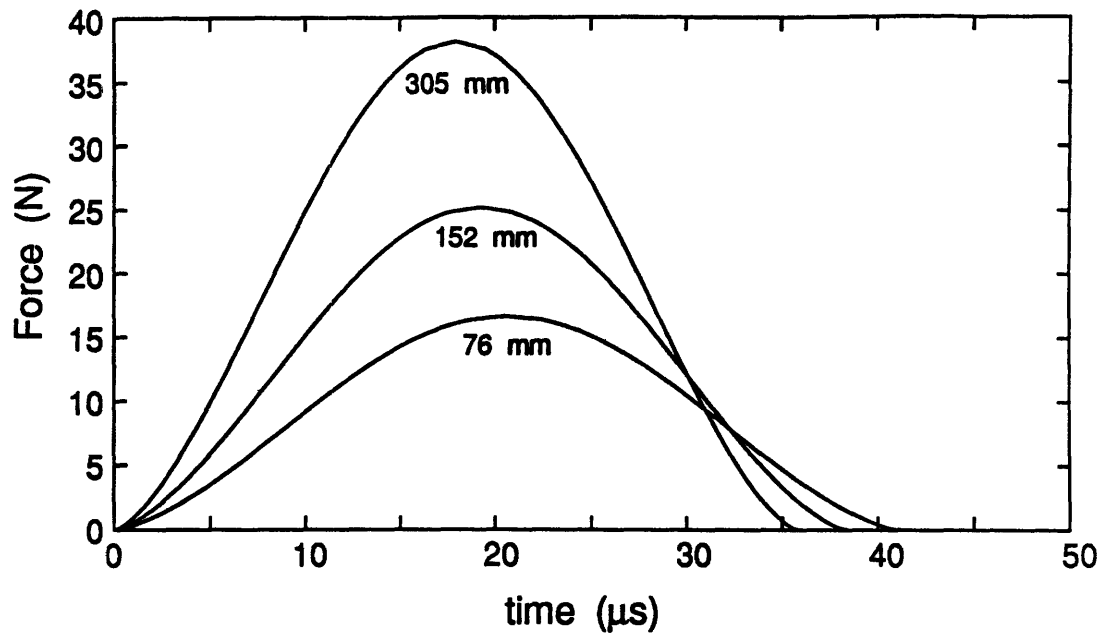


Figure 5.2: Hertz contact forces created by a 6.35 mm nylon ball dropped from 76, 152, and 305 mm height. Note that the FFT data is based on 50 KHz sampling frequency and 8192 data points.

Once the database was constructed, the force identification technique could be tested. A new series of tests were performed on the enlarged slider. The 6.35 mm nylon ball was dropped from 76, 152, and 305 mm height onto the first seven locations marked on the slider. (Locations 8-14 were not tested to reduce the number of tests required.) The acceleration signals were acquired the same way as before. This time, however, the acceleration was not calculated. It was assumed that neither the location nor the magnitude of the input force was known. The acceleration signals were transformed into the frequency domain using an FFT and the uncorrected modal constants rA_{jk}^* were extracted using the magnitude only modal parameter extraction technique. Once again, since the sign (+/-) of the uncorrected modal constants might not be correct, so all the uncorrected modal constants were made to be positive.

Once the uncorrected modal constants, from a single test, were extracted, they were run through the pattern matching process. Figure 5.3 illustrates the pattern matching process using a series of graphs. The fourteen graphs on the left represent the database of modal constants. The one graph on the right represents a set of uncorrected modal constants extracted from an impact at a certain location along the slider rail. The pattern matching must compare the one graph on the right to the fourteen graphs on the left to determine the most likely impact location. The force of the impact is determined by the relative scaling (or ratio) of the matching graph to the graph at the right.

The results of the pattern matching are shown in Figures 5.4, 5.5, and 5.6 for the ball drop tests from heights of 76, 152, and 305 mm respectively. By comparing the three figures, it can be seen that the pattern matching is not affected by the drop height, or more fundamentally, the impact force. The figures show that there is a uniqueness problem in the pattern matching. This is a result of the symmetry of the slider geometry. Consequently, an impact at location 1 on the slider might be misinterpreted as an impact at location 14. The same is true for the combinations of locations 2 and 13, 3 and 12, ..., 7 and 8. If the pattern matching is limited, for a moment, to location 1-7, then the magnitude of the impact force can be estimated from the pattern matching, as shown in Figure 5.7. For convenience, Figure 5.7 shows the impact force relative to the impact force created by the nylon ball dropped from 305 mm (12") high. Scaled this way the three lines should be located at 1, 0.707, and 0.5 for the ball drops from 305, 152, and 76 mm height, respectively. The impact forces predicted from the pattern matching agree well with this expected result. It is also worth noting that even if the wrong impact location is selected due to a symmetry problem, the estimate of the force magnitude will still be correct.

5.3 Results of the Magnitude and Phase Technique

In order to use the magnitude and phase modal parameter extraction technique, the experimental setup needed a slight modification, as shown in Figure 5.8. A small photoelectric sensor was added to the guide tube. The output from the sensor was used to trigger the data acquisition system. It was necessary to drill a small hole through the guide tube so that the sensor could "see" the ball. The addition of the photosensor was necessary to get the pretrigger acceleration

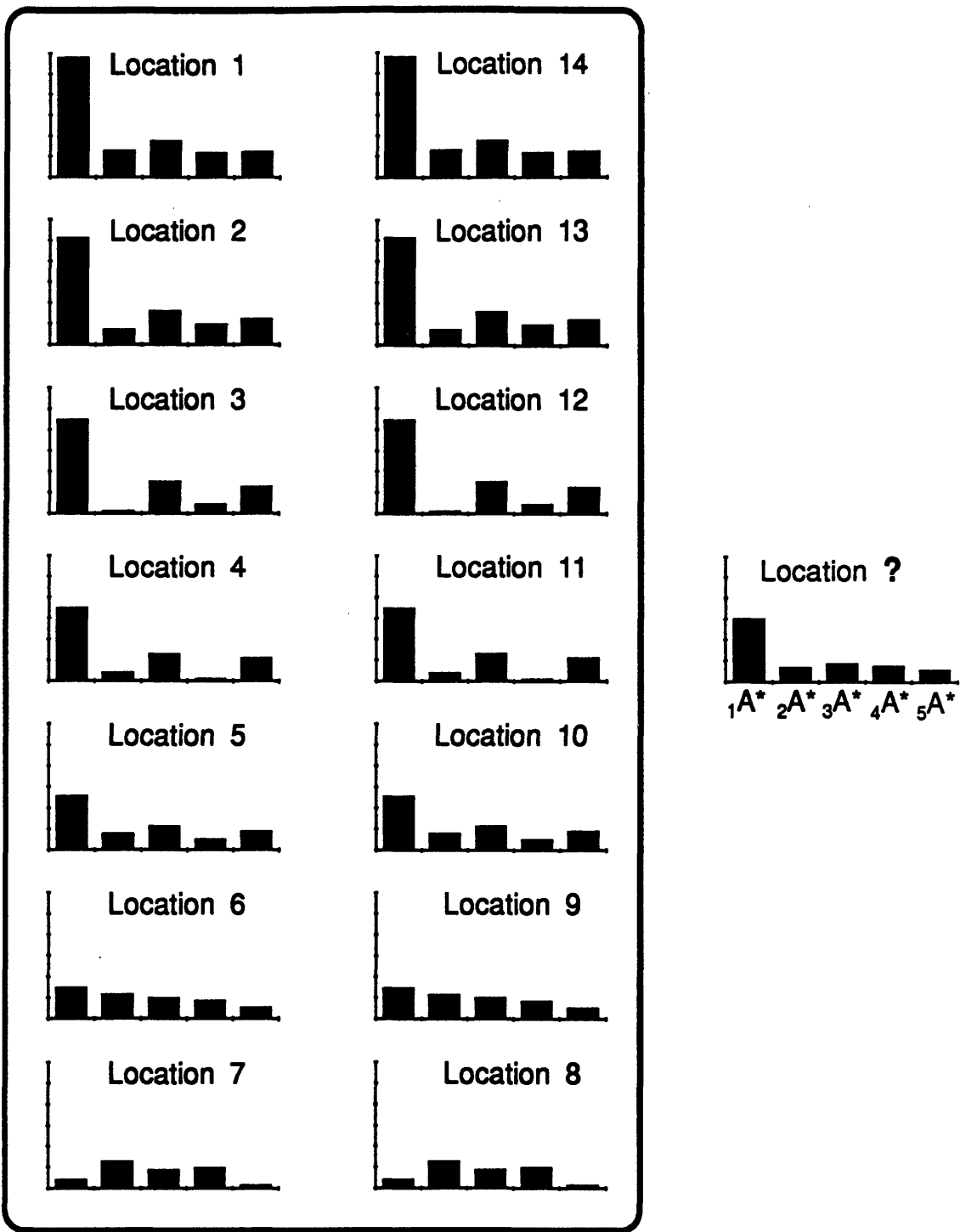


Figure 5.3: Patterns of modal constants extracted using the magnitude only modal parameter extraction technique. The pattern of uncorrected modal constants at the right comes from an impact at an unknown location.

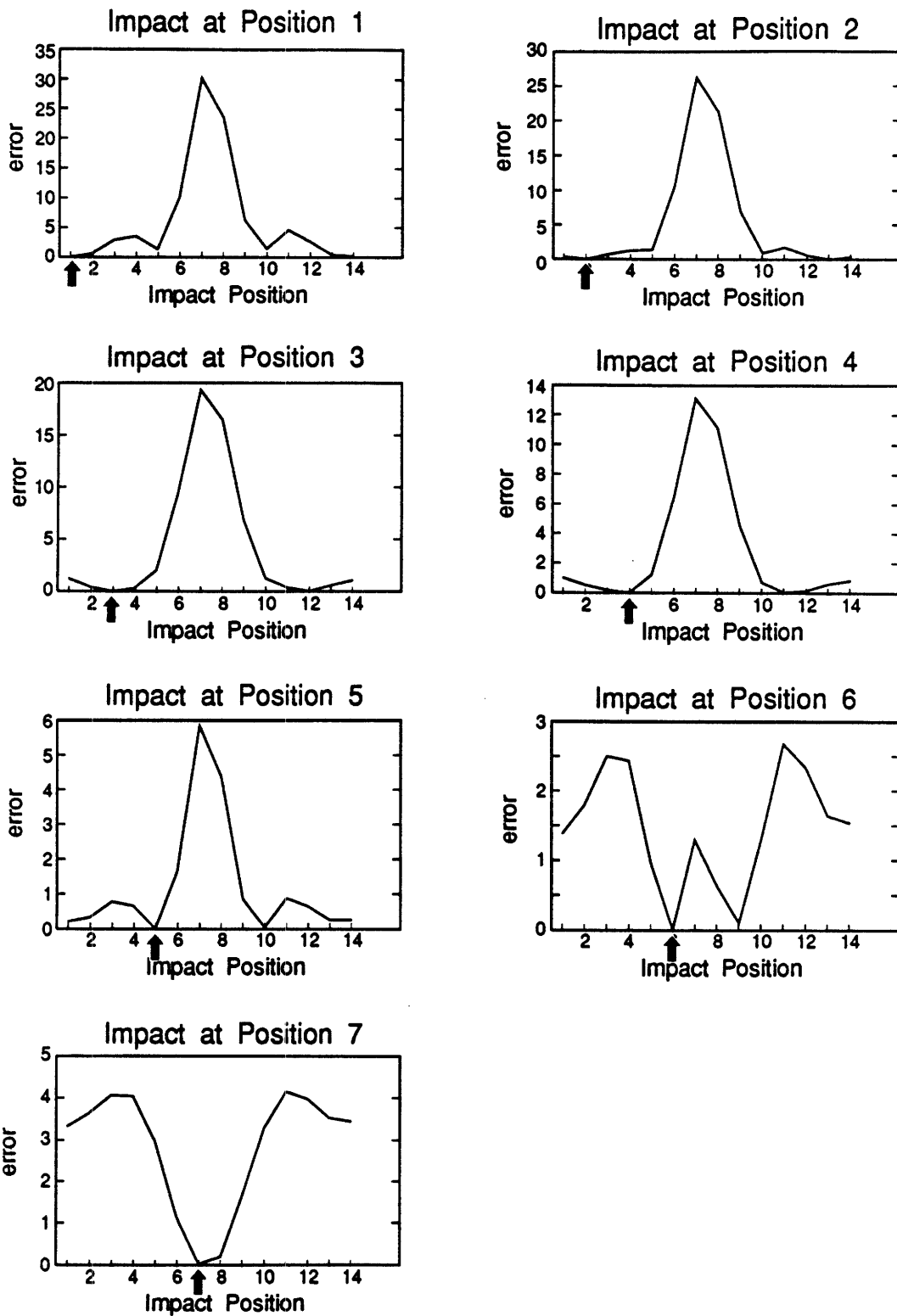


Figure 5.4: Results of pattern matching (using the magnitude only modal parameter extraction technique) from the drop of a 6.35 mm diameter nylon ball from a height of 76 mm.

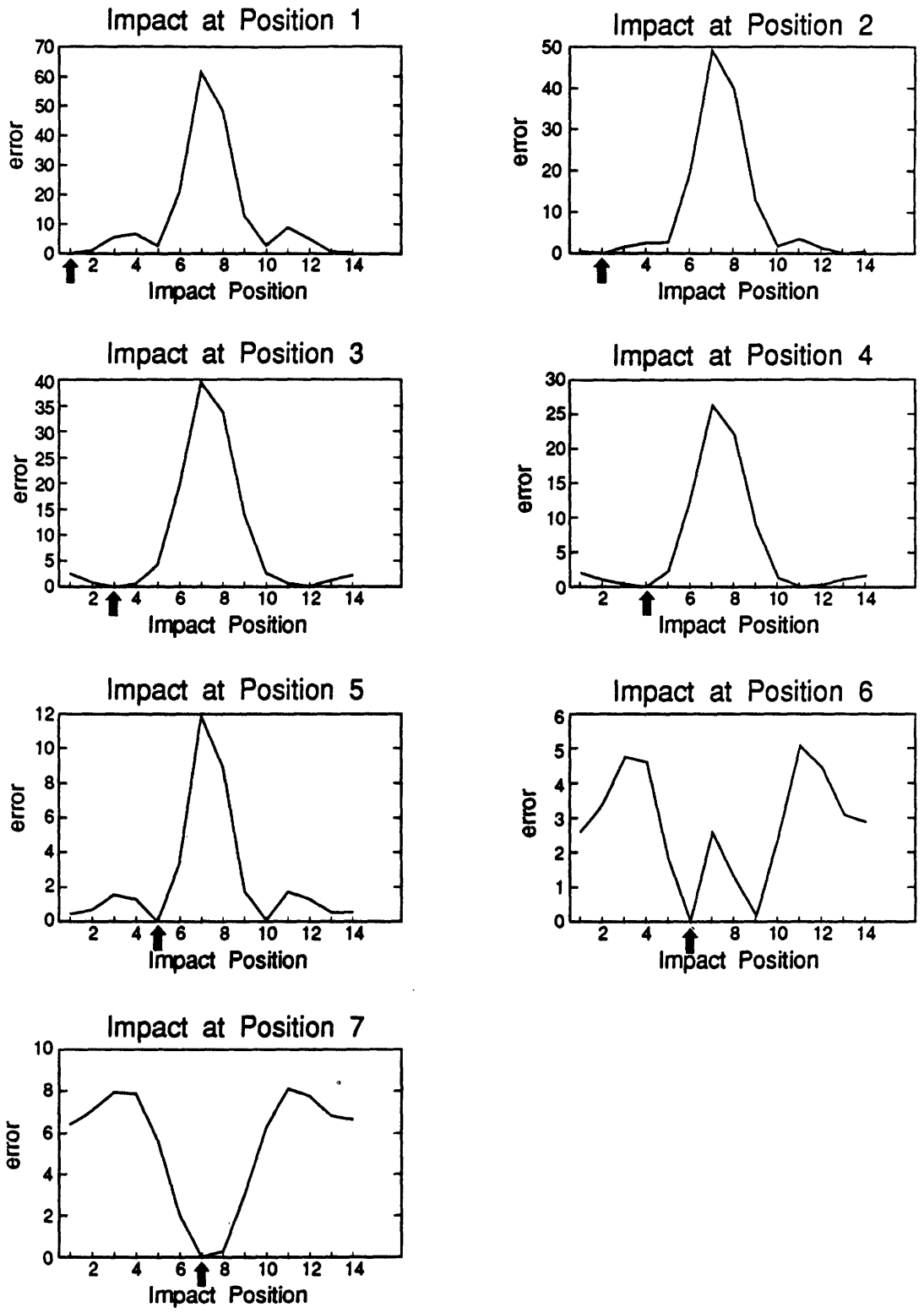


Figure 5.5: Results of pattern matching (using the magnitude only modal parameter extraction technique) from the drop of a 6.35 mm diameter nylon ball from a height of 152 mm.

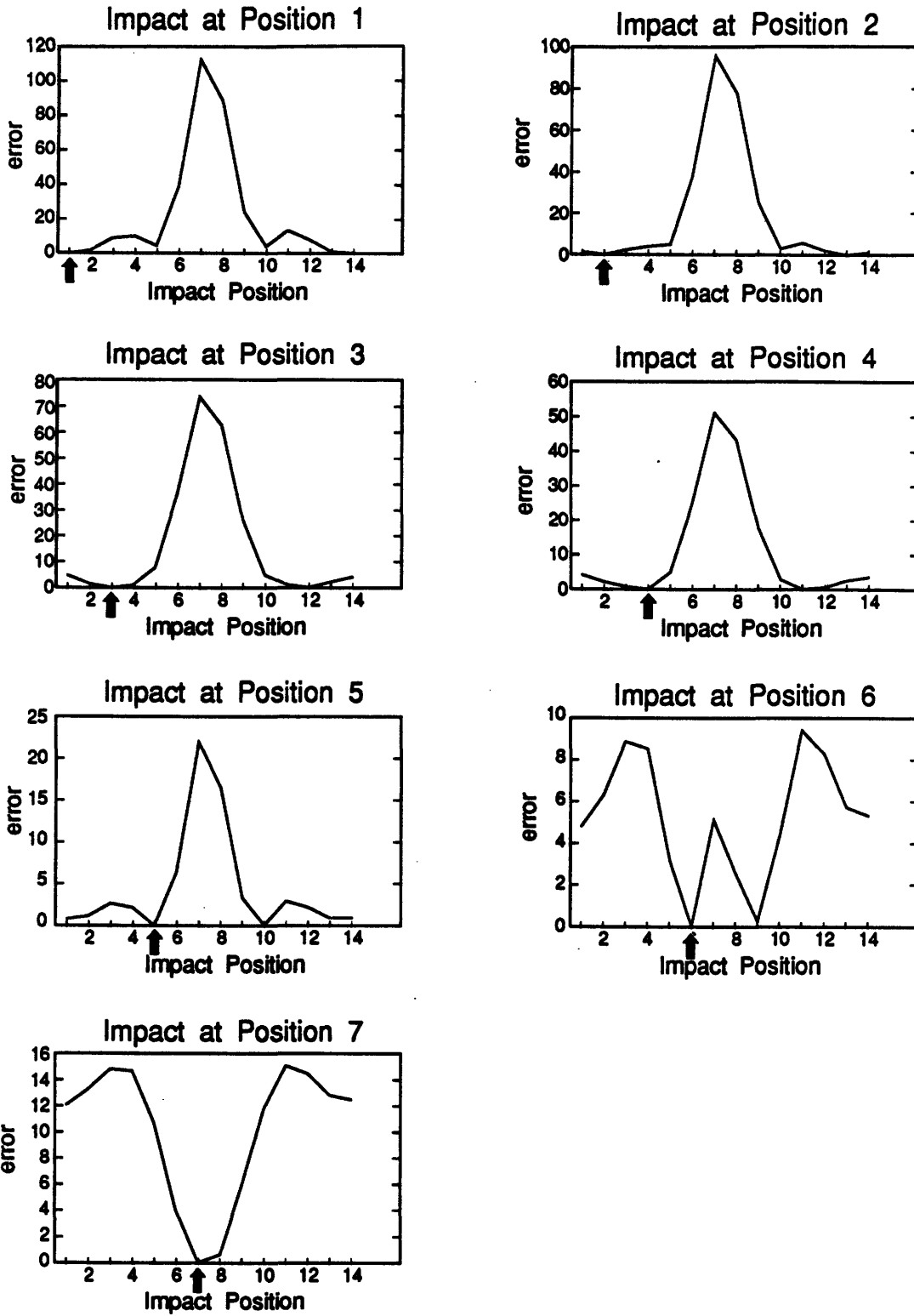


Figure 5.6: Results of pattern matching (using the magnitude only modal parameter extraction technique) from the drop of a 6.35 mm diameter nylon ball from a height of 305 mm.

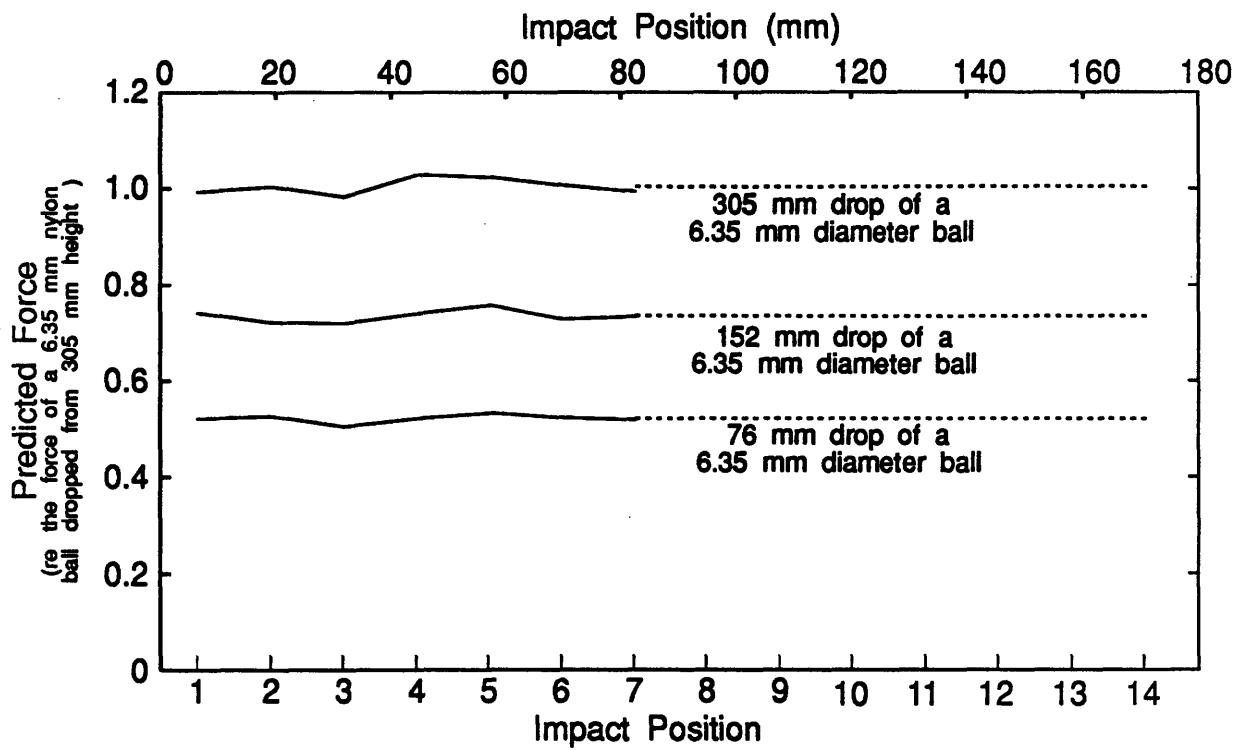


Figure 5.7: Impact forces predicted from pattern matching algorithm using modal parameters extracted using magnitude only modal parameter extraction technique.

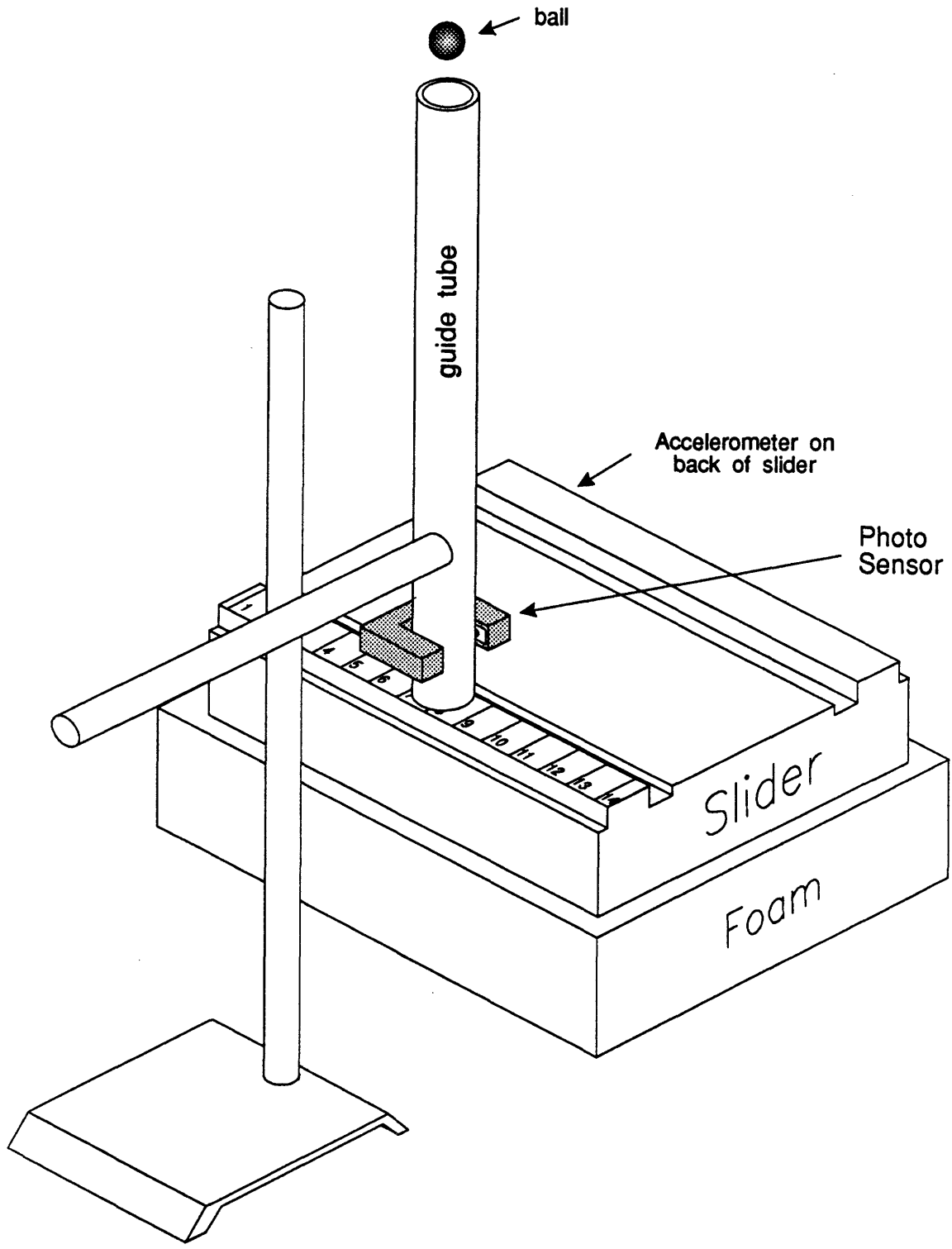


Figure 5.8: A photo sensor is added to the ball drop test apparatus so that pretrigger acceleration signals could be acquired. A small hole had to be drilled in the copper guide tube.

data that is important to getting the proper phase information out of the acceleration signal.¹

It would appear that by measuring the time of impact of the ball, we are violating the condition that nothing about the impact can be measured (Recall that the whole purpose of force identification is to determine the impact force when it cannot be directly measured.) But really all we are doing is making up for deficiencies in the hardware that was available to the research program. More expensive hardware, would have enabled us to acquire pretrigger information without the use of the photosensor. More advanced systems continuously acquire data in what is called a circular memory buffer. Thus, acceleration information is available for the time before the event even happens. The key point is that the photosensor is not necessary, if the right data acquisition system is available.

The procedure for running the ball drop tests is about the same as before. A database was assembled from ball drop tests on each of the 14 input locations. The only difference this time is that the phase taper was removed from the acceleration data and the magnitude and phase modal parameter extraction technique was used to extract the modal constants. With the database built, more ball drop tests were run for use in the force identification procedure. Balls were dropped at each of the 14 input locations along the slider rail from drop heights of 76, 152, and 305 mm. After removing the phase taper, the uncorrected modal constants rA_{jk}^* were extracted using the magnitude and phase modal parameter extraction technique. For each test, the set of uncorrected modal constants, $({}_1A_{jk}^*, {}_2A_{jk}^*, {}_3A_{jk}^*, {}_4A_{jk}^*)$ was run through the pattern matching process to predict the impact force magnitude and location.

Graphically, the pattern matching is illustrated by Figure 5.9. Since the phase information is now used, the sign of the modal constants can be determined. Thus, some of the values of the modal constants are positive and some are negative. This makes the pattern matching process easier both visually, and numerically. As a result, there is less chance for error. The results of the pattern matching are shown in Figure 5.10 for impact locations 1-7 and in Figure 5.11 for locations 8-14. In both of these figures, the drop height is 305 mm. The results of the pattern matching are basically the same for the 76 and 152 mm drop heights.

The error graphs clearly show that the pattern matching can detect the impact location accurately. In addition, the previous problems with symmetry are gone, i.e. an impact at location 1 can be easily distinguished from an impact at location 14. This is very clear from Figure 5.9. The distinguishing feature between locations 1 and 14 is that the modal constant for the torsional mode (mode 1) is negative at location 1 and positive at location 14. Thus, the pattern from location 1 is easily distinguished from the pattern at location 14, whereas they look very similar if the sign of the modal constant is unknown, see Figure 5.3.

The forces predicted by the force identification technique are shown in Figure 5.12. Once again the force is plotted on a normalized scale so that the lines should be at 0.5, 0.707, and 1.0 for the 76, 152, and 305 mm drop heights, respectively. The agreement with this expected

¹The author was puzzled for some time about the fact that the sensor did not seem to be able detect the nylon ball passing through the tube. Repeated checking of the electronics showed them to be fine. Finally it was determined that even though the nylon ball appears off-white in color, it is transparent to the infrared light used by the sensor. The nylon balls were colored using a black marker and the problem was solved.

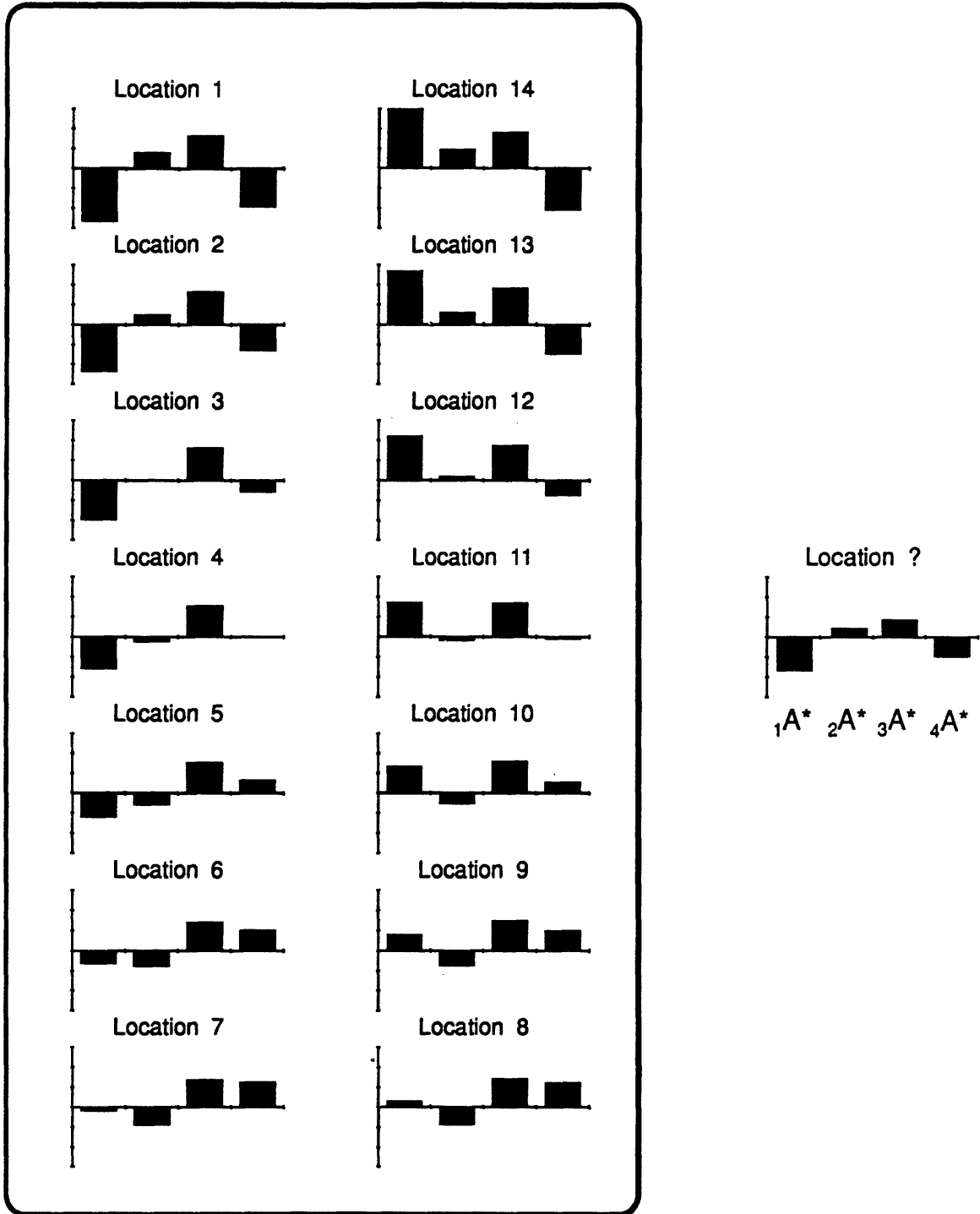


Figure 5.9: Patterns of modal constants extracted using the magnitude and phase modal parameter extraction technique. The pattern of uncorrected modal constants at the right comes from an impact at an unknown location.

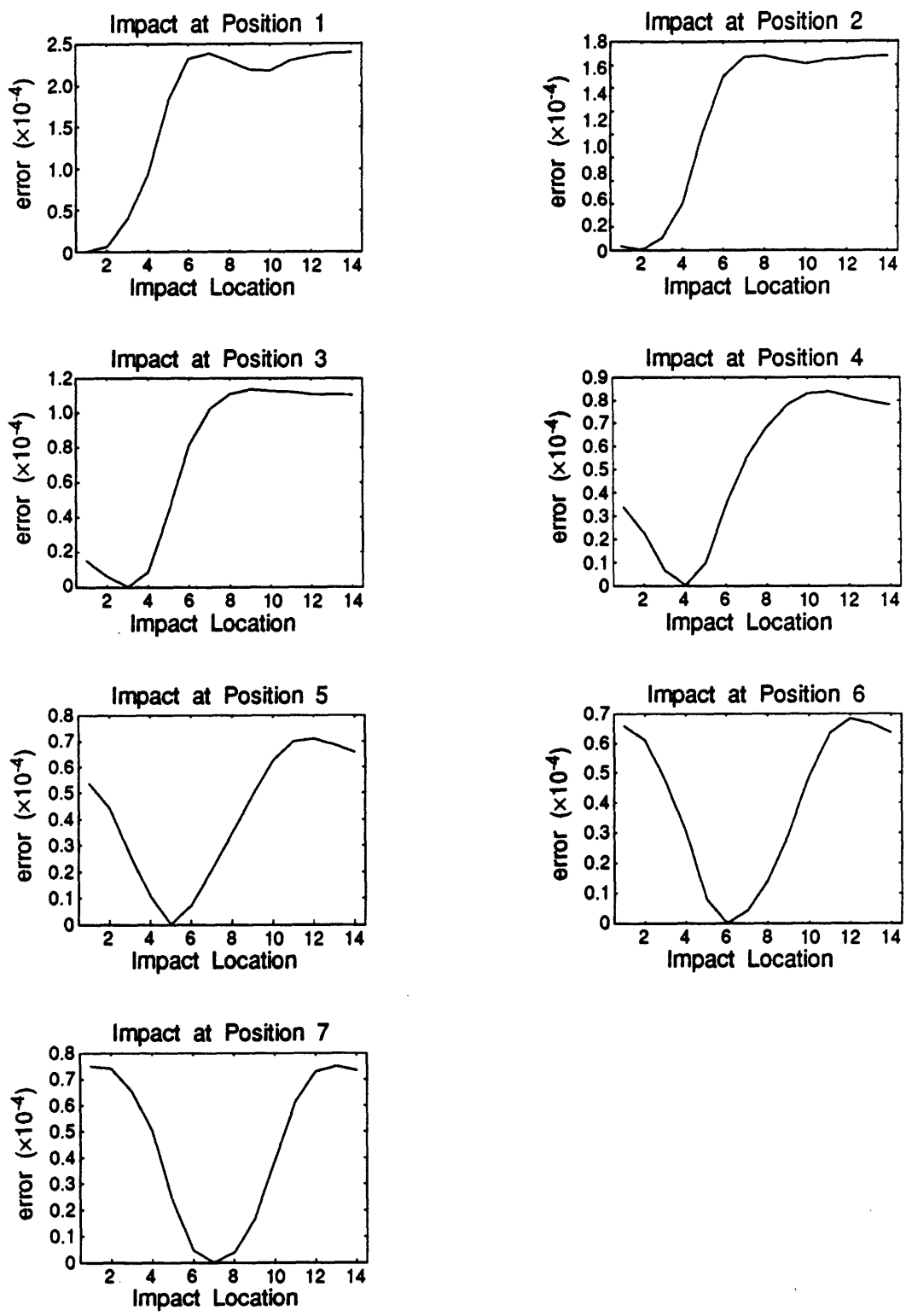


Figure 5.10: Results of pattern matching from the drop of 6.35 mm diameter nylon ball from a height of 305 mm. The modal constants, rA_{jk} , used in the pattern matching were extracted from the magnitude and phase information in $a(\omega)$.

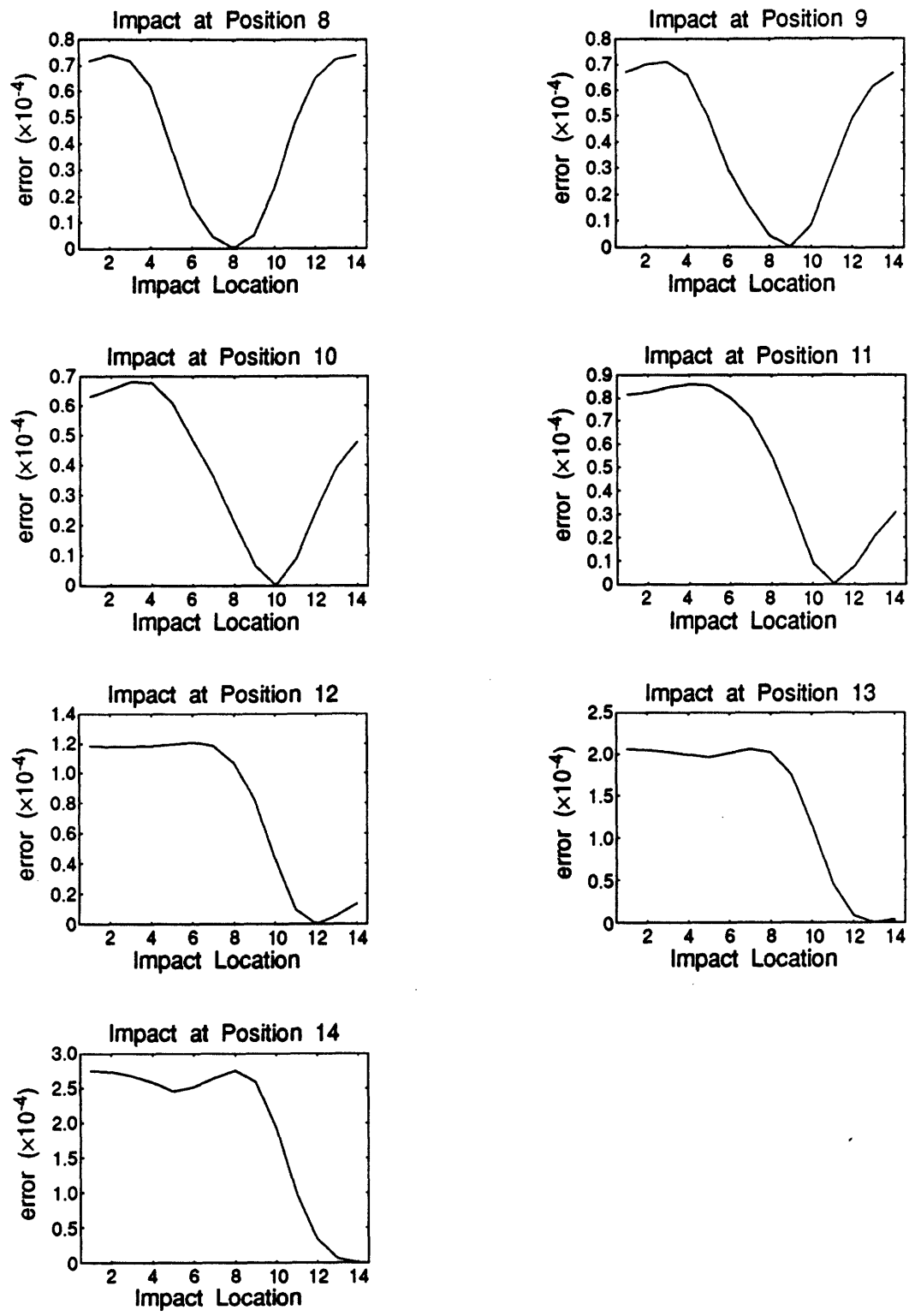


Figure 5.11: Results of pattern matching from the drop of 6.35 mm diameter nylon ball from a height of 305 mm. The modal constants, rA_{jk} , used in the pattern matching were extracted from the magnitude and phase information in $a(\omega)$.

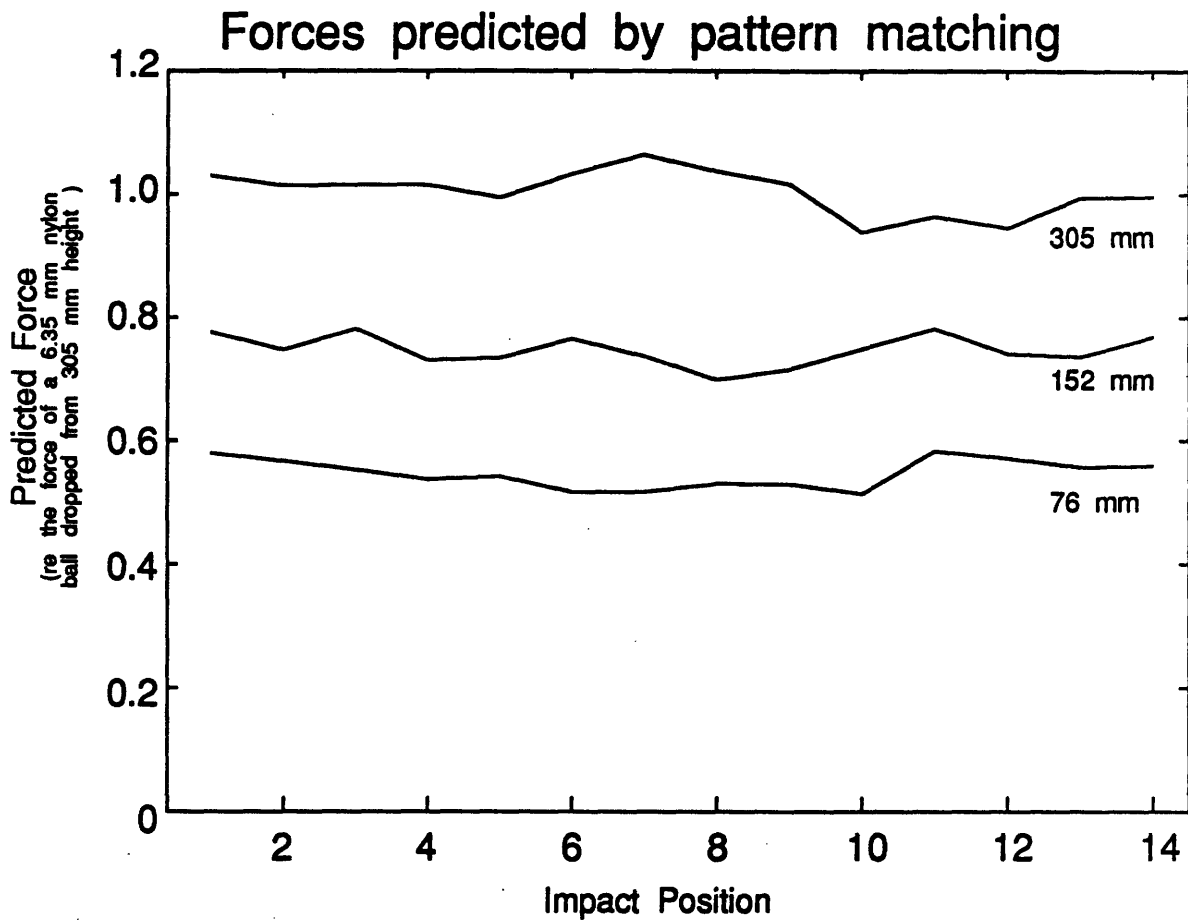


Figure 5.12: Forces predicted from pattern matching from the drop of 6.35 mm diameter nylon ball from a height of 305 mm. The modal constants, rA_{jk} , used in the pattern matching were extracted from the magnitude and phase information in $a(\omega)$.

result is fairly good, but not as good as it was when the magnitude only modal parameter extraction technique was used, compare with Figure 5.7. This is probably a reflection of the fact that the magnitude and phase modal parameter extraction technique is more complicated than the magnitude only technique. As result, the modal constants from the former technique are probably less accurate than the ones extracted from the latter technique. In either case, the error in the predicted forces might also be reduced by improving the pattern matching technique, as will be discussed later.

One important question is what happens if an impact occurs between two of the input locations, rather than exactly at one of the input locations. To answer this question, an impact was created directly between locations 2 and 3. The results of the pattern matching are shown in the top graph of Figure 5.13. As might have been expected, the pattern matching algorithm finds the best match with one of the nearest locations to the actual point of impact, in this case, location 2. Thus, the question then becomes, how much accuracy is need for the particular application.

There is, however, a straightforward approach to increasing the accuracy of the predicted impact location. The accuracy can be improved by simply performing an interpolation on the database of modal constants to estimate the values of the modal constants at locations where they were not measured. For the current database, a linear interpolation was performed changing the 4×14 database into a 4×53 . The pattern matching was then repeated and the results are shown in the middle and bottom graphs of Figure 5.13. With this interpolated database, the impact location accurately predicted to be halfway between locations 2 and 3. This interpolation works because the modal constants were taken at enough locations to capture the spatially varying nature of the mode shapes. If higher order mode shapes were used, testing would have to be done at more than 14 locations. Otherwise, the linear interpolations would give poor estimates of the modal constants at the intermediate locations.

5.4 Comparison of the Two Techniques

There are significant differences in the results obtained from the force identification technique when the magnitude only modal parameter extraction technique is used versus when the magnitude and phase technique is used. Perhaps the biggest difference is that the magnitude and phase technique can properly identify the impact location without confusing symmetric locations along the rails, e.g. locations 1 and 14. Even though the magnitude only technique appears to predict the force magnitude better, this does not seem to outweigh the problems that the technique has with symmetry. However, these are not the only considerations.

The tests presented in this chapter were performed with an enlarged model of the slider, an accelerometer, a 12 bit data acquisition system, and processing that was done off-line at a time which was convenient. Actually glide height tests are performed with a $4 \times 3 \times 1$ mm slider, a resonant PZT transducer, an 8 bit data acquisition system, and processing must be done on-line in about 10 milliseconds per contact and be able to process hundreds of contacts per disk. Under these conditions, use of the phase information in the vibration signal might

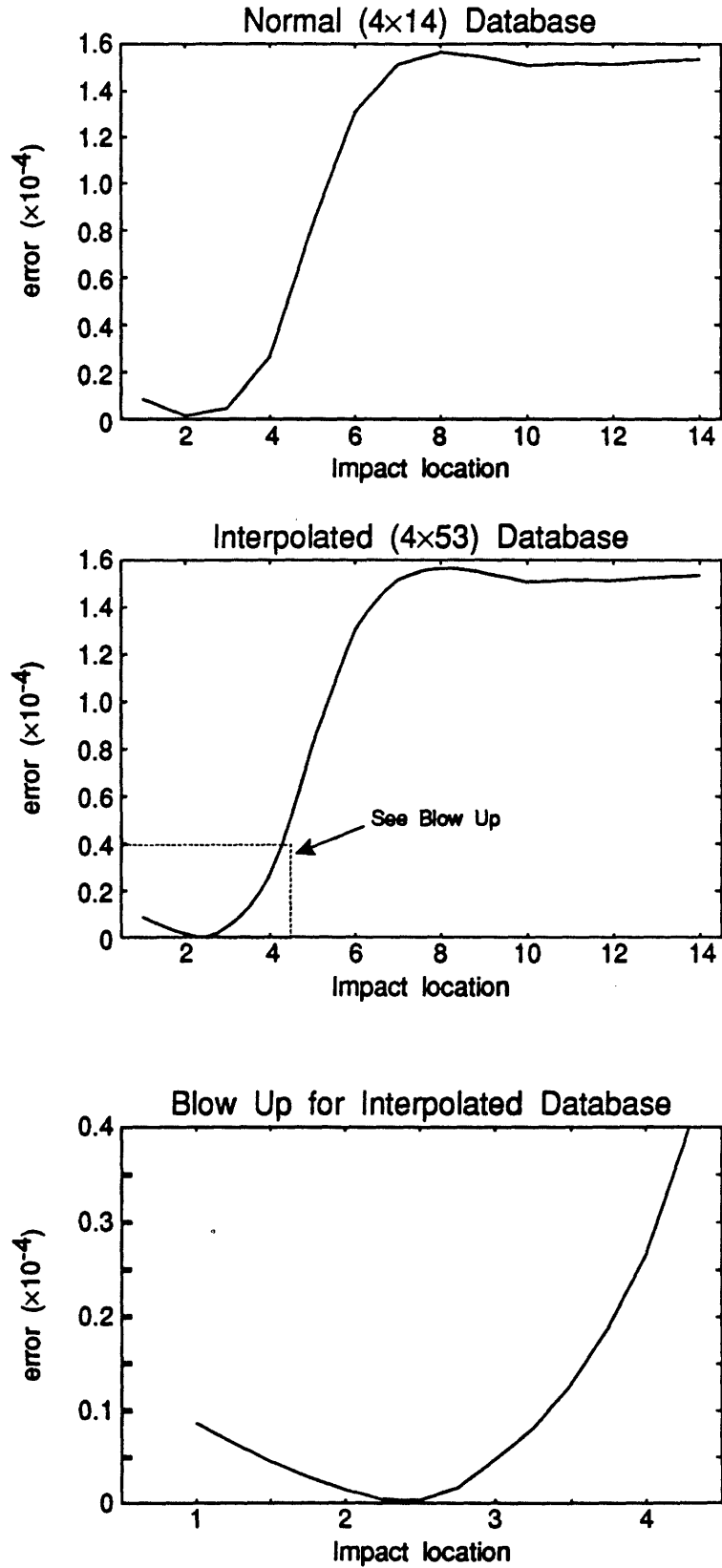


Figure 5.13: Results of pattern matching for an impact between locations 2 and 3. The top graph is for the normal database, the middle graph is for an interpolated database, and the bottom graph is a blow up of the middle graph.

be impossible. Thus, although the magnitude and phase technique might be preferred when the testing conditions are good, the magnitude only technique may be the only choice when test conditions are not so good. Simply put, without a good accelerometer, it is very easy for the phase to become distorted and ruin the possibility for using it reliably in any diagnostic processing.

The big advantage of the magnitude only technique, for glide height testing, is that it is not strongly dependent on the characteristics of the transducer. Even though the force identification technique has only been shown as using modal constants, this is not the only way that it can be used. For example, if the PZT sensor used in glide height testing had neither flat magnitude transfer function nor a flat phase transfer function, the magnitude only technique might still be used. The only requirement is that the modes of vibration still show up as resonant peaks. The magnitudes of these peaks might then be used as the pattern for use in the pattern matching. Thus, as long as the transfer function of the transducer did not change over time, the force identification procedure might still be used. On the other hand, the magnitude and phase modal parameter extraction technique is so dependent on the principles modal analysis that there is probably no simple modification that can be made to make it work without a good (flat response) accelerometer. Thus, it may not be possible to use the magnitude and phase technique in conjunction with the sensors that are currently available for glide height testing.

Although PZT sensors are the only ones currently being used for glide height testing, this might change in the not too distant future. Recently, a number of researchers have begun to make micro-accelerometer out of silicon using chip manufacturing technology[36][37]. These sensors are small enough to be placed right on top of the slider. Currently, the accelerometers are being manufactured as cheap vibration sensors for the automotive industry and not as high precision devices. Perhaps, in a few years they may become readily available and be precise enough to allow the magnitude and phase modal parameter extraction technique to be used in force identification for glide height testing.

It is still too early to tell if force identification (using magnitude only or magnitude and phase) will be practical for use in glide height testing. More work has to be done with tests on the actual, not enlarged, slider. The characteristics of the PZT sensors need to be determined and other types of sensors explored.

5.5 Summary

In this chapter, the force identification technique has been demonstrated with one particular application, glide height testing. The technique was demonstrated by performing ball drop tests on an enlarged model of the slider. Both the magnitude only as well as the magnitude and phase modal parameter extraction techniques were tested.

The magnitude only technique was able to accurately determine the impact force magnitude and location, but it was unable to distinguish between symmetric input locations. In other words, it could not distinguish between an impact at the leading edge of the slider and an impact at the trailing edge.

The magnitude and phase technique could determine the input location and had no symmetry problem. The predicted magnitude of the impact force was not as accurate with the magnitude only technique. This is believed to be the result of the introduction of the errors into the modal constants because of the lengthy processing needed for the modal parameter extraction procedure.

Overall, the force identification technique performed well with the tests on the enlarged slider model. However, additional work is needed to apply this technique to actual glide height testing.

Chapter 6

Discussion

The force identification technique presented in this thesis is not derived based on the fundamental principles of mechanics. Instead, it is put forth as a proposition to be contemplated. The technique's demonstrated success in identifying impact force magnitudes and locations on the read/write head (slider) indicates that the technique is of some value. The real question is, what is the *general* value of the new force identification technique? This is a difficult question to answer, as it is usually not possible to draw conclusions about a general problem by looking at the results of a specific problem.¹ However, this does not prevent one from carefully examining the results of a specific example, determining what factors effect the results for the specific case, and speculating how those same factors might effect the general case. That is the purpose of this chapter. The results of the specific application of the force identification technique to glide height testing will be examined and the more general application of the technique will be contemplated.

6.1 Strengths and Limitations of the New Technique

The first point, which must be reiterated, is that the technique is not applicable to all force identification problems. The force input must be a short duration pulse. This is a necessary requirement for the technique to work. The identification technique assumes that the magnitude of the force in the frequency domain is nearly constant in the frequency range of the vibration modes. Without this constraint, the technique cannot tell the difference between a change in the acceleration spectrum, due to change in source location, from a change in the acceleration spectrum due to a change in the force spectrum.

In practice, this constraint may not be difficult to meet. The lowest vibrational modes for a machine or structure might be below 100 Hz. Thus, if the impact time duration was around 1 ms, the condition of having a short duration pulse would be met. Of course, it would always depend on the particular application, but it does seem that the condition might be

¹This statement is true even for force identification procedures such as deconvolution.

met fairly easily. In AE research, the force source tend to be from propagating cracks and similar deformation mechanisms. These event are of very short duration (on the order of μs), and the short duration pulse requirement should easily be met for most structures undergoing AE testing. The precise time duration of the impacts in glide height testing are not currently known, as was discussed in Chapter 2. However, they appear to be of short enough duration to excite at least the first four vibration modes of the slider. The precise contact duration needs further investigation.

As was found by other researchers who used a modal model as part of their force identification procedure, the quality of the modal parameter extraction procedure is very important the accuracy of the predicted forces. First of all, it is important that the behavior of the structure or system have a response that is primarily modal in nature. Nonlinear and other effects would not be properly represented in a modal model of the system. Once the structural response has been determined to be primarily modal, a modal parameter extraction technique must be chosen. The two modal parameter extraction techniques used in this thesis were chosen for their simplicity. The accuracy of the curve fitting was only verified graphically. This was done by overlaying the reconstructed FRF over the experimental data. The accuracy of the fitting was not checked numerically, or verified by a second curve fitting using a different modal parameter extraction technique. Hansen 1990 [6] did find it necessary to use a combination of single degree of freedom (SDOF) and multi-degree of freedom (MDOF) modal parameter extraction techniques during the development of the modal model for his force identification procedure. But no detailed study was done to determine how errors in the modal parameter extraction effected the force identification procedure.

In general, it is expected that better modal parameter extraction will lead to better accuracy in the force identification. So it is important that the most accurate modal parameter extraction technique be used. Two different modal parameter extraction techniques were used in Chapter 5. With the circle fit method, the error in the predicted forces was much greater than with the least squared technique, compare Figures 5.7 and 5.12. This increased error is most likely due to the fact that the circle fit technique is less accurate. It can be particularly difficult to apply the circle fit method to lightly damped structures, such as the enlarged slider. Furthermore, the circle fit method does not work well when modes are very close together. Most commercial software for modal parameter extraction uses the MDOF rational fraction polynomial (RFP) technique. This is because it achieves reasonable accuracy over a wide range of experimental situations. However, RFP is not necessarily the best technique and other SDOF techniques yield better results for some situations. Unfortunately, there is no single technique that gives the best results under all situations. So, different modal parameter extraction techniques must be tried on experimental data, and the technique that works best for the given structure should be incorporated into the force identification procedure for that structure.

Another very important influence on the accuracy of the force identification procedure is the quality of the pattern matching algorithm. The pattern matching used in this thesis is the simplest pattern matching that exists, a least-squares comparison. It is literally a single line of computer code. Considering this fact, it is reasonable to suggest that more sophisticated pattern

matching algorithms can only improve the accuracy of the predicted forces and locations.

The biggest problem with the least squares technique is that it equally weights all modal constants during the pattern matching. It is certainly the case that some modal constants are more reliable than others. Modes of vibration with a low amplitude are likely to have less reliable modal constants. Hence, these modal constants should be weighted less. When an impact occurs at node point for a certain vibration mode, the modal constant for that mode will be small and inaccurate. Hence, it should be weighted less. Some pattern matching algorithms use a form of Bayesian estimation to optimize the weights used in the pattern matching. For the force identification procedure, this would require setting up not only the database of modal constants, but a database of variances of these modal constants as well. Obviously, the modal constants that showed the least variance would be weighted the most in the pattern matching. This technique could significantly improve the accuracy of the predicted forces and locations.

It is important that a "good" location is available to place the transducer. If the transducer is placed on a nodal line of a mode (stationary point), then it will be insensitive to the mode. Thus it may be necessary, or advisable, to locate the transducer at a location that is not on a line or axis of symmetry. Furthermore, some difficulties may be encountered with modes where the vibration motion is mostly orthogonal to the sensing direction of the transducer. The modal constants extracted from these modes will not be very accurate.

The question of transducer location also has associated with it the question of whether more than one transducer should be used. Having more than one transducer is one good way to reduce errors. Separate databases of modal constants will be needed for each transducer position. However, the consistency of results from the various transducers can be compared to make sure that no significant error has been made in the estimates of the impact location and impact force magnitude. The use of multiple transducers may be most useful in cases where one transducer is not sufficiently sensitive to certain modes.

The final question about transducers is what kind of transducers can be used. Because modal parameter extraction techniques can be performed on displacement, velocity, and acceleration signals; displacement transducers, velocity transducers, and accelerometers can all be used. In AE work, however, the AE transducers are never true displacement, velocity, or acceleration transducers. Since the magnitude only modal parameter extraction technique does not use the phase information, its curve fitting is probably robust enough to handle an AE transducer that does not have a very flat response over the frequency range of interest. Yet, if the transducer has a strong resonance peak in the frequency range of interest, it may be difficult to measure the modal constants at all because the measurement will be overwhelmed by resonance of the transducer itself. The magnitude and phase modal parameter extraction technique, on the other hand, is strongly dependent on having good phase information. This technique is not simply fitting a bunch of peaks. It assumes that the peaks will form circles in the Nyquist plot. Thus, it is important that a flat response vibration transducer be used. It should be noted that recent improvements in accelerometers may soon make it possible to manufacture a true accelerometer with a flat response up to 1 MHz. This would allow the magnitude and phase modal parameter extraction technique to be used for many AE applications.

The issue of uniqueness of solution is always present in any inverse problem solving, and force identification is no exception. It has been shown that for impacts on the read/write head (slider), the solution is not unique unless the phase information is used. This uniqueness problem comes from the symmetric shape of the slider. If only the magnitude of the vibration is used, then an impact at each of the four corners of the slider would all look the same. If the phase information is used, then each corner causes a different phase pattern and the impact location can be identified.

One interesting question is how many vibrational modes must be included in the pattern matching for the solution to be unique. This is a difficult question to answer in general, but it can be determined for the case of the slider. Figure 6.1 shows graphical depictions of the slider phase for different vibration modes, called phase diagrams. A phase diagram is sort of a two dimensional mode shape drawing. The part of the mode shape that is deformed upward is unshaded (or marked with +). The part of the mode shape that is deformed downward is shaded (or marked with -). The shaded and unshaded parts could be drawn reversed, because the sign is arbitrary. The main point is to see which parts of the slider move in-phase and which move out-of-phase. Consider the first two modes of vibration of the slider, torsion and longitudinal bending, shown in the upper left of the figure. Also consider an impact at each of the four corners of the slider, labeled A, B, C, and D. Due to the symmetry, the magnitude of vibration will be the same for each impact. The only way to distinguish between the four corners is the phase. Note that for the torsional mode (mode 1), corner pairs (A,B) and (C,D) can be distinguished by phase, but (A,D) and (B,C) cannot. In the longitudinal bending mode (mode 2), all four corners have the same phase and thus cannot be distinguished by using the phase information. Now consider monitoring both the torsional and longitudinal bending modes (modes 1 and 2). This combination gives four possible phase combinations (1+,2+), (1+,2-), (1-,2+), and (1-,2-), as shown at the top right of the figure. It can be seen that no additional phase information is gained by combining the two modes. It is still not possible to distinguish corner pairs (A,D) and (B,C). The figure shows that the same is true for combining the torsional mode with the transverse bending mode (modes 1 and 3). However, when the torsional mode is combined with the second torsional mode (modes 1 and 4), all impact locations become unique. The graph at the bottom right of the figure shows this combination. The four corners of the slider have different sign combinations, and thus can be distinguished by phase. Therefore, the inclusion of the second torsion mode in the force identification procedure is vitally important to the uniqueness of the solution.

Addressing the question of uniqueness for more general structures is very difficult. In general, the inclusion of more modes should improve the uniqueness. It might also be noted that the more symmetric a structure is, the more likely that uniqueness will be a problem. It is conceivable that inclusion of orthogonal modes of vibration, e.g. longitudinal, transverse, and side bending of the slider, may be useful in reducing symmetry problems. However, a general answer to the uniqueness question may be unknowable.

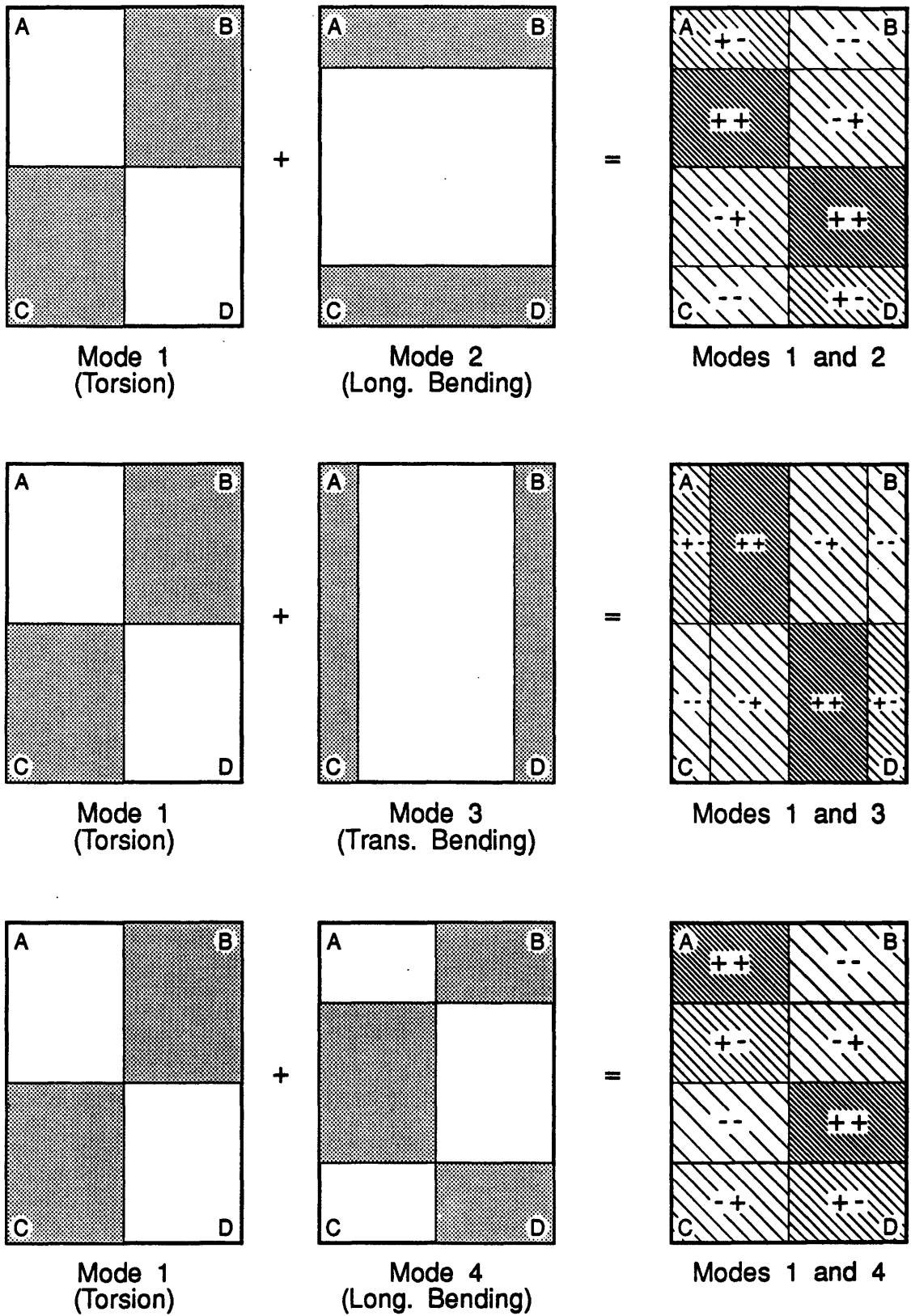


Figure 6.1: Phase diagrams for the different vibration modes of the slider. Note that only the combination of modes 1 and 4 can differentiate impacts at the four corners A, B, C, and D.

6.2 Summary

All of the issues discussed above, including the choice of modal parameter extraction algorithm, choice of pattern matching algorithm, placement of the transducer, and selection of modes, all have their part to play in the reliability of the force identification procedure. While one might speculate forever about the general application of the technique, it is probably far better to simply try the technique with a given application and determine if the technique works well for that application. For identifying impact locations and force magnitudes on the slider, the technique worked well, particularly if the phase information was included. The technique had a good ability to distinguish between different impact locations along the rail, and gave a reasonable estimate of the impact force magnitude. When the phase information is included in the pattern matching, there is a very sharp minimum in the error plot. This indicates that it is very unlikely that the force identification technique will make a mistake about the impact location along the rail. While it is not possible to draw general conclusions from the specific application with the slider, it would be most unusual for the technique to work so well for one application and not be found useful for other applications.

Chapter 7

Conclusions

It has been the main goal of this thesis to develop and demonstrate a technique for determining input force magnitude and location, using the acceleration signals from an accelerometer mounted on a structure. The force identification technique developed in this thesis, presents a new approach to solving this problem. The technique works from the observation that short duration “impulse type” forces on a structure excite different vibration modes unequally, depending on the impact location. Thus, the magnitude of the different vibrational modes can be used as a “pattern” (or fingerprint) to determine the impact location. The magnitude of the different vibrational modes is determined by modal parameter extraction. The pattern of modal constants extracted are compared, using pattern matching, with a modal model of the structure. The result of the pattern matching is an estimated impact location and impact force magnitude. The technique has demonstrated that the frequency domain acceleration signals $a(\omega)$ (vibration spectrum) can be used as a “pattern” to identify the impact location, when the input force is a short pulse.

The conclusions of the thesis regarding force identification can be summarized as follows

- Deconvolution, inverse filtering, and cepstrum windowing techniques have limitations that make the new force identification technique a valuable alternative.
- The new technique can properly identify input force locations, when the location of the input force is unknown.
- The new technique can identify the magnitude of the impact force.
- The technique was applied to the problem of identifying impacts in glide height testing and found to work well on an enlarged model of the slider.
- The technique has also been shown to properly identify the impact location even when the impact occurs at a location that is not in the database. This works provided that the database has information about the points on either side of the impact (to provide for interpolation).

- The new technique may have many applications (e.g. AE monitoring in material research) where the source location cannot be determined a priori, but the force magnitude and location of the source is of interest.
- Because the technique curve fits in the frequency domain only near the resonance peaks, a high S/N ratio can be expected. This should result in better robustness than other techniques that use the whole frequency spectrum directly.
- A reliable technique for removing phase taper from noisy vibration signals has been developed.

The nature of the force identification technique is such that it can only be used under the condition that the input force is a short pulse. It also cannot recover the complete time domain input waveform. It, therefore, offers only a partial solution to the problem of force identification. However, it does have the important ability to determine the magnitude of the input force, even when the location of the input force is not known a priori.

The conclusions of the thesis regarding glide height testing can be summarized as follows

- The high frequency (> 300 KHz) AE in glide height testing is primarily the vibrational response of the slider due to impact.
- The location of asperity impact along the slider rail is an important factor in the resulting vibration spectrum.
- Likewise, the sensor location is also an important factor in the measured spectrum.
- Simple measures of AE do not take into account the effect of impact location, and can give misleading results that can lead to missed asperities.
- The force identification technique presented may provide a valuable new technique for processing AE signals from glide height testing.

While the force identification technique worked well for ball impacts on the enlarged slider, testing of the technique on the actual slider awaits further improvements in glide height test equipment and sensors.

Bibliography

- [1] David J. Ewins. *Modal Testing: Theory and Practice*. Research Studies Press, Somerset, England, 1984.
- [2] Julius T. Tou and Rafael C. Gonzalez. *Pattern Recognition Principles*. Addison-Wesley Publishing Company, Reading, Massachusetts, 1974.
- [3] Richard H. Lyon. *Machinery Noise and Diagnostics*. Butterworths Publishers, Boston, 1987.
- [4] N. Okubo, S. Tanabe, and T. Tatsuno. "Identification of Forces Generated by a Machine Under Operating Condition". *International Modal Analysis Conference*, 2:920-927, 1985. Call number TA654.I57 1985 v.2.
- [5] J. M. Starkey and G. L. Merrill. "On the Ill-Conditioned Nature of Indirect Force-Measurement Techniques". *The International Journal of Analytical and Experimental Modal Analysis*, 103-108, July 1989.
- [6] Mark Hansen and John M. Starkey. "On Predicting and Improving the Condition of Modal-Model-Based Indirect Force Measurement Algorithms". *International Modal Analysis Conference*, 115-120, 1990.
- [7] P. E. Hollandsworth and H. R. Busby. "Impact Force Identification Using the General Inverse Technique". *International Journal of Impact Engineering*, 8(4):315-322, 1989.
- [8] Nelson N. Hsu, D. G. Eitzen, F. R. Breckenridge, R. B. Clough, E. R. Fuller, and J. A. Simmons. "*Fundamental Developments for Quantitative Acoustic Emission Measurements*". EPRI NP-2089, Electric Power Research Institute, October 1981. Prepared by the National Bureau of Standards.
- [9] S. A. Rizzi and J. F. Doyle. "Force Identification for Impact Problems on a Half Plane". *Computational Techniques for Contact, Impact, Penetration and Perforation of Solids*, AMD-103:163-182, December 1989. Call number TA418.34.A44.

- [10] J. F. Doyle and T. N. Farris. "Spectral Analysis of Impact Induced Wave Propagation in 3-D Frames". *Computational Techniques for Contact, Impact, Penetration and Perforation of Solids*, AMD-103:9-29, December 1989. Call number TA418.34.A44.
- [11] D. M. Egle, C. A. Tatro, and A. E. Brown. "Frequency Spectra of Acoustic Emission from Nodular Cast Iron". *Materials Evaluation*, 39(3):1037-1044, December 1981.
- [12] R. W. Stephens and A. A. Pollock. "Waveform and Frequency Spectra of Acoustic Emission". *The Journal of the Acoustic Society of America*, 50(3):904-910, December 1971.
- [13] R. Brunner and J. Harker. "A Gas Film Lubrication Study, Part III, Experimental Investigation of Pivoted Slider Bearings". *IBM J. Res. Dev.*, 8(260), July 1959.
- [14] W. Gross. *Fluid Film Lubrication*. John Wiley Press, New York, 1980.
- [15] V. Ponnaganti, T. R. Kane, and J. W. White. "Dynamics of Head-Disk Contact/Impact in Magnetic Recording". *IEEE Transactions on Magnetics*, MAG-23(5), September 1987.
- [16] Richard C. Benson and Frank E. Talke. "The Transition Between Sliding and Flying of a Magnetic Recording Slider". *IEEE Transactions on Magnetics*, MAG-23(5), September 1987.
- [17] Richard C. Benson and Frank E. Talke. "The Stability of a Slider Bearing During Transition From Hydrodynamic to Boundary Lubrication". *Tribology and Mechanics of Magnetic Storage Systems*, 4(SP-22):6-11, 1987.
- [18] Richard C. Benson, Chisin Chiang, and Frank E. Talke. "The Dynamics of Slider Bearings During Contacts Between Slider and Disk". *IBM Journal of Research and Development*, 33(1):2-14, January 1989.
- [19] Private communications with Sylvia Lee of IBM's Almandan Research Center.
- [20] Private communications with Ben Hu of IBM's Almandan Research Center.
- [21] R. F. Hoyt, S. E. Millman, and D. E. Horne. "Motion Pictures of Air Bearing Dynamics Under Stressed Conditions". *IEEE Transactions on Magnetics*, MAG-23(5):3459-3461, September 1987.
- [22] Tetsuya Hamaguchi and Masaaki Matsumoto. "Measurement of Impulsive Forces Arising from Flying Head/Disk Collision in Magnetic Disk Storage Systems". *JSME International Journal*, 33(1):29-34, 1990.
- [23] T. Kita, K. Kogure, Y. Mitsuya, and T. Nakanishi. "New Method of Detecting Contact Between Floating-Head and Disk". *IEEE Transactions on Magnetics*, MAG-16(5):873-875, September 1980.

- [24] C. E. Yeack-Scranton. "Novel Piezoelectric Transducers to Monitor Head-Disk Interactions". *IEEE Transactions on Magnetics*, MAG-22(5):1011-1016, September 1986.
- [25] Don Boyer. "Glide Test Calibration for Rigid Disk Magnetic Media". *Sensors*, 80-88, September 1986.
- [26] Richard C. Benson, R. Sundaram, and F. E. Talke. "A Study of Acoustic Emission from the Slider/Disk Interface in a $5\frac{1}{4}$ Inch Hard Disk Drive". *Tribology and Mechanics of Magnetic Storage Systems*, V:87-93, September 1988. STLE Special Publication SP-25.
- [27] K. Mochizuki, I. Sato, and T. Hayashi. "Impulse Force Detection of Head-Disk Media Contact Using a Small Piezoelectric Transducer". *The Transactions of The Institute of Electronics, Information and Communication Engineers*, E71(4):360-362, April 1988.
- [28] T. Hayashi, K. Mochizuki, T. Ohkubo, and I. Sato. "A Study of Slider/Medium Interface Using a Small Piezoelectric Transducer". *International Conference on Advanced Mechatronics*, 360-362, May 21-24 1989.
- [29] T. G. Jeong and D. B. Bogy. "Natural Frequencies of Sliders and Transducers Used to Detect Slider-Disk Contacts". *IEEE Transactions on Magnetics*, 25(5):3725-3727, September 1989.
- [30] Mun-Kee Chang. *Modeling and Calibration of an Acoustic Emission Measurement System*. Master's thesis, M.I.T., May 1990.
- [31] H. Hertz. *Crelle's J.*, 92, 1881.
- [32] Timoshenko and Goodier. *Theory of Elasticity*. McGraw-Hill, N.Y., 1970.
- [33] D. J. Ewins and P. T. Gleeson. "A Method for Modal Identification of Lightly Damped Structures". *J. Sound and Vibration*, 84(1):57-79, 1982.
- [34] Gilbert Strang. *Introduction to Applied Mathematics*. Wellesly-Cambridge Press, Wellesly, Massachusetts, 1986.
- [35] J. M. Montalvão e Silva and M. M. Maia. "Single Mode Identification Techniques for use with Small Microcomputers". *J. Sound and Vibration*, 124(1):13-26, 1988.
- [36] Stephen D. Senturia and Rosemary L. Smith. "Microsensor Packaging and System Partitioning". *Ceram. Eng. Sci. Proc.*, 8(9-10):997-1009, 1987. Call number TP.C412V.18 1987.
- [37] Martin A. Schmidt and Roger T. Howe. "Silicon Resonant Microsensor". *Ceram. Eng. Sci. Proc.*, 8(9-10):1019-1034, 1987. Call number TP.C412V.18 1987.
- [38] Robert W. Ramirez. *The FFT Fundamentals and Concepts*. Prentice-Hall, Inc, New Jersey, 1985.

Appendix A

Hertzian Contact Analysis

One way to simulate an impulse force input into a dynamic mechanical system is to drop a small ball onto the system. Since such a contact is typically elastic, the ball inputs a force pulse over time that can be approximated by half of a sine, see Figure A.1a. The two most important features of this force pulse are its contact time (t_c) and the maximum force (P_{max}). The Fourier transform of this time signal shows the ability of the ball drop to excite different frequencies, see Figure A.1b. At frequencies lower than ($\approx 1/t_c$), the frequency response is flat and at higher frequencies the amplitude rolls off at -20 dB/decade. Therefore, if the system vibrational frequencies of interest are lower than $\approx 1/t_c$, then the ball drop is effectively an impulse input.

In order to estimate t_c and P_{max} , elastic Hertzian contact analysis can be used [32]. Because of the relatively simple geometry involved, an exact solution is available for the static stresses created when two balls (or a ball and a flat surface) are pressed against each other. By combining the static Hertzian solution with Newton's second law ($F = m \cdot a$), it is possible to calculate the forces created during a ball drop.

From the static Hertzian contact analysis, the relationship between the contact force (P) and the relative displacement of the two bodies (α) can be calculated. This relationship is given by the following equations.

$$P = n\alpha^{3/2} \quad (\text{A.1})$$

$$n = \sqrt{\frac{16}{9\pi^2} \frac{R_1 R_2}{(k_1 + k_2)^2 (R_1 + R_2)}} \quad (\text{A.2})$$

$$k_1 = \frac{1 - \nu_1^2}{\pi E_1} \quad k_2 = \frac{1 - \nu_2^2}{\pi E_2} \quad (\text{A.3})$$

In these equations E is the Young's modulus, ν is the Poisson's ratio, R is the radius of the ball, and the subscripts 1 and 2 indicate whether the property is for ball 1 or ball 2. To analyze the contact between a ball and a flat surface just let $R_2 \rightarrow \infty$.

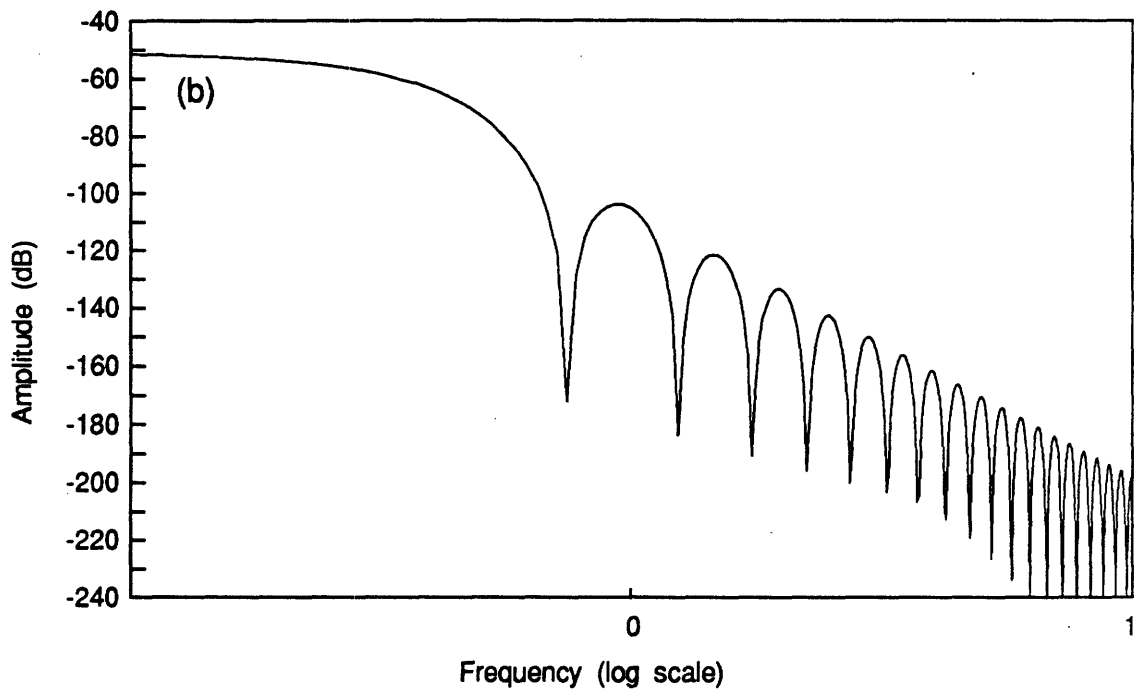
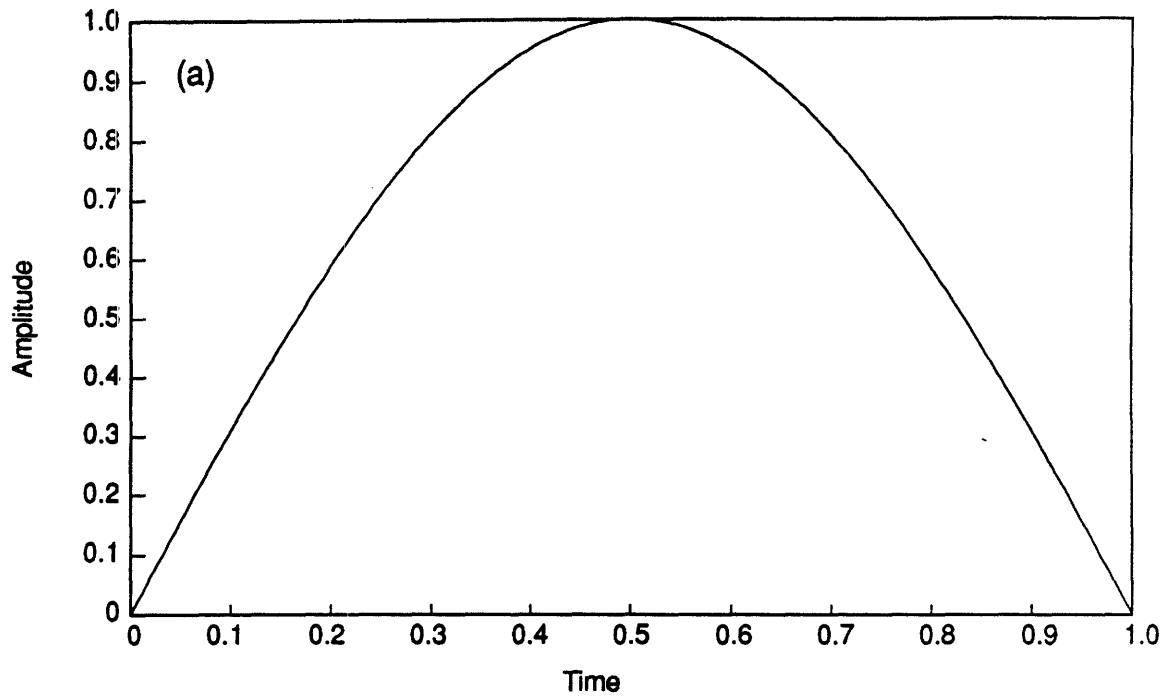


Figure A.1: a) Half cosine pulse and its b) FFT. Note that the magnitude is fairly constant at low frequencies.

For the dynamic aspects of the problem, consider two balls of different sizes coming into contact with each other, as shown in Figure A.2. The upper ball has an initial velocity v_1 and the lower ball has an initial velocity v_2 . Through the application of Newton's second law ($F = ma$), it can be determined that

$$m_1 \frac{dv_1}{dt} = -P \quad m_2 \frac{dv_2}{dt} = -P \quad (\text{A.4})$$

where m_1 and m_2 are the masses of the two spheres. Since α is the deformation between the two bodies, $\dot{\alpha}$ is the relative velocity of the two ball once they have made contact or

$$\dot{\alpha} = v_1 + v_2 \quad (\text{A.5})$$

Taking the derivative of this and combining with Equation A.4,

$$\ddot{\alpha} = \dot{v}_1 + \dot{v}_2 = -\left(\frac{P}{m_1} + \frac{P}{m_2}\right) \quad (\text{A.6})$$

or by rearranging,

$$\ddot{\alpha} = -P \frac{m_1 + m_2}{m_1 m_2}. \quad (\text{A.7})$$

Using the following notation, Equation A.7 becomes

$$\ddot{\alpha} = -P n_1 \quad n_1 = \frac{m_1 + m_2}{m_1 m_2} \quad (\text{A.8})$$

or using Equation A.1

$$\ddot{\alpha} = -n n_1 \alpha^{3/2} \quad (\text{A.9})$$

This is the differential equation of motion for dynamic contact as long as the balls are in contact.

To solve this equation, start by multiplying both sides by $\dot{\alpha}$,

$$\dot{\alpha} \ddot{\alpha} = -\dot{\alpha} n n_1 \alpha^{3/2} \quad (\text{A.10})$$

$$\dot{\alpha} \frac{d\dot{\alpha}}{dt} = -\frac{d\alpha}{dt} n n_1 \alpha^{3/2} \quad (\text{A.11})$$

$$\frac{1}{2} d(\dot{\alpha})^2 = -n n_1 \alpha^{3/2} d\alpha \quad (\text{A.12})$$

By integrating,

$$\frac{1}{2} (\dot{\alpha} - v)^2 = -\frac{2}{5} n n_1 \alpha^{5/2} \quad (\text{A.13})$$

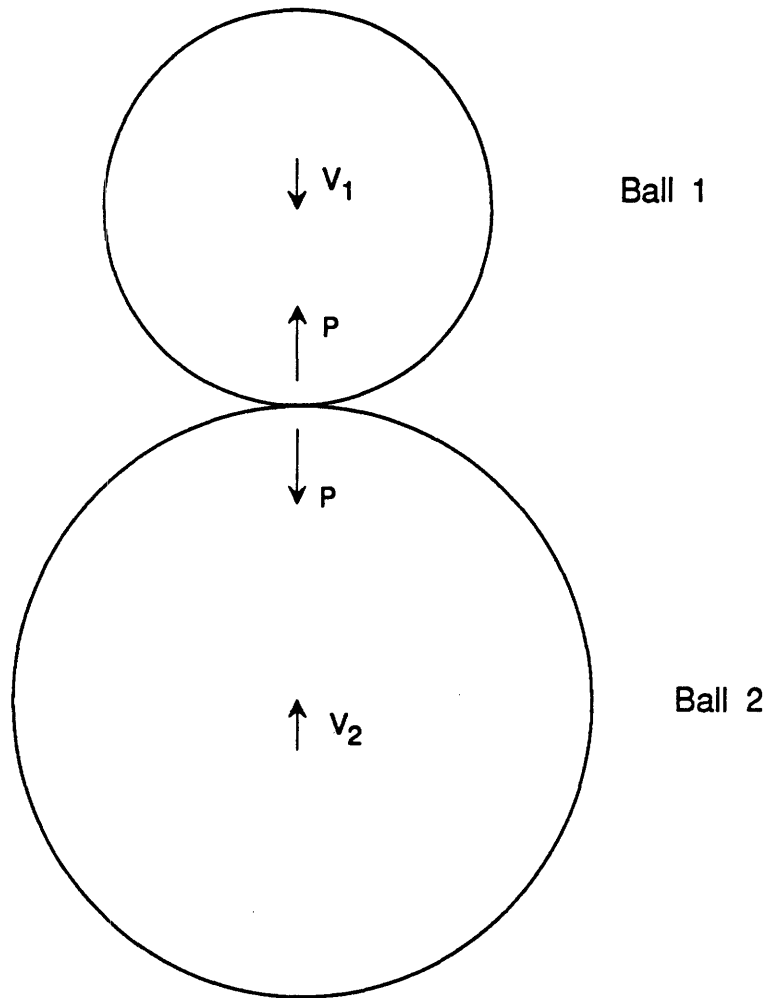


Figure A.2: Diagram of two balls colliding with each other. P is the contact force and V is the velocity.

Where v is the initial approach velocity of the two balls. By setting the relative velocity to zero $\dot{\alpha} = 0$, the maximum compression α_{max} can be found

$$\alpha_{max} = \left(\frac{5}{4} \frac{v^2}{nn_1} \right)^{2/5} \quad (\text{A.14})$$

Using the value calculated from this equation and Equation A.1, the maximum force (P_{max}) can be calculated.

For calculating the contact duration of the impact (t_c), we can rewrite the equation of motion, Equation A.13 as

$$dt = \frac{d\alpha}{\sqrt{v^2 - \frac{4}{5}nn_1\alpha^{5/2}}} \quad (\text{A.15})$$

or using $\alpha/\alpha_{max} = x$ and Equation A.14, we find that,

$$dt = \frac{\alpha_{max}}{v} \frac{dx}{\sqrt{1 - x^{5/2}}} \quad (\text{A.16})$$

By integrating this equation the contact time (t_c) can be calculated

$$t = \frac{2\alpha_{max}}{v} \int_0^1 \frac{dx}{\sqrt{1 - x^{5/2}}} = 2.94 \frac{\alpha_{max}}{v} \quad (\text{A.17})$$

A.1 Ball Drop on a Semi-infinite Elastic Half-Space

If the contact is not between two balls but between a ball and a large flat surface, then the equations can be modified by letting $R_2 \rightarrow \infty$ and $m_2 \rightarrow \infty$. As $m_2 \rightarrow \infty$ Equation A.8 becomes

$$\ddot{\alpha} = -Pn_1 \quad n_1 = \frac{1}{m_1} \quad (\text{A.18})$$

and as $R_2 \rightarrow \infty$ Equation A.2 becomes

$$n = \sqrt{\frac{16}{9\pi^2} \frac{R_1}{(k_1 + k_2)^2}} \quad (\text{A.19})$$

By simply substituting these equations into Equation A.14, the maximum compression (α_{max}) for a ball and a flat surface can be calculated.

Property	Carbide	Al ₂ O ₃ TiC
ρ	14950 Kg/m ³	4280 Kg/m ³
E	6.76·10 ¹¹ N/m ²	3.92·10 ¹¹ N/m ²
ν	0.26	0.35
k	4.39·10 ⁻¹³ m s ² /Kg	7.13·10 ⁻¹³ m s ² /Kg

Table A.1: Mechanical Properties of Tungsten Carbide and Al₂O₃TiC.

A.2 Analysis for a 0.28 mm Ball Drop on 3380 Slider

In order to simulate an impulse input for the 3380 slider, a 0.28 mm diameter carbide ball is used. The slider is made of a ceramic called alumina titanium carbide Al₂O₃TiC. The properties of these materials are shown in Table A.1.

The mass of the carbide ball can be calculated from its volume and density.

$$\begin{aligned}
 m_1 &= \frac{4\pi R_1^3}{3} \rho_1 & (A.20) \\
 &= \frac{4\pi \cdot 0.00014^3}{3} \cdot 14950 \\
 &= 1.72 \cdot 10^{-7} \text{ Kg}
 \end{aligned}$$

The initial velocity (v_1) of the ball can be calculated from the potential energy at 0.305 meter (12") drop height.

$$\begin{aligned}
 v_1 &= \sqrt{2gh} & (A.21) \\
 &= \sqrt{2 \cdot 9.8 \cdot 0.305} \\
 &= 2.44 \text{ m/s}
 \end{aligned}$$

Using Equations A.19 and A.18 the values of the constants n and n_1 can be calculated.

$$\begin{aligned}
 n &= \sqrt{\frac{16}{9\pi^2} \frac{R_1}{(k_1 + k_2)^2}} & (A.22) \\
 n &= \sqrt{\frac{16}{9\pi^2} \frac{0.00014}{(4.39 \cdot 10^{-13} + 7.13 \cdot 10^{-13})^2}} \\
 &= 4.36 \cdot 10^9 \frac{\text{Kg}}{\sqrt{\text{m s}^2}}
 \end{aligned}$$

$$\begin{aligned}
n_1 &= \frac{1}{m_1} & (A.23) \\
&= \frac{1}{1.72 \cdot 10^{-7}} \\
&= 5.82 \cdot 10^6 \frac{1}{\text{Kg}}
\end{aligned}$$

Using Equation A.14 the maximum compression can be calculated

$$\begin{aligned}
\alpha_{max} &= \left(\frac{5 v^2}{4 n n_1} \right)^{2/5} & (A.24) \\
&= \left(\frac{5 \cdot 2.44^2}{4 \cdot 4.36 \cdot 10^9 \cdot 5.82 \cdot 10^6} \right)^{2/5} \\
&= 6.13 \cdot 10^{-7} \text{ m}
\end{aligned}$$

and the maximum force

$$\begin{aligned}
P_{max} &= n \alpha^{3/2} & (A.25) \\
&= 4.36 \cdot 10^9 (6.13 \cdot 10^{-7})^{3/2} \\
&= 2.09 \text{ N}
\end{aligned}$$

The contact time can be calculated from Equation A.17

$$\begin{aligned}
t &= 2.94 \frac{\alpha_{max}}{v} & (A.26) \\
&= 2.94 \frac{6.13 \cdot 10^{-7}}{2.44} \\
&= 7.37 \cdot 10^{-7} \text{ s}
\end{aligned}$$

Although the peak force (P_{max}) and contact time (t_c) are the two key parameters from the contact analysis, sometimes the shape of the force vs. time or deflection vs. time curves are of interest. The time at which a given deflection is reached can be calculated from the following.

$$t = \frac{\alpha_{max}}{v} \int_0^x \frac{dx}{\sqrt{1 - x^{5/2}}} \quad (A.27)$$

where x is the normalized deflection $x = \alpha/\alpha_{max}$. The equation is only valid in the range $0 \leq x \leq 1$. Figure A.3 shows the deflection vs. time for the 0.28 mm carbide ball and the FFT of the time domain signal. Note that to calculate the FFT, it is necessary to re-interpolate the time domain data to even time increments. Using Equation A.1, the force vs time curve can be calculated from the deflections. Figure A.4 shows the results for the 0.28 mm carbide ball.

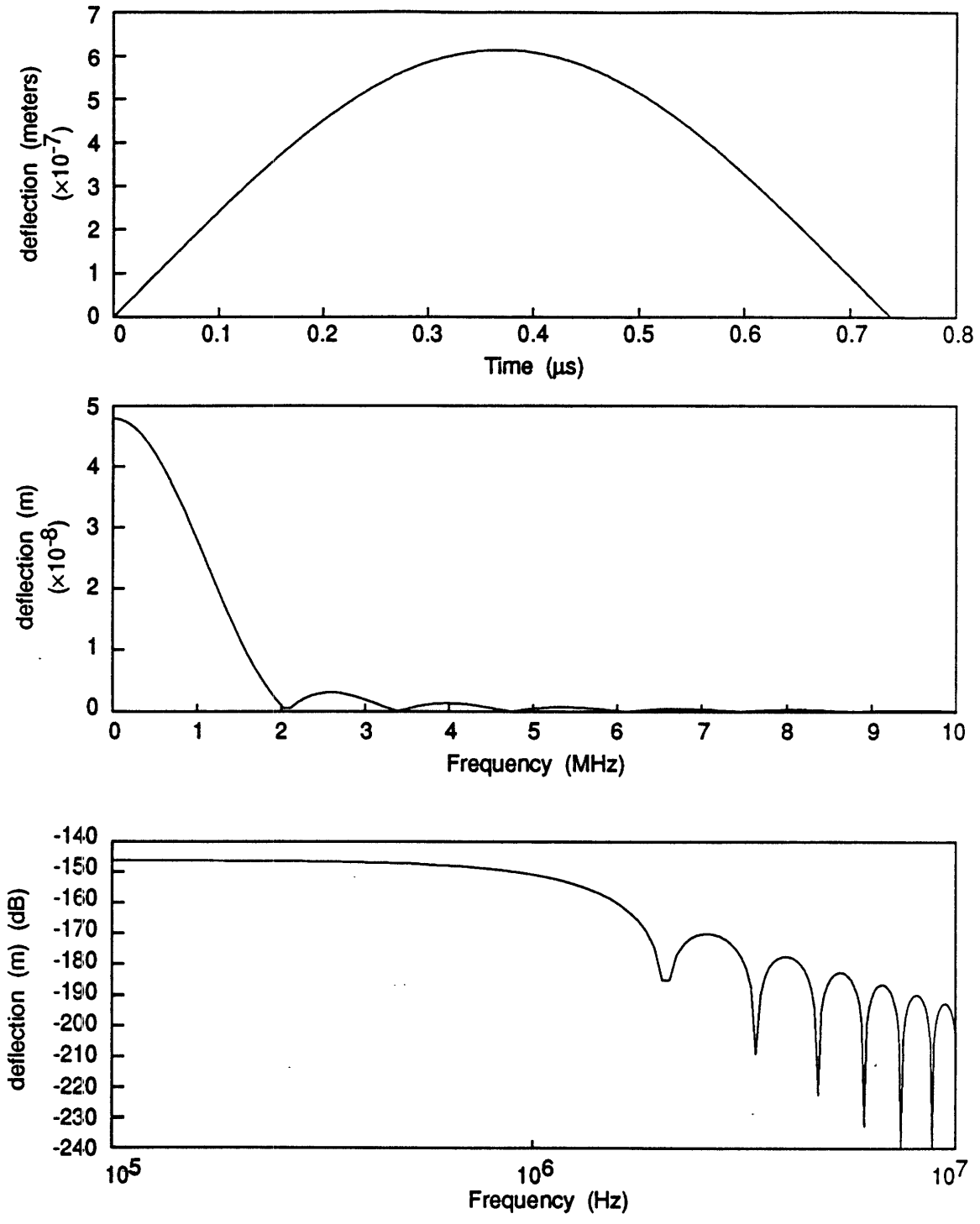


Figure A.3: Displacement vs. time calculated from Hertz contact theory for a 0.28 mm carbide ball dropped from a height of 0.305 m onto an alumina titanium carbide surface.

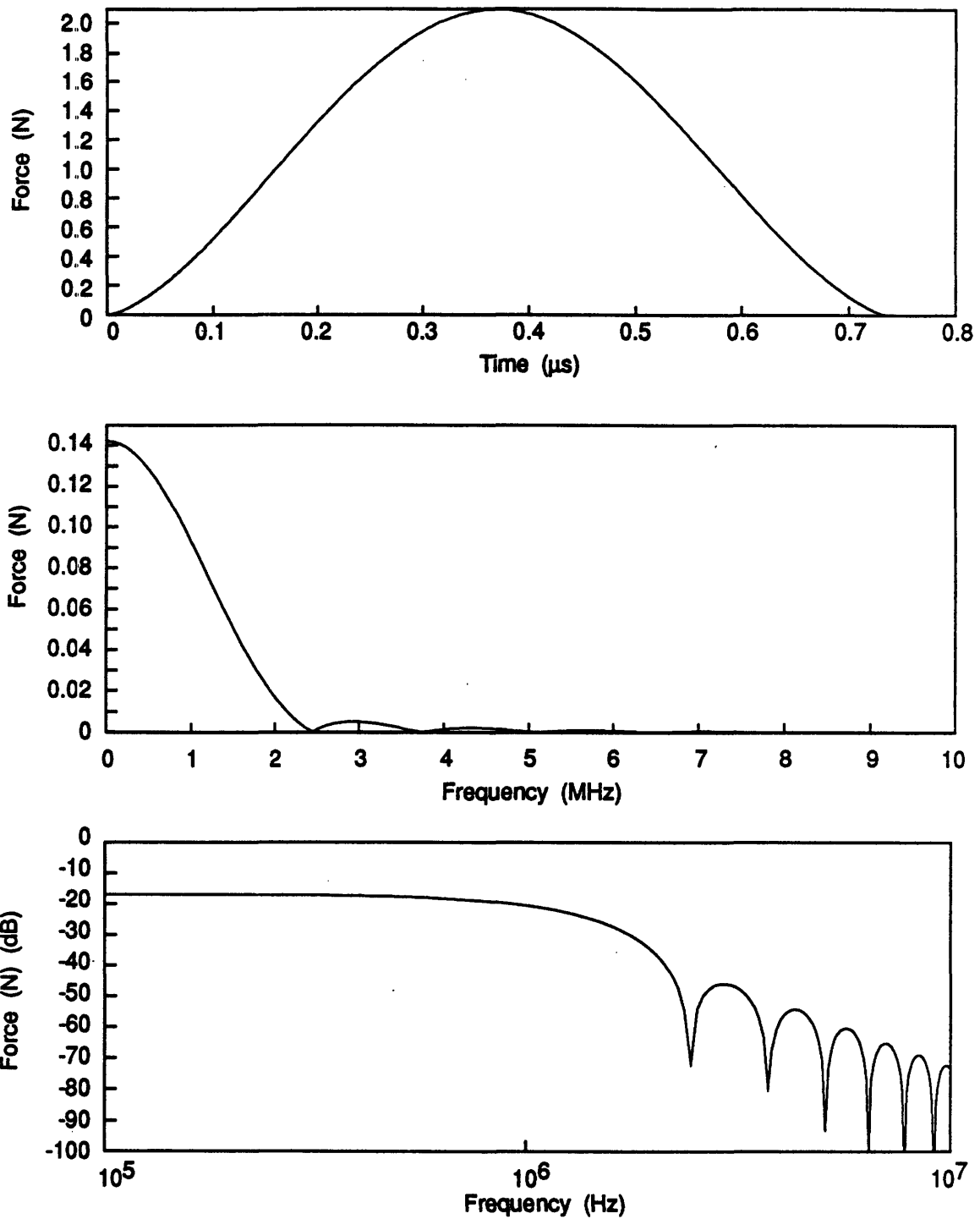


Figure A.4: Force vs. time calculated from Hertz contact theory for a 0.28 mm carbide ball dropped from a height of 0.305 m onto an alumina titanium carbide surface.

Appendix B

FFT's on Transient Signals

There are a number of subtleties involved in calculating FFT's [38]. Most of these subtleties are the result of differences in the way an FFT calculates frequency information for discrete waveforms versus the way the Fourier Integral calculates frequency information for continuous waveforms. Equation B.1 shows the formula for the Fourier integral. The limits of integration are $-\infty$ and $+\infty$, i.e. all time from the beginning of time to the end of all future time. In contrast, Equation B.2 shows that for a DFT (discrete Fourier transform), the limits of summation are limited to the number of points (N) in the acquired waveform, or from time 0 to time T . Beyond the number of point (N), for the DFT or FFT, there is an assumption of periodicity, i.e. that the signal keeps repeating itself in the same way that it did in the N points. This assumption of periodicity is the cause of some subtle problems.

$$X(f) = \int_{-\infty}^{+\infty} x(t)e^{-j2\pi ft} dt \quad (\text{B.1})$$

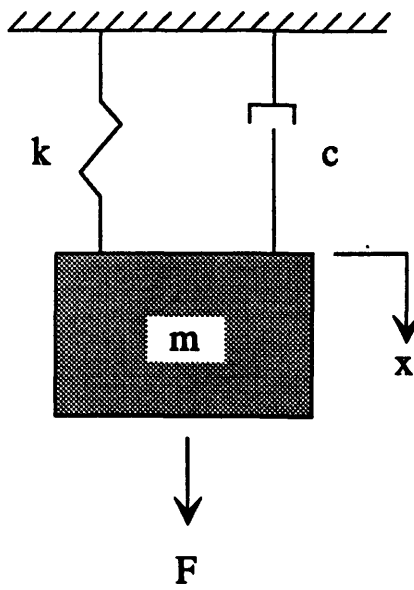
$$X_d(k) = \frac{1}{N} \sum_{n=0}^{N-1} x(n)e^{-j2\pi kn/N} \quad (\text{B.2})$$

To illustrate one such subtlety, consider the simple second order spring-mass-dashpot system shown in Figure B.1a. The receptance (x/F) of this system can be readily calculated by the following.

$$\begin{aligned} F - F_k - F_c &= m\ddot{x} \\ F_c &= c\dot{x} \\ F_k &= kx \end{aligned} \quad (\text{B.3})$$

$$F = m\ddot{x} + c\dot{x} + kx \quad (\text{B.4})$$

A) Second Order System



B) Theoretical receptance calculation

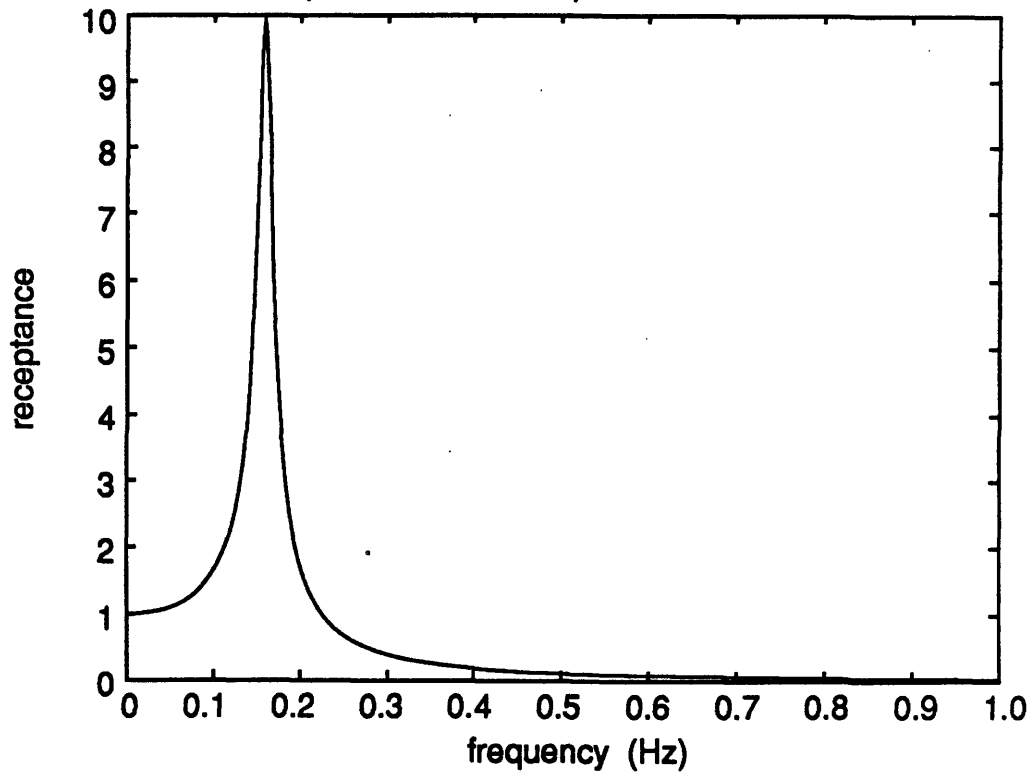


Figure B.1: A) Second order spring-mass-dashpot system and B) its receptance for $m = 1$, $k = 1$, and $c = 0.1$

$$F = ms^2x + csx + kx$$

$$\frac{x}{F} = \frac{1}{ms^2 + cs + k}$$

where s is the Laplace operator. By replacing the Laplace operator s by $j\omega$, the frequency response can be determined.

$$\frac{x}{F} = \frac{1}{m(j\omega)^2 + cj\omega + k} \quad (\text{B.5})$$

$$\frac{x}{F} = \frac{1}{k - m\omega^2 + jc\omega} \quad (\text{B.6})$$

The frequency response (receptance) in Equation B.6 is shown in Figure B.1b. This demonstrates how the Fourier Integral can be used to determine the frequency response of a system analytically.

In the real world, frequency responses are usually determined experimentally. To illustrate this process, some simulations were performed using MATLAB. The second order system, discussed above, was used with $m = 1$, $k = 1$, and $c = 0.1$. The response of the system to a unit impulse input was simulated and results plotted in Figure B.2. In Figure B.2a the results are shown for a time step of 0.5 and 256 points were calculated. Figure B.2b shows the FFT of this waveform. Figures B.2c and B.2e show simulations calculated for longer times with 512 and 1024 points. The FFT's of these signals are shown in Figures B.2d and B.2f. *Notice that the magnitude of the FFT decreases as more points are included.* This seems reasonable from the standpoint that as more time is included in the waveform, there is proportionally less energy in the signal. If the simulation were continued for very long times, there will be a proportional decrease of energy in the signal.

The problem is that the signal is transient. With a continuous waveform, as more time is included, more energy is added to the signal. This keeps the magnitude of the FFT independent of the number of points used in the calculation. The same is not true for transient signals. As more points are added, very little additional energy is added and the magnitude of the FFT decreases. Therefore, if confusion is to be avoided, care must be used when examining FFT's of transient signals.

For modal testing (and analysis) there is another way to address this issue. Since, in modal analysis, we are usually concerned with a quantity that is a ratio, e.g. receptance (x/F), the FFT can be calculated as the ratio of two FFT's. To illustrate this more carefully, consider Figure B.3. This figure illustrates, in more detail, the simulation discussed above. In Figure B.3a the impulse force input is shown and its FFT is shown in B.3b. Once again the displacement response (B.3c) and its FFT (B.3d) are shown. By considering both the FFT of the input and FFT of the response, the actual receptance can be calculated. This is done by dividing the FFT of the response by the FFT of the input. (Note that this is a complex division.) The result is shown in (B.3e) and the Fourier integral result is shown in (B.3f) for comparison. We now see that the results are in good agreement. An important feature about Figure (B.3e)

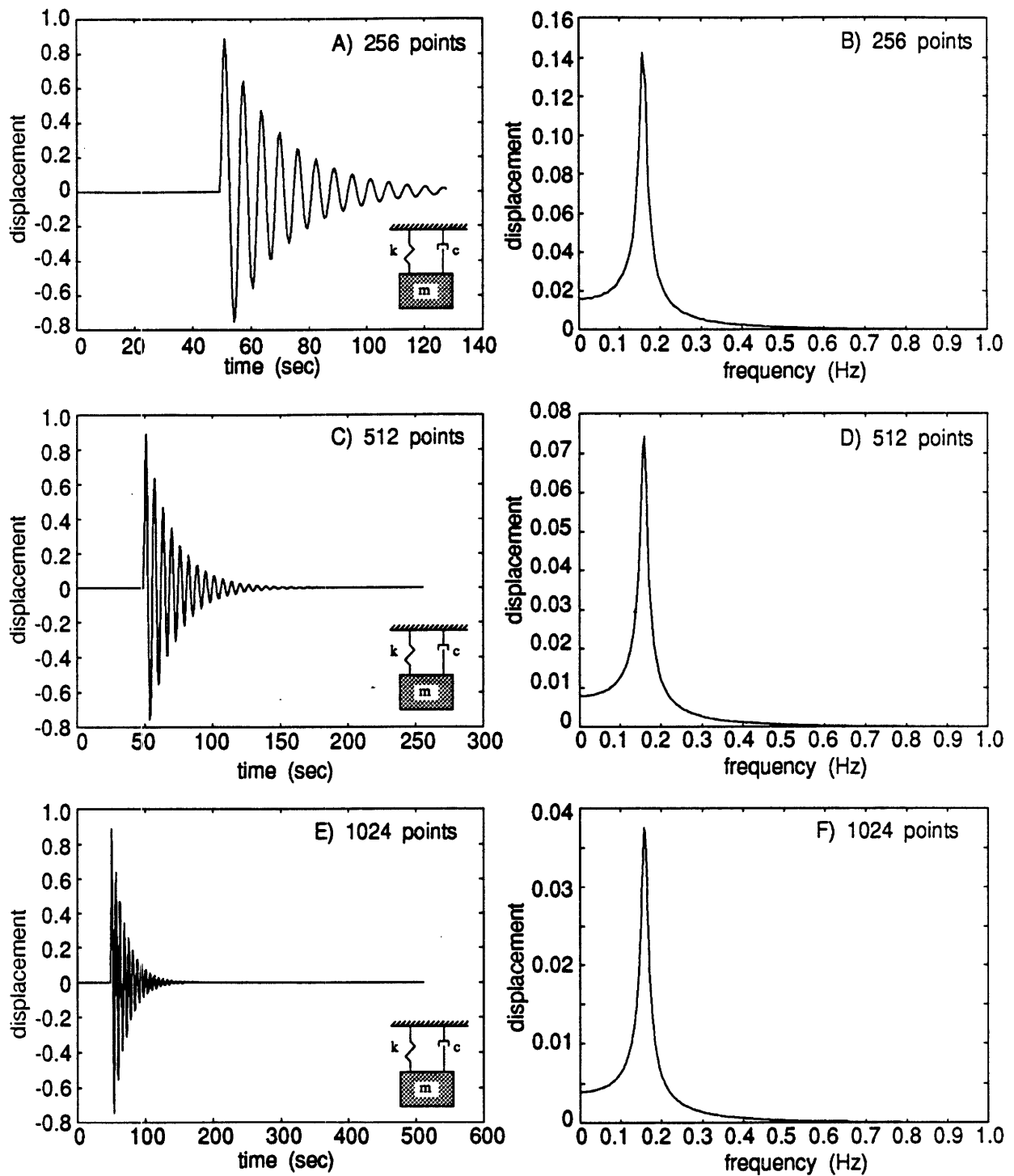


Figure B.2: This is a demonstration of the effect of including more time domain points in a transient signal. A), C), and E) show the response of a second order system calculated for 256, 512, and 1024 points, respectively. B), D), and F) show the FFT's for these signals. Notice how the magnitude of the FFT's decrease as more points are included.

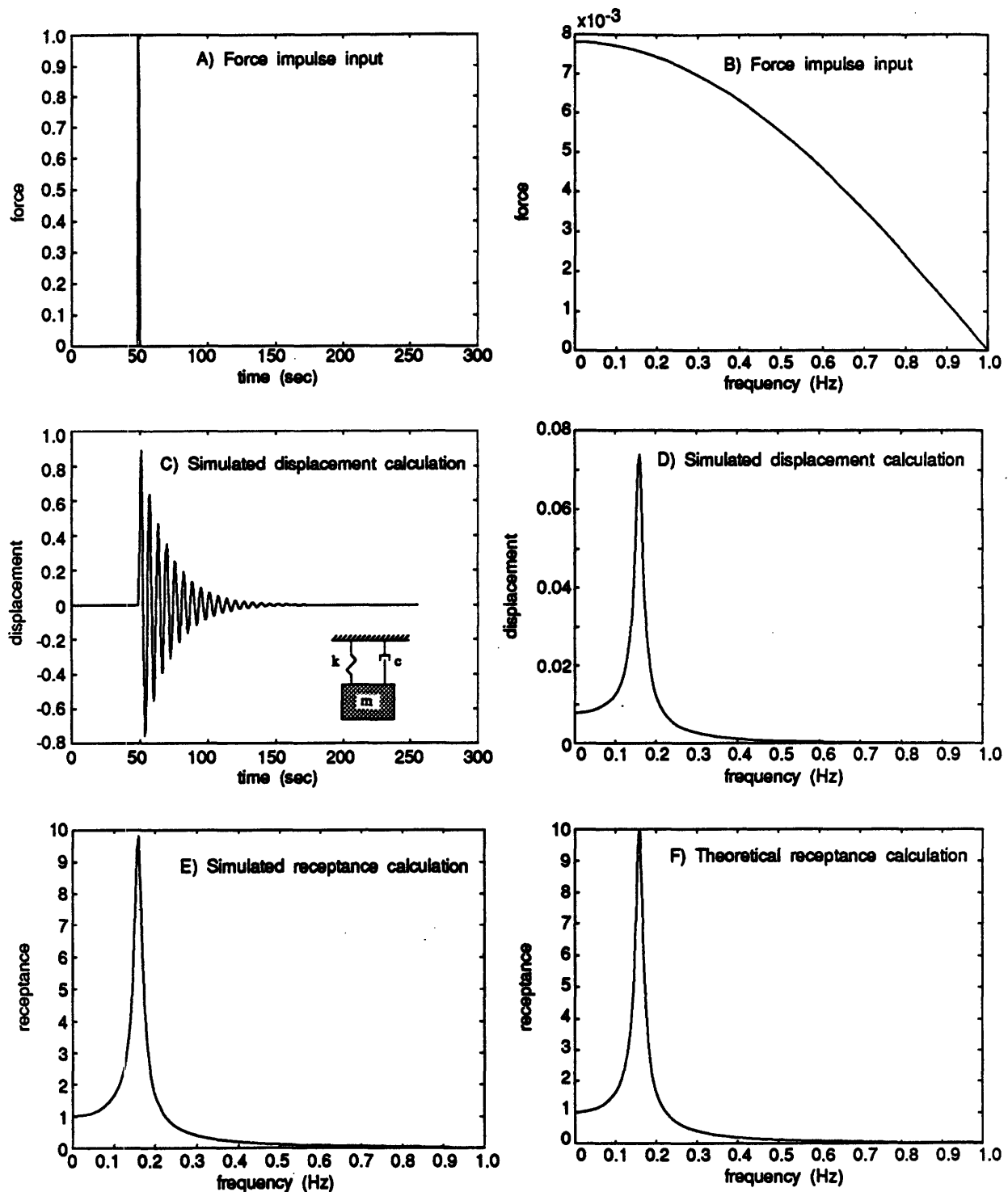


Figure B.3: Simulation of receptance calculation. a) Shows the unit impulse force input 1 second wide and b) its FFT. c) Shows the simulated displacement response to the impulse force input and d) its FFT. e) Shows the receptance calculated from d) divided by b). f) Shows the theoretically calculated receptance. Parameters, $m = 1$, $c = 0.1$, $k = 1$, delta time = 0.5, 512 points.

is that the result no longer depends on the number of points used. To illustrate this point, Figure B.4 shows the results for 1024 points instead of 512 points. It can be seen that the resulting receptance is again in agreement with the result from the Fourier integral. Thus, while the magnitude of an FFT of a transient signal is poorly defined, the ratio of the FFT's of two related signals (e.g. receptance) are properly defined.

B.1 Application to Ball Drop

Although receptance can be experimentally determined using the above technique, a serious problem is encountered if the force input signal cannot be measured. If an impulse hammer is used to excite a structure, then the input waveform is readily available. However, if a ball drop, or similar technique, is used, then the input waveform is not available.

One possible solution to this problem, is to estimate the input waveform. For the ball drop technique, the input force waveform can be estimated using Hertz contact theory (see Appendix A). The Hertz contact theory determines not only the magnitude and the contact time for the force pulse, but it also determines the complete waveform. To make use of this waveform, it must be digitized at the same frequency and with the same number of points as the displacement output, similar to the signals in Figures B.4a and B.4c.

There still is one more variable to be determined; the time of contact. A decision must be made as to when the impulse force input occurred, as shown in Figure B.5. Although the impulse must occur some time prior to there being any response, the exact location must be decided. By positioning the impulse in the wrong location, an error will be introduced into the receptance calculation. Fortunately, the error is only in the phase of the receptance, as shown in Figure B.6. The results are shown for the same second order system previously discussed. In Figure B.6a, the exact solution for the receptance is given, both magnitude and phase. As before, a simulation was done using MATLAB. This time however, after the simulation was calculated, a one second time shift was added to the location of the impulse force input. Then the receptance was determined with this error included. As shown in Figure B.6b, this error only effects the phase of the receptance and not the magnitude. Figure B.6c, shows the result for a negative one second offset.

These results are very encouraging because small errors in the location of the impulse input only affect the receptance phase. Therefore the magnitude of the receptance can be calculated with confidence using the force input waveform calculated from the Hertz contact theory. Of course it is still better to measure the contact force simultaneously with the displacement output, but this is not always possible. If the phase is needed for a modal parameter extraction procedure, then the linear phase taper must be removed as discussed in Subsection 4.2.2.

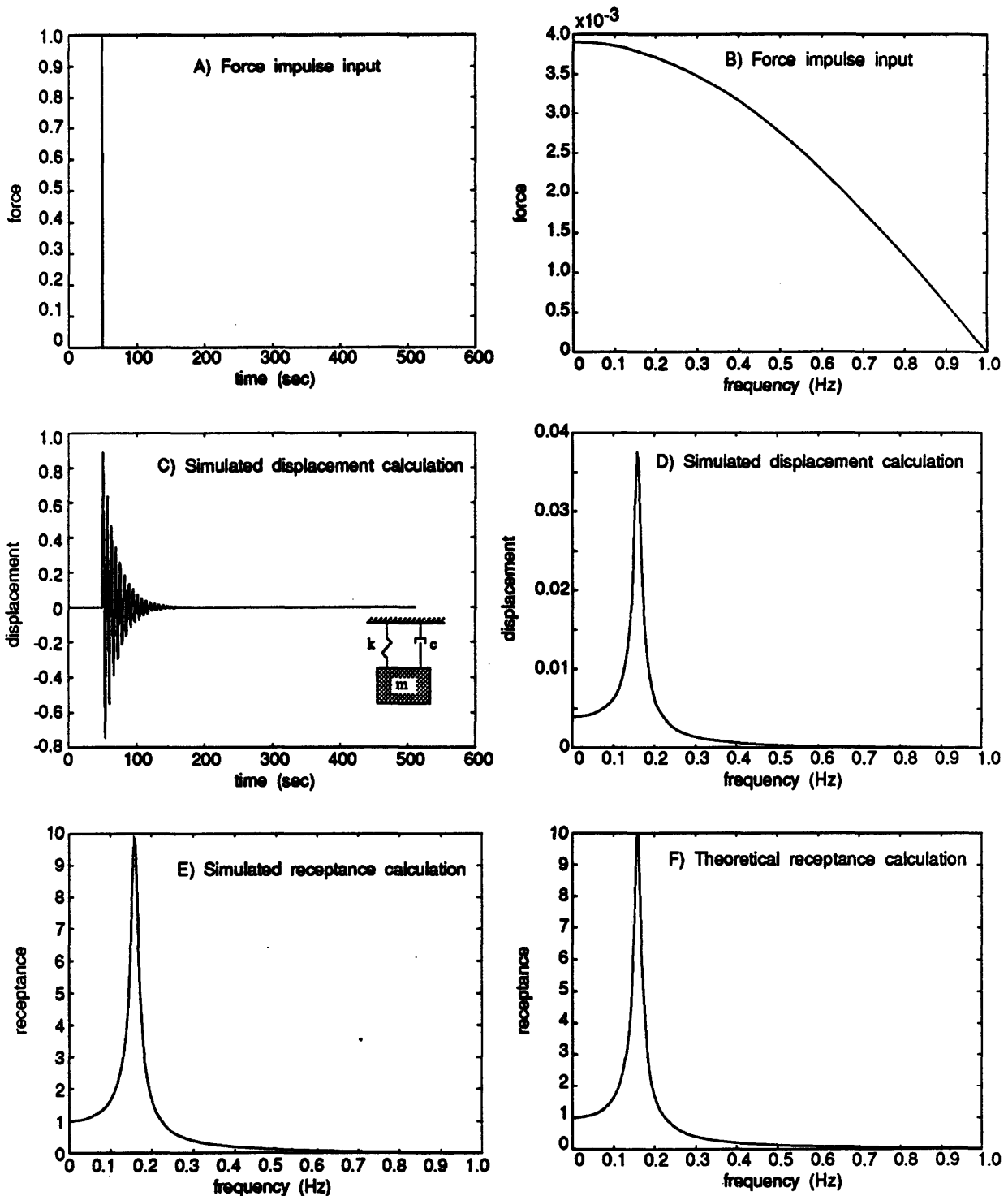


Figure B.4: Simulation of receptance calculation. a) Shows the unit impulse force input 1 second wide and b) its FFT. c) Shows the simulated displacement response to the impulse force input and d) its FFT. e) Shows the receptance calculated from d) divided by b). f) Shows the theoretically calculated receptance. Parameters, $m = 1$, $c = 0.1$, $k = 1$, delta time = 0.5, 1024 points.

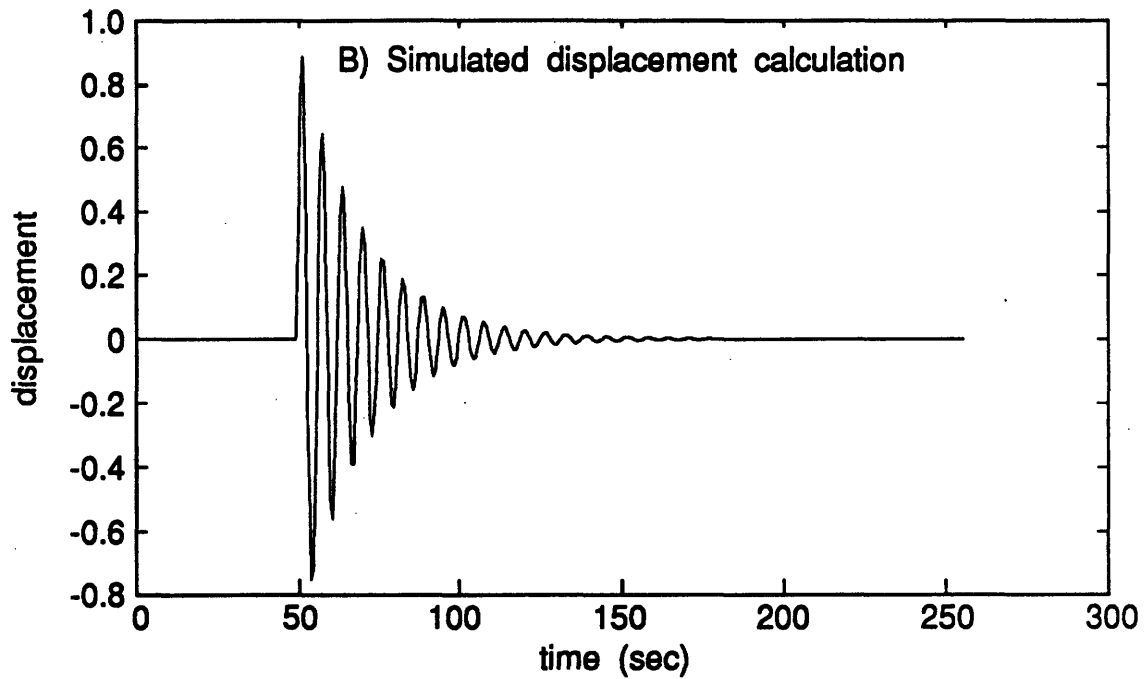
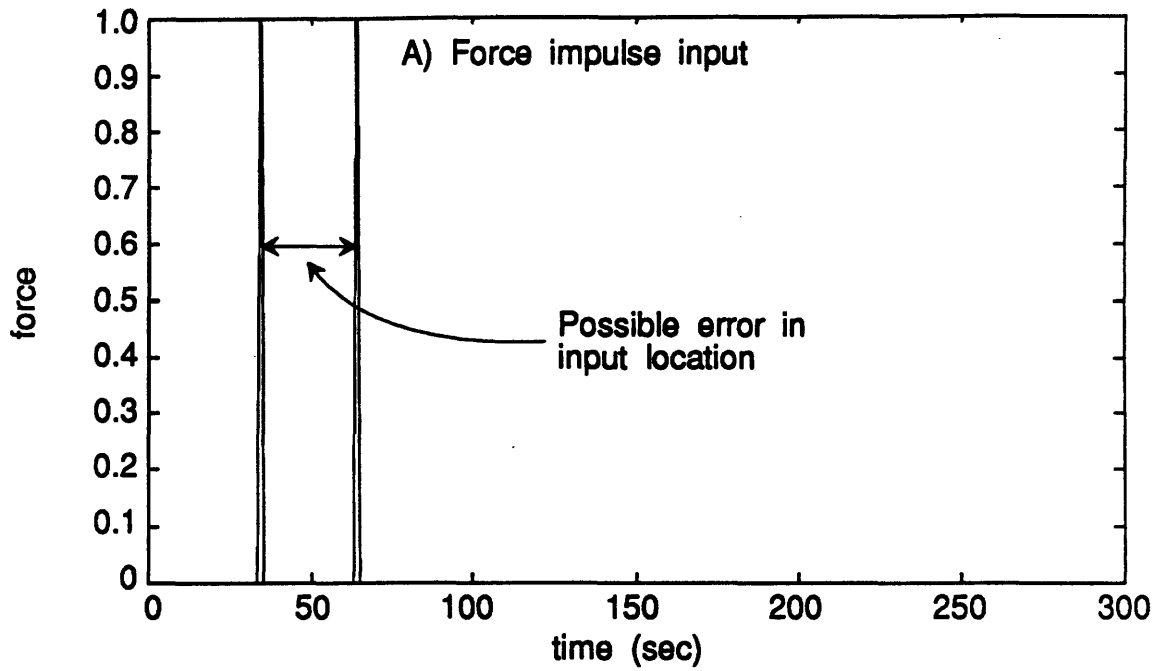


Figure B.5: Possible error in impulse input location due to an inability to directly measure the input force.

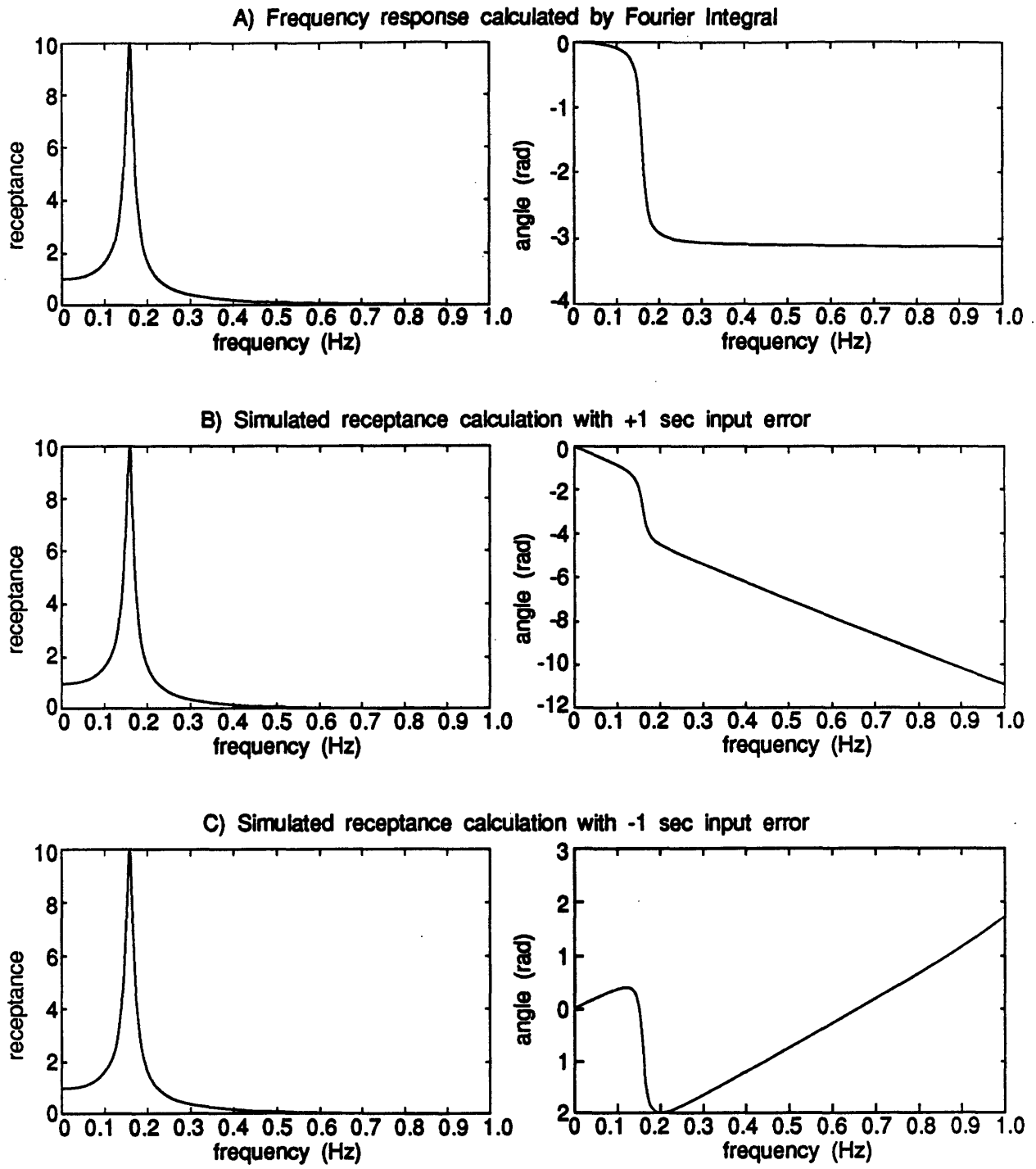


Figure B.6: Illustration of the effect of error in locating the appropriate position in time for the impulse force input. Note that only the phase is affected by the error.

Appendix C

Input File for FEM Model of Slider

The following is the Abaqus input file for the FEM model of the actual (not enlarged) 3380 style slider (read/write head). The model uses 20 node brick elements and calculates the natural frequencies (eigenvalues) and mode shapes (eigenvectors) of the slider. The dimensions are given in millimeters, even though the use of meters would have been preferred. There is a “bug” in the Abaqus software that causes the hidden-line removal routine to fail if the dimensions of the part are too small. As a result, the dimensional units of this model are kg, mm , and seconds.

The Abaqus input file for the enlarged model of the slider is basically the same as the input file for the actual slider. The main differences are that the dimensions are 44 times larger and the properties are changed to the properties of aluminum rather than alumina titanium carbide ($\text{Al}_2\text{O}_3\text{TiC}$).

```
*HEADING
3380 SLIDER, 258 ELEMENTS, 4602 DEGREES OF FREEDOM
**DEFINE THE FIRST ROW OF SLIDER-----
*NODE,NSET=SLIDER
** nodes for first end
   1, 0.000,0.000,0.000
  41, 0.000,0.000,0.089
  81, 0.000,0.000,0.178
 241, 0.000,0.000,0.876
   13, 4.064,0.000,0.000
   53, 4.064,0.000,0.089
   93, 4.064,0.000,0.178
  253, 4.064,0.000,0.876
*NGEN,NSET=EDGEONE
   1,  41,  20
  41,  81,  20
  81, 241,  20
```

```

*NGEN,NSET=EDGETWO
    13, 53, 20
    53, 93, 20
    93, 253, 20
*NFILL,NSET=PLANEA
    EDGEONE,EDGETWO,12,1
*NCOPY,CHANGE NUMBER=2000,OLDSET=PLANEA,SHIFT,NEW SET=PLANEQ
    0.000,0.102,0.000
    0.0,0.0,0.0,0.0,0.0,0.0,0.0
*NFILL,NSET=FILLIN
    PLANEA,PLANEQ,2,1000
*NCOPY,CHANGE NUMBER=4000,OLDSET=PLANEA,SHIFT,NEW SET=PLANEV
    0.000,0.533,0.000
    0.0,0.0,0.0,0.0,0.0,0.0,0.0
*NFILL,NSET=FILLIN
    PLANEQ,PLANEV,2,1000
*NCOPY,CHANGE NUMBER=6000,OLDSET=PLANEA,SHIFT,NEW SET=PLANEG
    0.000,0.761,0.000
    0.0,0.0,0.0,0.0,0.0,0.0,0.0
*NFILL,NSET=FILLIN
    PLANEV,PLANEG,2,1000
*NCOPY,CHANGE NUMBER=12000,OLDSET=PLANEA,SHIFT,NEW SET=PLANEM
    0.000,2.413,0.000
    0.0,0.0,0.0,0.0,0.0,0.0,0.0
*NFILL,NSET=FILLIN
    PLANEG,PLANEM,6,1000
*NCOPY,CHANGE NUMBER=14000,OLDSET=PLANEA,SHIFT,NEW SET=PLANEQ
    0.000,2.642,0.000
    0.0,0.0,0.0,0.0,0.0,0.0,0.0
*NFILL,NSET=FILLIN
    PLANEM,PLANEQ,2,1000
*NCOPY,CHANGE NUMBER=16000,OLDSET=PLANEA,SHIFT,NEW SET=PLANEQ
    0.000,3.073,0.000
    0.0,0.0,0.0,0.0,0.0,0.0,0.0
*NFILL,NSET=FILLIN
    PLANEQ,PLANEQ,2,1000
*NCOPY,CHANGE NUMBER=18000,OLDSET=PLANEA,SHIFT,NEW SET=PLANES
    0.000,3.175,0.000
    0.0,0.0,0.0,0.0,0.0,0.0,0.0
*NFILL,NSET=FILLIN
    PLANEQ,PLANES,2,1000

```

```

*ELEMENT,ELSET=SLIDERE,TYPE=C3D20
37,2001,2003,4003,4001,2041,2043,4043,4041,2002,3003,4002,3001,2042,3043,4042,
3041,2021,2023,4023,4021
*ELGEN,ELSET=SLIDERE
  37, 6,2,1, 2,40,6
  43, 2,40,6
  49, 2,-2000,-36
  13, 6,2,1, 4,40,6, 9,2000,36
 121, 2,-40,-6
 115, 6,2,1, 3,2000,36
 265, 3,-40,-6
 253, 6,2,1, 2,40,6
** MATERIAL Al203-TiC
*SOLID SECTION,MATERIAL=Al203,ELSET=SLIDERE
*MATERIAL,NAME=Al203
** elastic modulus = 3.92e11 Pa, or 3.92e8 kg/(mm sec^2)
*ELASTIC
  3.92E8,0.35
** density = 4.280e3 kg/m^3 or 4.280e-6 kg/mm^3
*DENSITY
  4.280E-6
*ELSET, ELSET=VISIBLE
  37,38,39,40,41,42,
  43,44,45,46,47,48,
  13,14,15,16,17,18,
  19,20,21,22,23,24,
  25,26,27,28,29,30,
  31,32,33,34,35,36,
  67,68,69,70,71,72
 103,104,105,106,107,108,
 139,140,141,142,143,144,
 175,176,177,178,179,180,
 211,212,213,214,215,216,
 247,248,249,250,251,252,
 283,284,285,286,287,288,
 319,320,321,322,323,324,
 318,312,306,
 258,264,270,276,282,
 234,240,246,
 192,198,204,210,
 156,162,168,174,

```

```

120,126,132,138,
90,96,102,
54,60,66
*ELSET, ELSET=FRAME
37,38,39,40,41,42,
43,44,45,46,47,48,
13,14,15,16,17,18,
19,24,
25,30,
31,32,33,34,35,36,
67,72
103,108,
139,144,
175,180,
211,216,
247,252,
283,288,
319,320,321,322,323,324,
318,312,306,
258,264,
234,192,156,120,90
** *****
**          Plot the Initial SLIDER Geometry
** *****
*ELSET, ELSET=SMALL
37
** *****
**          Plot the Initial SLIDER Geometry
** *****
*PLOT
*DETAIL, ELSET=SLIDERE
*VIEWPOINT
  0.5,-1.0,0.5
*DRAW,HIDE
*DRAW,ELNUM
*DRAW,NODENUM
*RESTART,WRITE
*STEP,LINEAR
  GET VIBRATION FREQUENCIES AND MODE SHAPES
*FREQUENCY
  6,,4.57E11,,25

```

```
*PLOT
*DETAIL
*VIEWPOINT
  0.5,-1.0,0.5
*DISPLACED,HIDE
  U,,1
*NODE FILE
  U
*EL PRINT, ELSET=SMALL
  E11
*END STEP
```


Appendix D

Programs for Modal Analysis and Force Identification

D.1 Modal Analysis Programs

The following programs are used to convert ABAQUS output files into frequency response functions (FRF's). In other words, they are used to convert the eigenvalues and eigenvectors into a modal analysis.

The program ABA_READ.C searches through the ABAQUS output file for the eigenvalues and eigenvectors. It writes each eigenvector into its own file, with file names like `file1.`, `file2.`, ..., `file6.` It also writes one file with the eigenvalues, with a file name like `file_evl.`

The matlab program S380TLAC.M uses the data in these files to calculate the frequency response functions using Equation 3.31. The first step is to load the files into Matlab using the program S380.M. The second step is to use MODAL.M and FRF_ACC.M to calculate the accelerance (FRF) for any force input and sensor locations of interest. The sensor location would be the subscript j in Equation 3.31 and the force input location would be the subscript k .

Obviously these programs are not very general purpose. They would only be written to serve the purposes of the research in this thesis.

D.1.1 ABA_READ.C

```
/* Program for extracting eigenvectors from ABAQUS data files */
```

```
#include <stdio.h>
#include <string.h>
#include <ctype.h>
```

```

#include <float.h>
#include <math.h>

main()
{
    double sqrt(double);
    double find_value(char*);
    int number_count(char*);
    int alpha_count(char*);
    int fgetline(FILE*,char*);
    size_t strlen(const char*);
    int strstrsearch(char*,char*);
    void make_search_string(char*,int);
    void make_value_string(char*,int);
    void shorten_string(char*,char*,int);
    char c,input_filename[80];
    char output_filename[80];
    char output[80];
    FILE *stream1,*stream2,*stream3;
    char buffer[151];          /* buffer for a line of text */
    int i,j,k;
    int ch;
    int skip;
    int number_of_rows;
    int buffer_len=0;        /* len of the text buffer */
    int search_string_len=0; /* length of search string */
    char search_string[80];
    char start_buffer[9];    /* first 8 char of buffer */
    int not_found = 1;      /* logical variable */
    int location;           /* where the string was found */
    int end_of_evalues;    /* Have all evalues been found */
    long unsigned line_number=0; /* current line in file */
    int num_of_num=0;      /* number of digits in buffer */
    int num_of_alpha=0;    /* number of letters in buffer */
    char *digits = "+-0123456789";
    int numresult=0,result;
    long unsigned node1,node2;
    float x1,y1,z1,x2,y2,z2,eigenvalue[30];
    long unsigned num_of_data_lines=0;
    int evector = 1;       /* number of correct eigenvector */

```

```

int total_evector;                /* total number of eigenvectors */
char s_evector[17];              /* string of evector */
int len_s_evector;              /* length of s_evector */

/* open input file */
printf("\nEnter input file name: ");
scanf("%s",input_filename);
if ((stream1 = fopen(input_filename,"rt")) == NULL)
{
printf("Could not open file %s\n",input_filename);
exit(0);
}

/* get name of output file */
printf("\nOutput file names are limited to 4 letters with no extension\n");
printf("\nEnter output file name: ");
scanf("%s",output_filename);

/* open index file */
strcpy(output,output_filename);
strcat(output,"_ind");
if ((stream3 = fopen(output,"wt")) == NULL)
{
printf("Could not open file %s\n",output);
exit(0);
}
else
printf("writing file to %s\n",output);

/* FIND LABEL FOR EIGENVALUE OUTPUT */
strcpy(search_string,"E I G E N V A L U E   O U T P U T");
line_number = 0;                /* count lines in file */
not_found = 1;
while(not_found && (feof(stream1)==0) )
{
line_number++;
buffer_len=fgetline(stream1,buffer); /* get a line of text */
location = strstr(buffer,search_string);
if(location != 0)
{

```

```

not_found = 0;      /* found string */
}
}

/* FIND EIGENVALUES */
end_of_evalues =1;
while(end_of_evalues && (feof(stream1)==0) )
{
/* create string to search for like "      1" */
make_evalue_string(search_string, evector);

not_found = 1; /* start the search */
while(not_found && (feof(stream1)==0) )
{
line_number++;
buffer_len=fgetline(stream1,buffer); /* get a line of text */
shorten_string(buffer,start_buffer,8); /* compare first 8 char */
result = strcmp(search_string,start_buffer);
if(result == 0) /* found string */
{
not_found = 0;
eigenvalue[evector]=find_evalue(buffer);
printf("eigenvalue = %e (r/s)} %e Hz\n",
eigenvalue[evector],
((float)sqrt(eigenvalue[evector]))/(2.0*3.14159));
evector++; /* increment to find next e-value */
}
else /* check for end of evalues */
{
location = strstr(buffer,"P A R T");
if(location != 0)
{
end_of_evalues = 0;
not_found = 0; /* found PARTISIPATION FACTOR */
}
}
}
}

total_evector=evector-1;
printf("total number of eectors = %d\n",total_evector);

```

```

/* FIND LABEL FOR FIRST EIGENVECTOR IN THE FILE */
evector = 1;
make_search_string(search_string, evector);
printf("Searching for  %s\n", search_string);
not_found = 1;
while(not_found && (feof(stream1) == 0) )
{
line_number++;
buffer_len = fgetline(stream1, buffer);    /* get a line of text */
location = strstr(buffer, search_string);
if(location != 0)
{
not_found = 0;
printf("Found %s\n", search_string);
}
}

```

```

/* Now we are positioned in the file so that the data is all
sequencial from this point on.  We do have to avoid the page
label heading.  The program reads in a line and determines
the number of digits in the line with the number_count()
function.  If there is more than 30 digits than the program
assumes it is eigenvector data.  If it is less than 30 then
it checks to see if there is a new eigenvector by looking for
"E I G E N V A L U E  N U M B E R".
The criterion used to see if a line contains eigenvector data
is 1) less than 4 alpha,  2) greater than 16 numbers,
and 3) 50 characters long */

```

```

while((feof(stream1) == 0))          /* loop for all eigenvectors */

```

```

{
/* open output file */
strcpy(output,output_filename);
itoa(evector,s_evector,10);
strcat(output,s_evector);
if ((stream2 = fopen(output,"wt")) == NULL)
{
printf("Could not open file %s\n",output);
exit(0);
}
else
printf("writing file to %s\n",output);

evector++;
make_search_string(search_string,evector);
num_of_data_lines=0;

not_found=1;
while((feof(stream1)==0)&&not_found)
{
line_number++;
buffer_len=fgetline(stream1,buffer); /* get a line of text */
num_of_num=number_count(buffer);
num_of_alpha=alpha_count(buffer);
if(num_of_num>16 && (buffer_len==50) && (num_of_alpha<4))
/* it is eigenvector data */
{
num_of_data_lines++;
numresult = strchr(buffer,digits);
sscanf(&buffer[numresult],"%lu",&node1);
numresult += strchr(&buffer[numresult]," ");
numresult += strchr(&buffer[numresult],digits);
sscanf(&buffer[numresult],"%f",&x1);
numresult += strchr(&buffer[numresult]," ");
numresult += strchr(&buffer[numresult],digits);
sscanf(&buffer[numresult],"%f",&y1);
numresult += strchr(&buffer[numresult]," ");
numresult += strchr(&buffer[numresult],digits);
sscanf(&buffer[numresult],"%f",&z1);
/* write data to file */
fprintf(stream2,"%+e\n%+e\n%+e\n",x1,y1,z1);
}
}
}

```

```

        if((evector-1) == 1)      /* only write index file once */
    {
        fprintf(stream3,"%lu\t%lu\tX\n",
        3*(num_of_data_lines-1)+1,node1);
        fprintf(stream3,"%lu\t%lu\tY\n",
        3*(num_of_data_lines-1)+2,node1);
        fprintf(stream3,"%lu\t%lu\tZ\n",
        3*(num_of_data_lines-1)+3,node1);
    }
    }
    else                          /* labels in the ABAQUS file */
    {                              /* look for EIGENVECTOR label */
        location = strstr(buffer,search_string);
        if(location == 0)
not_found = 1;
        else                      /* found EIGENVECTOR label */
    {
        not_found = 0;
        printf("closing file to %s\n\n",output);
        fclose(stream2);
        printf("%s\n",search_string);
    }
    }
}

        fclose(stream1);
        fclose(stream2);
        fclose(stream3);

        /* open eigenvalue file */
        strcpy(output,output_filename);
        strcat(output,"_ev1");
        if ((stream3 = fopen(output,"wt")) == NULL)
    {
        printf("Could not open file %s\n",output);
        exit(0);
    }
    else
        printf("writing file to %s\n",output);

```

```

    /* write eigenvalues */
    for(i=1;i<=total_evector;i++)
fprintf(stream3,"%+e\n",eigenvalue[i]);
    fclose(stream3);

```

```

    exit(0);

```

```

}

```

```

/* ***** */
/* ***** function to get a line of text ***** */
/* ***** */

```

```

int fgetline(stream,buffer)
FILE *stream;
char buffer[];
{
    int i,j;
    int ch;

    ch = fgetc(stream);
    for(i=0; (i<150)&&(feof(stream)==0)&&(ch != '\n');i++)
{
buffer[i] = ch;
ch = fgetc(stream);
}
    buffer[i] = '\0';
    return(i);
}

```

```

/* ***** */
/* ***** String search function ***** */
/* ***** */

```

```

/* function returns the location of the string if it is found,
otherwise it returns a zero. */

```



```

int strstrsearch(buffer,search_string)
char buffer[];          /* string to be search through */
char search_string[];  /* string to be search for */
{
    int buffer_len;          /* number of characters in string */
    int search_string_len;
    int i,k,not_found;

    search_string_len = strlen(search_string);
    buffer_len = strlen(buffer);

    not_found = 1;
    for(i=0;i<buffer_len && not_found ;i++)
    {
        if(buffer[i] == search_string[0]) /* find first character */
        {
            k=1;          /* check the rest of the characters */
            while((buffer[i+k]==search_string[k]) && k<search_string_len)
                k++;
            if(k == search_string_len) /* did they all match */
                not_found = 0;
        }
    }
    if(not_found == 0)
        return(i);
    else
        return(0);
}

```

```

/* ***** */
/* ***** Count the number of Digits ***** */
/* ***** */

```

```

int number_count(buffer)
char buffer[];          /* string */
{
    int buffer_len;          /* number of characters in string */

```

```

int i,number_of_digits=0;

buffer_len = strlen(buffer);
for(i=0;i<buffer_len;i++)
{
    if(isdigit(buffer[i]))
number_of_digits++;
}
return(number_of_digits);
}

```

```

/* ***** */
/* ***** Count the number of alpha ***** */
/* ***** */

```

```

int alpha_count(buffer)
char buffer[];          /* string */
{
    int buffer_len;    /* number of characters in string */
    int i,number_of_alpha=0;

    buffer_len = strlen(buffer);
    for(i=0;i<buffer_len;i++)
    {
        if(isalpha(buffer[i]))
number_of_alpha++;
    }
    return(number_of_alpha);
}

```

```

/* ***** */
/* Function to make a string to search for in the ABAQUS output file */
/* ***** */

```

```

void make_search_string(string,evector)
char *string;
int evector;
{

```

```

char s_evector[17];          /* string of evector */
int len_s_evector;         /* length of s_evector */
int i;

itoa(evector,s_evector,10);
len_s_evector = (int)strlen(s_evector);
strcpy(string,"E I G E N V A L U E   N U M B E R");
for(i=0;i<(6-len_s_evector);i++) /* pad with spaces */
    strcat(string," ");
strcat(string,s_evector);
}

/* ***** */
/* Function to make a EIGENVALUE search string */
/* ***** */

void make_evalue_string(string,evector)
char *string;
int evector;
{
    char s_evector[17];          /* string of evector */
    int len_s_evector;         /* length of s_evector */
    int i;

    /* make a string like "      1" */

    itoa(evector,s_evector,10);
    len_s_evector = (int)strlen(s_evector);
    strcpy(string,"");
    for(i=0;i<(8-len_s_evector);i++) /* pad with spaces */
        strcat(string," ");
    strcat(string,s_evector);
}

/* ***** */
/* Function to shorten a string */
/* ***** */

```

```

void shorten_string(string,return_string,len)
char *string;
char *return_string;
int len;          /* amount to shorten */
{
    int string_len;
    int i;

    string_len = strlen(string);
    if(string_len >(len+1)) /* if long enough to shorten */
        {
            /* copy first 8 char to return_string */
            for(i=0;i<len;i++)
return_string[i] = string[i];
            return_string[len] = '\0';
        }
    else
        strcpy(return_string,string);
}

/* ***** */
/* find the value of the eigenvalue within a string */
/* ***** */

double find_evalue(buffer)
char *buffer;

{
    double eigenvalue = 0;
    int location,numresult;
    char *digits = "--+0123456789";

    location = 0; /* search for first digit */
    numresult = strcspn(&buffer[location],digits);
    location = numresult+location;
    numresult = strcspn(&buffer[location]," ");
    location = numresult+location;
    /* position now past the evalue number, e.g. 1,2,3,4,5,6 */
    numresult = strcspn(&buffer[location],digits);

```

```
location = numresult+location;
/* position now at location of eigenvalue in (r/s) */
sscanf(&buffer[location],"%le",&eigenvalue);
return(eigenvalue);
}
```

D.1.2 S380TLAC.M

```
% CALCULATE MODAL ANALYSIS FOR s3806 SLIDER
% Data comes from ABAQUS output files
% The accelerance is calculated for a variety of input locations
%
%
clear
!erase s380.met
% load the e-value and e-vectors
s380
% Frequency vector in radians
w = (2*pi).*[0:500:1000000]';
%
%
% FIRST POSITION
%
% input 3013z, sensor 15251z
a1 = modal(evec,3816,804);
% calc data for drawing graph
r1 = frf_acc(a1,eval,w);
axis([0,1000000,1,9]);
semilogy(w./(2*pi),abs(r1))
title('accelerance 3816,804; input 3013z, sensor 15251z')
xlabel('Frequency (Hz)')
ylabel('Accelerance')
meta s380
%
%
% SECOND POSITION
%
% input 3011z, sensor 15251z
a2 = modal(evec,3816,801);
r2 = frf_acc(a2,eval,w);
axis([0,1000000,1,9]);
semilogy(w./(2*pi),abs(r2))
title('accelerance 3816,801; input 3011z, sensor 15251z')
xlabel('Frequency (Hz)')
ylabel('Accelerance')
meta s380
%
```

```

%
% THIRD POSITION
%
% input 3009z, sensor 15251z
a3 = modal(evec,3816,798);
r3 = frf_acc(a3,eval,w);
axis([0,1000000,1,9]);
semilogy(w./(2*pi),abs(r3))
title('accelerance 3816,798; input 3009z, sensor 15251z')
xlabel('Frequency (Hz)')
ylabel('Accelerance')
meta s380
%
%
% FOURTH POSITION
%
% input 3007z, sensor 15251z
a4 = modal(evec,3816,795);
r4 = frf_acc(a4,eval,w);
axis([0,1000000,1,9]);
semilogy(w./(2*pi),abs(r4))
title('accelerance 3816,795; input 3007z, sensor 15251z')
xlabel('Frequency (Hz)')
ylabel('Accelerance')
meta s380
%
%
% FIFTH POSITION
%
% input 3005z, sensor 15251z
a5 = modal(evec,3816,792);
r5 = frf_acc(a5,eval,w);
axis([0,1000000,1,9]);
semilogy(w./(2*pi),abs(r5))
title('accelerance 3816,792; input 3005z, sensor 15251z')
xlabel('Frequency (Hz)')
ylabel('Accelerance')
meta s380
%
%
% SIXTH POSITION

```

```

%
% input 3003z, sensor 15251z
a6 = modal(evec,3816,789);
r6 = frf_acc(a6,eval,w);
axis([0,1000000,1,9]);
semilogy(w./(2*pi),abs(r6))
title('accelerance 3816,789; input 3003z, sensor 15251z')
xlabel('Frequency (Hz)')
ylabel('Accelerance')
meta s380
%
%
% SEVENTH POSITION
%
% input 3001z, sensor 15251z
a7 = modal(evec,3816,786);
r7 = frf_acc(a7,eval,w);
axis([0,1000000,1,9]);
semilogy(w./(2*pi),abs(r7))
title('accelerance 3816,786; input 3001z, sensor 15251z')
xlabel('Frequency (Hz)')
ylabel('Accelerance')
meta s380
%
%
% REPEAT FOR TANGENTIAL FORCE, X DIRECTION
%
% FIRST POSITION
%
% input 3013x, sensor 15251z
aix = modal(evec,3816,802);
% calc data for drawing graph
rix = frf_acc(aix,eval,w);
axis([0,1000000,1,9]);
semilogy(w./(2*pi),abs(rix))
title('accelerance 3816,802; input 3013x, sensor 15251z')
xlabel('Frequency (Hz)')
ylabel('Accelerance')
meta s380
%

```



```

%
% SECOND POSITION
%
% input 3011x, sensor 15251z
a2x = modal(evec,3816,799);
r2x = frf_acc(a2x,eval,w);
axis([0,1000000,1,9]);
semilogy(w./(2*pi),abs(r2x))
title('accelerance 3816,799; input 3011x, sensor 15251z')
xlabel('Frequency (Hz)')
ylabel('Accelerance')
meta s380
%
%
% THIRD POSITION
%
% input 3009x, sensor 15251z
a3x = modal(evec,3816,796);
r3x = frf_acc(a3x,eval,w);
axis([0,1000000,1,9]);
semilogy(w./(2*pi),abs(r3x))
title('accelerance 3816,796; input 3009x, sensor 15251z')
xlabel('Frequency (Hz)')
ylabel('Accelerance')
meta s380
%
%
% FOURTH POSITION
%
% input 3007x, sensor 15251z
a4x = modal(evec,3816,793);
r4x = frf_acc(a4x,eval,w);
axis([0,1000000,1,9]);
semilogy(w./(2*pi),abs(r4x))
title('accelerance 3816,793; input 3007x, sensor 15251z')
xlabel('Frequency (Hz)')
ylabel('Accelerance')
meta s380
%
%
% FIFTH POSITION

```

```

%
% input 3005x, sensor 15251z
a5x = modal(evec,3816,790);
r5x = frf_acc(a5x,eval,w);
axis([0,1000000,1,9]);
semilogy(w./(2*pi),abs(r5x))
title('accelerance 3816,790; input 3005x, sensor 15251z')
xlabel('Frequency (Hz)')
ylabel('Accelerance')
meta s380
%
%
% SIXTH POSITION
%
% input 3003x, sensor 15251z
a6x = modal(evec,3816,787);
r6x = frf_acc(a6x,eval,w);
axis([0,1000000,1,9]);
semilogy(w./(2*pi),abs(r6x))
title('accelerance 3816,787; input 3003x, sensor 15251z')
xlabel('Frequency (Hz)')
ylabel('Accelerance')
meta s380
%
%
% SEVENTH POSITION
%
% input 3001x, sensor 15251z
a7x = modal(evec,3816,784);
r7x = frf_acc(a7x,eval,w);
axis([0,1000000,1,9]);
semilogy(w./(2*pi),abs(r7x))
title('accelerance 3816,784; input 3001x, sensor 15251z')
xlabel('Frequency (Hz)')
ylabel('Accelerance')
meta s380

```

D.1.3 S380.M

```
% load the eigenvectors output from ABA_READ.EXE program
% the units are in Kg, mm , sec
load s3801
load s3802
load s3803
load s3804
load s3805
load s3806
% load eigenvalues
load s380_evl
eval=s380_evl;
% make them mass normalized, see Ewins page 40-41
general_mass = [6.48845e-6
                1.03677e-5
                8.41808e-6
                6.10529e-6
                8.75976e-6
                1.52078e-5];
evec1 = s3801/sqrt(general_mass(1));
evec2 = s3802/sqrt(general_mass(2));
evec3 = s3803/sqrt(general_mass(3));
evec4 = s3804/sqrt(general_mass(4));
evec5 = s3805/sqrt(general_mass(5));
evec6 = s3806/sqrt(general_mass(6));
evec = [evec1 evec2 evec3 evec4 evec5 evec6];
pack
```

D.1.4 MODAL.M

```
function alpha = modal(evector,j,k)
% modal analysis based on equation 2.40 for D.J. Ewins book
% Modal Testing: Theory and Practice
%
%
%           N   rhj*rhk
%   '(j,k) = d  -----
%           r=1 (wr} - w})
%
% the function is used as follows
%
%           alpha = modal(evector,j,k)
%
% alpha is the receptance for a force at k
% and a displacement at j.
% evector is the M-orthonormalized eigenvector matrix
%
%
[M,N] = size(evector);
% create a vector to hold the rhj*rhk products (equ 2.40)
alpha = ones(N,1);

% value of r determines the column of evector
for r = 1:N,
alpha(r,1) = evector(j,r)*evector(k,r);
end
```

D.1.5 FRF_ACC.M

```
function response = frf_acc(alpha,eval,w)
% takes the alpha values from MODAL.M and calculate the
% response to a given range of frequencies w. The values
% of eval should be in (rad/sec)} and w should be in
% (rad/sec).
[M,N] = size(alpha);
[M1,N1] = size(w);
% M is the number of modes
response = zeros(M1,1);
for i = 1:M,
    response = response -(w.*w).*( alpha(i)./(eval(i) -w.^2) );
end
```

D.2 Force Identification using Magnitude and Phase

The following Matlab programs were used in the force identification process using magnitude and phase. The raw data comes from the Unkelscope program, is converted for use in Matlab, and is processed in Matlab.

The steps for the procedure are the following.

1. Convert the Unkelscope data files to Matlab files using the UTRANS.EXE program that comes with Unkelscope.
2. Use the USCO2MAT.M program to patch the time split files together. (Note that the UTRANS.EXE program splits up the data files into two parts like `file1.mat` and `file2.mat`.) But the following must be changed in the USCO2MAT.M program.
 - (a) Gain of the amplifier used.
 - (b) Filename
 - (c) End of the filename, for example change all occurrences of 11 and 21 to 21 and 22 or a1 and a2, respectively.
3. Clear away any unwanted variables. Set up the frequency vector, e.g.
`f = 50000*(0:4095)'/8191;` and set up a vector with the locations of the peaks, e.g.
`peaks = [596;840;1287;1348];`.
4. Calculate the FFT and remove the linear phase taper, e.g.
`A1d01 = re_taper(f,a1d01,peaks);`
5. find modal constants, e.g.
`mp01a = find_all(peaks,f,A1d01);`
6. Save data, e.g.
`save set2_a`
7. Begin pattern matching
8. Load the database of modal constants, A, into DATABASE.MAT.
9. Use the PATMATCH.M program to compare the modal constants from an individual ball drop test with the database, e.g.
`[loc(1),for(1),err01] = patmatch(mp01a(3,:).*sign(mp01a(4,:)))'`;

D.2.1 USCO2MAT.M

% USCO2MAT.M translates uscope (utrans) files into more
% reasonable matlab files

```
gain = 50;                % amplifier gain
file = 'da';              % part file name
for i = 1:14,
    ai = num2str(i);      % index of test number
    if i<10
        ai= ['0',int2str(i)]; % pad with a zero
    end
    eval(['load ',file,ai,'1']); % load a31
    uclear
    eval(['t',file,ai,' = T1;']); % td3 = T1;
    eval(['a1',file,ai,' = V1;']); % aid3 = V1;
    eval(['a2',file,ai,' = V2;']); % aid3 = V2;
    eval(['load ',file,ai,'2']); % load a32
    uclear;
    eval(['t',file,ai,' = [t',file,ai,';T1;']);
        % td3 = [td3;T1];
    eval(['a1',file,ai,' = 9.8/(0.010*gain)*[a1',file,ai,';V1;']);
    eval(['a2',file,ai,' = 9.8/(0.010*gain)*[a2',file,ai,';V2;']);
        % a2d3 = (1.0/0.010)*9.8*(1.0/100)*[a2d3;V1];
        % 0.010 V/g and 9.8 m/sec^2/g and gain 100
    clear T1 V1 V2
    eval(['save ',file,ai,' t',file,ai,' a1',file,ai,' a2',file,ai])
        %save a3 td3 aid3 a2d3
    whos
end
```

D.2.2 RE_TAPER.M

```
function frf = re_taper(f,acceler,peaks);
% Keep changing the angle until all the resonant circles
% are at +/- 90 degrees.
% name = 'a2d04';
%
% Usage
%
%     frf = re_taper(freqHz,acceler,peaks);
%

% find the starting point of the vector
offset = mean(acceler(1:100));
maxacc = max(acceler-offset);
i = 1;
while (acceler(i)-offset) < (maxacc*0.05),
    i = i + 1;
end

disp(i)

frfnew = fft(shift(acceler,i-10))/(length(acceler)/2);
frfnew = frfnew(1:1600);
f = f(1:1600);
frfnew(1) = 0;
parameters=peaksfit(peaks,f,frfnew);
clear perr;
i = 1;
perr = 90/360*(2*pi);
while((perr/(2*pi)*360 > 10) & (i <=20)), % 10 degree error limit
    frfnew=r_taper(parameters,peaks,f,frfnew);
    parameters=peaksfit(peaks,f,frfnew);
    p_err = peak_err(parameters);
    perr=mean(abs(p_err));
    if abs(frfnew(peaks(4)))/max(abs(frfnew)) < 0.05,
        disp('peak 4 eliminated from error');
        perr=mean(abs(p_err(1:3)));
    end
    if abs(frfnew(peaks(2)))/max(abs(frfnew)) < 0.05,
        disp('peak 2 eliminated from error');
```



```
    perr=mean(abs([p_err(1);p_err(3);p_err(4)]));
end
    i = i + 1;
end

if i > 20,
    error('could not line up circles after 20 tries, RE_TAPER.M')
end
frf = frfnew;
%axis([1,10,0,60]);
%axis('normal');
%eval(['meta ',name,'err'])
%eval(['meta n',name,int2str(i)]);
```

SHIFT.M

```
function x2 = shift(x1,shiftd);
% Turns a vector around
%      x2 = shift(x1,amount_of_shift);
xlen = length(x1);
x2 = ones(xlen,1);
xsize = size(x1);
if shiftd < 0,
    error('shift must be positive, SHIFT.M')
end
if xsize(1) < xsize(2),
    error('row vector given when column expected, SHIFT.M')
end
x2 = [x1(shiftd+1:xlen,:);x1(1:shiftd,:)];
```

PEAKSFIT.M

```
function parameters = peaksfit(peaks,freq,frf);
% Function PEAKSFIT.M fits circles the peaks in the frequency
% response function
% Usage
%
%   parameters = peaksfit(peaks,freq,frf);
%
%
npeaks = length(peaks);
para= ones(4,npeaks);      % space for results
for i = 1:npeaks,
    x = real(frf(peaks(i)-10:peaks(i)+10));
    y = imag(frf(peaks(i)-10:peaks(i)+10));
    para(:,i)=circ_fit(x,y);
end
parameters = para;
%
%
% make plot of original data and fit circle
yp = ones(101,npeaks);
xp = ones(101,npeaks);
for j = 1:npeaks,
    R0 = para(1,j);
    x0 = para(2,j);
    y0 = para(3,j);
    for i = 1:101,
        theta = (i-1)/100*2*pi;
        xp(i,j) = R0*cos(theta)+x0;
        yp(i,j) = R0*sin(theta)+y0;
    end
end
axis('square')
xrange=max([abs(max(max(xp))),abs(min(min(xp)))]);
yrange=max([abs(max(max(yp))),abs(min(min(yp)))]);
trange = max([xrange,yrange]);
axis([-trange,+trange,-trange,+trange]);
plot(real(frf),imag(frf),'+w',xp,yp,'-r');
```

R_TAPER.M

```
function frfnew = r_taper(parameters,peaks,freq,frf);
% Function R_TAPER.M removes a linear phase taper from the frf
% data. It does this by making sure that the centers of the
% circle line up with +/- 90 degrees.
% Usage
%
%   frfnew = r_taper(parameters,peaks,freq,frf);
%
% The PARAMETERS parameter is whos columns are
% [R0;X0;Y0;sum_of_error] and each column is for an new peak in
% the PEAKS vector. This PARAMETERS is provided
% by the PEAKSFIT.M function. The PEAKS vector contain the index
% location of the peaks in FREQ and FRF. The FREQ vector is
% in Hz.
%
% calculate angle of the center of the first peak
x0 = parameters(2,1);
y0 = parameters(3,1);
G = atan2(y0,x0);
% this dG is how close the circle can be to +/- 90
% before it is rotated 180 degrees
dG = 0.01;
% determine its quadrant
if (pi/2-dG < G) & (G <= pi),
    %disp('CASE 1A')
    Gerror = 3*pi/2-G;
elseif (-pi < G) & (G <= -pi/2-dG),
    %disp('CASE 1B')
    Gerror = -pi/2-G;
elseif (-pi/2-dG < G) & (G <= pi/2-dG),
    %disp('CASE 2')
    Gerror = pi/2-G;
else
    error('R_TAPER.M, angle of circle does not meet conditions')
end
%disp(Gerror)

t0 = Gerror/(2*pi*freq(peaks(1)));
```

```
%disp(t0)
```

```
% Create a new FRF by dividing by an exponential taper  
frfnew = frf./exp(-sqrt(-1)*2*pi*freq*t0);  
plot(real(frf),imag(frf),real(frfnew),imag(frfnew))
```

PEAK_ERR.M

```
function p_error = peak_err(parameters);
% Function PEAK_ERR.M determines how well the resonant circles
% line up with the +/- 90 angle.
% Usage
%
%   peak_error = peak_err(parameters);
%
%
temp=size(parameters);
npeaks = temp(2);
Gerror = ones(npeaks,1);

for i = 1:npeaks,
    x0 = parameters(2,i);
    y0 = parameters(3,i);
    G = atan2(y0,x0);
    % determine its quadrant
    if (0 < G) & (G <= pi),
        Gerror(i) = pi/2-G;
    elseif (-pi < G) & (G <= 0),
        Gerror(i) = -pi/2-G;
    else
        error('PEAK_ERR.M, angle of circle does not meet conditions')
    end
end
p_error = Gerror;
```

D.2.3 FIND_ALL.M

```
function modal_p = find_all(peaks,f,frf)
% FIND_ALL.M uses FINDFREQ.M to find all the modal constants
% for a frf. The function FINDFREQ.M only finds the modal
% constants for a single peak. This function takes a vector
% of peak locations (as an index) and runs them through the
% FINDFREQ.M function one at a time and assembles them into
% a matrix of modal constants
% Usage
%           modal_p = find_all(peaks,freqHz,frf)
% where
%           modal_p = [ f_r1  f_r2  f_rn
%                       eta_r1 eta_r2 eta_rn
%                       A_r1  A_r2  A_rn
%                       phi_r1 phi_r2 phi_rn ]
%
% f_rn is the resonance frequency in Hertz, eta_rn is the
% loss factor, A_rn is the modal constant, and phi_r is the
% angle of the modal constant.
%
% The function MAKE_ACC.M can be used to make a graph of the
% frf from the modal parameters.

for i = 1:length(peaks),
    modal_p(1:4,i) = findfreq(peaks(i),f,frf);
end
```

FINDFREQ.M

```
function modal_p = findfreq(idd,f,frf);
% find the peaks frequency when given 4 points around the
% resonance frequency.
% Usage
%     modal_parameters = findfreq(peak_location,freqHz,frf);
% where
%     modal_parameters = [f_r;eta_r;A_r;phi_r]
%
% It look for a change in sign in the second derivative of
% of the angle theta in a range of +/-10 of the user given
% peak location. It uses this result to select 2 data points
% before and after the resonant frequency for use in second
% order interpolation scheme.

% *****
% ***** set up a table of finite differences *****
% *****
ind = (idd-2:idd+2); % select data points near peak
theta = angle(frf(ind)); % phase angle of frf
n = length(theta); % number of data points
dtheta = theta(1:n-1)-theta(2:n);
ddtheta = dtheta(1:n-2)-dtheta(2:n-1);
dddtheta = ddtheta(1:n-3)-ddtheta(2:n-2);
clg;subplot(111);clg;subplot(221);
plot(ddtheta);
%plot(dddtheta);
[junk,ipeak]=max(abs(dddtheta)); % find maximum change

% *****
% ***** Begin second order interpolation *****
% *****
idd = idd + ipeak - 2;
ind = (idd-1:idd+2); % select 4 data points near peak
omega = 2*pi*f(ind); % convert to radian frequency
theta = angle(frf(ind)); % phase angle of frf
omega2 = omega.^2;
v0 = omega2(0+1);
v1 = omega2(1+1);
```



```

v2 = omega2(2+1);
v3 = omega2(3+1);
fv0 = theta(0+1);
fv1 = theta(1+1);
fv2 = theta(2+1);
fv3 = theta(3+1);
fv0v1 = (fv0 - fv1)/(v0-v1);
fv1v2 = (fv1 - fv2)/(v1-v2);
fv2v3 = (fv2 - fv3)/(v2-v3);
fv0v1v2 = (fv0v1-fv1v2)/(v0-v2);
fv1v2v3 = (fv1v2-fv2v3)/(v1-v3);
fv0v1v2v3 = (fv0v1v2-fv1v2v3)/(v0-v3);

% create a range of omega^2 to plot the data over.
v = (v0:(v3-v0)/50:v3)';

% make interpolation function
fv= fv0 + ..
    (v-v0)*fv0v1 + ..
    (v-v0).*(v-v1).*fv0v1v2 + ..
    (v-v0).*(v-v1).*(v-v2)*fv0v1v2v3;
% calculate the minimum of the function.
v_min = (1/3)*((v0+v1+v2)-fv0v1v2/fv0v1v2v3);
omega_r = sqrt(v_min); % resonance frequency (radian)
f_r = omega_r/(2*pi); % resonance frequency (Hz)

fv_min= fv0 + ..
    (v_min-v0)*fv0v1 + ..
    (v_min-v0).*(v_min-v1).*fv0v1v2 + ..
    (v_min-v0).*(v_min-v1).*(v_min-v2)*fv0v1v2v3;
plot(sqrt(omega2)/(2*pi),theta/(pi)*180,..
    sqrt(v)/(2*pi),fv/(pi)*180, ..
    sqrt(v_min)/(2*pi),fv_min/(pi)*180,'bo');
ylabel('angle(degrees)');xlabel('freq (Hz)');

df = fv0v1 + ..
    (2*v-(v0+v1))*fv0v1v2 + ..
    (3*(v.^2)-2*(v0+v1+v2)*v+(v0*v2+v0*v1+v1*v2))*fv0v1v2v3;
plot(sqrt(v)/(2*pi),df);
ylabel('d(theta)/d(omega^2)');xlabel('freq (Hz)');
peakfreq = f_r;

```

```

% *****
% ***** find peak magnitude of frf *****
% *****
% find the magnitude of the FRF at the resonant frequency by
% finding the intersection of the line to the resonant frequency
% and the circle fit to the data.
pa= circ_fit(real(frf(idd-10:idd+10)),imag(frf(idd-10:idd+10)));
R0 = pa(1); x0 = pa(2); y0 = pa(3);
[xr,yr] = linecirc(fv_min,R0,x0,y0);
frf_peak = xr+sqrt(-1)*yr;
plot(f(idd-5:idd+5),abs(frf(idd-5:idd+5)),...
     [f_r;f_r],[max(abs(frf(idd-5:idd+5)));0],f_r,abs(frf_peak),'go')
ylabel('vibration');xlabel('freq (Hz)');title('Peak Frequency')

% *****
% ***** find loss factor *****
% *****
xr = xr; yr = yr;           % location of resonance
xc = x0; yc = y0;         % location of center
subplot(111);clg,axis('square');
for i = 1:5,
    for j = 1:5,
        xa=real(frf(idd-i)); % location of a point before resonance
        ya=imag(frf(idd-i));
        omega_a = f(idd-i)*2*pi;
        xb=real(frf(idd+j)); % location of a point after resonance
        yb=imag(frf(idd+j));
        omega_b = f(idd+j)*2*pi;
        maxplot=max(abs([xc,yc,xa,ya,xb,yb,xr,yr]))*1.20;
        axis([-maxplot,maxplot,-maxplot,maxplot]);
        plot(xc,yc,'go',xa,ya,'r+',xb,yb,'r+',xr,yr,'g+');
        if i == 1 & j == 1, hold; end
        gamma_a = -atan2(yr-yc,xr-xc) + atan2(ya-yc,xa-xc);
        gamma_b = -atan2(yb-yc,xb-xc) + atan2(yr-yc,xr-xc);
        eta(i,j)= (omega_b^2-omega_a^2)/omega_r^2 ..
            *1/(tan(gamma_a/2)+tan(gamma_b/2));
    end
end
end
hold,axis('normal');           % free axis
pause(1);

```

```

mesh([[0*ones(5,2),eta];0*ones(2,7)]);
pause(1);
axis([1,5,0,max(max(eta))])
plot(eta);pause(1)
axis;
%disp(eta)
eta_r = mean(mean(eta));

% *****
% ***** find Modal Constant *****
% *****
%A_r = 2*R0*omega_r^2*eta_r % for receptance
A_r = 2*R0*eta_r;          % for accelerance
phi_r=atan2(yr-yc,xr-xc);

% *****
% ***** compare fit by plotting *****
% *****
omega = 2*pi*f;           % radian frequency
omegat = 0.05*2*pi*max(f):2*pi*max(f)/2000:2*pi*max(f);
Inert = - omegat.^2 * A_r*sign(sin(phi_r)) ..
        ./((omega_r.^2 - omegat.^2 + sqrt(-1)*omega_r.^2*eta_r);
subplot(211);
semilogy(omegat/(2*pi),abs(Inert),...
         f(5:length(frf)),abs(frf(5:length(frf))));
plot(omegat/(2*pi),angle(Inert),...
     f(5:length(frf)),angle(frf(5:length(frf))));
subplot(111);

modal_p=[f_r;eta_r;A_r;phi_r]; % vector of returned constants

```

MAKE_ACC.M

```
function [f,frf] = make_acc(modal_p);
% function MAKE_ACC.M takes modal parameters and turns
% them into a vector of frequency and accelerance. This
% is useful for plotting the results of extracted modal
% parameters.
% Usage
%     [f,frf] = make_acc(modal_parameters)
%
% where
%     modal_parameters = [ f_r1  f_r2  f_rn
%                          eta_r1 eta_r2 eta_rn
%                          A_r1  A_r2  A_rn
%                          phi_r1 phi_r2 phi_rn ]
%
% f_rn is the resonance frequency in Hertz, eta_rn is the
% loss factor, A_rn is the modal constant, and phi_r is the
% angle of the modal constant.

n_peaks = size(modal_p);
n_peaks = n_peaks(2);

f_max = 1.2*modal_p(1,n_peaks);
f = (0:f_max/2048:f_max)';
omega = 2*pi*f;
frf = 0*ones(length(f),1);
for i = 1:n_peaks,
    omega_r = 2*pi*modal_p(1,i);
    eta_r = modal_p(2,i);
    A_r = modal_p(3,i);
    phi_r = modal_p(4,i);
    frf = frf - (omega.^2 * A_r*sign(sin(phi_r))) ..
        ./ (omega_r.^2 - omega.^2 + sqrt(-1)*omega_r.^2*eta_r);
end
```

D.2.4 PATMATCH.M

```
function [location,force,er] = patmatch(unknown)
% Function PATMATCH.M takes four unknown modal constants
% and compares them with database in file DATABASE.MAT.
% it reports the estimated impact location.
% Usage
%      [location,force,error] = patmatch(modal_constants);
load database
if(max(size(unknown)) ~= 4)
    disp('function PATMATCH requires 5 modal constants')
end

for i = 1:14,
    AA = A(1:4,i);
    b = unknown(1:4);
    x(i) = inv(AA'*AA)*AA'*b;    % pseudo inverse
    e = b - AA*x(i);
    er(i) = e'*e;
end
plot(er)
[location,l_index] = min(er(1:14));
location = l_index;
force = x(l_index);
```